Information as a Hydrodynamic Slow Mode: Operator Spreading in the Memory Matrix Formalism

by

Ewan McCulloch

A thesis submitted to the
University of Birmingham
for the degree of
DOCTOR OF PHILOSOPHY

School of Physics and Astronomy
College of Engineering and Physical Sciences
University of Birmingham
July 4, 2022

ABSTRACT

The study of many-body quantum systems is an incredibly diverse and active field of research, connecting many disparate fields, from condensed matter systems to quantum gravity and black hole physics. Understanding the far-from-equilibrium physics of these systems is of particular importance as state-of-the-art experimental platforms now allow for exceptional control over many-body dynamics. A focal point in the study of far-from-equilibrium many-body physics is the quantum foundation of statistical mechanics, and in quantum chaos and thermalisation in particular. In this thesis we investigate a concept closely related to thermalisation, known as scrambling, which explains the apparent loss of the initial state data as the 'hiding' of information in increasingly non-local and difficult to measure observables. In systems with local interactions, information (and operators) spreads ballistically, at a speed set by the *butterfly velocity*. We show that a standard hydrodynamical tool, the memory matrix formalism (MMF), can be repurposed to investigate the transport of quantum information, making explicit the connection between operator spreading and hydrodynamics. By viewing information as hydrodynamical slow mode in the MMF, the ballistic spreading of information is natural on symmetry grounds. This new perspective also serves as a starting point for the perturbative calculation of information transport. Much of what is known about operator spreading is restricted to minimally structured models, where almost all of the spatio-temporal structure (such as spatial and time translation symmetries) has been relinquished. In this thesis, we apply the MMF to different one-dimensional circuit models with large local Hilbert space (dimension q), each with different spatio-temporal symmetries, and compute information

transport coefficients perturbatively in the small parameter $1/q$. We find that both spatial and time translation symmetries lead to an enhancement of information transport.

DEDICATION

This thesis is dedicated to my parents for their enduring support.

ACKNOWLEDGEMENTS

First and foremost, I must thank my supervisor, Dr Curt W. von Keyserlingk, without whom I could not have completed this thesis. His insight, patience, and encouragement is deeply appreciated and have made working with him a wonderful and joyful experience. I also thank the theoretical physics research group who have helped my development as a physicist and my fellow post graduate researchers, who always kept spirits high. I must also thank Prof. Frank Pollmann and Dr Tibor Rakovszky for their many interesting and insightful discussions.

CONTENTS

CHAPTER 1

INTRODUCTION

Quantum mechanics shapes the world around us, determining the behaviour of fundamental particles and underpinning the technologies we rely on everyday. Developments in semiconductor technology has driven the information age for over half a century, making possible the LED, computers and smart phones. Quantum mechanics will undoubtedly also underpin the technologies of the future – there is already an enormous collective effort in the development of quantum computation and quantum cryptography.

Although the discovery of quantum mechanics is now over a century old, quantum phenomena continue to surprise us to this day. There is perhaps no better example of this than the field of quantum many-body physics, where microscopic degrees of freedom working in concert give rise to a myriad of complex phenomena, from superconductivity to nuclear fusion. The recent discovery of the fractional quantum Hall effect, topological insulators and, more generally, topologically protected phases has caused us to rethink Landau's theory of phase transitions and led to a broader and richer understanding of equilibrium phases of matter. Far-from-equilibrium many-body dynamics offers an even more diverse zoo of behaviours, distinct from near-equilibrium phenomena and insusceptible to equilibrium methods. This field has seen an explosion of interest, leading to the prediction and observation of exotic dynamical behaviours including quantum dynamical phase transitions (QDPT) [1–9], prethermalisation [10, 11], anomalous transport in spin

chains [12–17] and period doubling in time crystals [18–20].

A focal point for research in far-from-equilibrium many-body dynamics is in the quantum foundation of statistical mechanics. This has been spurred on by the ultra cold atom and trapped ion experimental platforms, which allow for excellent control over state preparation and real time evolution. The ability to separate the system and environment with a high degree of precision makes these platforms uniquely positioned for precision measurements in closed quantum dynamics [21–24], while the control over real time dynamics enables near exact time reversed evolution [25–27], an important tool when studying the tension between reversible microscopic evolution and the macroscopic irreversibility in statistical mechanics. Together with state of the art numerical tools, often employing matrix product state representations, these platforms have allowed physicists to pursue questions in quantum foundations with new intensity – what properties must a system have in order to thermalise and what mechanisms drive thermalisation? The pursuit of these questions in particular have led physicists to a broad classification of interacting systems as either *quantum chaotic*, *integrable* or *many-body localised*. Chaotic and integrable systems thermalise to a Gibbs ensemble and generalised-Gibbs ensemble respectively, whereas many-body localised systems fail to thermalise, retaining initial state information to arbitrary late times. The study of ergodic-localised transition and mechanisms that drive this transition remains an area of considerable interest and a source of contention in the field [28, 29].

On the localised side of the transition some analytical methods have been successfully deployed; impressively, a multi-scale perturbation theory approach [30] has been used to prove localisation (under a fairly mild assumption of limited level attraction) in sufficiently disordered one dimensional systems. Whereas individual quantum ergodic systems, having no extensive number of conserved quantities, would appear to be more challenging to study analytically. However, one can greatly simplify calculations by appealing to ensembles of systems with the same statistical properties or by studying large-N field theories which permit saddle-point approximations. One particularly powerful tool for studying strongly

ergodic systems with local interactions has been random unitary circuits [31–37]. These tools have revealed a process, known as *scrambling*, which is responsible for the delocalised of information throughout the entire system. Scrambling has also been an intense focus of research in the fields of black holes physics and holography [38–49].

The phenomenology of scrambling is remarkably universal. Regardless of the details of a (local) chaotic system, be it a chaotic spin chain, random circuit, interacting quantum field theory or otherwise, information invariably spreads ballistically through the system, with a velocity referred to as the *butterfly velocity*. This fact is closely connected to the universally observed linear growth of entanglement – a phenomenon we discuss further in Sec. 2.3. Another view-point re-frames this universality as a hydrodynamic equation of motion for operator spreading; it appears that in chaotic systems the size of (i.e., the support set of) Heisenberg evolved operators obeys a biased diffusion equation [32, 33] (with modified tails in the presence of conserved quantities [34,35], i.e., energy or charge).

In this thesis we investigate the hydrodynamics of information in a variety of circuit models by viewing an often ignored symmetry of unitary dynamics – the conservation of quantum information – as a hydrodynamical mode. This thesis is organised as follows. In Chapter 2 we introduce important ideas in many-body quantum physics such as the eigenstate thermalisation hypothesis (Sec. 2.1) and hydrodynamics (including the memory matrix formalism, Sec. 2.2), as well as several important concepts in diagnosing quantum chaos (Sec. 2.3).

In Chapter 3 we view quantum information as a bona fide hydrodynamical slow mode and show that (after a technical modification) a well-known hydrodynamical formalism – the *memory matrix formalism* (MMF) – can be applied wholesale. In this formalism, we postulate a slow manifold for the spreading of information in an analogous manner to the slow manifold of locally conserved charge densities postulated in systems with a single diffusive charge. Once we choose an appropriate slow manifold, the ballistic spreading of operators, and information, becomes inevitable.

Before applying the modified MMF in a new setting, we use Chapter 4 to develop

a toolkit of Haar ensemble averaging results that will be useful for the more involved MMF calculations of Chapter 5. The memory matrix shares a lot of similarities with a self-energy, including being amenable to perturbative diagrammatic expansions. In Chapter 5 we take advantage of this by perturbatively calculating the memory matrix – and information transport coefficients (e.g., the butterfly velocity v_B) – for circuit models with varying degrees of spatio-temporal symmetry. We note that a similar approach, an effective theory of the *entanglement membrane*, has been suggested [50]. Finally, we leave concluding remarks and an outlook to future research in Chapter 6.

CHAPTER 2

PRELIMINARIES: FAR-FROM-EQUILIBRIUM DYNAMICS IN ERGODIC SYSTEMS

In this thesis, we will be concerned with the far-from-equilibrium dynamics of closed quantum ergodic systems in one-dimension. For concreteness, we choose to work on a lattice of sites with local interactions. The evolution of closed quantum systems is governed the Schrodinger equation $|\Psi(t)\rangle = U(t)\,|\Psi(0)\rangle$, where $U(t)$ is a unitary evolution operator which may be continuous in t, in the case where evolution is generated by a (possibly time dependent) Hamiltonian, or discrete, as is the case for quantum circuits where unitary gates are applied in sequence. An important fact about unitary evolution is that it maps pure states to pure states, given this fact, how is it that a closed quantum system can be described by a thermal ensemble at late times? To resolve this apparent paradox, we must relax our requirements that the full state asymptotically approaches a thermal density matrix in favour of a weaker requirement that *locally* the state approaches a local thermal density matrix. These concepts are formalised in the section below where we give

an overview of the celebrated *eigenstate thermalisation hypothesis* (ETH) [51]. While the ETH implies thermalisation, it is less transparent about a systems behaviour at intermediate times (after the initial non-universal dynamics and before eventual equilibration) and the mechanisms that drive thermalisation. To gain intuition here, quantities such as the out-of-time-ordered correlator and more recently, measures of operator spreading, have been introduced as a means of quantifying scrambling and as direct measures on the delocalisation of initially local observables. In the following, we discuss these quantities in a general context as well as in the specific context of random unitary circuits. Haar unitary ensembles are an important tool in random circuit analysis and also heavily used in this thesis and will also be discussed in this chapter. Finally, we introduce a standard hydrodynamical tool – the memory matrix formalism – that, as well as giving qualitative predictions for transport, will serve as a platform for the perturbative calculation of transport coefficients in Chapter 5.

2.1 Thermalisation and the eigenstate thermalisation hypothesis

Statistical mechanics is enormously successful at describing the macroscopic observables of a system at (or near) equilibrium, distilling the microscopic details of a system into only a handful of useful macroscopic properties (temperature, pressure, etc). In *classical* systems, ergodicity is often invoked, drawing a connection between time averages and (thermal) ensemble averages: the long time average of an observables agrees with the thermal average in systems that uniformly sample their accessible phase space. This form of thermalisation is known as *weak* thermalisation [52] and requires times exponentially large in the number of degrees of freedom of the system for time averages to converge to thermal averages. For many-body systems these times are far larger than any experimentally relevant timescale. What we would prefer to prove is known as *strong* thermalisation [52], where the instantaneous values of macroscopic observables at late times are close to their

thermal values for almost all times. A refinement on ergodicity, *mixing*, places stronger requirement on dynamics and implies thermalisation[1] in the strong sense. In some cases mixing can actually be proven, most notably in chaotic billiards [53–55].

The concepts of ergodicity and mixing form the foundations of classical statistical mechanics, but how does statistical mechanics emerge in isolated quantum systems, where the dynamics are unitary? The answer is in a shift of perspective, focusing on the expectation value of local observables rather than the full state of a system. In this spirit, thermalisation (strong and weak) will now refer to the expectation values of local observables. More formally, a system prepared with an average energy E and sub-extensive energy fluctuations will thermalise (in the strong sense) if the instantaneous expectation value of any local observable relaxes to the microcanonical prediction and is close to this value for most later times. To see how thermalisation can be achieved in generic many-body systems, consider a pure state $|\Psi\rangle = \sum_n c_n |n\rangle$ evolved under a Hamiltonian H. The time evolved state is given by

$$|\Psi(t)\rangle = \sum_n c_n e^{-\mathrm{i}E_n t} |n\rangle \,, \tag{2.1}$$

where E_n are the energy eigenvalues associated with H, $H|n\rangle = E_n |n\rangle$. The expectation value of a local observable $\hat{\mathcal{O}}$ is given by

$$\langle \mathcal{O} \rangle(t) \equiv \langle \Psi(t)| \hat{\mathcal{O}} |\Psi(t)\rangle = \sum_{n,m} c_n^* c_m e^{\mathrm{i}(E_n - E_m)t} \langle n| \hat{\mathcal{O}} |m\rangle \,. \tag{2.2}$$

In order for this system to thermalise in the weak sense, the long time average of $\langle \mathcal{O} \rangle(t)$, dubbed $\overline{\mathcal{O}}$, must agree with a thermal average. Assuming no degeneracies in the spectrum of H, $\overline{\mathcal{O}}$ is found to be

$$\overline{\mathcal{O}} \equiv \lim_{T\to\infty} \frac{1}{T} \int_0^T dt \langle \mathcal{O} \rangle(t) = \sum_n |c_n|^2 \langle n| \hat{\mathcal{O}} |n\rangle \equiv \mathrm{Tr}\Big(\rho_{\mathrm{DE}} \hat{\mathcal{O}}\Big), \tag{2.3}$$

[1] Mixing implies the decay of correlations that underpins the *principle of molecular chaos* (used to derivation of the Boltzmann equation and H-theorem of thermodynamics).

The final equality introduces the density matrix for the diagonal ensemble $\rho_{\mathrm{DE}} \equiv \sum_n |c_n|^2 |n\rangle \langle n|$. By contrast, the microcanonical ensemble average is given by

$$\mathcal{O}_{\mathrm{ME}}(E) \equiv \mathrm{Tr}\Big(\rho_{\mathrm{ME}}(E)\hat{\mathcal{O}}\Big), \tag{2.4}$$

where the microcanonical density matrix $\rho_{\mathrm{ME}}(E)$ is defined on a narrow energy window around E, where once again the width of the energy window δE is sub-extensive in the system volume V. Unlike the diagonal ensemble, the microcanonical ensemble is independent of the coefficients c_n. However, provided that the distribution $|c_n|^2$ is sufficiently narrow (as guaranteed by sub-extensive energy fluctuations) and the matrix elements $\mathcal{O}_{n,n} \equiv \langle n| \hat{\mathcal{O}} |n\rangle$ sufficiently smooth in energy, i.e, $\mathcal{O}_{n,n} \approx \mathcal{O}(E_n)$, then the microcanonical average and diagonal ensemble average agree up to corrections that vanish as $V \to \infty$ [56],

$$\mathrm{Tr}\Big(\rho_{\mathrm{ME}}(E)\hat{\mathcal{O}}\Big) \approx \mathcal{O}(E) \approx \mathrm{Tr}\Big(\rho_{\mathrm{DE}}\hat{\mathcal{O}}\Big). \tag{2.5}$$

Before introducing the eigenstate thermalisation hypothesis, we first seek to reassure the reader that energy fluctuations in a typically prepared state Ψ are sub-extensive. A typical eigenstate in a quantum chaotic system has a finite correlation length. In this case, the energy variance only scales linearly with system volume. I.e., for a system with local Hamiltonian $H = \sum_i H_i$, where i labels clusters of sites, the energy variance is given by

$$\mathrm{Var}(E) = \sum_{i,j} \left[\langle H_i H_j\rangle - \langle H_i\rangle\langle H_j\rangle\right]. \tag{2.6}$$

For a state Ψ with short range correlations, this sum picks out $i \approx j$. This gives $\mathrm{Var}(E) \sim V$, where V is the volume of the system (the number of lattice sites). As energy scales extensively with system volume, the energy fluctuations scale as $\frac{\sqrt{\mathrm{Var}(E)}}{\langle E\rangle} \sim 1/\sqrt{V}$. This guarantess that the diagonal and microcanonical ensemble are equivalent up to sub-extensive terms provided that $\mathcal{O}_{n,n}$ is sufficiently smooth, but we are still a long way from strong thermalisation. The missing ingredient is the eigenstate thermalisation hypothe-

sis [51], a hypothesised general form for the matrix elements of a local operator in the energy eigenbasis,

$$\mathcal{O}_{m,n} = \mathcal{O}(\overline{E})\delta_{m,n} + e^{-S(\overline{E})/2} f_{\mathcal{O}}(\overline{E}, \omega) R_{m,n}, \tag{2.7}$$

where $\overline{E} = (E_n + E_m)/2$, $\omega = E_n - E_m$ and $S(E)$ is the thermodynamic entropy at energy E. $\mathcal{O}(\overline{E})$ and $f_{\mathcal{O}}(\overline{E}, \omega)$ are a smooth $\mathcal{O}(1)$ functions, and where $\mathcal{O}(\overline{E})$ is identical to the expectation value in the microcanonical ensemble at energy $\overline{E}$. $R_{m,n}$ are random independent variables with zero mean and unit variance. We have just seen the motivation for the smooth, diagonal component of the ETH ansatz, $\mathcal{O}(\overline{E})$; the second part of the ansatz is chosen to satisfy the requirements of strong thermalisation as we will see now. The time averaged deviation of $\langle \mathcal{O}(t) \rangle$ from $\overline{\mathcal{O}}$ is given by

$$\lim_{T\to\infty} \frac{1}{T} \int_0^T \left[\langle \mathcal{O}(t) \rangle - \overline{\mathcal{O}} \right]^2 = \sum_{\substack{n,m \\ n \neq m}} |c_m|^2 |c_n|^2 |\mathcal{O}_{m,n}|^2 \leq \max_{n \neq m} |\mathcal{O}_{m,n}|^2 \propto \exp\left[-S(\overline{E}) \right]. \tag{2.8}$$

Temporal fluctuations in the expectation value of a local observable are exponentially suppressed in system volume.

The picture we have laid out here has been for a non-degenerate Hamiltonian H. The addition of symmetries introduces degeneracies to the spectrum of H, but does not jeopardise the ETH; one simply considers each symmetry sector separately. In this way the ETH appears to be remarkably general. However, the ETH does have some failings, it cannot capture higher point correlation functions such as out-of-time-ordered four-point functions [57, 58].

2.2 Hydrodynamics and slow modes

While ergodic system undergo non-universal dynamics at early times and are eventually reach thermal equilibrium at late times, the system relaxation to equilibrium has a remarkably simple and universal effective description, hydrodynamics. This effective theory describes the long wavelength, late time dynamics of conserved densities with only a

handful of parameters, the transport coefficients. Relating these transport coefficients to the details of the underlining microscopic model is highly non-trivial and extremely challenging. Nevertheless, hydrodynamics makes sweeping qualitative predictions, explaining phenomena from diffusion to superfluidity. The simplest hydrodynamical regime is that of a single conserved charge in one dimension $Q = \int dx\ \rho(x,t)$, with charge density $\rho(x,t)$. The local conservation of charge is expressed by the continuity equation

$$\partial_t \rho(x,t) + \partial_x j(x,t) = 0, \tag{2.9}$$

where $j(x,t)$ is the current density associated with the charge Q. Before this can be useful, we require a constitutive equation relating the current to the charge density. Determining appropriate constitutive models is an industry itself. However, rather than finding a constitutive model valid for all configurations of the charge, it is often enough to use the *linear approximation*, by expressing the current as a linear functional of the charge density an its derivatives[2]. The general linear constitutive equation for $j(x,t)$ is given by

$$j(x,t) = \int dt' \int dx' \mathcal{D}(x-x', t-t')\rho(x',t'), \tag{2.10}$$

where $\mathcal{D}(t,x)$ is, in general, a differential operator. One often makes the further assumption of Markovian dynamics, the assumption that the experimentally probed timescales are far larger than the memory time of the system, this assumption is encapsulated in setting $\mathcal{D}(x,t) = \mathcal{D}(x)\delta(t)$. A final approximation, motivated by studying only long wavelength deviations in the density, is to keep only the low order derivatives in $\mathcal{D}(x)$, this is known as taking the *gradient expansion* of $j(x,t)$,

$$j(x,t) = (v - D\partial_x + \cdots)\rho(x,t). \tag{2.11}$$

[2]In low dimensional ($d = 1, 2$) momentum conserving [59] or integrable systems [60], non-linearities in the constitutive equation become RG relevant, requiring a more involved treatment (i.e., by solving the KPZ equation in the case of $d = 1$).

In general, the current vanishes at equilibrium, forcing $v = 0$. However, an important exception to this is in systems with momentum conservation (i.e., Galilean or Lorentz invariance [59]), or in certain integrable systems [60], where the equilibrium current need not vanish. This is discussed shortly when incorporating non-linearities in the constitutive equation. Nevertheless, by taking $v = 0$ and neglecting (irrelevant) higher order derivatives, the constitutive equation Eq. 2.11, together with the continuity equation Eq. 2.9, yield a diffusion equation for the density $\rho(x, t)$,

$$\partial_t \rho(x,t) = D\partial_x^2 \rho(x,t). \tag{2.12}$$

This formulation of hydrodynamics, modelling only dissipation, neglects the thermal fluctuations that fluctuation-dissipation theorems (FDT) imply must exists. A more complete theory, *stochastic hydrodynamics*, models these fluctuations with a stochastic forcing term. These fluctuations are removed by coarse-graining to recover the purely dissipative hydrodynamics as the long times/wavelength theory. The one-dimensional linear stochastic diffusion equation for the density is given by

$$\partial_t \rho - D\partial_x^2 \rho + \partial_x \xi = 0, \tag{2.13}$$

where the current is given by $j \equiv -D\partial_x \rho + \xi$. The fluctuations are modelled as Gaussian white-noise,

$$\langle \xi(x,t)\xi(x',t')\rangle = \sigma^2 \delta(x-x')\delta(t-t'). \tag{2.14}$$

The fluctuation strength σ is fixed by FDT [61]. Along with the FDT, the Green-Kubo formula constitutes another way to connect the microscopic and macroscopic theories, relating thermal averages (over fluctuations) with macroscopic transport coefficients,

$$D = \int_0^\infty dt \int dx \langle j(x,t) j(0,0)\rangle. \tag{2.15}$$

Where $\langle\cdot\rangle$ is an average over thermal fluctuations. In the example of stochastic diffusion this is an average over the noise ξ. To see how non-linearities affect hydrodynamics, we write down a time-local (i.e., using the Markovian approximation) constitutive equation in the gradient expansion,

$$j(x,t) = F(\rho) - D(\rho)\partial_x\rho(x,t) + \cdots . \tag{2.16}$$

As we have already briefly mentioned, we generically expect that in ergodic systems without momentum conservation, the current must vanish at equilibrium. This requires there to be no 'Euler' contribution, $F(\rho)$, to the current[3]. Non-linearities then enter into the equation through $D(\rho)$ and at higher order terms in the derivative expansion. These non-linearities can be treated as irrelevant corrections (in the RG sense) and lead to hydrodynamic long-time tails. The stability of the diffusion fixed point is attributed to the irrelevancy of both the non-linear and higher derivative corrections.

In order to avoid the seemingly ubiquitous diffusion of charge, the Euler current $F(\rho)$ must be active. For this to occur, a system must have certain symmetry properties, for instance Galilean or Lorentz invariance [59], integrability [60], or chiral edge states [62]. For $d \geq 2$ the non-linearities in $F(\rho)$ can be treated perturbatively, yielding power-law tails $t^{-d/2}$ in the current-current correlator. These corrections are integrable and hence the Green-Kubo formula Eq. 2.15 yields a finite diffusion constant. In $d = 1, 2$, the Green-Kubo expressions formally diverge leading to infinite diffusivity. For $d = 2$ the divergence is mild (logarithmic), with the current-current correlator decaying as $(t\log(t))^{-1}$. For $d = 1$, the addition of the Euler current yields the stochastic Burgers equation, equivalent to the famed Kardar–Parisi–Zhang (KPZ) equation. Solving the Burgers equation non-perturbatively, one finds the current-current correlations have the scaling behaviour

$$\int dx\langle j(x,t)j(0,0)\rangle \sim t^{-2/3}. \tag{2.17}$$

[3]Macroscopically, the charge distribution ρ is uniform at equilibrium, with a density set by the chemical potential μ. The requirement that $j(\rho) = 0$ for all μ forces $F(\rho)$ to be the zero function.

Rather than diffusing, the charge superdiffuses, $\langle x(t)^2 \rangle \sim t^{4/3}$. The collection of models whose long-wavelength physics is determined by the KPZ equation is known as the KPZ universality class.

2.2.1 Memory matrix formalism

In the previous section we gave arguments for diffusion as an effective theory for the long-wavelength dynamics of a single conserved quantity. In this section we provide a different strategy, in which one formally divides the space of observables into fast and slow subspaces using the projection operator techniques of Mori and Zwanzig [63, 64] – also known as the memory matrix formalism. This strategy yields exact expressions for transport coefficients while making clear the effects of memory in transport, all without relying on either a quasiparticle picture or assumptions of slowly varying fields. Assuming all long-lived modes (associated with conserved or 'nearly conserved' quantities) are identified and included in the slow space, the projected 'fast' dynamics should have a short memory time, allowing for an efficient truncation of the feedback of fast processes on the slow space. These fast processes are packaged into the *memory matrix*, a quantity sharing many similarities with a self energy. In the remainder of this section we review the derivation of the memory matrix representation found in *Hydrodynamical Fluctuations, Broken Symmetries and Correlation Functions* by D. Forster [65], and specialise to the case of a single conserved charge.

The starting point, and the objects of interest, are dynamical correlation functions of conserved densities q_a,

$$C_{a,b}(t) \equiv \langle q_a q_b(t) \rangle, \tag{2.18}$$

where $\langle \cdot \rangle \equiv \mathrm{Tr}\big[e^{-\beta H} \cdot\big]/Z$ is a thermal ensemble average at inverse temperature β for a given system with Hamiltonian H. To apply the projection operator machinery, we turn this correlator into an overlap of vectors in the space of operators,

$$C_{a,b}(t) = \langle q_a^\dagger | q_b(t) \rangle = \langle q_a^\dagger | e^{it\mathcal{L}} | q_b \rangle, \tag{2.19}$$

where we have introduced the inner-product $\langle A|B\rangle \equiv \langle A^\dagger B\rangle$ and the Liouvillian superoperator $\mathcal{L}[A] \equiv [H, A] = -\mathrm{i}\partial_t A$. For the derivation that follows, the details of the inner-product $\langle\cdot|\cdot\rangle$ are not important. The memory matrix formalism can just as easily be applied to classical systems, so long as we are able to prescribe an inner-product for observables[4]. For concreteness we will assume the system to be quantum mechanical, and the observables to be Hermitian operators. The space of operators is divided into the slow space $\mathcal{P} = \mathrm{Span}(\{q_a\})$ (the space spanned by the long lived hydrodynamic modes) and the fast space $\mathcal{Q}$, the othorgonal compliment of $\mathcal{P}$[5]. In a system with conversed total z-component of spin and no other conserved quantities, the slow variables are the local densities Z_j, $\mathcal{P} = \mathrm{Span}(\{Z_j\})$. Introduce also the projectors onto the slow and fast space, P and Q respectively. Before performing any formal operator manipulations, we find it convenient to Laplace transforming the correlator $C_{a,b}(t)$,

$$C_{a,b}(z) \equiv \int_0^\infty dt\; e^{\mathrm{i}z} C_{a,b}(t) = \langle q_a| \frac{i}{z+\mathcal{L}} |q_b\rangle\,, \quad \mathrm{Im}\, z > 0. \tag{2.20}$$

From here we split the dynamics into the fast and slow space by making use of the operator identity $\frac{1}{X+Y} = \frac{1}{X} - \frac{1}{X} Y \frac{1}{X+Y}$ with $X = z + \mathcal{L}Q$ and $Y = \mathcal{L}P$, finding the following

$$C_{a,b}(z) = \left\langle q_a \middle| \left[\frac{i}{z+\mathcal{L}Q} - \frac{1}{z+\mathcal{L}Q} \mathcal{L}P \frac{i}{z+\mathcal{L}} \right] \middle| q_b \right\rangle. \tag{2.21}$$

Making further use of this operator identity and the orthogonality of the fast and slow spaces, the spectral function $C_{a,b}(z)$ is given by

$$C_{a,b}(z) = i\chi_{a,a'} \left[z - i\Omega + i\Sigma(z) \right]^{-1}_{a',b} \tag{2.22}$$

where repeated indices are summed over in accordance with the Einstein summation convention. We define the static susceptibility $\chi_{a,b} \equiv \langle q_a|q_b\rangle$ and the z-independent

[4] An inner-product of observables in classical systems can be fashioned from thermal ensembles averages in much the same way as we have done for quantum mechanical systems above.

[5] Orthogonal with respect to the inner-product $\langle\cdot|\cdot\rangle$.

frequency $\Omega_{a,b} \equiv \chi^{-1}_{a,a'} \langle q_{a'}|\partial_t q_b\rangle$. The memory matrix $\Sigma_{a,b}$, packaging all of the fast space processes, is defined as

$$\Sigma\left(z\right)_{a,b} \equiv \chi^{-1}_{a,a'} \langle \dot{q}_{a'}| \, Q \frac{i}{z + \mathcal{L}Q} Q \, |\dot{q}_b\rangle \tag{2.23}$$

In real time, the correlators satisfy the equation

$$\partial_t C_{a,b}(t) = C_{a,a'}(t)\Omega_{a',b} - \int_0^t dt' C_{a,a'}(t')\Sigma_{a',b}(t-t'), \tag{2.24}$$

making obvious that memory effects are stored in the memory matrix Σ. More precisely, the memory matrix sums over all processes in which a slow operator at time t' returns to the slow space at time t via a path exclusively in the fast space, such a process is shown in Fig. 2.1. On the other hand, exclusively slow processes are contained in Ω. A explicit connection to stochastic hydrodynamics can be made by using the projection operator manipulations to write

$$\partial_t \, |q_b(t)\rangle = |q_c(t)\rangle \, \Omega_{c,b} - \int_0^t dt' \, |q_c(t')\rangle \, \Sigma_{c,b}(t-t') + |\xi_b(t)\rangle \, , \tag{2.25}$$

where $|\xi_b(t)\rangle = Qe^{it\mathcal{L}Q} \, |\dot{q}_b\rangle$ is a fast variable that plays the same role as random fluctuations in stochastic hydrodynamics. For short memory times $\xi(t)$ quickly becomes uncorrelated. In the Markovian limit (zero memory time), equation 2.25 takes the form of a Langevin equation, for this reason it is known as the *generalised Langevin equation*[6] [66]. The strength of the noise term is determined by a generalised fluctuation-dissipation theorem,

$$\langle \xi_a(t')|\xi_b(t)\rangle = \langle \dot{q}_a| \, Qe^{i(t-t')\mathcal{L}Q} Q \, |\dot{q}_b\rangle = \chi_{a,a'}\Sigma_{a',b}(t-t'). \tag{2.26}$$

As we can see, the Mori-Zwanzig formalism provides both a firm foundation and clear physical picture for the framework of hydrodynamics. It is also of practical use, notably in mode-coupling theory [65], the theory of momentum relaxation [67] and more recently,

[6]One can also derive Eq. 2.24 by taking the product of the generalised Langevin equation with $\langle q_a|$.

in the theory of strange metals [68]. We will be focused on its utility as a platform for perturbative calculations of transport coefficients.

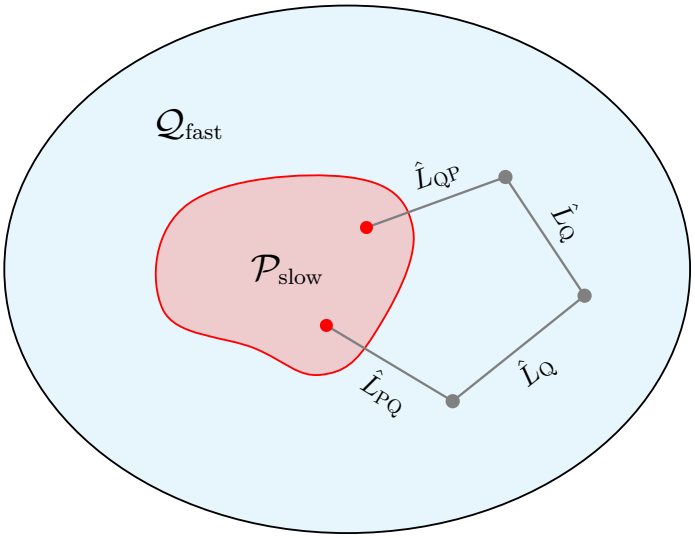

Figure 2.1: *The Hilbert space is divided into two pieces, the slow-subspace $\mathcal{P}$ and the fast-subspace $\mathcal{Q}$. L_{PQ} (L_{QP}) takes elements from $\mathcal{P}$ ($\mathcal{Q}$) to $\mathcal{Q}$ ($\mathcal{P}$) while L_Q takes elements from $\mathcal{Q}$ to $\mathcal{Q}$. This diagram shows a 'virtual process' contributing to the memory matrix, connecting two points in the slow-space via a path through the fast-space.*

The Memory Matrix in the General Diffusive Case

Following Forster, we now give a simple example which results in diffusive transport of a locally conserved quantity. Consider a system with a conserved charge Q, expressible as a sum or integral over local charge densities, an example of this is the total energy of a Hamiltonian system or the total z-component of spin in z-spin conserving models. Since we are assuming a time-independent Hamiltonian evolution, the total energy will always be conserved in addition to any other conserved charge Q. In the following, for simplicity, we assume that these modes are uncoupled. Consider then a system with a $U(1)$ conserved charge Q in the continuum, where the local densities operators are orthonormal, $\chi_{\boldsymbol{x},\boldsymbol{y}} = \langle \rho(\boldsymbol{x}) | \rho(\boldsymbol{y}) \rangle = \delta^d(\boldsymbol{x} - \boldsymbol{y})$. The slow operators are now labelled by a continuum coordinate $\boldsymbol{x}$. The long-wavelength, late-time behaviour of the dynamical correlation function $C_{\boldsymbol{x},\boldsymbol{y}}(t - t') = \langle \rho(\boldsymbol{x}, t') \rho(\boldsymbol{y}, t) \rangle$ is determined by the pole structure of the spectral function in momentum space $C(\boldsymbol{k}, z)$, the Fourier transform of Eq. 2.22. For

translationally invariant systems, the memory matrix and Ω are diagonal in momentum space, giving the simple expression

$$C(\boldsymbol{k}, z) = \frac{i}{z - i\Omega(\boldsymbol{k}) + i\Sigma(\boldsymbol{k}, z)}. \tag{2.27}$$

If we further assume that the system has time reversal symmetry $\mathcal{T}$ and that the slow operators (i.e., the local charge operators) transform identically under time reversal, $\mathcal{T}\rho(x) = \rho(x)$, then $\Omega(k) = 0$[7]. Restricting to one dimension and making use of the continuity equation Eq. 2.9 for $\rho(x,t)$, the memory matrix takes the form

$$\Sigma(k,z) = k^2\mathcal{D}(k,z), \quad \mathcal{D}(k,z) = \langle j(k)| \frac{i}{z + \mathcal{L}Q} |j(k)\rangle, \tag{2.28}$$

where we have used the fact that the current has no component in the slow space in time reversal symmetric theories to write $Q|j(k)\rangle = |j(k)\rangle$. The currents in momentum space have the normalisation convention $j(k) = \frac{1}{\sqrt{L}} \int dx e^{-\mathrm{i}kx} j(x)$, where L is the systems size. The pole is located at $iz = k^2\mathcal{D}(k,z)$, showing that (after factoring out k^2) the memory matrix is a kind of generalised diffusion coefficient. We can now use a trick [65] to express the diffusion constant in terms of the current-current correlator. Using the following resolvent operator identity,

$$\frac{1}{X+Y} = \frac{1}{X} - \frac{1}{X} Y \frac{1}{X+Y}, \tag{2.29}$$

we write

$$\Sigma(k,z) = \frac{\sigma(k,z)}{1 + \mathrm{i}\sigma(k,z)/z}, \quad \sigma(k,z) = k^2 \langle j(k)| \frac{\mathrm{i}}{z + \mathcal{L}} |j(k)\rangle. \tag{2.30}$$

Provided that we take $k \to 0$ before taking $z \to \mathrm{i}0^+$, we find the equality $\lim_{k\to 0} \Sigma(k,z)/k^2 = \lim_{k\to 0} \sigma(k,z)/k^2$. This allows us to express the diffusion constant in terms of the full (un-

[7] To see this, we insert the time reversal operator $\mathcal{T}$, using $\mathcal{T}^2 = \mathbb{1}$, into the expression for Ω, $\Omega_{\boldsymbol{x},\boldsymbol{y}} = \langle \rho(\boldsymbol{x})| \mathcal{T}^2 |\dot{\rho}(\boldsymbol{y})\rangle = -\langle \rho(\boldsymbol{x})|\dot{\rho}(\boldsymbol{y})\rangle = -\Omega_{\boldsymbol{x},\boldsymbol{y}} = 0$.

projected) evolution,

$$D = \lim_{z\to i0^+} \lim_{k\to 0} \langle j(k)| \frac{i}{z+\mathcal{L}} |j(k)\rangle = \lim_{\varepsilon\to 0^+} \lim_{L\to\infty} \frac{1}{L} \int_0^\infty dt e^{-\varepsilon t} \langle J(0)J(t)\rangle. \tag{2.31}$$

where $J = \int dx j(x)$ is the total current. This is the celebrated Green-Kubo formula.

2.3 Characterising quantum chaos

While hydrodynamics is the effective theory for both classical and quantum systems at long wavelengths and late times, there are other important concepts in classical mechanics that don't immediately carry over to quantum mechanics. One such example is classical chaos. For example, the butterfly effect, the hallmark of chaos in classical mechanics, is the phenomenon in which small differences in initial states x_0 lead to exponentially diverging trajectories $x(t)$. Conversely, the overlap of two quantum states remains constant as they are evolved unitarily. Therefore, to quantify quantum chaos, we must go beyond states overlaps. One way to do this is to use the analogy between the Poisson bracket and the commutator. Mathematically, the (classical) butterfly effect is captured by a Lyapunov exponent λ,

$$\left|\frac{\partial x(t)}{\partial x_0}\right|^2 = |\{x(t), p(0)\}|^2 \sim e^{2\lambda t}, \tag{2.32}$$

where $\{A, B\}$ is the Poisson bracket and p is the canonical momentum. By promoting the Poisson bracket to a commutator, this is generalised to an important probe of chaos in quantum mechanical systems, first studied in Ref [69], the squared commutator $C(t)$,

$$C(t) \equiv \langle |[V(0), W(t)]|^2 \rangle. \tag{2.33}$$

Where $\langle\cdot\rangle \equiv \mathrm{Tr}\left[e^{-\beta H}\cdot\right]/Z$ denotes the thermal expectation value at inverse temperature β and where $V(0)$ and $W(0)$ are generally taken to be local Hermitian or unitary operators. It has been shown that in many systems – for example, in large N models [70], kicked rotor models [71] and large spin spin-chains [72] – the squared commutator experiences

an exponential growth regime. Note that two of these systems have a semi-classical limit, in the case of large N models this is controlled by N, and by the dimension of the spin representation in spin models. By analogy with the Poisson bracket in Eq. 2.32, we identify the quantum Lyapunov exponent λ_L via

$$\langle |[V(0), W(t)]|^2 \rangle \sim e^{2\lambda_L t}. \tag{2.34}$$

A key distinction between classical and quantum Lyapunov exponents is the existence of universal upper bound on quantum Lyapunov exponents, $\lambda_L \leq 2\pi k_B T/\hbar$ [44]. Notably, black holes are conjectured to be the fastest possible scramblers in nature [38–40], saturating this bound. Taking the semi-classical limit $\hbar \to 0$, the unboundedness of Lyapunov exponents is restored. Beyond the semi-classical limit, the connection between the commutator and the sensitive dependence on initial conditions is less obvious. Nevertheless, it remains a useful characteristic for scrambling, diagnosing the spread of Heisenberg evolved operators throughout the system, and hence the spread, or scrambling, or information. Conceptually, one can think of scrambling as the hiding of the 'detailed correlations' information in the initial state among more complicated, and increasingly difficult to measure observables[8].

2.3.1 Out-of-time-ordered correlators and locality

Locality of a Hamiltonian ensures that the generated dynamics has an emergent light-cone, with 'speed of light' given by the Lieb-Robinson velocity v_{LR}. Operators sitting outside each others light-cone commute up to exponentially small errors. This result is the celebrated Lieb-Robinson bound [73]

$$||[V_x, W_y(t)]|| \leq c \exp\left(-\left(|x-y| - v_{\mathrm{LR}}|t|\right)/\xi\right), \tag{2.35}$$

[8] In systems without a sense of locality, such as an SYK dot or all-to-all coupled spins, simple (complicated) observables refer to few-body (many-body) operators. Whereas in systems with local interactions simple observables typically refer to operators that are both local and few-body.

where V_x and W_y are local and bounded operators at positions x and y respectively. This inequality also bounds the squared commutator $C(t)$; at early times the operators V and $W(t)$ commute with only exponentially small errors so that $C(t)$ is very small. Only once the operator wave-front arrives at x from y does the squared commutator become $\mathcal{O}(1)$. The time taken for $C(t)$ to reach half it's saturation value is independent of V_x and W_y and is used to define the *butterfly velocity*, v_B – the speed at which operators, and information, propagate. The Lieb-Robinson velocity represents an upper bound on v_B. The squared commutator $C(x,t) = \langle||[V_x(0), W_0(t)]||^2\rangle$ is shown in figure 2.2. The diffusively broadening wave-fronts can be understood from the perspective of operator spreading as we will see in Sec. 2.4

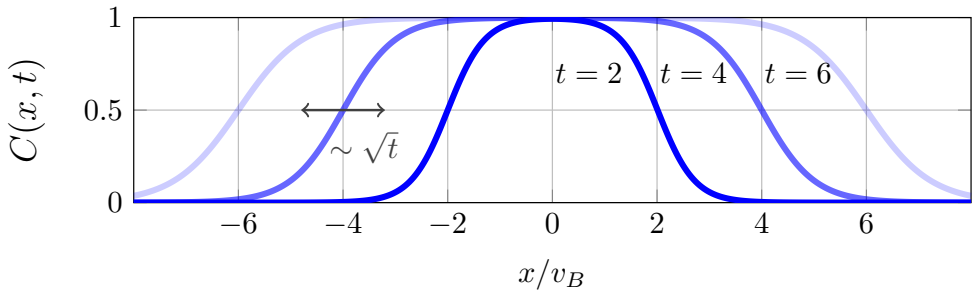

Figure 2.2: *The OTO-commutator* $C(x,t) = \langle||[V_x(0), W_0(t)]||^2\rangle$.

For V and W unitary, the squared commutator is given by

$$C(t) = 2(1 - \mathrm{Re}\, F(t)), \tag{2.36}$$

where $F(t) \equiv \langle V(0)^\dagger W(t)^\dagger V(0) W(t)\rangle$ is the *out-of-time-ordered correlator* (OTOC). Unlike time-ordered correlators, such as the two-point functions $\langle \mathcal{O}_x(0)\mathcal{O}_y(t)\rangle$ which exponentially decay with a dissipation time t_d[9] (unless these observables correspond to hydrodynamical modes), the OTOC diagnoses both the early chaotic behaviour (Lyapunov growth) and also the spreading of operators. Therefore, the OTOC remains a useful diagnostic tool for times up to the scrambling time t_* – the time at which information

[9] At short times the equilibration of local observables is characterised by a timescale t_d, $\langle A(0)B(t)\rangle_\beta = \langle A\rangle_\beta\langle B\rangle_\beta + \mathcal{O}\big(e^{-t/t_d}\big)$.

is completely scrambled throughout all the degrees of freedom of the system. In many strongly coupled systems there is a large separation of scales $t_d \ll t_*$. It is generically expected that in holographic systems the dissipation time scales as $t_d \sim \beta$ [74] and that the scrambling time t_* is parametrically larger than t_d. For instance, in large N conformal field theories, the scrambling time scales as $t_* \sim \beta \log N^2$ [41–43, 75].

2.3.2 Quantum entanglement

Another commonly used diagnostic for chaos is the growth of entanglement, quantified by entanglement entropies. The most famous example of an entanglement entropy is the *von Neumann entanglement entropy*, defined for a bi-partition of a system into subsystems A and B,

$$S_{vN}(\rho_A) = -\operatorname{Tr}(\rho_A \log \rho_A), \tag{2.37}$$

where the reduced density matrix ρ_A is the partial trace, over (the degrees of freedom of) B, of the full state ρ. The von Neumann entropy is the quantum mechanical extension of the Gibbs entropy of statistical mechanics (or Shannon entropy of classical information theory). The von Neumann entropy, and its coarse grained (classical) counterpart, is often expected to grow linearly with time. This feature appears in two distinct settings, the first being in quantum field theories [46, 47, 76–80] and interacting integrable systems [76, 81–89]. Here, a heuristic argument given by Calabrese and Cardy [76] explains this by viewing an initial highly energetic state as a source of ballistically propagating quasi-particles. The second setting is in chaotic systems, where it is generally believed that all systems with local interaction exhibit linear growth of S_{vN}. This is consistent with results from random unitary circuits [32, 33], Floquet systems [37, 90–92] and non-integrable spin chains [48, 93–96]. The von Neumann entropy is challenging to access, both in experiments and theoretical calculations. Instead, the more readily accessible Renyi entropies S_n can be used,

$$S_n(\rho_A) = \frac{1}{1-n} \log \operatorname{Tr}(\rho_A^n). \tag{2.38}$$

To measure the n-th Renyi entropy S_n, an observer must have access to n copies of the quantum state. The second Renyi entropy ($n = 2$) has been widely studied in experiment as the simplest non-trivial case, for example in quantum interference experiments [97,98]. Once all the Renyi entropies are known, the von Neumann entropy can be found by the replica trick, the analytic continuation $S_{vN} = \lim_{n\to 1} S_n$.

Surprisingly, the Renyi entropies $S_{n>1}$ are not generically expected to grow linearly with time, in the presence of a (diffusing) conserved charge S_n grow diffusively, as $\sqrt{t}$ [99]. In contrast, models with no conserved quantities, such as in random unitary circuit models, are observed to have linear growth of S_2. This is consistent with the operator spreading arguments of [48, 100], which we review in Sec. 2.4.1.

2.4 Operator spreading

We have seen arguments using both an effective hydrodynamical theory (in Sec. 2.2), and a memory matrix approach (in Sec. 2.2.1), for the universality of diffusion in systems with a single conserved charge. By viewing the conservation of information, a concept we make concrete below, as a local conservation law akin to the conservation of energy or charge, it is tempting to conclude that information will also diffuse. However, this turn out to be incorrect. In fact, information is expected to spread ballistically, with a velocity v_B – the butterfly velocity, as introduced in the context of out-of-time-ordered correlators (see section 2.3.1).

To quantify the spread of information, the *operator-weight* $\rho^O(x,t)$ is introduced, directly measuring the support (i.e., the spatial extent) of an operator $O(t)$. This, in a precise way, tells us how information stored in initially local observables is later encoded in increasingly delocalised and complex observables. With the ambition of developing a universal theory of information transport, one is led to ask whether operator spreading obeys a simple hydrodynamical equation of motion in the long-wavelength, late-time limit. In certain tractable limits, such as large N models [101–103], or by leveraging Haar

random matrix ensembles [32–35], operator growth can be studied analytically, yielding a hydrodynamic description of ballistically spreading operators and a diffusively broadening operator wave-front. Numerical studies also confirm this phenomenology in chaotic spin chains and interacting integrable systems in 1D [104], although the reasons for this apparent universality instead of KPZ universality are mysterious and deserving of further research. In section 2.5 we give a short review of operator spreading in random circuits (without symmetry[10]), finding the operator growth is described by a biased random walker. But first we must define the operator-weight, and motivate it's use a diagnostic of operator growth.

Before generalising to arbitrary spin, we consider operator spreading for a spin-1/2 chain. To do this, we express an operator $O(t)$ as a sum over Pauli strings σ^s, i.e., tensor products of Pauli operators on each site of the spin chain. An example of a Pauli string is given below, where the tensor product is made implicit by site labelling,

$$\cdots X_{j-2}Z_{j-1}\mathbb{1}_j Z_{j+1}Y_{j+2}\cdots . \tag{2.39}$$

The operator $O(t)$ can then be expressed as a linear combination of strings $\sigma^s = \sigma_1^{s_1}\sigma_2^{s_2}\sigma_3^{s_3}\cdots$, where $s_i \in \{0,1,2,3\}$ and $(\sigma^0,\sigma^1,\sigma^2,\sigma^3) = (\mathbb{1},X,Y,Z)$,

$$O(t) \equiv U^\dagger(t)OU(t) = \sum_s C_s^O(t)\sigma^s. \tag{2.40}$$

In the second equality only the coefficients $C_s^O(t)$ depend on time. We have normalised O such that $\sum_s |C_s^O|^2 = 1$. Following the work of [32, 33], we define the right-operator-weight $\rho_R^O(x,t)$ (the probability of an operator having right endpoint at position x at time t) by

$$\rho_R^O(x,t) \equiv \sum_s |C_s^O(t)|^2 \delta(\mathrm{Rhs}(s) - x), \tag{2.41}$$

where $\mathrm{Rhs}(s)$ denotes the rightmost site on which the Pauli string has non-trivial support.

[10] In $U(1)$ conserving circuits, the operator weight has long time tails and a diffusive component that has significant overlap with the conserved densities [34, 35]

An obvious consequence of unitarity is the conservation of the operator-weight[11],

$$\sum_x \rho_R^O(x,t) = \sum_x \sum_s |C_s^O(t)|^2 \delta(\mathrm{Rhs}(s) - x) = \sum_s |C_s^O(t)|^2 = 1. \tag{2.42}$$

The same steps can be taken for lattices with arbitrary single-site Hilbert space dimension q, $\mathcal{H}_{local} = \mathbb{C}^q$. The operator basis on each site is then replaced by the generalised Pauli matrices – those matrices generated by the shift and clock matrices X and Z, $\sigma^\mu = X^{\mu^{(1)}} Z^{\mu^{(2)}}$, where $X^q = Z^q = \mathbb{1}$ and $ZX = e^{\frac{2\pi \mathrm{i}}{q}} XZ$. For a one-dimensional lattice of L sites, the generalised Pauli strings form an orthonormal basis, with orthogonality relation $\mathrm{Tr}\big(\sigma^{s\dagger}\sigma^{s'}\big)/q^L = \delta^{s,s'}$. We express $O(t)$ as a sum over generalised Pauli strings in the same way as in the spin-1/2 case (Eq. 2.40), to once again write

$$O(t) = \sum_s C_s^O(t)\sigma^s, \tag{2.43}$$

except that now the string labels $s = (s_1, s_2, \cdots)$ take values $s_i \in \{0, 1, \cdots, q^2 - 1\}$. Equations 2.41 and 2.42 are also modified to have the sums over generalised strings s.

Because of the locality of the evolution, the operator weight is locally conserved. This is summarised in the continuity equation

$$\partial_t \rho_R(x,t) + \Delta_x J(x,t) = 0, \tag{2.44}$$

where J is the operator-weight current and Δ_x is the discrete spatial derivative. This is equivalent to the continuum equation $\partial_\tau \rho_R(r,\tau) + \partial_r J(r,\tau) = 0$ in the long wavelength, late time limit, with coarse grained coordinates τ and r. This limit permits gradient expansions in the coarse grained density ρ, resulting in a constitutitve equation for J,

$$J(x,t) = (v_B - D\partial_x + \cdots)\rho(x,t). \tag{2.45}$$

Unlike with diffusive charges, the Euler contribution is does not vanish, $F(\rho) = v_B$. Given

[11] This is nothing more than the conservation of Hilbert-Schmidt norm.

that the Euler current does not vanish, it is not clear why non-linear corrections do not put one-dimensional operator spreading into the KPZ universality class. Answering this question is left for future work.

This constitutive equation gives the anticipated biased diffusion equation for the operator weight,

$$\partial_t \rho_R(x,t) + v_B \partial_x \rho_R(x,t) - D\partial_x^2 \rho_R(x,t) = 0. \tag{2.46}$$

2.4.1 Operator growth implies entanglement growth

The growth of operators throughout a system provides a mechanism for entanglement growth. In this section we follow and review the arguments in [48, 100], where it is argued that 'linear in t' growth of the second Renyi entropy (in the absence of diffusive conserved charges) is a direct consequence of ballistic operator spreading. We will consider a one-dimensional spin-1/2 system, divided into two semi-infinite chains A and B by a *cut* at middle of the chain $x = 0$. For simplicity, we choose an initial state to be the spin polarised state $|\uparrow\uparrow\cdots\uparrow\rangle$. The density matrix is then given by

$$\rho = \prod_j \frac{\mathbb{1} + \sigma_j^z}{2} = \frac{1}{2^L} \sum_{z \text{ strings } s} \sigma^s, \tag{2.47}$$

where the sum is over strings s of identity and σ^z matrices. By evolving each string for time t and expanding each in the basis of Pauli strings, the state after time t is given by

$$\rho(t) = \frac{1}{2^L} \sum_{z\text{-strings } s} \sum_{\text{strings } s'} C_{s\to s'}(t)\sigma^{s'}. \tag{2.48}$$

The reduced density matrix $\rho_A(t)$ is found by tracing over the degrees of freedom of B, this eliminates any string with support in B,

$$\rho_A(t) = \frac{1}{2^L} \sum_{z\text{-strings } s} \sum_{\text{strings } s' \in A} C_{s\to s'}(t)\sigma^{s'}. \tag{2.49}$$

The purity for the bi-partition AB, $\gamma(\rho_A(t)) \equiv \mathrm{Tr}_A(\rho_A(t)^2)$, is given at time t by

$$\gamma(\rho_A(t)) = \frac{1}{2^{L_A}} \sum_{z\text{-strings } s_1,s_2} \sum_{\text{strings } s' \in A} C_{s_1 \to s'}(t) C_{s_2 \to s'}(t), \tag{2.50}$$

where L_A is the length of the subsystem A and where we have used the orthonormality of Pauli strings $\mathrm{Tr}\big(\sigma^s, \sigma^{s'}\big) = 2^L \delta^{s,s'}$. By neglecting the off-diagonal contributions $s_1 \neq s_2$, justified by the assumption of uncorrelated signs of the operator coefficients $C_{s\to s'}(t)$, this simplifies to

$$\gamma(t) \approx \frac{1}{2^{L_A}} \sum_{z\text{-strings } s} \sum_{\text{strings } s' \in A} C_{s \to s'}(t)^2. \tag{2.51}$$

In the following we will ignore the diffusively broadening operator front, instead we will model operator growth only by the ballistic lengthening with velocity v_B. This assumption can be relaxed but will greatly the simplify the analysis that follows. For a string s with right end-point $\mathrm{Rhs}(s) = x$, the proportion of the operator that remains exclusively in A after time t is given by

$$\sum_{s' \in A} C_{s \to s'}(t)^2 = \begin{cases} 1 & \text{if } x + v_B t < 0, \\ 0 & \text{otherwise.} \end{cases} \tag{2.52}$$

Eq. 2.50 for the purity then becomes

$$\gamma(t) \approx \frac{1}{2^{L_A}} \sum_{z\text{-strings } s} \theta(-\mathrm{Rhs}(s) - v_B t) = 2^{-v_B t}. \tag{2.53}$$

With this operator growth model, the second Renyi entropy is growths linearly with time,

$$S_2(t) = -\log(\gamma(t)) \approx v_B t. \tag{2.54}$$

This model of operator growth predicts that the entanglement velocity, $v_E \equiv dS/dt$, is equal to the butterfly velocity. However, we in fact expect $v_E < v_B$ [48]. The mistake we made was in assuming that operators grow exactly at the rate set by v_B, allowing the

operator front to broaden yields the inequality $v_E < v_B$.

2.5 Random unitary circuits

Random unitary circuits have been used extensively in the study of operator spreading [32–35, 105] and chaotic dynamics more generally [31, 106–109]. These models relinquish the time-translation symmetry of Hamiltonian models, replacing it with layers of local unitary gates, as shown in Fig. 2.3 for a circuit with two-local gates. By independently choosing each gate from a random distribution, we retain only the most basic properties of local ergodic systems, unitarity and locality. These minimally structured models offer a simplified setting for investigating entanglement and operator dynamics. In particular, by studying circuit averaged quantities, many exact analytical results can be obtained, including exact formulas for the OTOC and entanglement entropies. Importantly, random circuits are not only a platform for analytic calculations; many of the insights gained, such as the diffusive broadening of the operator wave-front, are thought to be universal in ergodic systems. This is borne out in studies of circuits with additional structure, such as $U(1)$ conserving circuits [34, 35]. However, the role that additional spatio-temporal structure plays in scrambling and transport remains largely mysterious. In chapter 5 we will investigate the consequences of spatio-temporal symmetries on operator spreading by studying circuits with spatial translation and Floquet time translation symmetries.

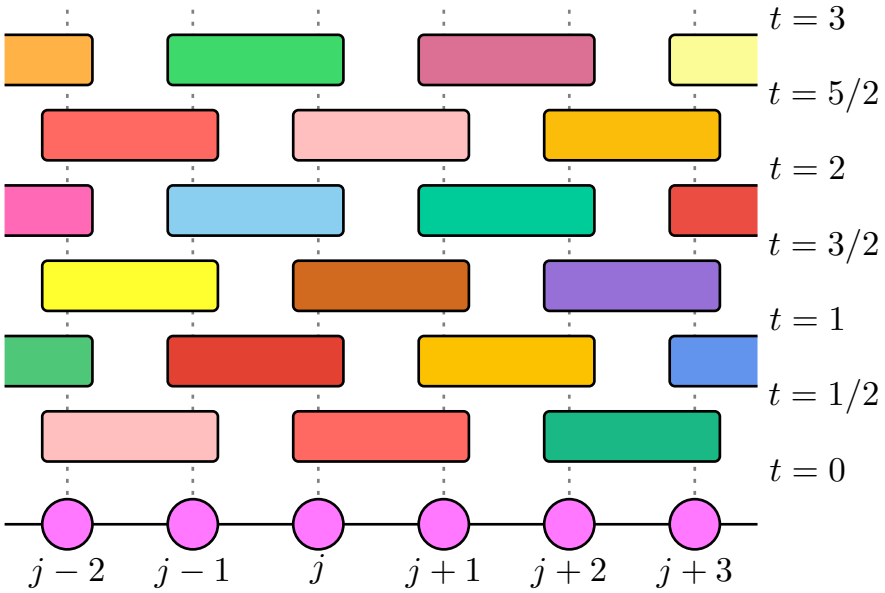

Figure 2.3: *The structure of a local unitary circuit with two site gates. The different colours represent the randomness in unitary gates chosen from the Haar distribution [33].*

The random circuits considered in [32,33] have no conserved quantities other than the conservation of quantum information guaranteed by unitarity. The absence of any locally conserved densities such as charge or energy simplifies the models hydrodynamic description. Instead of a potentially coupled set of hydrodynamical modes, the information mode (ρ_R) evolves according to a single hydrodynamic equation of motion, as seen already in Eq. 2.44 and 2.45. In section 2.5.2 we will compute the circuit averaged operator weight $\langle \rho_R \rangle$ exactly and find a simple hydrodynamic description of biased diffusion. However, before doing this, we briefly review the tools – in the form of random unitary ensembles – that make these calculations tractable.

2.5.1 Random unitary ensembles

Unitary gates in a random circuit are draw from an ensemble of unitaries. For gates of dimension N, unitaries are typically drawn Haar randomly from the unitary group $U(N)$, although occasionally subgroups such as the orthogonal and symplectic groups are used [105]. In the case of $U(1)$ conserving circuits (or circuits with more general conservation laws), one requires that each gate preserves certain symmetry sectors. However, in this

thesis we focus on the full $U(N)$ Haar ensemble.

Sampling uniformly from the Haar measure has the appealing property that the ensemble is left and right invariant[12],

$$\int_{U(N)} dU f(U) = \int_{U(N)} dU f(VU) = \int_{U(N)} dU f(UV), \tag{2.55}$$

for some function f and all $V \in U(N)$. The ensemble is normalised, $\int dU = 1$ and general moments are given by the formula [110, 111],

$$\int_{U(N)} dU U_{i_1,j_1} \cdots U_{i_m,j_m} U^\dagger_{j'_1,i'_1} \cdots U^\dagger_{j'_m,i'_m} = \sum_{\sigma,\tau \in S_m} \mathrm{Wg}(\sigma\tau^{-1}, N) \delta_{\boldsymbol{i},\sigma(\boldsymbol{i}')} \delta_{\boldsymbol{j},\tau(\boldsymbol{j}')}, \tag{2.56}$$

where $\delta_{\boldsymbol{i},\sigma(\boldsymbol{i}')} = \delta_{i_1,i'_{\sigma(1)}} \cdots \delta_{i_m,i'_{\sigma(m)}}$ and $\mathrm{Wg}(\sigma, N)$ are the unitary Weingarten function [110], which are given asymptotically (as $q \to \infty$) by the following [111, 112],

$$\mathrm{Wg}(q, \sigma) = \frac{1}{q^{M+|\sigma|}} \prod_{c \in C_\sigma} (-1)^{|c|-1} \mathrm{Cat}_{|c|-1} + \mathcal{O}\left(\frac{1}{q^{M+|\sigma|+2}}\right), \tag{2.57}$$

where $|\sigma|$ is the minimum number of transposition that σ can be written as a product of. C_σ is the set of cycles in σ and $|c|$ is the length of a cycle $c \in C_\sigma$. Cat_i are the Catalan numbers.

All Haar integrals with differing numbers of U's and $U^\dagger$'s vanish. Using the Weingarten function $\mathrm{Wg}((1), N) = \frac{1}{N}$, the first moment is given by

$$\int_{U(N)} dU U O U^\dagger = \langle O \rangle \mathbb{1}, \quad \langle O \rangle \equiv \frac{1}{N} \mathrm{Tr}(O). \tag{2.58}$$

In fact, only one Haar integral is needed to compute the circuit averaged operator weight, as well as other quantities whose construction uses only two replicas of the operator space such as the OTOC and the second Renyi entropy. This integral, relying on the second

[12]The Haar measure is the unique left and right invariant measure on $U(N)$.

moment of the Haar measure, is given by

$$\int_{U(N)} dU \langle UAU^\dagger B\rangle\langle UCU^\dagger D\rangle = \frac{1}{N^2-1}\left(N^2\langle A\rangle\langle B\rangle\langle C\rangle\langle D\rangle + \langle AC\rangle\langle BD\rangle \right. \\ \left. - \langle A\rangle\langle C\rangle\langle BD\rangle - \langle AC\rangle\langle B\rangle\langle D\rangle\right). \tag{2.59}$$

Using this alone, we are able to take the circuit average of operator weight $\rho_R(x,t)$, as we will do in the next section. In chapter 4 we greatly extend these results, finding large N asymptotics for Haar averaged n-point functions $\langle U^{t_1}A_1U^{t_2}A_2\cdots U^{t_n}A_n\rangle$ (both time-ordered and out-of-time-ordered) as well as products of n-point functions. This extended toolkit for Haar ensemble averages will be indispensable when studying circuits with spatio-temporal symmetries.

2.5.2 Operator spreading in local unitary circuits

In this section we will be interested in random unitary circuits with the circuit geometry of Fig. 2.3, where the layers of even-odd gates (gates U_i straddling sites $\{i, i+1\}$ for even i) occur on half-integer time-steps $t \in \{1/2, 3/2, \cdots\}$, and the odd-even gates on integer steps $t \in \{1, 2, \cdots\}$. Each gate is a Haar-random $q^2 \times q^2$ unitary matrix. Following the analysis of [32, 33], we will compute the circuit averaged operator weight, finding its dynamics to be that of a random walk. Using Eq. 2.41 and starting with a local operator O, the operator weight at time t is given by

$$\rho_R^O(x,t) = \sum_s |C_s(t)|^2\,\delta(\mathrm{Rhs}(s)-x), \quad C_s(t) = \frac{1}{q^L}\,\mathrm{Tr}(O(t)\sigma^s). \tag{2.60}$$

As in Sec. 2.4, the σ^s are generalised Pauli strings, normalised to $\mathrm{Tr}\left(\sigma^{s\dagger}\sigma^{s'}\right) = \delta^{s,s'}q^L$ where L is the system length. The coefficient $|C_s(t)|^2$ at time t can be related to previous

(half) time-step via the following equation,

$$\begin{aligned}|C_s(t)|^2 &= \frac{1}{q^{2L}}\sum_{p,p'} C_p(t-1/2)C_{p'}(t-1/2)^* \operatorname{Tr}\left(U_t^\dagger \sigma^p U_t \sigma^s\right)\operatorname{Tr}\left(U_t^\dagger \sigma^{p'\dagger} U_t \sigma^{s\dagger}\right), \\ &= \frac{1}{q^{2L}}\sum_{p,p'} C_p(t-1/2)C_{p'}(t-1/2)^* \prod_j \operatorname{Tr}\left(U_{t,j}^\dagger \sigma^p U_{t,j} \sigma^s\right)\operatorname{Tr}\left(U_{t,j}^\dagger \sigma^{p'\dagger} U_{t,j} \sigma^{s\dagger}\right),\end{aligned} \tag{2.61}$$

where U_t is the t-th layer of unitary gates, $U_t = \prod_j U_{t,j}$, with j taking odd values for integer t and even otherwise. We are interested in circuit averaged quantities as opposed to any particular circuit realisation, this allows to take the Haar average of the above expression. To do this, we use Eq. 2.59, which for a single (two-site) Haar random unitary $U \in U(q^2)$, reads as

$$\int_{U(q^2)} dU \operatorname{Tr}\left(U^\dagger \sigma^b U \sigma^a\right)\operatorname{Tr}\left(U^\dagger \sigma^{b'\dagger} U \sigma^{a\dagger}\right) = \frac{q^4}{q^4-1}\delta^{b,b'}\left(q^4\delta^{b,1}\delta^{a,1} + 1 - \delta^{b,1} - \delta^{a,1}\right). \tag{2.62}$$

The operators σ^a, σ^b and $\sigma^{b'}$ are all two-site Pauli strings. Using this, we are able to take the circuit average of Eq. 2.61, finding a linear equation for the circuit averaged quantity $P_s(t) = \overline{|C_s(t)|^2}$,

$$P_s(t) = \sum_{s'} W^\alpha_{s,s'} P_{s'}(t-1/2), \tag{2.63}$$

where α labels the parity of the t-th layer ($\alpha = E$ for half-integer t and $\alpha = O$ for integer t[13]) and where the matrix $W^\alpha_{s,s'}$ is given by

$$W^\alpha_{s,s'} = \prod_j \frac{1}{q^4-1}\left(q^4\delta^{s_j,1}\delta^{s'_j,1} + 1 - \delta^{s_j,1} - \delta^{s'_j,1}\right). \tag{2.64}$$

In the above equation for $W^\alpha_{s,s'}$, we have decomposed the Pauli strings σ^s into a product of two-site Pauli strings σ^{s_j}, $\sigma^s = \prod_j \sigma^{s_j}$, where j is either even (when $\alpha = E$) or odd (when $\alpha = O$) and labels the site clusters $\{j, j+1\}$. By combining the half time-steps to

[13]This distinction between integer and half-integer time-steps is necessary due to the alternating (even and odd) nature of the unitary layers

form full time-steps, we arrive at

$$P_s(t) = \sum_{s'} W_{s,s'} P_{s'}(t-1), \tag{2.65}$$

where $W_{s,s'} = \sum_{s''} W^E_{s,s''} W^O_{s'',s'}$ can be interpreted as a transition matrix in a Markov process. In particular, $W^\alpha_{s,s'}$ determines the probability that a Pauli string $\sigma^{s'}$ is transformed into a string σ^s after being updated (by a half time-step). A crucial observation allows us to reduce this classical stochastic process of Pauli strings into a process on the support set of the strings.

This observation is that the transition amplitudes $W^\alpha_{s,s'}$ are invariant under rotations of each two-site pair – all non-identity two-site strings are equivalent after the random rotation of a Haar random unitary gate. Without loss of generality, consider a half-integer step t. In this step, gates are applied across sites $\{j, j+1\}$ where j is even. $W^E_{s,s'}$ tells us that on every pair of sites $\{j, j+1\}$, the identity string $\mathbb{1}$ is mapped to itself with probability 1. Whereas any non-identity string is mapped to all non-identity strings with equal probability, $1/(q^4-1)$. This is consistent with simple counting, there are q^4-1 non-identity Pauli strings on two sites. For x and $2t$ of the same parity, the support of the string s updates as

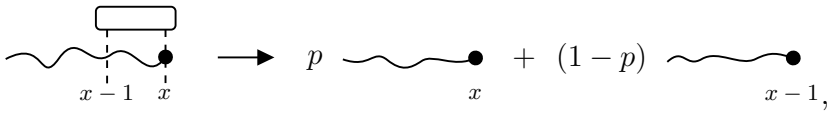

where $p = \frac{q^2}{q^2+1}$. Otherwise, for x and $2t$ with differing parities, the support of s updates as

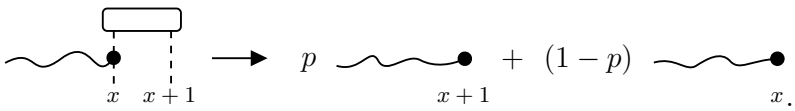

Putting the two half time-steps together, we find that for even x, the update rule for

the circuit averaged operator weight $\overline{\rho} \equiv \overline{\rho_R}$ is given by

$$\begin{aligned}\overline{\rho}(x, t+1) &= p^2 \left[\overline{\rho}(x-2, t) + \overline{\rho}(x-1, t)\right] + p(1-p)\left[\overline{\rho}(x, t) + \overline{\rho}(x+1, t)\right], \\ \overline{\rho}(x-1, t+1) &= p(1-p)\left[\overline{\rho}(x-2, t) + \overline{\rho}(x-1, t)\right] + (1-p)^2\left[\overline{\rho}(x, t) + \overline{\rho}(x+1, t)\right].\end{aligned} \tag{2.66}$$

We are able to remove the pesky parity dependence by combining the sites $2r$ and $2r+1$ into cells and defining the operator weight for the cell position r, $\tilde{\rho}(r, t) = \overline{\rho}(2r, t) + \overline{\rho}(2r+1, t)$. Using Eq. 2.66, $\tilde{\rho}$ updates in the following simple way,

$$\tilde{\rho}(r, t+1) = p^2 \tilde{\rho}(r-1, t) + 2p(1-p)\tilde{\rho}(r, t) + (1-p)^2 \tilde{\rho}(r+1, t). \tag{2.67}$$

This is an equation for a random walk (depicted in Fig. 2.4) with drift velocity $v = p^2 - (1-p)^2 \frac{\Delta r}{\Delta t}$ and diffusion constant $D = p(1-p)\frac{\Delta r^2}{\Delta t}$ (using the convention $\langle r^2 \rangle - \langle r \rangle^2 = 2Dt$). Using $\Delta r = 2$ for the real separation of lattice points in Fig. 2.4 (accounting for width of the cells $\{2r, 2r+1\}$) and $\Delta t = 1$ for duration of a time-step, we find that operators spread with butterfly velocity v_B and operator front diffusion constant D given by

$$v_B = 2\frac{q^2 - 1}{q^2 + 1}, \quad D = \frac{4q^2}{(q^2+1)^2}. \tag{2.68}$$

To connect this with the results in [32], where the unitary layers of two site gates are labelled by integers times τ (a rescaling of time by a factor of 2), we simply take $\Delta t = 2$. In the hydrodynamic limit, the operator weight obeys a biased diffusion equation, just as we argued for in Sec. 2.4.

$$\partial_t \overline{\rho}(x, t) + v_B \partial_x \overline{\rho}(x, t) - D\partial_x^2 \overline{\rho}(x, t) = 0. \tag{2.69}$$

The solution to this equation is the Gaussian wave-packet

$$\overline{\rho}(x, t) = \frac{1}{\sqrt{D\pi t}} \exp\left[-\frac{(x - v_B t)^2}{4Dt}\right]. \tag{2.70}$$

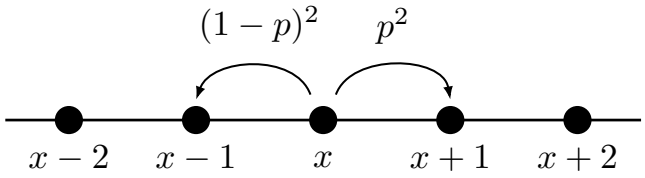

Figure 2.4: *A schematic for a biased random walk on a 1D lattice with probabilities p^2 of hopping to the right, $(1-p)^2$ of hopping to the left and $2p(1-p)$ of staying on the same site.*

All that we have discussed for the right-endpoint distribution ρ_R also applies to left-endpoints. We plot the (circuit averaged) left and right operator weights $\overline{\rho}_{R/L}$, as well as the integrated weights $R(x,t) = \sum_{y\leq x}\overline{\rho}_R$ and $L(x,t) = \sum_{y\geq x}\overline{\rho}_L$, in figure 2.5. As discussed previously, this story is modified in the presence of a conserved $U(1)$ charge; the (diffusive) conserved components acts as a source of non-conserved operators, giving rise to power-law tails in the operator weight.

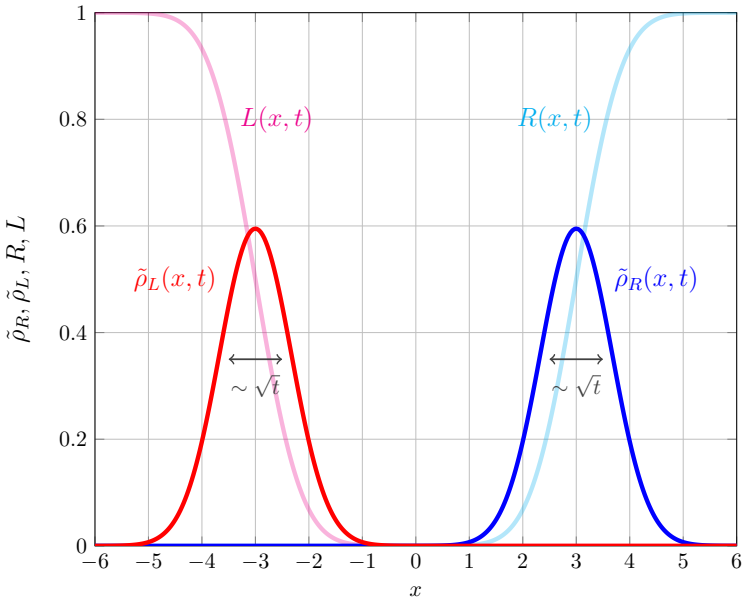

Figure 2.5: *The spreading after time $t/v_B = 3$ of a single-site operator initially at $x = 0$. $\tilde{\rho}_R(x,t)$ ($\tilde{\rho}_L(x,t)$) is the operator weight of right(left)-end-points and $R(x,t)$ ($L(x,t)$) is the integrated weight of right(left)-end-points.*

The geometry of the circuit imposes a maximum rate of information spreading characterised by a *light cone velocity* $v_{LC} = \frac{\Delta r}{\Delta t} = 2$ which plays a similar role as the Lieb-Robinson bound [73] does in systems with local Hamiltonians. Note that for any local Hilbert space dimension q the butterfly velocity is always smaller than the light cone

velocity $v_B < v_{LC}$.

CHAPTER 3

INFORMATION IS A SLOW MODE

REPURPOSING THE MEMORY MATRIX FORMALISM

It is suspected that in all ergodic systems, quantum information obeys a sort of hydrodynamics, with an unusual conservation law, "information conservation". We have seen this in random circuits where an operators support plays the role of a hydrodynamical slow mode, obeying a biased diffusion equation. This operator hydrodynamics is remarkably robust, having also been observed in ergodic Floquet [37, 90–92] and Hamiltonian models [93–96, 113], indicating that biased diffusion of operator support is universal in ergodic systems.

In sections 3.1 to 3.6, we closely follow the work we set out in [114] adapting the memory matrix formalism for information transport calculations. We show that information can be treated as a bona fide hydrodynamical slow mode and that after a relatively minor (but crucial) modification the MMF can be applied wholesale – once we postulate the correct slow manifold, ballistic transport is inevitable; in the same way that diffusion is inevitable in high temperature systems once charge is identified as the slow variable. We do this both for Hamiltonian and Floquet models, providing Kubo-Green formulas for

information-related transport coefficients such as the butterfly velocity and operator front diffusion constant. We also test the formalism against random circuit results in section 3.7.

3.1 Operator weight as an autocorrelation function

In order to use the MMF for information transport, we will need to express the operator weight ρ_R^O as a autocorrelation function – the starting point for the memory matrix formalism. To do this we will have to make several formal manipulations and make use of a super-operator abstraction. The first step is to introduce the *weight super-operator* $\hat{W}^x$ associated with the density ρ_R^O, analogously to the local operators associated with charge or energy density. The necessity for this super-operator abstraction stems from the fact that ρ_R^O is quadratic in the operator O.

3.1.1 The weight super-operator W^x

As in Sec. 2.5.2, we will be working with a translationally invariant one-dimensional spin chain with a single site Hilbert space $\mathbb{C}^q$. In order to write the operator weight ρ_R^O as a correlation function we will make use of a tensor diagram representation of the operator weight. To make this easier we will set up a dictionary for translating algebraic expressions into diagrams and introduce diagrammatic conventions. For operators A and B, the trace inner-product has a convenient diagrammatic representation,

$$\langle A|B\rangle \equiv \mathrm{Tr}\big(A^\dagger B\big) \equiv$$ 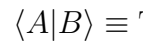

$$, \tag{3.1}$$

where the closed loop represents a trace. This can also be used to define the vectors $|A\rangle$ diagrammatically as

$$|A\rangle \equiv$$

$$. \tag{3.2}$$

For consistency, one also needs to include a convention for moving a symbol (operator) around a 'bend', reflecting that fact that the left and right indices have flipped,

$$\overline{\text{- } A \text{ -}} \equiv \overline{\text{- } A^T \text{ -}}.$$

Using this, we can write the coefficients $\left|C_s^O\right|^2 = \frac{1}{q^{2L}}\left|\mathrm{Tr}\left(O(t)^\dagger \sigma^s\right)\right|^2$ diagrammatically as

$$\left|C_s^O(t)\right|^2 \equiv \frac{1}{q^{2L}} \overline{\text{- } O(t)^\dagger \text{ -}}\, \overline{\text{- } \sigma^s \text{ -}}\,. \tag{3.3}$$

By using the above expression for $\left|C_s^O(t)\right|^2$ and the definition of the operator weight in Eq. 2.41, we arrive at diagrammatic picture for $\rho_R^O(x,t)$,

$$\rho_R^O(x,t) \equiv \overline{\text{- } O(t)^\dagger \text{ -}}\ W^x\ \overline{\text{- } O(t) \text{ -}}. \tag{3.4}$$

where we have defined the *weight super-operator* $\hat{W}^x$ diagrammatically as follows,

$$\hat{W}^x \equiv \frac{1}{q^{2L}} \sum_s \delta(\mathrm{Rhs}(s) - x)\ \overline{\text{- } \sigma^s \text{ -}}\, \overline{\text{- } \sigma^{s\dagger} \text{ -}}. \tag{3.5}$$

Denoting $\mathcal{B}$ as the vector-space of operators on the Hilbert space $\mathcal{H}$, Eq. 3.4 is given algebraically by the following,

$$\rho_R^O(x,t) \equiv \langle O(t)|\hat{W}^x|O(t)\rangle_{\mathcal{B}}, \quad \langle a|b\rangle_{\mathcal{B}} \equiv \mathrm{Tr}\left(a^\dagger b\right)\ a,b \in \mathcal{B}, \tag{3.6}$$

where $\langle\cdot|\cdot\rangle_{\mathcal{B}}$ is the infinite temperature inner-product. Algebraically, the weight super-operators are given by a (tensor) product of a operator-space projectors,

$$\hat{W}^x \equiv \frac{1}{q^L}\left(\bigotimes_{r\leq x-1} \hat{\Lambda}_r^+\right)\left(\bigotimes_x \hat{\Lambda}_x^0\right)\left(\bigotimes_{r\geq x+1} \hat{\Lambda}_r^-\right), \tag{3.7}$$

where $\hat{\Lambda}^+$ is the identity super-operator, $\hat{\Lambda}^-$ projects onto the identity operator and $\hat{\Lambda}^0$ projects onto the space of non-identity operators. The projectors $\hat{\Lambda}^\pm$ are given in terms

of generalised Pauli matrices by

$$\hat{\Lambda}^{+} \equiv \sum_{\mu} \frac{|\sigma^{\mu}\rangle\langle\sigma^{\mu}|}{q}, \quad \hat{\Lambda}^{-} \equiv \frac{|\mathbb{1}\rangle\langle\mathbb{1}|}{q}, \quad \hat{\Lambda}^{0} \equiv \hat{\Lambda}^{+} - \hat{\Lambda}^{-}. \tag{3.8}$$

We require a further abstraction to transform ρ_R^O into a correlation function. In particular, we will use the transformation from super-operators to super-super-operators $|A\rangle\langle B| \to \left|A \boxtimes B^{\dagger}\right\rangle$ (where $\boxtimes$ is a tensor product, the box shape is to distinguish it from tensor products between different sites). These new abstract vectors live in the space $\mathcal{V} \equiv \mathcal{B} \boxtimes \mathcal{B}$ of operators acting on two copies of the original Hilbert space. Diagrammatically, the elements $|A \boxtimes B\rangle \in \mathcal{V}$, are given by

$$|A \boxtimes B\rangle \equiv \begin{matrix} 1 & \overline{\quad - A \quad} \\ \overline{1} & \\ 2 & \\ \overline{2} & \overline{\quad - B \quad} \end{matrix} . \tag{3.9}$$

We have chosen to label the *legs* $1, \overline{1}, 2$ and $\overline{2}$, representing the indices of the operators A and B which act on the first and second replica respectively. An inner-product of two vectors has the obvious meaning of connecting legs,

$$\langle C \boxtimes D | A \boxtimes B\rangle \equiv \begin{matrix} \overline{\quad C^{\dagger} - A \quad} \\ \overline{\quad D^{\dagger} - B \quad} \end{matrix} \equiv \mathrm{Tr}\left(C^{\dagger}A\right) \mathrm{Tr}\left(D^{\dagger}B\right) \equiv \langle C|A\rangle \langle D|B\rangle .$$

Using this we can write $\left|C_s^O(t)\right|^2$ as the overlap of two vectors in the enlarged vector-space $\mathcal{V}$,

$$\langle O(t)|\sigma^s\rangle \langle \sigma^s|O(t)\rangle \equiv \left\langle O(t) \boxtimes O(t)^{\dagger} \middle| \sigma^s \boxtimes \sigma^{s\dagger} \right\rangle . \tag{3.10}$$

This is identical to the formal tensor diagram manipulations made below to write $\rho_R^O(x,t)$ as the overlap of two vectors,

$\langle O(t)|\hat{W}^x|O(t)\rangle_{\mathcal{B}} \equiv$ 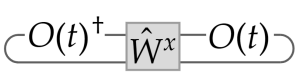

$\equiv$ 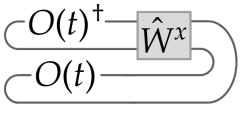

$\equiv$ 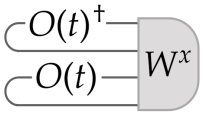

. (3.11)

Under the manipulation of Eq. 3.11, the projection super-operators $\hat{\Lambda}^{\pm}$ and $\hat{\Lambda}^{0}$ are converted into the following vectors,

$$\hat{\Lambda}^{+} \to q\,|+\rangle \equiv \frac{1}{q}\sum_{\mu}\left|\sigma^{\mu}\boxtimes\sigma^{\mu\dagger}\right\rangle, \quad \hat{\Lambda}^{-} \to |-\rangle \equiv \frac{1}{q}\,|\mathbb{1}\boxtimes\mathbb{1}\rangle, \quad \hat{\Lambda}^{0} \to q\,|0\rangle \equiv q\,|+\rangle - |-\rangle, \tag{3.12}$$

where we have chosen to normalise the vectors $|+\rangle$ and $|-\rangle$, $\langle\pm|\pm\rangle = 1$ (this introduces factors of q that differ from Eq. 3.8). The vectors $|\pm\rangle$ take a simple diagrammatic form,

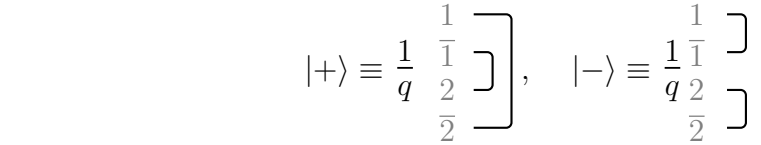

(3.13)

Using these definitions, the vectorised weight super-operator $|W^{x}\rangle$ is then given by

$$|W^{x}\rangle \equiv \frac{1}{q^{L_{>x}}}\left(\bigotimes_{r\leq x-1}|+\rangle_{r}\right)\left(\bigotimes_{x}|0\rangle_{x}\right)\left(\bigotimes_{r\geq x+1}|-\rangle_{r}\right), \tag{3.14}$$

where $L_{>x}$ is the number of sites to the right of site x. A closely related super-operator is the *purity super-operator* F^{x},

$$\hat{F}^{x} \equiv \frac{1}{q^{L_{\leq x}}}\hat{\Lambda}^{+}_{\leq x}\otimes\hat{\Lambda}^{-}_{>x}, \quad |F^{x}\rangle \equiv \left(\bigotimes_{r\leq x}|+\rangle_{r}\right)\left(\bigotimes_{r>x}|-\rangle_{r}\right), \tag{3.15}$$

where $L_{\leq x} \equiv L - L_{>x}$ is the number of sites left of, and including, site x. Using our algebra to diagram dictionary, we find that $|F^{x}\rangle$ has a simple form

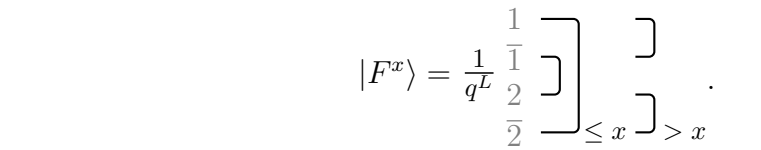

(3.16)

This diagrammatic representation makes the relationship to the purity obvious, with the leg configuration for positions $y > x$ taking a partial trace within each replica, while the legs configuration for $y \leq x$ connects the two replicas and takes a final trace over the

square of reduced density matrix,

$$q^L \left\langle \rho(t)^\dagger \boxtimes \rho(t) \middle| F^x \right\rangle =$$

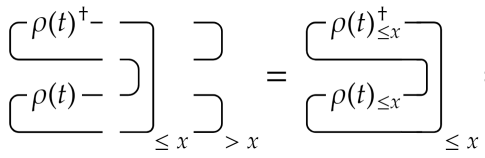

(3.17)

The purity super-operator is equal (up to an overall factor) to the integrated weight $\hat{F}^x = q^{L_{>x}} \sum_{y<x} \hat{W}^y$, or equivalently stated

$$\hat{W}^x = q^{-L_{>x}} \hat{F}^x - q^{-L_{>x-1}} \hat{F}^{x-1}. \tag{3.18}$$

3.1.2 Dynamics of W^x

The weight $\hat{W}^x$ inherits an crucially important property from the operator weight ρ_R^O; the sum of the weight super-operators is a conserved quantity,

$$q^L \sum_x \hat{W}^x = \mathbb{1}. \tag{3.19}$$

This raises the question, are the dynamics of $\hat{W}^x$ that of a locally conserved charge? To answer this, we restrict our attention to Hamiltonian dynamics with a local Hamiltonian H. Time evolution in the doubled operator space $\mathcal{V}$ is generated by a *doubled* Liouvillian $\mathcal{L} \equiv L \boxtimes \mathbb{1} + \mathbb{1} \boxtimes L$, $L(\cdot) = [H, \cdot]$, which evolves both replicas of the operator space independently. The time derivative of $\hat{W}^x(t) \equiv e^{i\mathcal{L}t}(\hat{W}^x)$ is given by $\partial_t \hat{W}^x(t) \equiv \mathrm{i}\mathcal{L}(\hat{W}^x(t))$. We can use this, and Eq. 3.18 for the relationship between the purity and weight super-operators, to write down a continuity equation for $\hat{W}^x$,

$$\partial_t \hat{W}^x + \Delta_x(\hat{J}^x) = 0, \quad \Delta_x(\hat{J}^x) \equiv \hat{J}^x - \hat{J}^{x-1}, \tag{3.20}$$

where $\hat{J}^x = -\mathrm{i}\mathcal{L}(\hat{F}^x)/q^{L_{>x}}$ is the current associated with the operator weight. The currents J^x are pseudo-local super-operators; they look, locally, like Λ^+ everywhere to the left the *cut* $\{x, x+1\}$ and Λ^- everywhere to the right. Local unitary evolution acts triv-

ially in the + and − domains. We show this by considering the action of a (single-site) Liouvillian $\mathcal{L}_i$ at site i in the + domain,

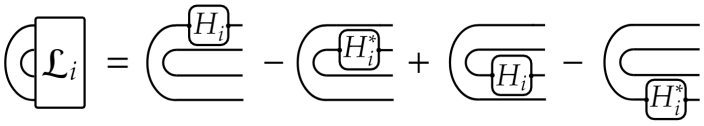

$$= 0. \tag{3.21}$$

By moving the conjugated Hamiltonians around the bend from the barred legs onto the unbarred legs, we find that the first and fourth terms cancel, as do the second and third. This can be easily generalised to l-local interactions. By swapping legs $1 \leftrightarrow 2$ in Eq. 3.21, we the find the action of $\mathcal{L}$ in the − domain. The region separating the + and − domains can only grow via the local evolution at its edges. In this sense, one can consider Eq. 3.20 to be an equation of local conservation of operator weight, and the weight super-operators to be hydrodynamical slow operators.

3.2 Operator averaging

So far we have expressed the operator weight as a dynamical correlation function (Eq. 3.6) in an abstract vector space $\mathcal{V}$. In doing so, we had to introduce the weight super-operator $\hat{W}^x$, whose dynamics is constrained by a local conservation law. In this section we will average over a choice of initial operators, and in doing so, express the (operator averaged) operator weight as a dynamical autocorrelation function of the slow (super)-operators W^x. In systems without symmetry, the operator spreading dynamics is not sensitive to the initial choice of operator and so averaging over operators with the same right endpoint x, we probe the operator-independent hydrodynamical transport (v_B, D, etc). Doing this in the basis of generalised Pauli matrices, the averaged density $\overline{\rho_R}(x, y, t)$ is given by

$$\overline{\rho_R}(x, y, t) \equiv \frac{q^{-2L_{\leq x}}}{1 - q^{-2}} \sum_{\substack{\text{strings } s, \\ \text{Rhs}(s)=x}} \left\langle \sigma^s \boxtimes \sigma^{s\dagger} \right| e^{-\mathrm{i}t\mathcal{L}} \left| W^y \right\rangle, \tag{3.22}$$

where we have pulled the time evolution out from the operators $\sigma^s(t)$. The factor $q^{-2L_{\leq x}}/(1-q^{-2})$ is normalisation for the average (the reciprocal of the number of linearly independent operators with right endpoint x). Eq. 3.22 is in fact just a dynamical correlation function between weight super-operators,

$$\overline{\rho_R}(x,y,t) = \frac{q^{2L_{>x}}}{1-q^{-2}} \langle W^x | \, e^{-it\mathcal{L}} \, |W^y\rangle \, . \tag{3.23}$$

To derive this result we write the resolution of the identity diagrammatically. For a single site, the identity super-operator is given below

$$\frac{1}{q}\sum_\mu |\sigma^\mu\rangle\langle\sigma^\mu| = \mathbb{1} \iff \frac{1}{q}\sum_\mu$$

$$. \tag{3.24}$$

Vectorising as we did in the previous section, we find the following useful identity

$$\frac{1}{q}\sum_\mu \left|\sigma^\mu \boxtimes \sigma^{\mu\dagger}\right\rangle = q\,|+\rangle \iff \frac{1}{q}\sum_\mu$$

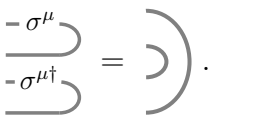

$$. \tag{3.25}$$

The operator average in Eq. 3.23 involves averaging over every generalised Pauli matrix on all sites $y < x$, and averaging over all non-identity Pauli matrices on site x. Using the above resolutions of identity we evaluate this average to find

$$\frac{q^{-2L_{\leq x}}}{1-q^{-2}} \sum_{\substack{\text{strings } s,\\ \text{Rhs}(s)=x}} \left|\sigma^s \boxtimes \sigma^{s\dagger}\right\rangle = \frac{q^{L_{>x}}}{1-q^{-2}} \, |+\rangle_{<x} \, |0\rangle_x \, |-\rangle_{>x} = \frac{q^{2L_{>x}}}{1-q^{-2}} \, |W^x\rangle \, . \tag{3.26}$$

Now that we have an autocorrelation function of our slow variables, the usual procedure is to assume translational invariance and proceed as we did in Sec. 2.2.1 for a diffusive charge. A simplifying assumption made in Sec. 2.2.1 was the orthogonality of different momentum modes under the standard thermal inner-product $\langle Q(k)|Q(q)\rangle_\beta = \langle Q(k)^\dagger Q(q)\rangle_\beta = \delta(k-q)$. It is here that we find a crucial difference between information hydrodynamics and the diffusive hydrodynamics of charge and energy. While the W^x are orthogonal, they have an x-dependent normalisation with respect to the trace inner-

product. The result of this is that the Fourier transformed weights $W^k = \frac{1}{\sqrt{L}} \sum_x e^{-ikx} W^x$ are not orthogonal,

$$\langle W^x | W^y \rangle = (1 - q^{-2}) q^{-2L_{>x}} \delta^{x,y}, \quad \langle W^k | W^{k'} \rangle = (1 - q^{-2}) \frac{e^{i\Delta_k r} - e^{i\Delta_k l}/q^2}{L(1 - e^{i\Delta_k}/q^2)}, \tag{3.27}$$

where r (l) is the position of the right (left) end of the chain of length $L = r - l$, and $\Delta_k = k - k'$. Checking the trivial case $q = 1$, so the real space weights are all normalised by the same factor, it is easy to check that the momentum space weights are orthogonal, one simply has to use $e^{i\Delta_k L} = 1$.

If we were to normalised the W^x, we would lose the simple form of the conservation law $\sum_x \hat{W}^x = \text{const.}$. Instead of doing this, we choose to restore normalisation by defining an unusual inner-product $(\cdot|\cdot)$. With respect to this inner-product the W^x are orthonormal,

$$(A|B) \equiv \langle \Phi(A) | B \rangle_{\mathcal{W}} = \text{Tr}\left(\Phi(A)^\dagger B \right), \tag{3.28}$$

where Φ is given by

$$\Phi \equiv \sum_x \frac{1}{\chi_x^2} |W^x\rangle \langle W^x| + Q, \quad \chi_x \equiv \langle W^x | W^x \rangle = \frac{q^2 - 1}{q^2 d_{>x}^2}, \implies \Phi |W^x\rangle = \frac{1}{\chi_x} |W^x\rangle . \tag{3.29}$$

Here we have already split $\mathcal{V}$ in a slow subspace $\mathcal{P} \equiv \text{Span}\{W^x\}$ and its orthogonal complement[1] – the fast subspace $\mathcal{Q}$, and associated with $\mathcal{Q}$ the projector Q seen in Eq. 3.29 above. A proof that $(\cdot|\cdot)$ satisfies the axioms of an inner-product is found in A. With this inner-product, both the position and momentum space weights form an orthonormal basis,

$$(W^x | W^y) = \delta^{x,y}, \quad \left(W^k | W^{k'} \right) = \delta^{k,k'}. \tag{3.30}$$

[1] Orthogonal with respect to the inner-product $\langle \cdot | \cdot \rangle$, or equivalently $(\cdot|\cdot)$.

In this language, the (averaged) operator weight also simplifies,

$$\rho_R(x,y,t) = \left(W^x|e^{-\mathrm{i}t\mathcal{L}}|W^y\right). \tag{3.31}$$

We must be careful with expression Eq. 3.31 as $\mathcal{L}$ is not self-adjoint with respect to this inner-product. The position dependent re-scaling of the right densities W^x by Φ reflects the strong entropic bias for operators to grow, i.e., for $y > x$ we find

$$\left(W^x|e^{-\mathrm{i}t\mathcal{L}}|W^y\right) = q^{2(y-x)}\left(W^y|e^{\mathrm{i}t\mathcal{L}}|W^x\right). \tag{3.32}$$

Operators are exponentially more likely to grow than to shrink[2].

3.3 Spectral and memory function

Now that we have expressed the operator weight as an autocorrelation function, we are able to apply the memory matrix machinery. As in the case of simple diffusion in Sec. 2.2.1, we will assume translational invariance. The upshot of this is that the operator weight and the memory matrix are diagonal in momentum space. After the resolvent operator manipulations of section 2.2.1 with the slow space $\mathcal{P} \equiv \mathrm{Span}\{W^k\}$, the spectral function $\rho_R(k,z)$ is given by[3]

$$\rho(z,k) \equiv \int_0^\infty e^{\mathrm{i}zt}\left(W^k\left|e^{-\mathrm{i}t\mathcal{L}}\right|W^k\right)dt = \frac{\mathrm{i}}{z + \mathrm{i}\Omega(k) + \mathrm{i}\Sigma(z,k)}. \tag{3.33}$$

Where $\Sigma(z,k)$ is the memory function,

$$\Sigma(z,k) = \left(W^k\left|\mathcal{L}Q\frac{\mathrm{i}}{z-\mathcal{L}Q}\mathcal{L}\right|W^k\right), \tag{3.34}$$

[2]Evolution with $\mathcal{L}$ and $-\mathcal{L}$ can give rise to differing butterfly velocities (in Sec. 3.5 we identify these as v_R and v_L, the right/left velocities).

[3]Notice that the unitary $e^{-\mathrm{i}t\mathcal{L}}$ comes with the opposite sign of t than in the correlation functions $\langle q_a|\, e^{itL}\,|q_b\rangle$ analysed in Sec. 2.2.1. This causes a difference $\Omega \to -\Omega$ between the expression presented in this section and those of Sec. 2.2.1.

and where $\Omega(k) \equiv \left(W^k \left|\mathrm{i}\mathcal{L}\right| W^k\right) = 0$. We show this in the boxed text below.

Aside: $\Omega(k) = 0$

To show that $\Omega(k) = 0$, it suffices to show that $\langle F^x| \mathcal{L} |F^y\rangle = 0$ (see Eq. 3.18). To see this, first write $\mathcal{L}$ as $\mathcal{L} = H_1 - H_{\bar{1}}^T + H_2 - H_{\bar{2}}^T$ (where the subscripts denote onto which leg the Hamiltonian H is multiplied). Diagrammatically, this looks like

$\mathcal{L} =$ 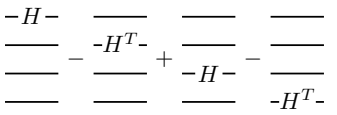 (3.35)

Evaluating $\mathcal{L} |F^y\rangle$ amounts to connecting up the outgoing barred legs ($\bar{i}$) with outgoing un-barred legs i on each site according to either configuration $|+\rangle$ or $|-\rangle$. Likewise, finding the matrix element $\langle F^x| \mathcal{L} |F^y\rangle$ involves connecting together the incoming legs according to $\langle \pm|$. On sites with the same input and output configuration, the barred and un-barred legs are closed into two loops, each representing a separate trace. Whereas, when the configurations are mismatched, the barred and unbarred legs are closed into a single loop. For any of the contributions $\langle F^x| H_i |F^y\rangle$ or $\langle F^x| H_{\bar{i}}^T |F^y\rangle$, we see that on every site, the Hamiltonian sits within a trace. This gives

$$\langle F^x| H_i |F^y\rangle = \langle F^x| H_{\bar{i}}^T |F^y\rangle = q^{-|y-x|} \operatorname{Tr}(H)/q^L. \tag{3.36}$$

Putting these together gives the desired result $\langle F^x| \mathcal{L} |F^y\rangle = 0$.

Using the k-space representation of the continuity equation Eq. 3.20,

$$\partial_t W^k \equiv \mathrm{i}\mathcal{L}\left(W^k\right) = -(1 - e^{-\mathrm{i}k}) J^k, \tag{3.37}$$

the memory function can be written as

$$\Sigma\left(k,z\right)=\mathrm{i}(1-e^{-\mathrm{i}k})\left(W^{k}\left|\mathcal{L}Q\frac{\mathrm{i}}{z-\mathcal{L}Q}\right|J^{k}\right) \tag{3.38}$$

$$=v\left(z\right)\mathrm{i}k-b\left(z\right)k^{2}+\cdots. \tag{3.39}$$

Unlike in the diffusive case, the Liouvillian $\mathcal{L}$ is not self-adjoint with respect to the inner product $(\cdot|\cdot)$, owing to the fact that in general $\mathcal{L}$ and Φ do not commute. This means that we are unable to move the $\mathcal{L}$ onto W^k in Eq. 3.38[4], picking up an additional factor of $(1-e^{\mathrm{i}k})\sim k$. In the second line we have Taylor expanded the memory function in k, identifying that the leading order term is linear in k. This gives the following pole structure

$$\rho(k,z)\sim\frac{\mathrm{i}}{z-v\left(z\right)k+\mathrm{i}b\left(z\right)k^{2}+\cdots}. \tag{3.40}$$

Provided the analyticity of $v(z)$ and $b(z)$ as $-\mathrm{i}z\to 0^{+}$, this is precisely the pole structure associated with biased diffusion. The condition for analyticity is that the fast variables J^k and $\mathcal{L}\Phi(W^k)$ have rapidly decaying correlations (faster than $1/t$).

3.4 Transport coefficients: v_B and D

Having expressed pole of the operator weight spectral function in terms of a memory function, we are now able to provide formal expression for the operator growth transport coefficients, the butterfly velocity v_B and operator front diffusion constant D.

3.4.1 Butterfly velocity v_B

Using equation (3.39), the butterfly velocity v_B is given by

$$v_{B}=\lim_{z\to\mathrm{i}0^{+}}v(z),\quad v(z)=\lim_{k\to0}-\mathrm{i}\partial_{k}\Sigma(k,z). \tag{3.41}$$

[4] $\left(W^{k}\right|\mathcal{L}=\left\langle\Phi(W^{k})\right|\mathcal{L}=\left\langle\mathcal{L}\Phi(W^{k})\right|\neq\left\langle\Phi\mathcal{L}(W^{k})\right|$.

We introduce the quantity $\sigma(k,z)$, which will act as a proxy for Σ, defined as

$$\sigma(k,z) = \left(W^k \left| \mathcal{L} \frac{\mathrm{i}}{z - \mathcal{L}} \mathcal{L} \right| W^k \right), \quad \Sigma(k,z) = \frac{\sigma(k,z)}{1 + \sigma(k,z)/z}. \tag{3.42}$$

Using $\mathcal{L}(W^k) \sim k$, we conclude that $\lim_{k\to 0} \sigma/k = \lim_{k\to 0} \Sigma/k$, provided that we take the $k \to 0$ limit before taking $z \to \mathrm{i}0^+$. Using this, we give a Green-Kubo formula for v_B,

$$v_B = \lim_{s\to 0} \int_0^\infty dt\ e^{-st} \left(W \left| \mathrm{i}\mathcal{L} \right| J(-t) \right), \tag{3.43}$$

where $J \equiv J^{k=0}$ and $W \equiv W^{k=0}$. Converting to the usual trace inner-product, we have $\left(W \left| \mathcal{L} \right| J(-t) \right) = \langle \mathcal{L}\Phi(W) | J(-t) \rangle$. As discussed previously, Φ and $\mathcal{L}$ do not in general commute. An example where $[\Phi, \mathcal{L}] = 0$ is in the case where the Hamiltonian is a sum of only 1-local terms; in this case we arrive at the correct conclusion, $v_B = 0$. Using this Kubo-Green formula, it is relatively simple to show that v_B is positive semi-definite. This is done below in the boxed text.

Aside: $v_B \geq 0$

Writing Eq. 3.43 with $\mathcal{L} = -\mathrm{i}\partial_t$ and taking the $z \to i0^+$ limit by approaching from directly above along the positive imaginary axis $z = is,\ s > 0$, the butterfly velocity is given by

$$v_B = -\lim_{s\to 0} \sum_x \int_0^\infty dt\ e^{-st}\ \partial_t^2 \left(W^0 \left| e^{-itL} \right| q^{\Delta - N} F^x \right) \tag{3.44}$$

$$= -\lim_{s\to 0} \sum_\Delta \int_0^\infty dt\ e^{-st}\ \partial_t^2 R(x,t), \tag{3.45}$$

where $R(x,t) = \sum_{y \le x} \rho_R(y,t)$ is the integrated operator weight, $0 \le R(x,t) \le 1$. Integrating by parts twice with s as a regulator and using $\langle F^y | \partial_t F^x \rangle = 0$ we find

$$v_B = \lim_{s \to 0} \; s \sum_x \left(R(x,0) - s \int_0^\infty dt \; e^{-st} \; R(x,t) \right). \tag{3.46}$$

Initially $R(x \ge 0, 0) = 1$ and $R(x < 0, 0) = 0$. We can express the integrated weight in terms of matrix elements $\langle F^y | \, e^{-\mathrm{i}t\mathcal{L}} \, | F^x \rangle$,

$$R(x,t) = q^x \left[\left\langle F^0 \right| e^{-\mathrm{i}t\mathcal{L}} \left| F^x \right\rangle - q^{-1} \left\langle F^{-1} \right| e^{-\mathrm{i}t\mathcal{L}} \left| F^x \right\rangle \right]. \tag{3.47}$$

The purity super-operators F^x are positive semi-definite (F^x is proportional to a projector, Eq. 3.15), and $e^{-\mathrm{i}t\mathcal{L}}$ is a completely positive map. This bounds the matrix element, $0 \le \langle F^y | \, e^{-itL} \, | F^x \rangle \le 1$, and in turn bounds $R(x,t)$. For $x < 0$ we have

$$|R(x < 0, t)| \le q^{-|x|}(1 + 1/q). \tag{3.48}$$

This bounds the sum over $x < 0$ in Eq. 3.46 by

$$\left| s^2 \sum_{x<0} \int_0^\infty dt \; e^{-st} \; R(x,t) \right| \le s \; \frac{q+1}{q(q-1)} \tag{3.49}$$

In the limit $s \to 0^+$ this contribution vanishes, giving an expression for v_B which includes a sum over $x \ge 0$ only.

$$v_B = \lim_{s \to 0} \; s^2 \sum_{x \ge 0} \int_0^\infty dt \; e^{-st} \; [1 - R(x,t)] \ge 0 \tag{3.50}$$

3.4.2 Diffusion constant D

Using the biased diffusion ansatz for the pole location,

$$z = v_B k - \mathrm{i}Dk^2 + \mathcal{O}\big(k^3\big), \tag{3.51}$$

the diffusion constant is given by

$$D = \lim_{z\to \mathrm{i}0^+} \lim_{k\to 0} \left(v_B \partial_z \partial_k \Sigma + \frac{1}{2} \partial_k^2 \Sigma \right). \tag{3.52}$$

In the case of v_B, we were able to exploit the fact that at $\mathcal{O}(k)$, the processes contributing to $\sigma(k,z)$ are processes that explore exclusively the fast space (hence the equivalence $\lim_{k\to 0} \sigma/k = \lim_{k\to 0} \Sigma/k$). However, at $\mathcal{O}(k^2)$ this is no longer the case and there is no similar Green-Kubo expression for D.

3.5 Operator spreading lightcone

Generically, in systems without spatial inversion symmetry, the right and left butterfly velocities are not equal [115–117], $v_R \neq v_L$. In this section we will show, using replica symmetry, that operator spreading has the structure of a lightcone. Moreover, we are able to determine sufficient conditions for symmetric operator spreading $v_L = v_R$ and $D_L = D_R$. In order to talk about left and right operator weight distributions at once, we must improve our notation. In this section, W_R^x refers to the familiar right weight super-operator used in the previous sections, whereas W_L^x refers to the left weight super-operator. Less obvious is the fact that the inner-product itself, as introduced in Eq. 3.28, is left/right dependent and therefore also now carries a label $(\cdot|\cdot)_{R/L}$. The right and left operator weight distributions are then given by

$$\rho_R^H(x,t) = \left(W_R^0 \left| e^{-\mathrm{i}t\mathcal{L}} \right| W_R^x\right)_R, \quad \rho_L^H(x,t) = \left(W_L^0 \left| e^{-\mathrm{i}t\mathcal{L}} \right| W_L^x\right)_L, \tag{3.53}$$

where we have introduced a label H for the Hamiltonian under which the system is being evolved. With the spatially inverted Hamiltonian H_I, the left and right butterfly velocities and diffusion constants are related by

$$v_L^{(H)} = v_R^{(H_I)}, \quad D_L^{(H)} = D_R^{(H_I)}. \tag{3.54}$$

This is an obvious result, but it is reassuring to see it fall out of our memory matrix expressions, as shown in the boxed section below.

The equations for v_L and D_L in terms of the memory function Σ_L (equivalent to Eq. 3.41 and Eq. 3.52 for the right velocity and diffusion constant), are given by

$$v_L^H = \lim_{z\to \mathrm{i}0^+} \lim_{k\to 0} i\partial_k \Sigma_L^H(k,z), \quad D_L^H = \lim_{z\to i0^+} \lim_{k\to 0} \left(-v_L^H \partial_z \partial_k + \frac{1}{2}\partial_k^2 \right) \Sigma_L^H(k,z). \quad (3.55)$$

In order to convert between the left and right weights, we introduce the spatial inversion operator $\mathcal{I}$, taking $x \to -x$. Under this symmetry operation, the weight super-operators and Liouvillian transform as

$$\mathcal{I} \left| W_L^x \right\rangle = \left| W_R^{-x} \right\rangle, \quad \mathcal{I}\mathcal{L}_H\mathcal{I} = \mathcal{L}_{H_I}, \quad (3.56)$$

where H_I is the spatially inversion of the (translationally invariant) Hamiltonian H. Inserting $\mathcal{I}^2 = \mathbb{1}$ ($\mathcal{I}$ is an involution) into the expression Eq. 3.53 for ρ_L allows us to convert between left and right operator weight,

$$\begin{aligned} \rho_L^H(x,t) &= \left(W_L^0 \left| e^{-\mathrm{i}t\mathcal{L}} \right| W_L^x \right)_L = \frac{1}{\chi_0} \left\langle W_L^0 \right| \mathcal{I}^2 e^{-\mathrm{i}t\mathcal{L}} \mathcal{I}^2 \left| W_L^x \right\rangle = \frac{1}{\chi_0} \left\langle W_R^0 \right| e^{-\mathrm{i}t\mathcal{L}_I} \left| W_R^{-x} \right\rangle \\ &= \left(W_R^0 \left| e^{-\mathrm{i}t\mathcal{L}_I} \right| W_R^{-x} \right)_R = \rho_R^{H_I}(-x,t), \end{aligned} \quad (3.57)$$

where $\chi_0 = \langle W_R^0 | W_R^0 \rangle = \langle W_L^0 | W_L^0 \rangle$. This implies following correspondence between the left and right operator weight memory functions,

$$\Sigma_L^H(k,z) = \Sigma_R^{H_I}(-k,z). \quad (3.58)$$

Using Eq. 3.55), this implies the physically obvious result in Eq. 3.54.

By using the swap operator $S = (1 \leftrightarrow 2)$, which exchanges the replica indices (legs) 1 and 2 on every site, we are able to show that operator spreading obeys a light-cone structure. Under the action of S, the weight super-operators transform as $S \left| W_R^x \right\rangle = \left| W_L^x \right\rangle$

and the Liouvillian transforms invariantly, $S\mathcal{L}S = \mathcal{L}$. Using this and noticing that S is an involution, we make the following observations,

$$\begin{aligned}\rho_L^H(x,t) &= \left(W_L^0 \left| S^2 e^{-\mathrm{i}t\mathcal{L}_H} S^2 \right| W_L^x\right)_L = \frac{1}{\chi_0}\left\langle W_L^0\right| S e^{-\mathrm{i}t\mathcal{L}_H} S \left|W_L^x\right\rangle = \frac{1}{\chi_0}\left\langle W_R^x\right| e^{-\mathrm{i}t\mathcal{L}_H}\left|W_R^0\right\rangle \\ &= \frac{1}{\chi_0}\left\langle W_R^0\right| e^{\mathrm{i}t\mathcal{L}_H}\left|W_R^{-x}\right\rangle^* = \left(W_R^0\left|e^{\mathrm{i}t\mathcal{L}_H}\right| W_R^{-x}\right)_R^* = \rho_R^{-H}(-x,t), \end{aligned} \tag{3.59}$$

These steps can be adjusted (as we will shortly show) to arrive at the less obvious result:

Remark. *For a translationally invariant Hamiltonian H, if there exists a transformation $\mathcal{R}$ that performs single site basis rotations, such that $\mathcal{R}^\dagger H\mathcal{R} = -H$ or $\mathcal{R}^\dagger H\mathcal{R} = H^*$, the operator growth light-cone is symmetric, $v_L = v_R$ and $D_L = D_R$.*

The second condition means that time-reversal symmetric systems have symmetric operator growth, provided that the symmetry transformation can be written as a product of single site transformations. An example of such a model is the spin-1/2 chain with $H = -\sum_{i,j}\sum_{\alpha,\beta} J_{i,j}^{\alpha,\beta}\sigma_i^\alpha\sigma_j^\beta$. By choosing $\mathcal{R} = Y^{\otimes N}$, only the terms containing a single σ^y matrix have their sign flipped, every other term remains unchanged. This has the effect of taking the complex conjugate $H \to H^*$, and so satisfies the second condition above. Another example is the non-integrable Hamiltonian studied in [115], at the point $\lambda = 0$ the Hamiltonian lacks inversion symmetry, but satisfies both of the previous sufficient conditions, explaining the symmetric operator spreading.

To show that these conditions imply symmetric operator spreading, we will use the fact that the weight super-operators are invariant under single-site basis rotations to rewrite Eq. 3.59 as

$$\rho_L^H(x,t) = \rho_R^{-\mathcal{R}^\dagger H\mathcal{R}}(-x,t), \tag{3.60}$$

where $\mathcal{R} = \prod_x R_x$ is a product of unitary rotations. Repeating this but bringing the complex conjugation onto each term in the final equality of Eq. 3.59, we instead find

$$\rho_L^H(x,t) = \rho_R^{\mathcal{R}^\dagger H^*\mathcal{R}}(-x,t). \tag{3.61}$$

Using the definitions of $v_{L/R}$ and $D_{L/R}$ in Eq. 3.41, 3.52 and 3.55, these equations imply the aforementioned symmetric operator spreading conditions.

3.6 MMF with Floquet models

In this chapter, we have so far focused on Hamiltonian evolution, and expressed operator spreading hydrodynamical transport in terms of a memory matrix. Continuing to follow the analysis in [114], in this section we generalise the MMF treatment to Floquet evolution, repeating several steps for clarity.

Consider a Floquet unitary U, the Heisenberg evolution of an operator O is given by

$$O(n) = U^{-n} O U^{n}. \tag{3.62}$$

Writing $U^{\mathrm{ad}} = l_U r_{U^{-1}}$, where l_A (r_A) is left (right) multiplication by A, allows us to rewrite the Heisenberg operator evolution as

$$O(n) = (U^{\mathrm{ad}})^{-n}(O). \tag{3.63}$$

Heisenberg evolution in the replicated operator space is then given by

$$(A \boxtimes B)(n) = (U^{\mathrm{ad}} \boxtimes U^{\mathrm{ad}})^{-n}(A \boxtimes B), \tag{3.64}$$

which can be shortened further by introducing the shorthand $\mathcal{U} = U^{\mathrm{ad}} \boxtimes U^{\mathrm{ad}}$. Evolution of a 'doubled' operator X is given simply as

$$X(n) = \mathcal{U}^{-n}(X). \tag{3.65}$$

Analogously to Hamiltonian case, the weight super-operators W^X obey a pseudo-local

conservation law,

$$\Delta_t W^k(t) = -(1 - e^{-\mathrm{i}k})J^k(t), \quad J^x \equiv q^{-L_{>x}}\mathcal{L}(F^x), \tag{3.66}$$

where Δ_t is the discrete time derivative, $\Delta_t X(t) \equiv X(t) - X(t-1) = -\mathcal{L}X(t)$, and where $\mathcal{L} = \mathcal{U} - \mathbb{1}$. By averaging over operator strings as we did in Sec. 3.2, we find the averaged operator weight ρ_R is given by,

$$\rho_R(x, y, n) = \left(W^x \middle| \mathcal{U}^n \middle| W^y\right). \tag{3.67}$$

Assuming translational invariance, the momentum-space spectral function is given in terms of a memory function $\Sigma(k, z)$ and a z-independent frequency $\Omega(k)$ (in analogy with Eq. 3.33 for Hamiltonian systems),

$$\rho(k, z) = \frac{1}{1 - e^{\mathrm{i}z}(1 + \Omega - \Sigma)}. \tag{3.68}$$

Ω and Σ are slightly modified from their Hamiltonian counterparts (Eq. 3.34),

$$\Omega(k) = \left(W^k \left|\mathcal{L}\right| W^k\right), \quad \Sigma(k, z) = \left(W^k \middle| \mathcal{L}Q\frac{-1}{e^{-\mathrm{i}z} - 1 - \mathcal{L}Q}\mathcal{L}\middle| W^k\right). \tag{3.69}$$

For discrete time evolution Ω is generally non-zero. The equation for the pole of $\rho_R(k, z)$ is,

$$z = \mathrm{i}\log(1 + \Omega(k) - \Sigma(k, z)). \tag{3.70}$$

Using this equation, the butterfly velocity and operator front diffusion constants are found to be given by

$$v_B = \lim_{z\to \mathrm{i}0^+}\lim_{k\to 0} \mathrm{i}\partial_k\left(\Omega - \Sigma\right), \quad D = -\lim_{z\to \mathrm{i}0^+}\lim_{k\to 0}\left(\partial_z\partial_k + \frac{1}{2}\partial_k^2\right)(\Omega - \Sigma) - \frac{v_B^2}{2}. \tag{3.71}$$

In order to express v_B in a Green-Kubo formula, we introduce a auxiliary quantity σ, just

as we did for Hamiltonian systems,

$$\sigma(k,z) \equiv \left(W^k \left| \mathcal{L}Q \frac{-1}{e^{-\mathrm{i}z} - 1 - \mathcal{L}} Q\mathcal{L} \right| W^k \right), \quad \Sigma = \frac{\sigma}{1 - \frac{\sigma}{e^{-\mathrm{i}z}-1-\Omega}}. \tag{3.72}$$

Once again, we use the fact that the time derivative of the weight super-operator is linear in k $\mathcal{L}(W^k) = \mathrm{i}(1 - e^{-\mathrm{i}k})J^k \sim k$, to replace $\partial_k \Sigma(k,z)$ with $\partial_k \sigma(k,z)$ in Eq. 3.71 for v_B. Splitting the current J it up into its slow and fast components $J_P^k = P(J^k)$ and $J_Q^k = Q(J^k)$, we find the following Green-Kubo formula for v_B (in Floquet systems),

$$v_B = -(W|J_P) - \lim_{s\to 0^+} \sum_{t=0}^{\infty} e^{-st} (W|\mathcal{L}Q|J_Q(-t)), \tag{3.73}$$

where $J \equiv J^{k=0}$ and $W \equiv W^{k=0}$. The asymmetry of the inner-product $(\cdot|\cdot)$ once again ensures that v_B does not in general vanish.

3.7 MMF with Random circuits

An obvious test for the formalism is random circuits, where circuit averaged results are known exactly, Eq. 2.68. In this section we apply the MMF to Haar random unitary circuits and reproduce the exact expressions for v_B and D. However, before we can apply the MMF, we must abandon the assumptions of discrete time translation and spatial translation symmetry we made in the previous section. Instead we will make use of the time and spatial translation symmetry of the random circuit ensemble. The Mori-Zwanzig formalism can be generalised to time-dependent evolution. For a time dependent Liouvillian $L(t)$, the generalised Langevin equation is given by [118]

$$\partial_t |q_b(t)\rangle = |q_c(t)\rangle \Omega_{c,b}(t) - \int_0^t dt' |q_c(t')\rangle \Sigma_{c,b}(t',t) + |\xi_b(0,t)\rangle, \tag{3.74}$$

where $\Omega_{a,b}(t) \equiv \langle q_a | \, \mathrm{i}L(t) \, | q_b \rangle$, the noise term $\xi_a(0,t)$ is given by

$$|\xi_a(s,t)\rangle = T \exp\left[\mathrm{i}\int_s^t d\tau Q L(\tau)\right] \mathrm{i}L(0) \, |q_a\rangle \, , \tag{3.75}$$

where T is the time-ordering operator. The memory kernel $\Sigma_{a,b}(s,t)$ now depends not only on the difference $t-s$, but on the earlier time s itself,

$$\Sigma_{a,b}(s,t) = \chi^{-1}_{a,a'} \, \langle q_{a'} | \, L(s) Q T \exp\left[\mathrm{i}\int_s^t d\tau Q L(\tau)\right] Q L(t) \, |q_b\rangle \, . \tag{3.76}$$

Analogously, for time-dependent discrete time evolution, where at the n-th time-step the time evolved operators are updated to time $n+1$ by a unitary $U(n)$ (doubled so as to evolve operators q_a), the memory matrix is given by

$$\Sigma_{a,b}(s,n) = -\chi^{-1}_{a,a'} \, \langle q_{a'} | \, (U(s) - \mathbb{1}) Q U(s+1) Q \cdots U(n-1) Q (U(n) - \mathbb{1}) \, |q_b\rangle \, . \tag{3.77}$$

The charge-charge correlation function satisfies

$$\Delta_n C_{a,b}(n) = C_{a,a'}(n-1)\Omega_{a',b}(n) - \sum_{n'=0}^{n-2} C_{a,a'}(n')\Sigma_{c,b}(n'+1,n), \tag{3.78}$$

where Δ_n is the discrete time derivative and $\Omega_{a,b}(n) = \langle q_a | \, (U(n) - \mathbb{1}) \, | q_b \rangle$. By taking the charge operators to be the weight super-operators $q_a \to W^x$, and using our unusual inner-product $(\cdot|\cdot)$, Eq. 3.78 gives the time evolution of the operator weight and is given in terms of the real-time memory matrix and $\Omega_{x,y}(n) = (W^x|(\mathcal{U}(n) - \mathbb{1})|W^y)$. Additionally, to avoid the complication of site parity dependence, we define super-sites $(r) = \{2r-1, 2r\}$ (as we did in Sec. 2.5.2), and choose the slow space to be the space of weight super-operators $W^{(x)} \equiv W^{2x-1} + W^{2x}$. These slow operators are just (slightly) coarse grained versions of original weight super-operators. The benefit of this choice is that circuit averaged quantities are translationally invariant in cell super-site position. Therefore, by

taking the circuit average of Eq. 3.78, we diagonalise equation 3.78 in momentum space,

$$\Delta_n \overline{\rho_R}(k,n) = \overline{\rho_R}(k,n-1)\overline{\Omega}(k,n) - \sum_{n'=0}^{n-2} \overline{\rho_R}(k,n')\overline{\Sigma}(k,n'+1,n). \tag{3.79}$$

In fact, the circuit average ensures that $\overline{\Omega}(k,n)$ is independent of n, while $\overline{\Sigma}(k,n'+1,n)$ depends only the difference $n-n'-1$. Performing a discrete Laplace transformation on equation 3.79, we find the spectral function

$$\overline{\rho_R}(k,z) = \left[e^{-iz} - 1 - \overline{\Omega}(k) + \overline{\Sigma}(k,z)\right]^{-1}. \tag{3.80}$$

Unsurprisingly, the circuit averaged memory matrix vanishes – a Haar random circuit is, by definition, memory-less. We show this explicitly in boxed section below.

Aside: $\overline{\Sigma} = 0$

In this section, we will see that the circuit averaged current $\overline{J^{(x)}}$ is a slow variable[a], ensuring that $\overline{\Sigma}(k,z) = 0$. Concretely, the circuit averaged current is given by

$$\overline{J(n)^{(x)}} \equiv q^{-2L_{>(x)}} \left(\overline{\mathcal{U}(n)} - \mathbb{1}\right) F^{(x)}. \tag{3.81}$$

The second term, $-q^{-2L_{>(x)}} F^{(x)}$, is manifestly slow. We therefore only need to check whether $\overline{\mathcal{U}(n)} F^{(x)} \in \mathcal{P}$. Recalling that the + and − domains are invariant under local unitary evolution (see Sec. 3.1.2), we focus on the unitary gate applied over the cut, i.e., we are interested in the (Haar averaged) following quantity,

$$\overline{\mathcal{U}_{x,x+1}} \left|+,-\right\rangle_{x,x+1}, \tag{3.82}$$

where the replicated unitary gate $\mathcal{U}_{x,x+1} = U_{x,x+1} \otimes U^*_{x,x+1} \otimes U_{x,x+1} \otimes U^*_{x,x+1}$ is given diagrammatically by

$$\mathcal{U}_{x,x+1} \equiv$$ 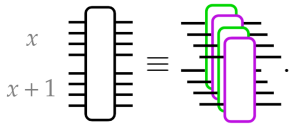 (3.83)

where the underlying unitary gates are

$$U_{x,x+1} \equiv$$ 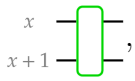 , $\quad U^*_{x,x+1} \equiv$  . (3.84)

Using $|+-\rangle = |0-\rangle + \frac{1}{q}|--\rangle$ and the invariance of the identity state $\mathcal{U}|--\rangle = |--\rangle$, we re-write Eq. 3.82 as $\overline{\mathcal{U}}|0,-\rangle + \frac{1}{q}|--\rangle$. The first term just represents the scrambling of a non-identity Pauli matrix on site x over the two-site cluster $\{x, x+1\}$. Expressing $|0,-\rangle$ as a sum over generalised Pauli matrices, using the definition Eq. 3.12, we write $\overline{\mathcal{U}}|0,-\rangle$ as

$$\overline{\mathcal{U}_{x,x+1}}\,|0,-\rangle_{x,x+1} = \frac{1}{q^3}\sum_{\sigma^s_x \neq \mathbb{1}} \left|\overline{\sigma^s_x(1) \boxtimes \sigma^s_x(1)^\dagger}\right\rangle_{x,x+1} . \tag{3.85}$$

Expressing the generalised Pauli matrices as a sum over two-site Pauli strings, $\sigma^s_x(1) = \sum_{a\neq 0} C^s_a \sigma^a$, we re-write this equation once again,

$$\overline{\mathcal{U}_{x,x+1}}\,|0,-\rangle_{x,x+1} = \frac{1}{q^3}\sum_{\sigma^s_x \neq \mathbb{1}} \sum_{\text{strings } a,b\neq 0} \left|\sigma^a \boxtimes \sigma^{b\dagger}\right\rangle_{x,x+1} \overline{C^s_a C^{s*}_b}. \tag{3.86}$$

Using the Haar averaging result Eq. 2.62, we see that the Haar average sets the Pauli strings a and b to be equal. Moreover, all non-identity transitions are equi-probable, $\overline{|C^s_a|^2} = \frac{1}{q^4-1}$. Re-summing the generalised Pauli matrices σ^s_x then gives a factor q^2-1,

$$\overline{\mathcal{U}_{x,x+1}}\,|0,-\rangle_{x,x+1} = \frac{1}{q^3(q^2+1)}\sum_{\text{strings } a\neq 0} \left|\sigma^a \boxtimes \sigma^{a\dagger}\right\rangle_{x,x+1} = \frac{1}{q+q^{-1}}\,|(0)\rangle_{x,x+1}\,, \tag{3.87}$$

where we have defined $|(0)\rangle_{x,x+1} \equiv |+,+\rangle_{x,x+1} - \frac{1}{q^2}|-,-\rangle_{x,x+1}$, the two-site analogue of $|0\rangle_x$. Altogether, and after de-cluttering some notation, the (Haar averaged) gate

has the following action at the cut,

$$\overline{\mathcal{U}_{x,x+1}}\,|+-\rangle = \frac{1}{q+q^{-1}}\left(|++\rangle + |--\rangle\right). \tag{3.88}$$

Leaving the Haar averaging implicit, the full two unitary time-step $\mathcal{U}(n)$ (both the even-odd and odd-even layers) acting on the state $\left|F^{(x)}\right\rangle = |F^{2x}\rangle$ is then given by the diagrammatic equation below,

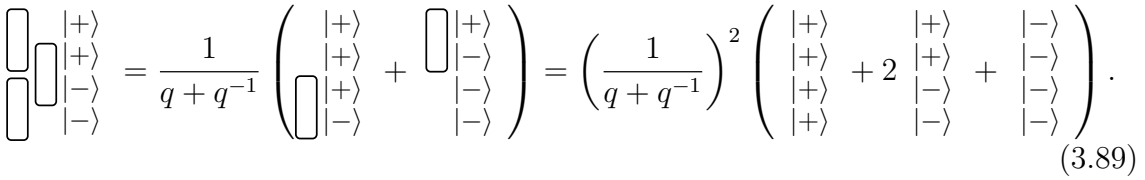

(3.89)

This is precisely what we wanted to show,

$$\overline{\mathcal{U}(n)}\left|F^{(x)}\right\rangle = \left(q+q^{-1}\right)^{-2}\left(\left|F^{(x+1)}\right\rangle + 2\left|F^{(x)}\right\rangle + \left|F^{(x-1)}\right\rangle\right) \in \mathcal{P}. \tag{3.90}$$

[a] Notice that the super-sites have dimension q^2, affecting $q \to q^2$ in previous formulae using local Hilbert space dimension q.

The circuit averaged operator dynamics is then packaged exclusively in Ω. We now verify that we recover the exact expressions for v_B and D from Ω. Explicitly, $\overline{\Omega}$ is given by

$$\overline{\Omega}(k) = \left(W^{(k)}|\left(\overline{\mathcal{U}} - \mathbb{1}\right)|W^{(k)}\right), \tag{3.91}$$

where the momentum space weights are defined by $W^{(k)} = \frac{1}{\sqrt{N_{\text{cells}}}}\sum_x e^{-ikx}W^{(x)}$ with $N_{\text{cells}} = L/2$ the number of cells. Writing this in terms of the purity super-operators $F^{(x)}$ and using Eq. 3.90, we have

$$\overline{\Omega}(k) = -\frac{q^2-1}{q^2+1}\eta_{q^2}(k)\left(1-e^{-ik}\right), \tag{3.92}$$

where $\eta_\lambda(k) = \frac{1-\lambda^{-2}e^{ik}}{1-\lambda^{-2}}$. As the spectral function $\overline{\rho_R}(k,z)$ shares the same dependence on Ω and Σ as in the Floquet case, v_B and D are as given in Eq. 3.71, albeit with circuit averaged quantities. Using the equation for $\overline{\Omega}$ above and accounting for the width of a

cell $\Delta_r = 2$, we find v_B and D to be,

$$v_B = 2\frac{q^2-1}{q^2+1}, \quad D = \frac{4q^2}{q^2+1}, \tag{3.93}$$

in agreement with the expressions Eq. 2.68 found using the equivalence between operator growth and a random walk.

CHAPTER 4

HAAR ENSEMBLE AVERAGES: A TOOLKIT

AVERAGING N-POINT CORRELATION FUNCTIONS AND THEIR MOMENTS

In chapter 5, we will apply our modified MMF to systems with additional structure, those with spatial translation and discrete time translation symmetry. In order to ensure short memory times and allowing for efficient truncation of memory effects, we will consider a family of circuit models with a time-step consisting of a layer single-site random unitary rotations (repeated over all sites and time-steps) and a layer of nearest-neighbour interactions. The repetition of a Haar random unitary requires more sophisticated Haar integration techniques than those reviewed in Sec. 2.5.1.

This chapter is a reformatted and extended version of my single author preprint, E. McCulloch, "Haar averaged moments of correlation functions and OTOCs in Floquet systems," 2021, arXiv:2110.15151 [119] and introduces the Haar averaging toolkit we developed and reviews the large q asymptotic behaviour of a selection of n-point correlation functions, out-of-time-ordered correlators (OTOCs), and their moments. We will assume

that the number of instances $\mathcal{N}_U$ of a random unitary U appearing in an expression to be averaged does not scale with the dimension q. This is necessary for finding $q \to \infty$ asymptotics. In Sec. 4.6, we discuss the limitations of large q asymptotics and what happens away from this limit.

4.1 Correlators and contours

In this chapter, we restrict our attention to n-point correlations function of the form

$$\langle \mathcal{Z}(\boldsymbol{t}) \rangle = \langle Z(t_1) \cdots Z(t_n) \rangle = \frac{1}{q} \operatorname{Tr}[Z(t_1) \cdots Z(t_n)], \tag{4.1}$$

where $\boldsymbol{t} = (t_1, \cdots, t_N)$ and $\mathcal{Z}(\boldsymbol{t}) = Z(t_1) \cdots Z(t_n)$ is a product of n 'scrambled' Pauli Z matrices, $Z(t) = U^t Z U^{-t}$ (with a unitary U drawn from the Haar distribution on the group $\mathcal{U}(q)$ of $q \times q$ unitary matrices).

A correlator $\langle \mathcal{Z}(\boldsymbol{t}) \rangle$ is called contour-ordered for a given contour $\mathcal{C}$ if the sequence of times $\boldsymbol{t} = (t_1, \cdots, t_n)$ is contour ordered on $\mathcal{C}$. An example is given below for contours with only a single forward and backward segment and for contours with two forward and backward segments. The later is of out-of-time-ordered (OTO) type as OTOCs, $\langle AB(t)AB(t) \rangle$, naturally live on these contours. The former is referred to as a contour of time-ordered (TO) type.

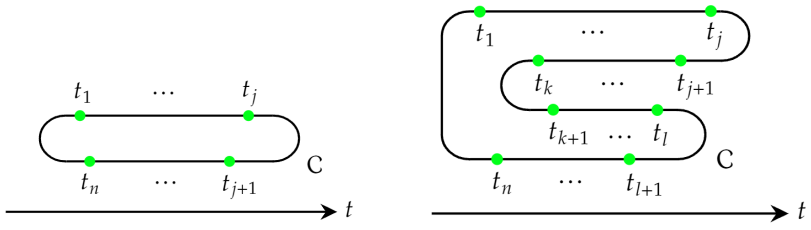

Figure 4.1: *TO type contours and OTO type contours.*

The condition that $\mathcal{N}_U$ (the number of instances of the random unitary U) does not scale with q places a condition on the 'length', $l(\boldsymbol{t}) = \max(t_i) - \min(t_i)$, of TO and OTO correlation functions. For TO correlators, $\mathcal{N}_U = l(\boldsymbol{t})$, whereas for OTO correlators,

$\mathcal{N}_U \leq 2l(\boldsymbol{t})$. In both cases, keeping the length of correlators fixed as $q \to \infty$ ensures that $\mathcal{N}_U$ remains fixed. When considering products of correlators, we keep the lengths and number of correlators fixed.

While some results will be specific to TO and OTO correlators, several of the results we will present are for arbitrary time-ordered (ATO) correlations functions – correlation functions with no restrictions on the ordering of times t_i.

4.2 Haar averaging theorems

In this section we review several useful Haar averaging theorems for the n-point correlation functions $\langle \mathcal{Z}(\boldsymbol{t}) \rangle$. The proofs of these theorems are found in [119] and reviewed in sections 4.3-4.5.

Many correlation functions $\langle \mathcal{Z}(\boldsymbol{t}) \rangle$, although having a different sequence of times $\boldsymbol{t}$ are equivalent. We will find it helpful to remove some of this redundancy. There are three types of redundancy that we can encounter. Firstly, due to the cyclic property of the trace, all cyclic permutations of the times $\boldsymbol{t}$ are equivalent. Secondly, two sequences of times that differ by a global shift, $(t_1, \cdots, t_n) \to (t_1 + t, \cdots, t_n + t)$, are equivalent. Thirdly, using the property $Z(t)^2 = \mathbb{1}$, different times $\boldsymbol{t}$ may be equivalent, for example $\langle Z(t)Z(t)Z(t') \rangle = \langle Z(t') \rangle$. To remove third type of redundancy, we introduce a concept that we call the *reduced form* of $\mathcal{Z}(\boldsymbol{t})$, or equivalently, of the sequence of times $\boldsymbol{t}$.

Definition 1 (Reduced form)**.** With a sequence of times $\boldsymbol{t} = (t_1, \cdots, t_n)$, the reduced form of $\boldsymbol{t}$, $\mathrm{Red}(\boldsymbol{t})$, is sequence found after (exhaustively) deleting all twice-repeated consecutive times, $(\cdots, t_i, t, t, t_{i+2}, \cdots) \to (\cdots, t_i, t_{i+2}, \cdots)$. This also allows us to define the reduced form of a product $\mathcal{Z}(\boldsymbol{t}) = Z(t_1) \cdots Z(t_n)$ as $\mathrm{Red}(\mathcal{Z}(\boldsymbol{t})) \equiv \mathcal{Z}(\mathrm{Red}(\boldsymbol{t}))$.

A consequence of this definition is that no consecutive times repeat in $\mathrm{Red}(\boldsymbol{t})$. Additionally, the correlation functions associated with the sequence of times $\boldsymbol{t}$ and its reduced form are equivalent, $\langle \mathcal{Z}(\boldsymbol{t}) \rangle = \langle \mathcal{Z}(\mathrm{Red}(\boldsymbol{t})) \rangle$. As well as removing some redundancy from ATO correlators, the reduced form can also be used to check whether two products

$A = Z(a_1)\cdots Z(a_n)$ and $B = Z(b_1)\cdots Z(b_n)$ are equal, $AB^{-1} = \mathbb{1}$, for all unitaries U. This defines a U-independent 'delta function' for operators.

Definition 2 (Decoration delta constraint)**.** Define the delta constraint $\delta^{A,B}$ for operators $A = Z(a_1)\cdots Z(a_n)$ and $B = Z(b_1)\cdots Z(b_n)$ as

$$\delta^{A,B} = \begin{cases} 1, & \text{if } \mathrm{Red}(\boldsymbol{a}) = \mathrm{Red}(\boldsymbol{b}) \\ 0, & \text{otherwise.} \end{cases} \tag{4.2}$$

We also define the *minimal form* of a sequence of times $\boldsymbol{t}$ which uses the cyclic property of the trace to identify the first and final times in a sequence $\boldsymbol{t}$ as consecutive.

Definition 3 (Minimal form)**.** Given a sequence of times $\boldsymbol{t} = (t_1, \cdots, t_n)$, the minimal form $\mathrm{Min}(\boldsymbol{t})$ is the sequence found after the following protocol. While identifying the first and final times in $\boldsymbol{t}$ as consecutive, delete all twice-repeated consecutive times, $(\cdots, t_i, t, t, t_{i+2}, \cdots) \to (\cdots, t_i, t_{i+2}, \cdots)$. Repeat this step until left with a sequence with no repeated consecutive times. The resulting sequence is the minimal form $\mathrm{Min}(\boldsymbol{t})$.

This definition allows us to define a delta function that checks whether two sequences of times have equal minimal forms up to a cyclic permutation and a global shift, removing all redundancy in ATO correlators.

Definition 4. For sequences $\boldsymbol{a} = (a_1, a_2, \cdots)$ and $\boldsymbol{b} = (b_1, b_2, \cdots)$, the delta function $\tilde{\delta}^{\boldsymbol{a},\boldsymbol{b}}$ is defined to be unity if there exists a permutation σ and integer τ such that $\sigma(\mathrm{Min}(\boldsymbol{a}_\tau)) = \mathrm{Min}(\boldsymbol{b})$ where $\boldsymbol{a}_\tau = (a_1 + \tau, a_2 + \tau, \cdots)$, and zero otherwise,

$$\tilde{\delta}^{\boldsymbol{a},\boldsymbol{b}} = \begin{cases} 1, & \text{if } \exists\ \sigma \text{ and } \tau \in \mathbb{Z} \text{ such that } \sigma(\mathrm{Min}(\boldsymbol{a}_\tau)) = \mathrm{Min}(\boldsymbol{b}) \\ 0, & \text{otherwise.} \end{cases} \tag{4.3}$$

Equipped with these delta functions, we are able to compactly give the $q \to \infty$ scaling behaviour of n-point ATO correlators and products of ATO correlators, as well as the exact $q \to \infty$ asymptotic behaviour of Haar averaged OTO correlators and the product

of two ATO correlators. We assume that correlation functions $\langle \mathcal{Z}(\boldsymbol{t})\rangle$ are non-trivial, i.e. $\mathrm{Red}(\mathcal{Z}(\boldsymbol{t})) \neq \mathbb{1}$.

Theorem 1. *The Haar average of a product of p ATO correlators has the scaling behaviour,*

$$\int dU \langle \mathcal{Z}(\boldsymbol{t}^1)\rangle \cdots \langle \mathcal{Z}(\boldsymbol{t}^p)\rangle = \mathcal{O}\big(1/q^{2\lceil p/2\rceil}\big) \quad \text{as } q \to \infty. \tag{4.4}$$

Theorem 2. *The Haar average of a product of two ATO correlators is given by*

$$\int dU \langle \mathcal{Z}(\boldsymbol{t})\rangle \langle \mathcal{Z}(\boldsymbol{t}')\rangle^* = \frac{S(\boldsymbol{t})}{q^2}\tilde{\delta}^{\boldsymbol{t},\boldsymbol{t}'} + \mathcal{O}\big(1/q^3\big) \quad \text{as } q \to \infty, \tag{4.5}$$

where we have used the delta function $\tilde{\delta}^{\boldsymbol{t},\boldsymbol{t}'}$ to fix $\mathrm{Min}(\boldsymbol{t}) = \mathrm{Min}(\boldsymbol{t}')$ up to a cyclic permutation and global shift. The symmetry factor $S(\boldsymbol{t})$ counts the degree of cyclic symmetry of the list of times $\boldsymbol{t}$, if there exists n cyclic permutations α such that $\alpha(\boldsymbol{t}) = \boldsymbol{t}$, then $S(\boldsymbol{t}) = n$.

We will often study a special subset of ATO correlators, which we dub *physical OTOCs*. These take the form $\langle Z\Gamma_1 Z(T)\Gamma_{\overline{2}}^\dagger Z\Gamma_2 Z(T)\Gamma_{\overline{1}}^\dagger\rangle$, where $\Gamma_i = Z(1)^{s_1^i} Z(2)^{s_2^i}\cdots Z(T-1)^{s_{T-1}^i}$ for binary strings $\boldsymbol{s}^i = (s_1^i, \cdots, s_{T-1}^i)$.

Theorem 3. *The Haar average of a physical OTOC is given by*

$$\int dV \langle Z\Gamma_1 Z(T)\Gamma_{\overline{2}}^\dagger Z\Gamma_2 Z(T)\Gamma_{\overline{1}}^\dagger\rangle = \frac{1}{q^2}\left(\delta^{\Gamma_1\Gamma_{\overline{1}}^\dagger\Gamma_2\Gamma_{\overline{2}}^\dagger,\mathbb{1}} - \delta^{\Gamma_1,\Gamma_{\overline{2}}}\delta^{\Gamma_2,\Gamma_{\overline{1}}} - \delta^{\Gamma_1,\Gamma_{\overline{1}}}\delta^{\Gamma_2,\Gamma_{\overline{2}}}\right) + \mathcal{O}\big(1/q^3\big), \tag{4.6}$$

where we have again used the decoration delta constraint. This result relies on theorem 4 of [119] and is obtained in Eq. B.6 of B. This result appears not to depend on the time T. For instance, with the physical OTOC $\langle ZZ(T)ZZ(T)\rangle$, the above theorem gives the asymptotic value as $\int dV \langle ZZ(T)ZZ(T)\rangle = -1/q^2 + \mathcal{O}(1/q^3)$. Indeed, the T dependence appears at lower order in $1/q$, as we show numerically in Sec. 4.6.2.

4.3 Products of ATO correlation functions

In this section we prove theorem 1 in Sec. 4.2 for the scaling behaviour of (the Haar average of) products of ATO correlation functions, repeating our proof in [119]. Without loss of generality, we assume that all ATO correlators are non-trivial and of minimal form[1]. Consider then, a product of p correlation functions $\langle \mathcal{Z}(\boldsymbol{t}^1)\rangle \cdots \langle \mathcal{Z}(\boldsymbol{t}^p)\rangle$, where $\langle \mathcal{Z}(\boldsymbol{t}^i)\rangle = \langle Z(t_1^{(i)}) \cdots Z(t_{n_i}^{(i)})\rangle$. The time differences $x_j^{(i)} = t_{j+1}^{(i)} - t_j^{(i)}$ (and the edge case $x_{n_i}^{(i)} = t_1^{(i)} - t_{n_i}^{(i)}$) are each non-zero (due to the minimal form assumption) and sum to zero, $\sum_j x_j^{(i)} = 0$. The product $\langle \mathcal{Z}(\boldsymbol{t}^1)\rangle \cdots \langle \mathcal{Z}(\boldsymbol{t}^p)\rangle$ can then be written as

$$\langle \mathcal{Z}(\boldsymbol{t}^1)\rangle \cdots \langle \mathcal{Z}(\boldsymbol{t}^p)\rangle = \langle ZU^{x_1^{(1)}} \cdots ZU^{x_{n_1}^{(1)}}\rangle \cdots \langle ZU^{x_1^{(p)}} \cdots ZU^{x_{n_p}^{(p)}}\rangle. \tag{4.7}$$

Making use of the left and right invariance of the Haar measure, $\int dU f(U) = \int dU f(UV)$ (similarly for left invariance), we represent the Haar average of Eq. 4.7 as a sum over permutations weighted by the Weingarten functions [110–112],

$$\begin{aligned}\int dU \langle \mathcal{Z}(\boldsymbol{t}^1)\rangle \cdots \langle \mathcal{Z}(\boldsymbol{t}^p)\rangle &= \iint dU dV \prod_{i=1}^{p} \langle ZVU^{x_1^{(i)}} V^\dagger \cdots ZVU^{x_{n_i}^{(i)}} V^\dagger\rangle \\ &= \sum_{\sigma,\tau \in S_M} \frac{Wg(q, \tau\sigma^{-1})}{q^p} H(\tau) \tilde{G}(\{\boldsymbol{x}^i\}, \sigma)\end{aligned} \tag{4.8}$$

where $M = \sum_i n_i$ an $H(\tau)$ is given by the tensor diagram,

$H(\tau) =$ 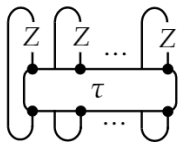

, (4.9)

and where $\tilde{G}(\{\boldsymbol{x}^i\}, \sigma)$ is the Haar average of a tensor diagram,

$\tilde{G}(\{\boldsymbol{x}^i\}, \sigma) = \int dU$ 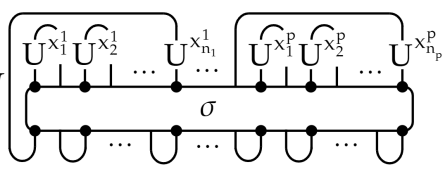

(4.10)

[1]This is fully general due to equivalence of correlation functions discussed in Sec. 4.2.

We have used the following convention for the legs of tensors,

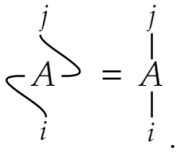

(4.11)

We will find it useful to briefly focus on the case $p = 1$. In this case, $\tilde{G}(\boldsymbol{x}, \sigma)$ is given by

$$\tilde{G}(\boldsymbol{x}, \sigma) =$$

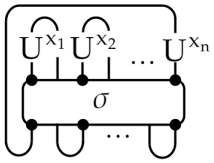

(4.12)

Define the permutation $\pi = (n, 1, 2, \cdots, n-1)$ (in cycle notation). Diagrammatically, with the lower legs as the incoming legs, this is given by

$$\pi =$$

(4.13)

By inserting the identity permutation as $\mathbb{1} = \pi\pi^{-1}$, we can simplify the contraction of the U^{x_i} using the following,

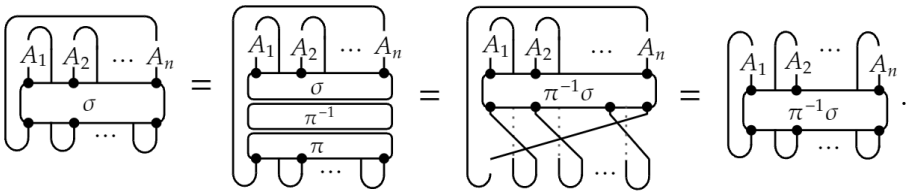

(4.14)

This allows us to write $\tilde{G}(\boldsymbol{x}, \sigma) = G(\boldsymbol{x}, \pi^{-1}\sigma)$, where

$$G(\boldsymbol{x}, \sigma) = \int dU$$

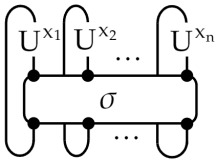

(4.15)

We can extend this manipulation to general p by re-defining the permutation π as

π = 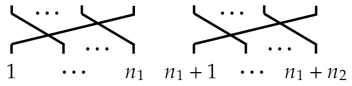

.

This allows us to write $\tilde{G}(\{\boldsymbol{x}^i\},\sigma) = G(\boldsymbol{y},\pi^{-1}\sigma)$, where $\boldsymbol{y} = (x_1^{(1)},\cdots,x_{n_1}^{(1)},x_1^{(2)},\cdots,x_{n_p}^{(p)})$ and where $G(\boldsymbol{x},\sigma)$ is as given in Eq. 4.15. Shifting the sum variable $\sigma \to \pi\sigma$ in Eq. 4.8 yields

$$\int dU \langle \mathcal{Z}(\boldsymbol{t}^1)\rangle \cdots \langle \mathcal{Z}(\boldsymbol{t}^p)\rangle = \sum_{\sigma,\tau\in S_M} \frac{Wg(q,\tau\sigma^{-1}\pi)}{q^p} G(\boldsymbol{y},\sigma)H(\tau). \tag{4.16}$$

The evaluation of $H(\tau)$ is simple,

$$H(\tau) = \begin{cases} q^{|C_\tau|}, & \text{if } \tau \text{ has cycles only of even length,} \\ 0, & \text{otherwise,} \end{cases} \tag{4.17}$$

where $|C_\tau|$ is the number of cycles in τ. An immediate consequence of this is that for odd M, $H(\tau) = 0$ for all τ. From now on we consider only even M. Letting $S_M^E \subset S_M$ refer to the set of permutations with cycles of even length only, we can restrict the sum from $\tau \in S_M$ to $\tau \in S_M^E$ in Eq. 4.16. To bound $G(\boldsymbol{y},\sigma)$, we notice that the tensor diagram in Eq. 4.15 is equal to a product of closed loops (representing a trace), each *decorated* by a power of U. This allows us to write

$$G(\boldsymbol{y},\sigma) = q^{N_{\text{ud}}} \int dU \prod_{m=1}^{l} \text{Tr}(U^m)^{a_m} \text{Tr}\big(U^{-m}\big)^{b_m}, \tag{4.18}$$

where the a_m and b_m count the multiplicity of the decorated loops corresponding with $\text{Tr}(U^m)$ and $\text{Tr}(U^{-m})$ respectively and depend on $\boldsymbol{y}$ and the permutation σ. We have also defined l to be the maximum power of U or U^{-1} decorating a loop in the contraction, whichever is larger. N_{ud} is the number of undecorated loops (loops that carry no decoration U^m or U^{-m}) and also depends on σ and $\boldsymbol{y}$. To evaluate this Haar average, we use a

result of Diaconis and Evans [120]. For $q \geq \max(\sum_{m=1}^{l} m a_m, \sum_{m=1}^{l} m b_m)$,

$$\int dU \prod_{m=1}^{l} \mathrm{Tr}(U^m)^{a_m} \mathrm{Tr}\big(U^{-m}\big)^{b_m} = \delta^{\boldsymbol{a},\boldsymbol{b}} \prod_{m=1}^{l} m^{a_m} a_m! \leq \delta^{\boldsymbol{a},\boldsymbol{b}} N!, \text{ where } N = \sum_{m=1}^{l} m a_m \tag{4.19}$$

where $\boldsymbol{a} = (a_1, \cdots, a_l)$ and $\boldsymbol{b} = (b_1, \cdots, b_l)$. This bound on the contribution to $G(\boldsymbol{y}, \sigma)$ from decorated loops does not scale with q as $q \to \infty$ for fixed $\boldsymbol{y}$ and σ. Therefore, for fixed $\boldsymbol{y}$ and σ, and large q, we are able to bound $G(\boldsymbol{y}, \sigma)$ by the following

$$G(\boldsymbol{y}, \sigma) \leq C(\boldsymbol{y}, \sigma) q^{N_{\mathrm{ud}}}, \quad \text{for some } C(\boldsymbol{y}, \sigma) > 0 \text{ independent of } q. \tag{4.20}$$

The number of undecorated loops is bounded by $N_{\mathrm{ud}} \leq M/2$, this bound is saturated if σ is composed of $M/2$ disjoint transpositions, producing $M/2$ loops on which each decoration U^{y_j} pairs with its inverse U^{-y_j} (if such a pair of decorations exist for a given $\boldsymbol{y}$). Due to $\sum_j y_j = 0$, the number of decorated loops cannot be one, this means that if N_{ud} does not saturate this bound, it must be bounded by $N_{\mathrm{ud}} \leq (M-2)/2$. Call $\mathcal{G}_{\boldsymbol{y}} \subset S_n$ the set of permutations that produce only undecorated loops. The value of such a loop contraction is given by $q^{|C_\sigma|}$, where $|C_\sigma|$ is the number of cycles in σ. The Haar average of this tensor diagram is trivial, giving

$$G(\boldsymbol{y}, \sigma) = q^{|C_\sigma|}, \text{ for } \sigma \in \mathcal{G}_{\boldsymbol{y}}. \tag{4.21}$$

We separate the sum in Eq. 4.16 into the decorated and undecorated pieces

$$\begin{aligned} \int dU \langle \mathcal{Z}(\boldsymbol{t}^1) \rangle \cdots \langle \mathcal{Z}(\boldsymbol{t}^p) \rangle = & \sum_{\sigma \in \mathcal{G}_{\boldsymbol{y}}, \tau \in S_M^E} \frac{\mathrm{Wg}(q, \tau\sigma^{-1}\pi)}{q^p} q^{|C_\sigma| + |C_\tau|} \\ & + \sum_{\sigma \in \overline{\mathcal{G}}_{\boldsymbol{y}}, \tau \in S_M^E} \frac{\mathrm{Wg}(q, \tau\sigma^{-1}\pi)}{q^p} q^{|C_\tau|} G(\boldsymbol{y}, \sigma) \end{aligned} \tag{4.22}$$

where $\overline{\mathcal{G}}_{\boldsymbol{y}}$ is the set of all the elements in S_n not in $\mathcal{G}_{\boldsymbol{y}}$. We will use the large q asymptotic

form of the Weingarten function [111, 112] as given in Eq. 2.57, which we repeat below,

$$\mathrm{Wg}(q,\sigma) = \frac{1}{q^{M+|\sigma|}} \prod_{c\in C_\sigma} (-1)^{|c|-1}\mathrm{Cat}_{|c|-1} + \mathcal{O}\bigg(\frac{1}{q^{M+|\sigma|+2}}\bigg) \tag{4.23}$$

where $|\sigma|$ is the minimum number of transposition that σ can be written as a product of. C_σ is the set of cycles in σ and $|c|$ is the length of a cycle $c \in C_\sigma$. Cat_i are the Catalan numbers. The terms in the second sum in Eq. 4.22 are all of the size $\mathcal{O}\Big(q^{|C_\tau|+N_{\mathrm{ud}}-M-\left|\tau\sigma^{-1}\pi\right|-p}\Big)$. Using $|C_\tau| \leq M/2$ and $N_{\mathrm{ud}} \leq (M-2)/2$[2], it is not hard to see that all these terms are at most $\mathcal{O}(1/q^{p+1})$. Moreover, the number of these terms scales with M and not q. This gives,

$$\int dU \langle \mathcal{Z}(\boldsymbol{t}^1)\rangle \cdots \langle \mathcal{Z}(\boldsymbol{t}^p)\rangle = \sum_{\sigma\in\mathcal{G}_{\boldsymbol{y}},\tau\in S_M^E} a(\tau\sigma^{-1}\pi) q^{r(\sigma,\tau)-p} + \mathcal{O}\big(1/q^{p+1}\big), \tag{4.24}$$

where $a(\tau\sigma^{-1}\pi) = \prod_{c\in C_\sigma}(-1)^{|c|-1}\mathrm{Cat}_{|c|-1}$ is independent of q and $r(\sigma,\tau) = |C_\tau| + |C_\sigma| - M - |\tau\sigma^{-1}\pi|$. Using the bounds $|C_\tau|, |C_\sigma| \leq M/2$, we find that $|C_\tau| + |C_\sigma| - M \leq 0$. Assuming that $|C_\tau| + |C_\sigma|$ is maximised (subject to $\sigma \in \mathcal{G}_{\boldsymbol{y}}$ and $\tau \in S_M^E$), both τ and σ must be composed of $n/2$ disjoint transpositions. Therefore they must have the same parity, $P(\sigma) = P(\tau)$. Assume also that $|\tau\sigma^{-1}\pi|$ is minimised, $|\tau\sigma^{-1}\pi| = 0$. This implies that the $\sigma\tau^{-1} = \pi$. Applying the parity operator, we find $P(\sigma\tau^{-1}) = P(\sigma)P(\tau) = P(\pi)$. Using $P(\sigma) = P(\tau)$ we find $P(\pi) = 1$. However, π is composed of a product of $M - p$ adjacent transpositions. Using the fact that M is even, then for odd p we find $P(\pi) = -1$. This is a contradiction. For odd p, we cannot simultaneously maximise $|C_\tau| + |C_\sigma|$ and minimise $|\tau\sigma^{-1}\pi|$. Therefore, for odd p, $r(\sigma,\tau) \leq -1$. Whereas, for even p, $r(\sigma,\tau) \leq 0$. Finally, using that the fact that the size of the sets $\mathcal{G}_{\boldsymbol{y}}$ and S_M^E are independent of q, we arrive at the large q scaling result,

$$\int dU \langle \mathcal{Z}(\boldsymbol{t}^1)\rangle \cdots \langle \mathcal{Z}(\boldsymbol{t}^p)\rangle = \mathcal{O}\big(1/q^{2\lceil p/2\rceil}\big) \quad \text{as } q\to\infty. \tag{4.25}$$

[2]Recall that it is not possible for a single loop to be decorated, a consequence of $\sum_j y_j = 0$. This means unless the number of undecorated loops is saturated $N_{\mathrm{ud}} = M/2$, it is bounded by $N_{\mathrm{ud}} \leq (M-2)/2$.

4.4 Product of two correlation functions

In the previous section we have found the bounds on the scaling behaviour of Haar averaged correlators and products of correlators as $q \to \infty$. In this section we present results that also capture the proportionality constants for the Haar average of a product of two correlators, repeating our proof in [119]. We assume without loss of generality that all correlation functions are in minimal form. We start by writing the product of two correlation functions, $\langle \mathcal{Z}(\boldsymbol{t})\rangle = \langle Z(t_1)\cdots Z(t_n)\rangle$ and $\langle \mathcal{Z}(\boldsymbol{t'})\rangle^* = \langle Z(t'_1)\cdots Z(t'_{n'}\rangle^*$, in terms of the time differences $x_i = t_{i+1} - t_i$ (with the edge case $x_1 = t_n - t_1$) and $y_i = t'_{i+1} - t'_i$ (with edge case $y_1 = t'_{n'} - t_1$),

$$\langle \mathcal{Z}(\boldsymbol{t})\rangle\langle \mathcal{Z}(\boldsymbol{t'})\rangle^* = \langle \prod_i (ZU^{x_i})\rangle\langle \prod_j (ZU^{y_j})\rangle^*. \tag{4.26}$$

By assumption, all consecutive times differ, $x_i \neq 0$ and $y_j \neq 0$. By using the left and right invariance of the Haar measure once again, we write the Haar averaged expression as

$$\int dU \langle \mathcal{Z}(\boldsymbol{t})\rangle\langle \mathcal{Z}(\boldsymbol{t'})\rangle^* = \frac{1}{q^2}\sum_{\sigma,\tau\in S_N} \mathrm{Wg}(\sigma\tau^{-1})\tilde{G}(\boldsymbol{x},\boldsymbol{y},\sigma)H(\tau), \tag{4.27}$$

where $N \equiv n + n'$ and where $H(\tau)$ is as given in Eq. 4.9. As before, $H(\tau)$ is zero unless N is even, in the remainder of this proof we will assume this is so. This proof differs from the previous proofs in that we choose not to shift the permutation σ by some fixed permutation π, we instead work directly with the $\tilde{G}(\boldsymbol{x},\boldsymbol{y},\sigma)$ given below,

$$\tilde{G}(\boldsymbol{x},\boldsymbol{y},\sigma) = \int dU$$

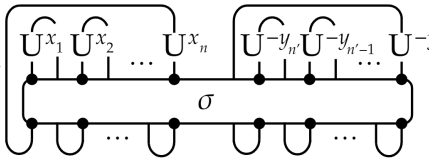

. (4.28)

Despite having a different wiring than the tensor diagram in Eq. 4.15, the same counting argument for undecorated loops applies. When each U^a decoration pairs up with a U^{-a} on $N/2$ loops, $\tilde{G}(\boldsymbol{x},\boldsymbol{y},\sigma)$ is maximised, giving $\tilde{G}(\boldsymbol{x},\boldsymbol{y},\sigma) = q^{N/2}$. Whereas, $H(\tau)$ is

maximised when all the Z's are paired up on separate loops, giving the maximum $N/2$ loops, $H(\tau) = q^{N/2}$. We therefore have two bounds,

$$H(\tau) \leq q^{N/2}, \ \tilde{G}(\boldsymbol{x}, \boldsymbol{y}, \sigma) \leq q^{N/2}. \tag{4.29}$$

Using the asymptotic form of the Weingarten function in Eq. 4.23, the sum in Eq. 4.27 is bounded by $C(\boldsymbol{x}, \boldsymbol{y}) q^{N/2+N/2-N-|\sigma\tau^{-1}|-2} = C(\boldsymbol{x}, \boldsymbol{y}) q^{-|\sigma\tau^{-1}|-2}$, for some $C(\boldsymbol{x}, \boldsymbol{y})$ that is independent of q. This is $\mathcal{O}(q^{-2})$ only when $\sigma = \tau$ and subleading otherwise. Our goal is to calculate the leading order $1/q^2$ contributions, i.e., those where $\sigma = \tau$ is a product of $N/2$ disjoint transpositions. Discarding subleading contributions yeilds

$$\int dU \langle \mathcal{Z}(\boldsymbol{t}) \rangle \langle \mathcal{Z}(\boldsymbol{t}') \rangle^* = \frac{1}{q^{2+N/2}} \sum_{\sigma \in \mathcal{T}_N} \tilde{G}(\boldsymbol{x}, \boldsymbol{y}, \sigma) + \mathcal{O}\big(q^{-3}\big), \tag{4.30}$$

where $\mathcal{T}_N \in S_N$ is the set of permutations σ that are products of $N/2$ disjoint transpositions. Given such a permutation σ, suppose that it contains a transposition $T_{1,i+1}$ between legs 1 and $i+1$ and that $i+1 \leq n$ (such that the transposition is 'within' the indices of first correlation function). Such a transposition puts the unitaries U^{x_1} and U^{x_i} on the same wire. We remind the reader that the theoretical maximum of $\tilde{G}$ is achieved if all unitaries are paired (U^x with U^{-x}) on separate loops. Therefore, to ensure that no other unitaries share the loop with U^{x_1} and U^{x_i}, we must choose the next transposition as $T_{2,i}$, this closes the wire with U^{x_1} and U^{x_i} into a loop. This is shown below,

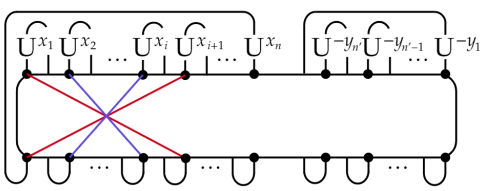

The requirement that unitaries are paired only, forces us pick transpositions that cascade inwards until one of two scenarios occur, depending on whether i is even or odd. If i is even, then the cascade ends as shown below, with a loop with a single unitary decorating it. This violates the conditions for maximising $\tilde{G}$.

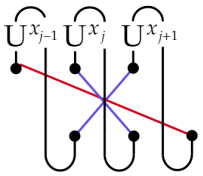

If i is odd, then the cascade ends by forcing the choice of a 1-cycle (shown below), instead of a transposition, in order to have the unitaries paired up. Therefore this permutation is not a member of $\mathcal{T}_N$ and so cannot contribute at leading order.

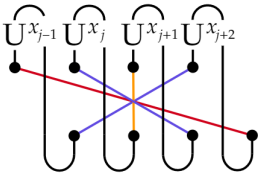

We need not have started with the transposition $T_{1,i+1}$ with $i < n$. If σ contains any transpositions $T_{i,j}$ with $1 \leq i, j \leq n$, $i \neq j$, then the same cascade argument above can be used to demonstrate that we cannot pair up unitaries onto separate loops with disjoint transpositions only. The same argument can be made by starting with a transposition exclusively within the indices of the second correlator. We therefore conclude that in order to maximise $\tilde{G}$, σ must be comprised of disjoint transpositions where every transposition spans between the two correlators. An immediate consequence of this is that the number of legs in each correlator must be equal, $n = n'$. Assuming a transposition $T_{1,n+1+i}$, $0 \leq i < n$, we again employ the cascade argument, where the transposition $T_{2,n+i}$ is forced next and then $T_{3,n+i-1}$ and so on until we stop at the transposition $T_{i+1,n+1}$. This is shown in the diagram below, where we have only displayed the time labels to de-clutter the picture.

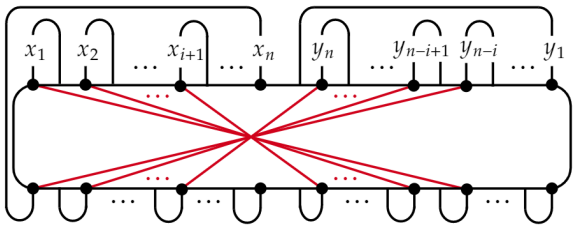

Notice that the final transposition added places the unitaries $U^{x_{i+1}}$ and U^{-y_1} on the

same wire, in order to close this loop with no other unitaries decorating it, we must choose the transposition $T_{i+2,2n}$, this starts another cascade with the next forced transposition being $T_{i+3,2n-1}$, until we finish with the final transposition $T_{n,n+2+i}$. This is shown below.

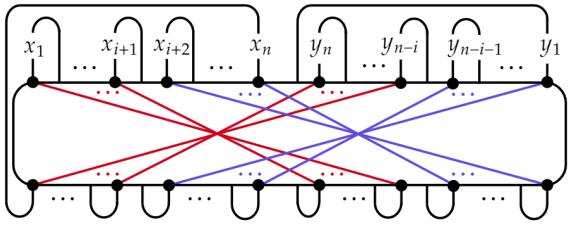

It is clearer to distinguish the two blocks of transpositions as shown below with the first block having i transpositions and the second having $n-i$.

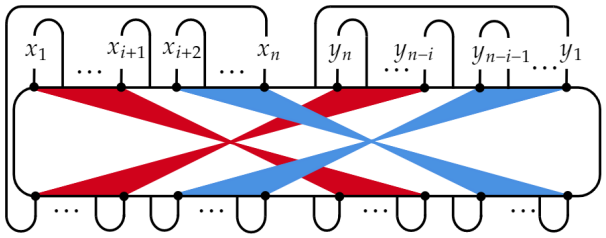

Figure 4.2: *permutations σ that pair the U^{x_i} and U^{-y_j} onto separate loops.*

Therefore, only permutations of the form below may contribute at leading order ($\tilde{G} = q^{N/2}$),

$$\sigma_m = \quad . \tag{4.31}$$

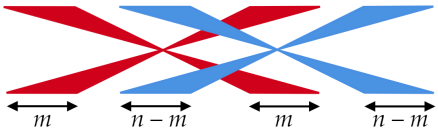

With σ_m, the trace diagram in Fig. 4.2 has value

$$\begin{aligned} &Tr(U^{x_1-y_{n-m+1}})Tr(U^{x_2-y_{n-m+2}})\cdots Tr(U^{x_m-y_n})Tr(U^{x_{m+1}-y_1}) \\ &\times Tr(U^{x_{m+2}-y_2})\cdots Tr(U^{x_{n-1}-y_{n-1-m}})Tr(U^{x_n-y_{n-m}}). \end{aligned} \tag{4.32}$$

For the Haar average of the trace diagram to contribute at leading order ($\tilde{G} = q^{N/2}$), all the indices must cancel, this is expressed below,

$$q^{-N/2}\int dU G(\boldsymbol{x},\boldsymbol{y},\sigma_m) = \delta^{\boldsymbol{y},\alpha_{m+1}(\boldsymbol{x})} + \mathcal{O}(1/q), \tag{4.33}$$

where $\alpha_{m+1}(\boldsymbol{x}) = (x_{m+1}, x_{m+2}, \cdots, x_n, x_1, \cdots, x_{m-1})$ is a cyclic permutation of $\boldsymbol{x}$ and where the Kronecker delta (not to be confused with the decoration delta function) checks that the $\boldsymbol{y}$ and $\alpha_{m+1}(\boldsymbol{x})$ are identical strings. Summing over all σ_m gives the final result,

$$\int dU \langle \mathcal{Z}(\boldsymbol{t})\rangle \langle \mathcal{Z}(\boldsymbol{t}')\rangle^* = \frac{1}{q^2} \sum_{m=1}^{n} \delta^{\boldsymbol{y},\alpha_m(\boldsymbol{x})} + \mathcal{O}\big(q^{-3}\big). \tag{4.34}$$

Or, in terms of the original times $\boldsymbol{t}$ and $\boldsymbol{t}'$,

$$\int dU \langle \mathcal{Z}(\boldsymbol{t})\rangle \langle \mathcal{Z}(\boldsymbol{t}')\rangle^* = \frac{S(\boldsymbol{t})}{q^2} \tilde{\delta}^{\boldsymbol{t}',\boldsymbol{t}} + \mathcal{O}\big(q^{-3}\big), \tag{4.35}$$

where $S(\boldsymbol{t})$ counts the degree of cyclic symmetry of the string $\boldsymbol{t}$ and the delta function $\tilde{\delta}^{\boldsymbol{t}',\boldsymbol{t}}$ checks that the strings are equivalent up to cyclic permutations and global shifts in time, just as it was introduced in Eq. 4.3.

4.5 Out-of-time-ordered correlators

OTOCs appear naturally in operator spreading memory matrix calculations, this is due to the mismatching of + and − wirings (Eq. 3.13) when the incoming and outgoing weight super-operators are offset in position. In the next chapter we calculate the memory matrix perturbatively in $1/q$ for a family of circuit models, and find that a specific class of OTOCs appear at leading order. For lack of a better name, we will refer to these OTOCs as *physical* OTOCs. Physical OTOCs are OTOCs of the form $\langle ZAZ(T)B^\dagger ZCZ(T)D^\dagger\rangle$ where A, B, C and D are time-ordered products of the form $Z(1)^{a_1}\cdots Z(T-1)^{a_{T-1}}$ for $a_1 \in \{0,1\}$. Physical OTOCs can also be represented as contraction of a tensor $\Gamma = \Gamma(1)\cdots\Gamma(T-1)$ as shown in Fig. 4.3 below.

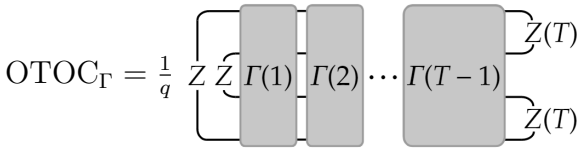

Figure 4.3: *A physical OTOC. Each layer $\Gamma(j)$ represents possible insertions of operators $Z(j)$ on legs 1 and 2 and operators $Z(j)^*$ on legs $\overline{1}$ and $\overline{2}$. From top to bottom, the leg ordering is $1, \overline{1}, 2, \overline{2}$.*

Each tensor $\Gamma(j)$ has the option of placing the operator $Z(j)$ on legs 1 and 2 and the operator $Z(j)^*$ on legs $\overline{1}$ and $\overline{2}$. Define $\langle Z_+|$ ($|Z(T)_-\rangle$) as the $\langle +|$ ($|-\rangle$) wiring with Z ($Z(T)$) operators decorating both the wires as they appear in Fig. 4.3. With this definition, we can rewrite the OTOC as

$$\text{OTOC}_\Gamma = q \langle Z_+| \Gamma |Z(T)_-\rangle \tag{4.36}$$

Finally, define the projector

$$K = \frac{1}{1-q^2} \left[|+\rangle \langle 0| + |-\rangle \langle \perp| \right], \tag{4.37}$$

where $\langle 0| = \langle +| - \frac{1}{q} \langle -|$ and $\langle \perp| = \langle -| - \frac{1}{q} \langle +|$. Checking that K is a projector is a simple task, and is omitted here.

Claim 1. *The Haar average of a physical OTOC,* $\text{OTOC}_\Gamma = q \langle Z_+| \Gamma |Z(T)_-\rangle$*, is found to leading order in* $1/q$ *by inserting the projector* K *either side of every layer* $\Gamma(j)$*,*

$$\int dU \, OTOC_\Gamma = q \langle Z_+| K\Gamma(1)K \cdots K\Gamma(T-1)K |Z(T)_-\rangle + \mathcal{O}\big(1/q^3\big) \quad \text{as } q \to \infty. \tag{4.38}$$

Proof. We have already proven in section 4.3 that the Haar average of a single correlation function is bounded by C/q^2 in the large q limit for some q independent constant C. We aim to identify which physical OTOCs are $\mathcal{O}(1/q^2)$ and what the numerical factor C is.

A generic physical OTOC is shown in the figure below

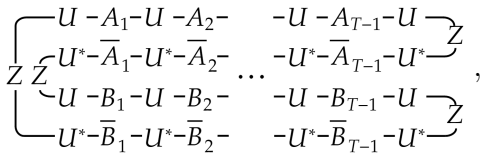

(4.39)

where $A_i, \overline{A}_i, B_i, \overline{B}_i \in \{\mathbb{1}, Z\}$. Writing its Haar average as a sum over permutations with Weingarten weights (without making use of an auxiliary unitary as done in the previous proofs), we find

$$\int dU \mathrm{OTOC} = \sum_{\sigma,\tau \in S_{2T}} \frac{Wg(\sigma\tau^{-1})}{q} \mathcal{G}(\sigma,\tau), \tag{4.40}$$

where the number of instances of U appearing in the OTOC (sum of the positive powers of U appearing in the OTOC) is $2T$ and where $\mathcal{G}(\sigma,\tau)$ is given by the trace diagram below. The trace is made clear by the repetition of leg labels on the incoming and outgoing legs,

$\mathcal{G}(\sigma,\tau) =$

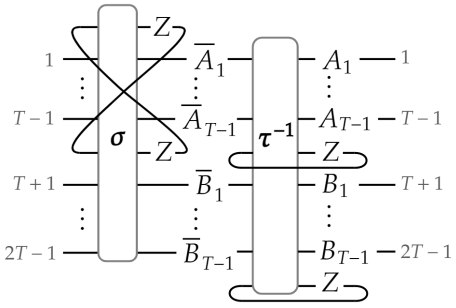

(4.41)

Bounding $\mathcal{G}(\sigma,\tau)$ takes a little work. Focus on the permutation σ and write down the qualitatively distinct options for the first and T-th legs.

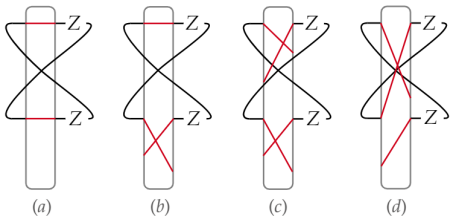

Figure 4.4: *(a) σ contains the 1-cycles $(1)(T)$; (b) σ contains a 1-cycle on only one of the legs, (1) or (T); (c) σ doesn't contain a 1-cycle on either leg 1 or T, neither does it contain a connection $1 \to T$ or $T \to 1$; (d) σ contains either the connection $1 \to T$ or $T \to 1$ or both.*

Assuming option (a) in Fig. 4.4, the closed loop in the σ block contributes a factor

q, the remainder of σ is given by some wiring from the $2T-2$ remaining input legs to the $2T-2$ remaining output legs. Likewise, with option (b) the σ block is given by some wiring between the $2T-2$ remaining incoming and outgoing legs but this time without the additional closed loop. With option (c), much the same as (b), the σ block is given by some wiring between $2T-2$ remaining input and output legs, however two of these output legs pick up a Z decoration. Finally, with option (d), the diagram is zero as this involves taking the trace of a Z decoration. We outline the τ block counterpart in the figure below.

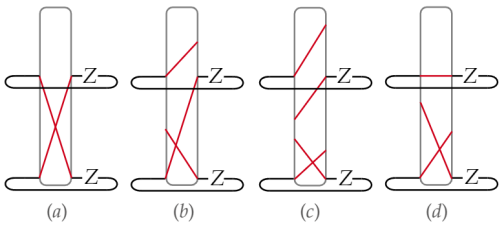

Figure 4.5: *(a) τ contains the 2-cycles $(T, 2T)$; (b) τ contains the connection $T \to 2T$ or $2T \to T$ but not both; (c) τ doesn't contain either connections $T \to 2T$ or $2T \to T$, neither does it contain either of the 1-cycles (T) or $(2T)$; (d) τ contains either or both of the 1-cycles (T) or $(2T)$.*

Assuming option (a) in Fig. 4.5, the τ block contributes an undecorated loop (a factor of q) and some wiring from the $2T-2$ remaining input legs to the $2T-2$ remaining output legs. With option (b), the τ block just contributes some wiring between the $2T-2$ remaining input and output legs. With option (c), the τ block also contributes some wiring between the $2T-2$ remaining input and output legs, but two of the output legs receive additional Z decorations. Option (d) involves the trace of a Z decoration and is therefore zero.

The maximum number of loops is found if all the $2T-2$ incoming legs return to their original positions after the σ and τ block wirings. In this case they contribute $2T-2$ loops, if we choose option (a) in both the σ and τ blocks we find two additional loops and have an upper bound of $2T$ loops total, whereas all other options give at most $2T-1$ loops. Let $|\sigma\tau^{-1}| \geq 2$, then even with the upper bound of $2T$ loops (a factor q^{2T} from $\mathcal{G}$), the factor $|\frac{Wg}{q}| \sim q^{-2T-1-|\sigma\tau^{-1}|}$ gives a combined contribution of order $\mathcal{O}(q^{-3})$ if

$|\sigma\tau^{-1}| \geq 2$. Therefore the $\mathcal{O}(q^{-2})$ contributions to the Haar averaged OTOC must come from contributions with $\sigma = \tau$ or $|\sigma\tau^{-1}| = 1$. We will study each case separately. This simplifies the OTOC Haar average as shown below,

$$\int dU \text{OTOC} = \langle OTOC \rangle_+ - \langle OTOC \rangle_- + \mathcal{O}\big(1/q^3\big). \tag{4.42}$$

where

$$\langle OTOC \rangle_+ = \frac{1}{q^{2T+1}} \sum_{\sigma \in S_{2T}} \mathcal{G}(\sigma), \quad \langle OTOC \rangle_- = \frac{1}{q^{2T+2}} \sum_{\substack{\sigma,\tau \in S_{2T} \\ |\sigma\tau^{-1}|=1}} \mathcal{G}(\sigma, \tau) \tag{4.43}$$

and where we have used the shorthand $\mathcal{G}(\sigma) \equiv \mathcal{G}(\sigma, \sigma)$.

4.5.1 Contributions with $\sigma = \tau$: $\langle \text{OTOC} \rangle_+$

$$\langle \text{OTOC} \rangle_+ = \frac{1}{q^{2T+1}} \sum_{\sigma \in S_{2T}} \mathcal{G}(\sigma) \tag{4.44}$$

While we already have a diagrammatic representation for $G(\sigma)$, there is a more convenient diagrammatic representation. With $\sigma = \tau$, each instance of a unitary U is paired with a $U^\dagger$ in the following manner:

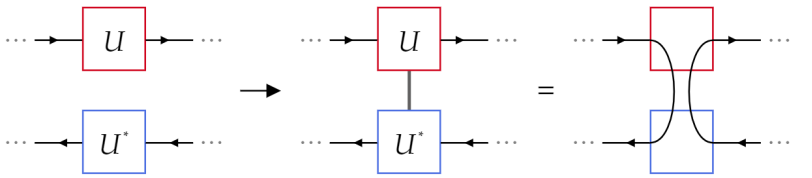

After choosing a pairing σ of unitaries U with $U^\dagger$ (or U^* if the incoming/outgoing legs have been switched in the tensor diagram, see Fig. 4.6), we draw a grey edge between each pair. This grey edge is a shorthand for a pair of edges which identify incoming and outgoing legs. The arrow direction follows the clockwise direction around the OTOC contour, as seen in Fig. 4.7.

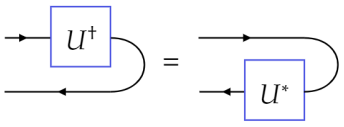

Figure 4.6: *We use the following shorthand for moving operators around a contour, switching the input and output leg order, this introduces a transposition. In this case, changing a $U^\dagger$ into a U^*.*

A shorthand for the U-U^* pairing is given below,

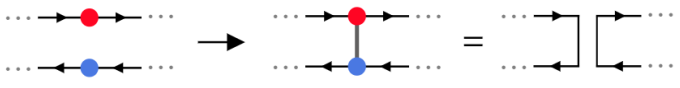

. (4.45)

We proceed by considering a generic physical OTOC and stretching OTO contour out into a ring,

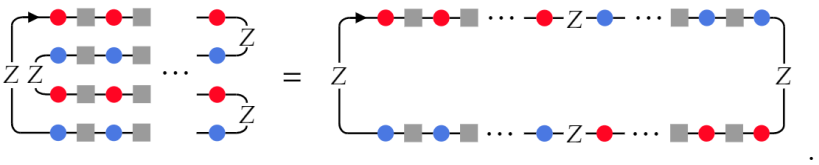

.

Figure 4.7: *A physical OTOC, the red dots represent the unitary U and blue dots U^* (or $U^\dagger$ depending on whether they have been brought around a bend). The grey boxes each represent either an identity operator or a Z operator.*

We find that this ring is divided into quarter arcs, with the first and third carrying the U's (red dots) and the second and fourth carrying the $U^\dagger$'s (blue dots). Each arc contains the same number of coloured dots, T. We simplify this further by suppressing every grey box (each of which can be a $\mathbb{1}$ or Z).

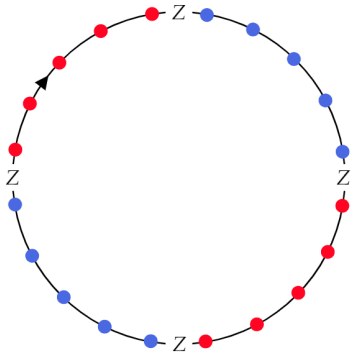

Figure 4.8: *A physical OTOC. We have suppressed every non U or $U^\dagger$ operator except for the Z decorations dividing each of the four OTO contour segments. The arrow signals the clockwise direction around the OTOC contour.*

A contribution $\mathcal{G}(\sigma)$ to $\langle OTOC \rangle_+$ is then simply a choice of pairings such as the one given in Fig. 4.9 below, and where we have introduced an additional shorthand that simply colours the arcs red or blue (to represent which arc contains U's or $U^\dagger$'s). The positions of the unitaries are given by the vertices of the internal grey edges with the boundary ring.

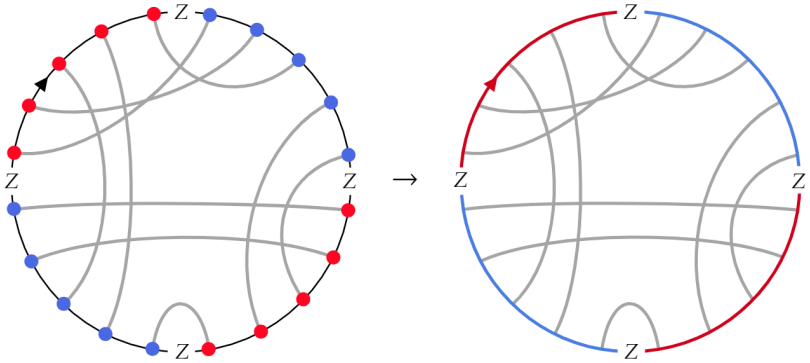

Figure 4.9: *Example of a choice of U-$U^\dagger$ pairings σ. We also introduce another shorthand which drops the U and $U^\dagger$ nodes and makes them implicit at the vertices of an interior edge and the perimeter edge, which is now coloured depending on whether the vertices are U's or $U^\dagger$'s.*

In the remainder of this section we will argue that minimising the number of internal edge crossings optimises the number of loops, thus maximising the contribution of the diagram. To do this, let us abstract these diagrams further and consider a diagram that is only a ring with interior edges between points on the ring and with no restrictions on

the positions of the vertices, such as the restriction above that edges must connect arcs with different colours. We also suppress the Z decorations as these are not important in the simple task of counting the number of loops in each diagram. We will refer to these abstracted diagrams as *cobweb diagrams*. An example of one of these cobweb diagram is given below

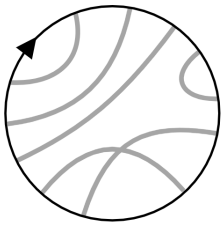

Figure 4.10: *A cobweb diagram is a perimeter ring with interior edges that connect two points on the ring. This diagram has $E = 6$ internal edges, $V = 12$ vertices and $C = 1$ crossing.*

The evaluation of these diagrams is done with an abstracted version of Eq. 4.45, which tells us how to interpret interior edges,

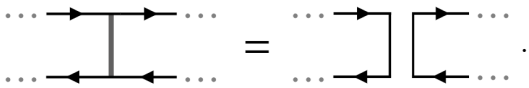

(4.46)

Using this rule, each cobweb diagram reduces to a number of loops, that we will refer to as index loops, each of which is associated with a factor q. We aim to find bounds on the number of index loops a cobweb diagram can have, depending on properties of the diagram such as the presence of edge crossings. Using Eq. 4.46, we can identify two simple ways of extracting index loops from a cobweb diagram,

Rule 1 (parallel-edge rule):

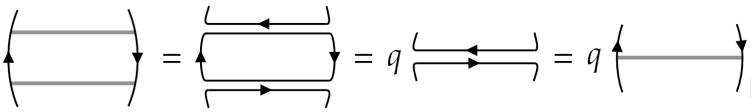

(4.47)

Rule 2 (edge-bubble rule):

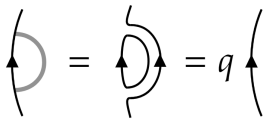

(4.48)

We refer to these rules as the *parallel-edge* rule and the *edge-bubble* rule respectively. Each time one of these rules is applied, an index loop (or factor q) is extracted from the diagram. Cobweb diagrams without any edge crossings (planar cobweb diagrams) are fully reducible to the perimeter ring with no internal edges (the *empty* cobweb diagram) through these rules alone. The empty cobweb is simply a single index loop and contributes one additional factor of q. With E being the number of internal edges, planar cobweb diagram have value q^{E+1} (i.e $E+1$ index loops).

However, one cannot completely evaluate all cobweb diagrams using these rules alone, the rules do not tell us how to deal with edge crossings. Rather than give a complete algorithm for determining the number of loops from a cobweb diagram, we will produce some useful bounds.

Given some cobweb diagram G with E internal edges, we exhaustively apply the parallel-edge and edge-bubble rules until we arrive at what we call a *reduced* cobweb diagram, where neither rule can be applied any further. Let E_p be the total number of edges removed through applications of these rules. If the $E_p = E$, then the diagram has had every edge removed and we arrive at the empty cobweb diagram. Otherwise the reduced diagram has $E' = E - E_p$ internal edges; all of which cross at least one other edge.

It will be helpful to enumerate some of ways of forming an index loop. We will focus on short index loops, i.e index loops containing only a small number of boundary edge segments. A boundary edge segment is the segment of the boundary ring bordered at each end by adjacent vertices, the total number of boundary segments is twice the number of internal edges. To form an index loop with only one boundary edge segment, start by picking a boundary edge segment. Then, to form an index loop which does not contain further boundary segments, one must draw an internal edge between the vertices connected by the boundary segment. These index loops are precisely those removed by the edge-bubble rule.

To form an index loop which contains two boundary segments, start by choosing two

segments. If the boundary edges share a vertex (i.e are adjacent) it is not possible to form an index loop that contains only these two segments. If they are separated, then there are two ways to connect up these vertices (without forming the single boundary-segment loops already considered previously), these are shown below:

1. non-crossing edges: 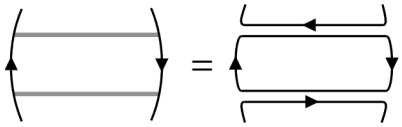

   Here we find an index loop that contains only two boundary segments.

2. crossed edges: 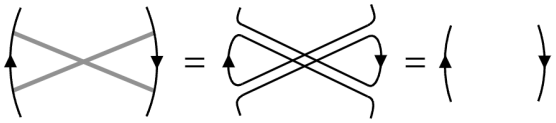

   We do not extract an index loop when the internal edges are crossed. In fact, the edges can be deleted without any change to the value of the diagram.

Therefore, index loops that involve exactly two boundary segments (draw a path through exactly two boundary segments) are the result of a pair of non-crossing edges of the form (1) above and are handled by the parallel-edge rule. While index loops passing through only one boundary segment are the result of edge-bubbles only and are dealt with using the edge-bubble rule. All other index loops must draw a path through three or more boundary segments.

We can use this information to bound the number of index loops in a reduced diagram. We have just seen that the parallel-edge rule and the edge-bubble rule remove all the one-boundary-segment and two-boundary-segment index loops from the diagram. The subsequent reduced diagram therefore contains index loops each of which contain three or more boundary segments. The number of internal edges in a reduced diagram is E' and the number of vertices is $V' = 2E'$. The number of boundary segments is $B' = V' = 2E'$. As each boundary segment is part of only one index loop, then for $E' \geq 2$ ($E' = 1$ is not possible), the number of index loops is bounded by $N' \leq B'/3 = 2E'/3$. For $E' = 0$, the number of index loops is given by $N' = 1$. We can combine these cases into the single inequality

$$N' \leq \max(1, 2E'/3) \tag{4.49}$$

The number, N, of index loops in the full (un-reduced) diagram is then bounded by

- planar cobweb diagrams ($E' = 0$): $N = E + 1$
- non-planar cobweb diagrams ($E' \geq 2$): $N \leq E_p + \frac{2}{3}(E - E_p) = E - E'/3$

where E is the total number of internal edges and $E_p = E - E'$ is the number of times the parallel-edge and edge-bubble rules were applied to arrive at the reduced diagram. A reduced diagram must have at least one crossing so $E' \geq 2$. The $E' = 2$ reduced diagram is unique and contains a single index loop and therefore $N = (E - 2) + 1 = E - 1$. With $E' = 3$, N is bounded by $N \leq E - 1$. For $E \geq 4$, the number of loops is bounded by $N \leq E-2$ (where we have used the fact that N must be an integer). Therefore, combining the Weingarten factor $\mathrm{Wg}(\sigma)/q$, $E' \geq 4$ cobweb diagrams contribute at order $\mathcal{O}(1/q^3)$ or smaller. We will now study planar cobweb diagrams, $E' = 2$ and $E' = 3$ cobweb diagrams in detail.

Planar diagrams

In this section, we re-decorate planar cobweb diagrams with the red and blue contour colouring and also the four compulsory Z decorations at the interfaces of each coloured contour. By doing this, we investigate the contribution of the planar cobweb diagrams to $\langle \mathrm{OTOC} \rangle_+$. The important distinction of the diagrams with U (red) and U^* (blue) contours is that there is an added condition that edges must pair points on contours of differing colour.

It is not possible to draw a planar diagram without a bubble edge, this bubble edge must either: (1) straddle a Z decoration at the interface of a red and blue contour, and hence take the trace $\mathrm{Tr}(Z) = 0$ as shown in Fig. 4.11; or (2) connect adjacent vertices within a single contour, however, this is not permitted as edges must connect vertices in contours of different colour.

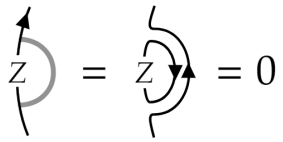

Figure 4.11: *The edge-bubble rule applied to an edge straddling a Z decoration.*

Therefore, no planar cobweb diagrams contributes to the physical OTOCs.

$E' = 3$ cobweb diagram

The only reduced diagram with $E' = 3$ edges is shown below,

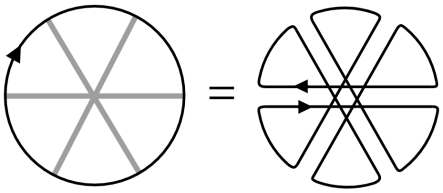

We can apply the parallel-edge and edge-bubble rules in reverse in order add back in edges and construct every diagram that reduced to this $E' = 3$ diagram. We do this to build a diagram G, but keep the three initial edges highlighted in our minds. We then reintroduce the Z decorations and the coloured U and $U^\dagger$ contours and find that there are two qualitatively different types of $E' = 3$ diagram. In the first, three contours are connected by the highlighted edges, in the second, only two contours are connected by the highlighted edges. Below we show these two cases but only display the highlighted edges in order to de-clutter the diagrams.

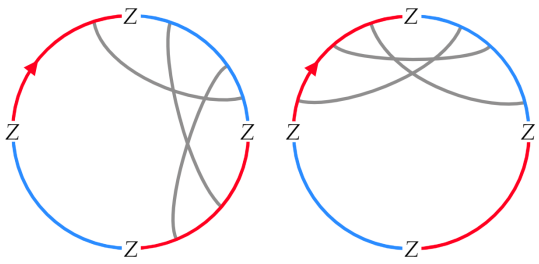

Figure 4.12: *The two qualitatively different $E' = 3$ diagram. (Left) Three contours are connected by the highlighted edges. (Right) Only two contours are connected by the highlighted edges.*

The edges that have not been displayed must either be parallel to another edge (in the sense used in the parallel edge rule) or be an edge-bubble. The edge-bubble option, as in the case of the planar diagrams, will lead to the trace of a Z decoration and is therefore not allowed. In the first case (on the left of Fig. 4.12), it is not possible to add edges connecting the lower left blue contour to one of the red contours using only the reversed parallel-edge. Therefore, the lower left blue contour must have no vertices in the full diagram G. However, another condition of the coloured diagrams is that each must have the same number of vertices, this excludes the diagram G just discussed. Next, consider the second case (on the right of Fig. 4.12), it is not possible to add edges that connect to either of the lower two contours (and avoid taking the trace of a Z) using only the reversed parallel-edge rule. Using again, the fact that each contour must have the same number of vertices, we are forced to dismiss this second type of $E' = 3$ diagram. Therefore, there are no $E' = 3$ diagrams that contribute to the Haar averaged OTOC. This leaves only the $E' = 2$ contributions to consider.

$E' = 2$ cobweb diagram

The only $E' = 2$ reduced diagram is given below.

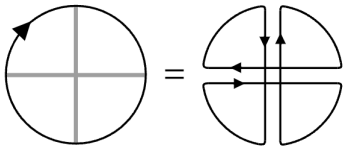

(4.50)

As before, by using the parallel-edge and edge-bubble rules in reverse, we can build every cobweb diagram that reduces to a $E' = 2$ reduced diagram. Doing this we build a diagram G, keeping the initial two edges highlighted in our minds before reintroducing the coloured contours and the Z decorations at each of the four interfaces. This gives two qualitatively distinct types of diagram which are shown below (where only the highlighted edges are drawn).

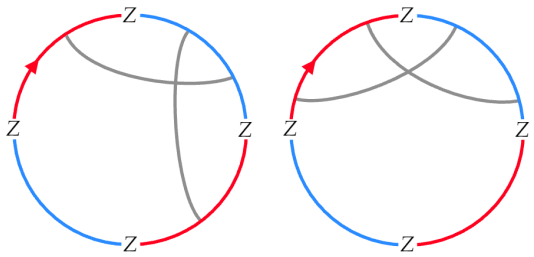

Figure 4.13: *The two qualitatively different $E' = 2$ diagram. (Left) Three contours are connected by the highlighted edges. (Right) Only two contours are connected by the highlighted edges.*

As in the case of $E' = 3$ diagrams, any edges added using the edge-bubble rule in reverse would have to straddle a Z decoration and therefore take the trace $\mathrm{Tr}(Z) = 0$. Consider the diagram on the right of Fig. 4.13, no edge can be added that connects to either of the lower two contours using the reversed parallel-edge rule. Therefore, by requiring each contour has the same number of vertices, this type of $E' = 2$ diagram is excluded. This leaves only the diagram on the left of Fig. 4.13. Adding edges using the parallel-edge rule in reverse generates a family of diagrams shown below, parameterised by four numbers $E_{1,\bar{2}}$, $E_{2,\bar{1}}$, $E_{1,\bar{1}}$ and $E_{1,\bar{1}}$, where $E_{i,\bar{j}}$ counts the number of edges connecting contour i with $\bar{j}$.

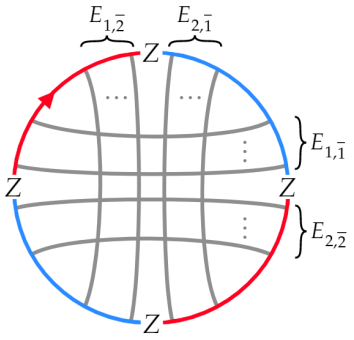

Using once more the fact that the diagram must have equal number of vertices on all of four of the arcs, $V_1 = V_{\bar{1}} = V_2 = V_{\bar{2}}$, we find the condition $E_{1,\bar{1}} + E_{1,\bar{2}} = E_{1,\bar{1}} + E_{2,\bar{1}} = E_{2,\bar{1}} + E_{2,\bar{2}} = E_{1,\bar{2}} + E_{2,\bar{2}}$ in the diagram above. This solved by $E_{1,\bar{1}} = E_{2,\bar{2}}$ and $E_{1,\bar{2}} = E_{2,\bar{1}}$. Therefore, the $E' = 2$ diagrams contributing to the averaged OTOC are in fact parameterised only by the total number of edges $E = 2T$ and by N_-, the number of edges connecting arc 1 to $\bar{1}$, where $1 \leq N_- < T$. Each of these diagrams with $E = 2T$

total edges has $E-1$ loops, combining the accompanying factor $\frac{1}{q^{2T+1}}$ this gives $\mathcal{O}(1/q^2)$ contributions to $\langle \text{OTOC} \rangle_+$.

Folding one of these diagrams back up into the OTOC contour reveals a useful correspondence,

$$\langle \text{OTOC} \rangle_+ = \sum_{N_-=0}^{T} \frac{1}{q^2}$$

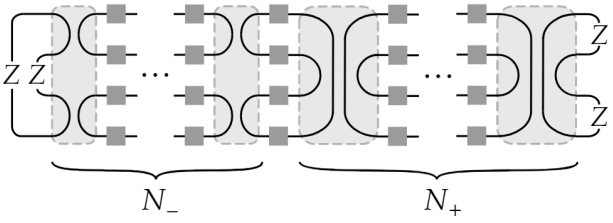

(4.51)

where $N_+ + N_- = T$ in the case of physical OTOCs with length T. We have been a little sloppy with the factors of q in this picture, this is easily resolved by associating with each closed loop a factor of $1/q$ to keep each loop normalised. Therefore, the $\mathcal{O}(q^{-2})$ contributions to $\langle \text{OTOC} \rangle_+$ are found simply inserting into the OTOC the projector $K_- = |-\rangle\langle -|$ for the first N_- layers and then the projector $K_+ = |+\rangle\langle +|$ for the remaining layers and summing over N_- from $N_- = 1$ to $T-1$.

4.5.2 Contributions with $|\sigma\tau^{-1}| = 1$: $\langle OTOC \rangle_-$

$$\langle \text{OTOC} \rangle_- = \frac{1}{q^{N+2}} \sum_{\substack{\sigma,\tau \in S_N \\ |\sigma\tau^{-1}|=1}} \mathcal{G}(\sigma,\tau) \tag{4.52}$$

As in the $\sigma = \tau$ case, we can stretch the OTOC contour into a circle and then draw edges between U's and $U^\dagger$'s. However, this time, while almost every U is paired with a $U^\dagger$ as before, now two of the U's and two of the $U^\dagger$'s are grouped in a cycle $U_i \to U_j^\dagger \to U_k \to U_l^\dagger \to U_i$. This means that there are two kinds of internal edges: (1) the grey edges used previously which, because they carry two indices, we now also refer to them as *doubled edges*; (2) the new edge which we call a *single-index edges* as they carry only one index each, these are represented as thin black edges in the interior of the diagram. The rules for the single-index edges are shown below, where the curved edges are boundary segments (part of the boundary ring).

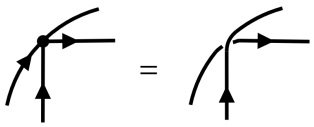

Before we consider the consequences for the diagrams with the four coloured contours (two red and two blue) and Z decorations, we will consider abstracted diagrams as we did before. These abstracted diagrams are the same as before, with the addition of a cycle of four single-index edges. There are four qualitatively different realisations of a cycle of four single-index edges. In each case, the diagram fragments into sub-diagrams, possibly connected by grey (doubled) edges. Individually, these sub-diagrams are identical to the cobweb diagrams seen in the previous section. However, unlike in the previous section and because there are now multiple cobwebs at once, they can be connected by grey edges. Below we shown an example for each of the four qualitatively different ways of fragmentation. We will choose a convention in which all edges belonging to a single sub-diagram are drawn entirely within the sub-diagram's interior, and all edges connected different sub-diagrams are drawn such that they never cross the interior of a sub-diagram. The usefulness of this convention is shown in section 4.5.2

1. 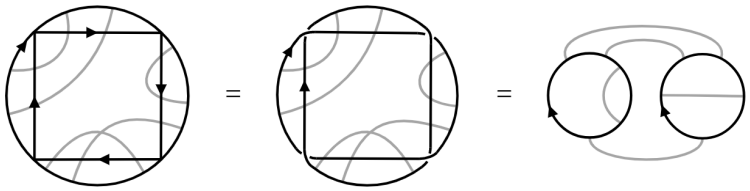

2. 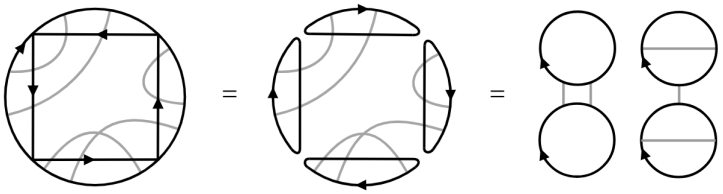

3. 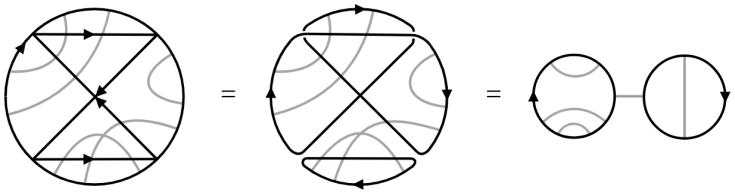

4. 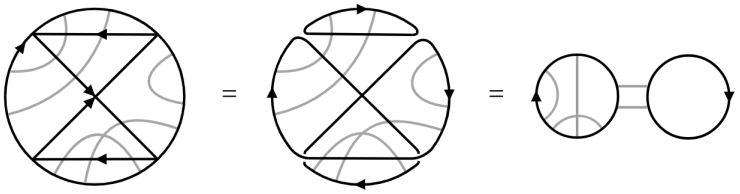

As before, we will attempt to identify index loops that contain as few boundary segments as possible. The analysis is almost identical to that of the previous section. All index loops that contain only one boundary segment must be those associated with the bubble-edge rule. All index loops that contain only two boundary segments are those associated with the parallel-edge rule, except for a special case that we will discuss in a moment. The proof of the two-boundary-segment index loop case is as follows: If the boundary segments belong to the same sub-diagram then the argument in the previous section applies. If they belong to different sub-diagrams then the vertices can be connected in only three ways (excluding pairings into one-boundary-segment index loops):

1. non-crossing edges: 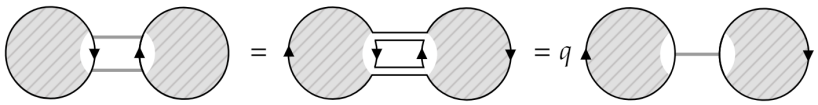

   Here we have found and eliminated an index looping involving two boundary segments on different sub-diagrams. This is in fact just an application of the parallel-edge rule.

2. crossed edges: 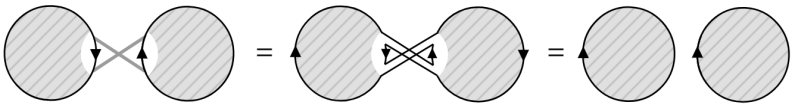

   Here we have not found an index loop. Instead we have managed to delete the crossed edges without accumulating any factors of q.

3. Special case: in this case we consider only a single edge between two sub-diagrams. If both of the sub-diagrams are otherwise empty, the diagram is equivalent to a single index loop, this index loops involves only two boundary segments. This is shown below.

   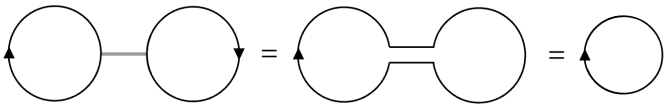

Therefore, two-boundary-segment index loops are either extracted using the parallel-edge rule or is found when two otherwise empty sub-diagrams are connected by a single grey edge.

Why the convention?

We have adopted a convention in which edges between sub-diagrams cannot cross the interior of any sub-diagram. If we didn't follow this convention when drawing diagrams, we would run into the following situations: (1) a pair of edges may appear to be crossing and yet the parallel-edge rule still applies, this is to do with the fact that the orientation of the arrows on the boundary edges differs from that shown in the parallel-edge rules; (2) a pair of edges that appear to be parallel are in fact dealt with by the edge crossing rule. Below we show examples of this.

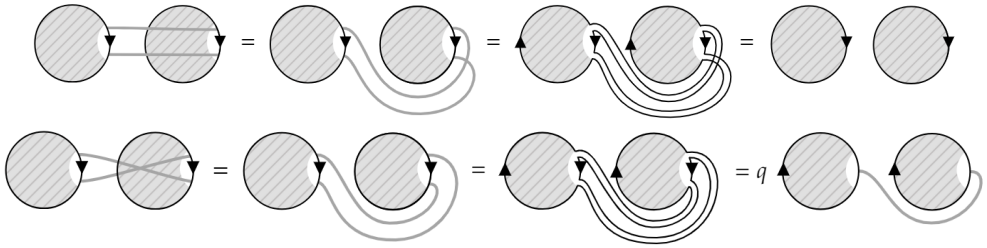

Any edges that appear parallel when drawn according to our convention can be treated with the parallel edge rule with no complications or subtleties.

We can now reduce a diagram G with N_S sub-diagrams by using the parallel-edge rule and edge-bubble rule. The diagram G' we arrive at after exhaustively applying the rules is again referred to as reduced diagram. We will use this strategy to find bounds on the number of index loops for an initial diagram G consisting of $N_S = 2$ or 4 sub-diagrams, E_i internal edges that belong to the i-th sub-diagram, and $E_{i,j}$ edges between sub-diagrams i and j. The reduced diagram will have E'_i edges belonging to i-th sub-diagram and $E'_{i,j}$ edges between sub-diagrams i and j, $i \neq j$. Each application of the parallel-edge rule and the edge-bubble rule reduces the number of edges in the diagram by one. Therefore,

$E' = E - E_p$, where $E = \sum_i E_i + \sum_{i \neq j} E_{i,j}$, $E' = \sum_i E'_i + \sum_{i,j} E'_{i \neq j}$ and E_p is the number of times an edge was removed by the rules. An important thing to note is that the rules cannot remove all edges between two sub-diagrams, unless they initially shared no edges. This is summarised below.

$$E'_{i,j} \geq 1 \text{ iff } E_{i,j} \geq 1, \quad E'_{i,j} = 0 \text{ iff } E_{i,j} = 0 \tag{4.53}$$

Let M be the number of times the special case configuration appears in G' and N'_{planar} the number of disconnected planar sub-diagrams in G'. We are able to bound the number of index loops in G' as follows: (1) each disconnected planar sub-diagram in G' is fully reduced (i.e the empty cobweb diagram) and therefore contributes a single index loop; (2) each special case configuration contributes a single index loop; (3) every remaining index loop in G' contains at least three boundary segments, allowing us to bound the number of these index loops from above by $2(E' - M)/3$, where $E - M$ is the number of edges left after removing the special case configuration. This gives the bound

$$N' \leq N'_{\text{planar}} + M + 2(E' - M)/3 = N'_{\text{planar}} + 2E'/3 + M/3, \tag{4.54}$$

where $N'_{\text{planar}} + M/2 \leq N_S$. The total number of index loops for a diagram G (that reduces to G') is then given by

$$N \leq E - (E' - M)/3 + N_{\text{planar}}, \tag{4.55}$$

where we have uses the fact that the number of disconnected planar sub-diagrams is conserved through the reduction process to say $N_{\text{planar}} = N'_{\text{planar}}$. We remind the reader that the Weingarten factor is given by $\text{Wg}(\sigma\tau^{-1}) \approx -q^{-2T-1} = -q^{-(E+2)-1}$, where because two of the $2T$ instances of U have been already allocated single-index edges, there are only $E = 2T - 2$ grey (doubled) edges. The contribution made from a diagram with N index loops has the size $\left|\frac{\text{Wg}(\sigma\tau^{-1})}{q} q^N\right| \approx q^{N-E-4}$. In order for the contribution to be $\mathcal{O}(1/q^2)$ or larger, the number of loops must satisfy $N - E \geq 2$. Comparing this to the inequality

Eq. 4.55, we see that

$$\frac{M - E'}{3} + N_{\text{planar}} < 2 \implies \text{contributes at } \mathcal{O}\big(1/q^3\big) \text{ or smaller.} \tag{4.56}$$

Importantly $M - E' \leq 0$ and $N_{\text{planar}} \leq N_S$. Therefore, for $N_S = 2$, a contribution can only be relevant if $N_{\text{planar}} = 2$, this accounts for both sub-diagrams and so $M = 0$. Therefore, the only $N_S = 2$ contributions at $\mathcal{O}(1/q^2)$ are those where the sub-diagrams are disconnected and planar. For $N_S = 4$, the situation is not so tightly constrained. Due to the fact that $M - E' \leq 0$ we can see that we need $2 \leq N_{\text{planar}} \leq 4$. For $N_{\text{planar}} = 2$ we require $M = E'$ and we only have two sub-diagrams to use, therefore $M \leq 1$. If $M = E' = 0$, these sub-diagrams must be planar which contradicts the assumption that $N_{\text{planar}} = 2$, therefore we must have $M = E' = 1$. For $N_{\text{planar}} = 3$ we are left with a single disconnected sub-diagram that, by assumption, is not planar, i.e $E' \geq 2$ and $M = 0$. Finally, for $N_{\text{planar}} = 4$, we obviously have $M = E' = 0$.

Therefore, for $N_S = 4$, there are only 3 configurations to consider: $(N_{\text{planar}}, E', M) = (2, 1, 1)$, $(3, 2, 0)$ and $(4, 0, 0)$. While for $N_S = 2$, there is only one $(2, 0, 0)$.

Reintroducing the coloured contours and Z decorations

It is now time to reintroduce the coloured contours and the Z decorations at the interfaces of these contours. Unlike in the abstracted colourless case, there six qualitatively different fragmentation schemes, depending on whether the cycle of four single-index edges explore all four contours, three contours, or only two contours. The six schemes are: each U and $U^\dagger$ belong to different contours and the cycle is (1) clockwise or (2) anti-clockwise; both U's ($U^\dagger$'s) belong to the same contour while the $U^\dagger$'s (U's) belong to different contours with different directions of the cycle being (3) and (4) as shown below; both U's belong to the same contour and both $U^\dagger$'s belong to the same contour with the two directions of the cycle being (5) and (6) as shown below.

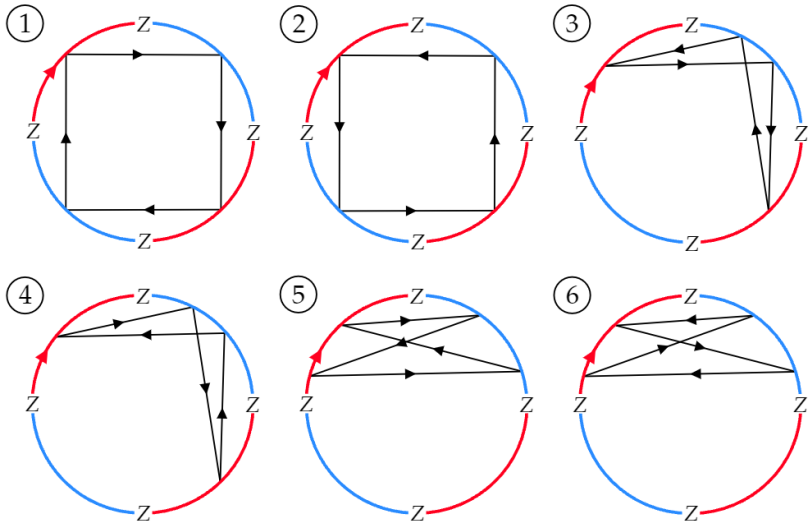

Figure 4.14: *The six qualitatively different configurations of the four-cycle.*

All grey edges have been suppressed. Keeping them suppressed and using the rule for single-index edges, the perimeter ring of the diagram fragments into a number of sub-diagrams. An example of the fragmentation scheme (1) is shown below.

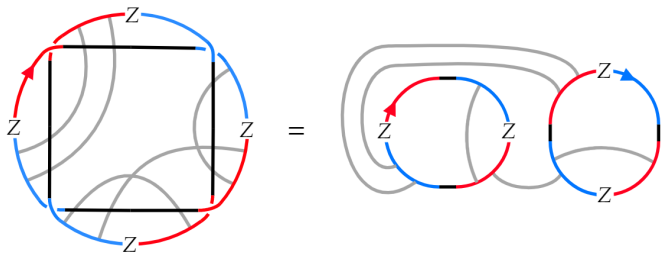

We have left a small portion of the single-index edges in the sub-diagrams on the right hand side to aid understanding of the fragmentation. From now on, we will omit this and simply connect together the blue and red contours. Suppressing the doubled-edges, we show each fragmentation scheme in Fig. 4.15.

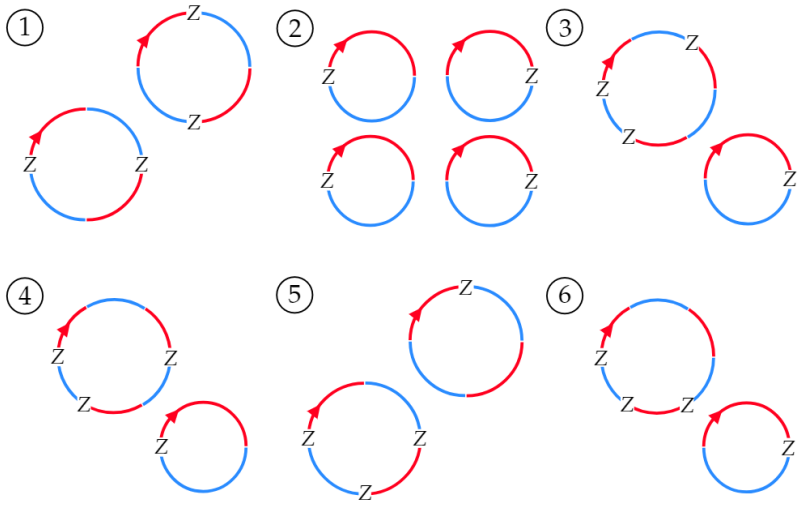

Figure 4.15: *The four-cycle fractures the diagram into one of six qualitatively different fragmentation schemes.*

Cases (1),(3)-(6) all have $N_S = 2$ and so the diagrams of interest are those with disconnected planar sub-diagrams. Consider a planar sub-diagram with only one red and one blue contour, the general form of such a diagram is shown below.

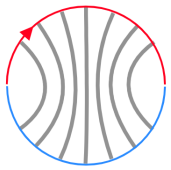

If there happens to be a Z decoration at the interface between a red and blue contour, as is the case in cases (3), (4) and (6), then the trace of the Z decoration appears in the evaluation of the diagram.

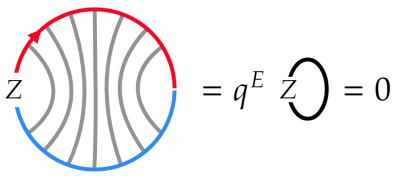

Therefore, cases (3), (4) and (6) can be discarded[3]. Planar diagrams with two red and two blue contours have the slightly more complex form shown in Fig. 4.16.

[3]If, due to the placement of a four-cycle vertex directly next door to a contour interface, one of these contours had zero length, then the sub-diagram would have only a single coloured contour. Unless this second contour also had zero length, then edges connected to this contour must connect to a different

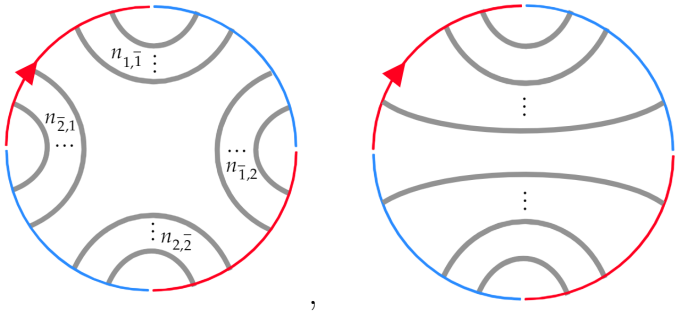

Figure 4.16: *(Left) A general planar diagram for diagrams with two red and two blue contours. (Right) An extremal planar diagram.*

In Fig. 4.16 we have shown an extremal case on the right. If there happened to be a Z decoration at the interface of a red and blue contour, then every non-extremal planar sub-diagram vanishes. If there happens to be an odd number of Z decoration at the interfaces of red and blue contours, then even the extremal planar diagrams vanish . Therefore, case (5) can be discarded. This leaves only case (1) and (2).

Next, consider the case (2), where $N_S = 4$. We must check both the case of four disconnected planar sub-diagrams, the case of disconnected sub-diagrams with all but one sub-diagram being planar and the case with two planar sub-diagrams and where the remaining two sub-diagrams reduce to the special case. Notice, however, that each sub-diagram has only one red and one blue contour and a single Z decoration at one of the interfaces. Planar diagrams will force the trace to be taken of these Z decorations, rendering them zero. Therefore, we can discard case (2) also[4].

We have recently seen the general form of a planar sub-diagram in Fig. 4.16 with two red and two blue contours. This applies to case (1) and we see that the following extremal planar diagrams manage to pair up the Z decorations onto the same index loop. Non-extremal planar diagrams would take the trace of these Z decorations, as would extremal diagrams with the wrong orientation,

sub-diagram, this we have argued is a sub-leading contribution. If indeed both the red and blue contour were of zero length, then the Z decoration must be traced and hence the contribution is zero. In any case, the conclusion about cases (3), (4) and (6) is the same.

[4]Should any of the contours be zero length, then that sub-diagram could not possible be planar.

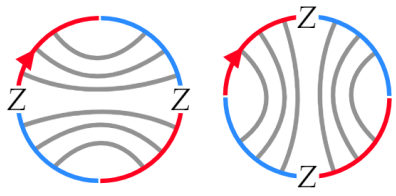

Therefore, the only contribution to $\langle \text{OTOC} \rangle_-$ is case (1) with disconnected extremal planar sub-diagrams. Reversing the fragmentation we find the following equivalent diagram,

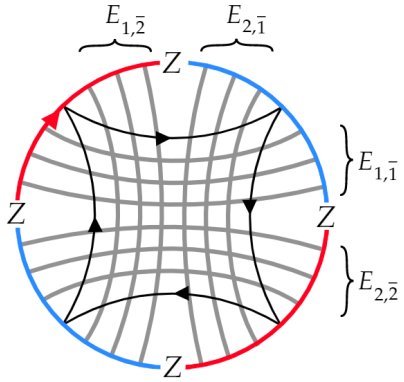

We must once again use the fact that the number of vertices in each arc is equal to argue that $E_{1,\bar{1}} = E_{2,\bar{2}}$ and $E_{1,\bar{2}} = E_{2,\bar{1}}$. Folding this diagram back into the OTOC contour gives

$$\langle \text{OTOC} \rangle_- = \sum_{N_-=0}^{T-1} \frac{1}{q^2} \quad (4.57)$$

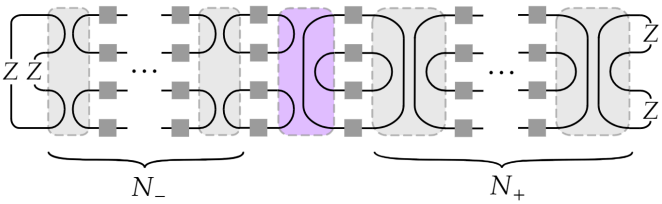

Where $N_+ + N_- + 1 = T$. We associated with each closed loop a factor of $1/q$ to keep each loop normalised.

4.5.3 Piecing everything together

Recalling definition Eq. 3.13 and the definition of the layer $\Gamma(t)$ in Fig. 4.3, $\langle \mathrm{OTOC} \rangle_+$ is given by

$$\langle \mathrm{OTOC} \rangle_+ = \frac{1}{q^2} \sum_{m=1}^{T-1} \left(\prod_{t=1}^{m-1} \langle - | \, \Gamma(t) \, | - \rangle \right) q \, \langle - | \, \Gamma(m) \, | + \rangle \left(\prod_{t=m+1}^{T-1} \langle + | \, \Gamma(t) \, | + \rangle \right) \tag{4.58}$$

and $\langle \mathrm{OTOC} \rangle_-$ is given by

$$\langle \mathrm{OTOC} \rangle_- = \frac{1}{q^2} \sum_{m=0}^{T-1} \left(\prod_{t=1}^{m} \langle - | \, \Gamma(t) \, | - \rangle \right) \left(\prod_{t=m+1}^{T-1} \langle + | \, \Gamma(t) \, | + \rangle \right) \tag{4.59}$$

Adding these together gives,

$$\begin{aligned} \int dU \mathrm{OTOC} = \frac{1}{q^2} \sum_{m=1}^{T-1} \left(\prod_{t=1}^{m-1} \langle - | \, \Gamma(t) \, | - \rangle \right) q \, \langle - | \, \Gamma(m) \, | 0 \rangle \left(\prod_{t=m+1}^{T-1} \langle + | \, \Gamma(t) \, | + \rangle \right) \\ - \frac{1}{q^2} \prod_{t=1}^{T-1} \langle + | \, \Gamma(t) \, | + \rangle \, . \end{aligned} \tag{4.60}$$

With a little work, which we will not do here, one can check that this is equivalent, at $\mathcal{O}(1/q^2)$ to

$$\int dU \mathrm{OTOC} = \tag{4.61}$$

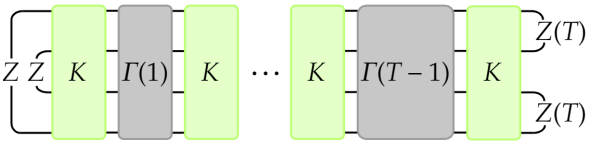

where K is as defined Eq. 4.37. □

This result is in fact identical, at $\mathcal{O}(1/q^2)$, to the result obtained when each layer $\Gamma(t)$ is scrambled by independently random unitaries. We did not require any information about the operators content of each layer $\Gamma(t)$ to arrive at this result and therefore, the result holds for any OTOCs of the form $\langle ZAZ(T)B^\dagger ZCZ(T)D^\dagger \rangle$ where A, B, C and D are time-ordered products of the form $O_1(1) \cdots O_{T-1}(T-1)$ for any normalised, traceless $O_i \in \mathbb{C}^{q \times q}$.

In appendix B, we show that Eq. 4.60 for the Haar average of a physical OTOC is equivalent, at $\mathcal{O}(1/q^2)$, to Eq. 4.6 presented in theorem 3.

4.6 Higher order corrections

These $q \to \infty$ results are not especially useful without some understanding of the error from higher order corrections. Developing a theory for such errors is very challenging, requiring a lot more bookkeeping. Instead of presenting a proper accounting of the errors for general ATO correlators (and products of correlators), we will study specific correlators in detail, and where possible give exact Haar averaged results. Using the intuition gained, we conjecture that the errors can be neglected provided that the number of unitaries appearing in an expression to be averaged scales sub-linearly in q, i.e., q^α with $\alpha < 1$.

4.6.1 Single correlation function

As a warm up, we will consider the Haar average of a single time-ordered (TO) correlation function. We have seen that at leading order this is $\mathcal{O}(1/q^2)$. However, we have not fixed the proportionality constant or quantified the subleading corrections. We will do this now for the following correlator $\langle \mathcal{Z}(t) \rangle = \langle Z U^t Z U^{-t} \rangle$, before discussing general TO correlators. We take the Haar average of $\langle \mathcal{Z}(t) \rangle$ by introducing a proxy Haar random unitary V via $U \to VUV^\dagger$ (left/right invariance of the Haar measure),

$$\int dU \langle \mathcal{Z}(t) \rangle = \int\int dU dV \langle Z V U^t V^\dagger Z V U^{-t} V^\dagger \rangle. \tag{4.62}$$

The Haar average over V involves only the second moment of the Haar ensemble. This yields the following,

$$\int dU \langle \mathcal{Z}(t) \rangle = \int dU \frac{|\operatorname{Tr} U^t|^2 - 1}{q^2 - 1}. \tag{4.63}$$

Using Eq. 4.19, this is evaluated to be

$$\int dU \langle \mathcal{Z}(t) \rangle = \frac{\min(t,q)-1}{q^2-1}. \tag{4.64}$$

For $t < q$ this is simply

$$\int dU \langle \mathcal{Z}(t) \rangle = \frac{t-1}{q^2} + \mathcal{O}\big(t/q^4\big). \tag{4.65}$$

General TO correlation functions

A general TO correlator is given by

$$\langle \mathcal{Z}(\boldsymbol{t}) \rangle = \langle ZUA_1 \cdots A_{t-1} U Z U^\dagger \overline{A}_{t-1} \cdots \overline{A}_1 U^\dagger Z U^\dagger \rangle. \tag{4.66}$$

Generalising the previous analysis to arbitrary TO correlation functions is a challenging task involving a tedious bookkeeping of diagrams of the type seen in Sec. 4.5 for physical OTOCs. Instead, we numerically Haar average a random selection of TO correlation functions. Randomly choosing a correlator amounts to randomly choosing each A_i and $\overline{A}_i$ as $\mathbb{1}$ or Z. We do this for correlators with different lengths $t \leq q$ and perform the Haar average by sampling with $N = 50,000$ (Haar) randomly chosen unitaries U. We show these results for $q = 16$ in Fig. 4.17. We see that the all (Haar averaged) TO correlators appear to be bounded from above by t/q^2. We conjecture that a tight inequality,

$$\int dU \langle \mathcal{Z}(\boldsymbol{t}) \rangle \leq \frac{t}{q^2} \quad \text{for } t \leq q. \tag{4.67}$$

Proving this is left for future work. We note that the analytically tractable correlation functions appear to be among the fastest growing with t.

4.6.2 Physical OTOCs

Estimating the errors in our $q \to \infty$ scaling expression for 'physical' OTOCs with analytically calculable OTOCs requires the use of the fourth moment of the Haar ensemble.

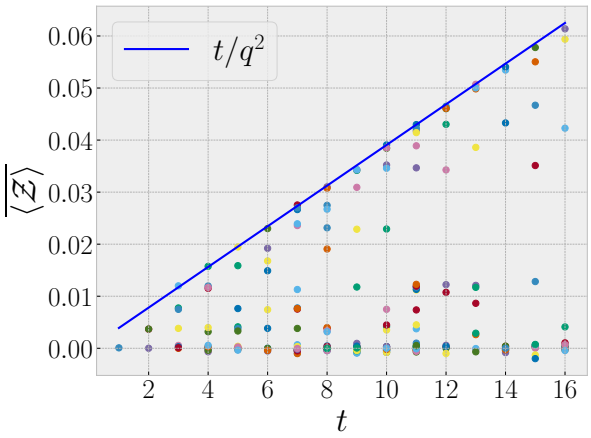

Figure 4.17: *Randomly chosen TO correlation functions $\langle \mathcal{Z} \rangle$ with $t \leq q$ and $q = 16$. Haar averaging is taken by sampling with $N = 50,000$ (Haar) randomly chosen unitaries U.*

Rather than doing this, we randomly choose physical OTOCs of length t (i.e., each time contour 1, $\overline{1}$, 2 and $\overline{2}$ has length t) and average them numerically by (Haar) randomly sampling $N = 200,000$[5]. In Fig. 4.18, we plot the (absolute value of the) difference $\delta\overline{\text{OTOC}}$ between the numerical Haar average and the large q asymptotic results of theorem 3. For $t < q$, the correction appears to be bounded by $2t(t+1)/q^4$.

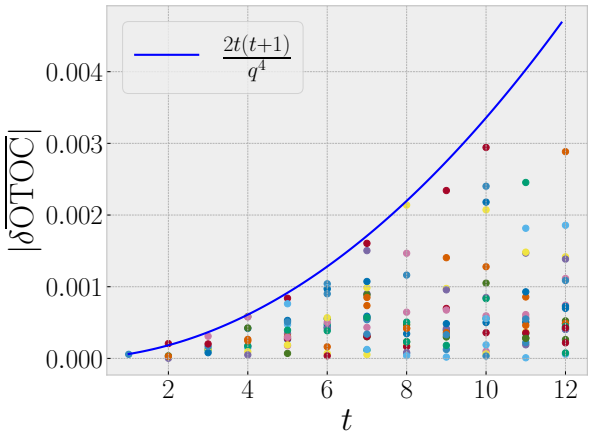

Figure 4.18: *The error in the $q \to \infty$ asymptotic results of Sec. 3 for randomly chosen OTO correlation functions $\langle \mathcal{Z} \rangle$ with length $t \leq q$ and $q = 16$. Haar averaging is taken by sampling with $N = 100,000$ (Haar) randomly chosen unitaries U.*

[5]Convergence of OTOC averages is noticeably slower than of TO correlators, leading us to increase in sample number N.

4.6.3 Correlators squared

Ideally, we would study the second moment of a correlation function such as $\langle ZU^t ZU^{-t}\rangle$ as a case study for the size of the errors. However, Haar averaging the second moment of this correlator involves using the fourth moment of the Haar measure and is a cumbersome task. Instead, we will study a similar correlation function $\langle \mathcal{Z}(t)\rangle = \langle VU^t V^\dagger U^{-t}\rangle$, where V is any unitary matrix. The left/right invariance of the measure dU implies the following

$$\int dU |\langle \mathcal{Z}(t)\rangle|^2 = \int\int dU dV |\langle VU^t V^\dagger U^{-t}\rangle|^2. \tag{4.68}$$

Where the measure dV is normalised, we take it to be the Haar measure. To integrate over V only requires the second moment of the Haar measure. This gives,

$$\int dU |\langle \mathcal{Z}(t)\rangle|^2 = \frac{1}{q^2(q^2-1)} \int dU \left[q^2 + |\operatorname{Tr}\big(U^t\big)|^4 - 2|\operatorname{Tr}\big(U^t\big)|^2\right] \tag{4.69}$$

We can use Eq. 4.19 to evaluate the U integral on the RHS. For $2t < q$ This gives,

$$\int dU |\langle VU^t V^\dagger U^{-t}\rangle|^2 = \frac{1}{q^2-1} + \frac{2t(t-1)}{q^2(q^2-1)}. \tag{4.70}$$

The first term is the leading order contribution predicted in theorem 2 for TO correlators (i.e., with symmetry factor $S = 1$). Whereas, the second term is the sub-leading correction not predicted by our $q \to \infty$ asymptotic results.

General TO correlators

We do not present a general theory for the sub-leading corrections to the Haar average of squared correlators. Instead, we present numerical data, where the Haar average has been taken by sampling over $N = 50,000$ (Haar) random unitaries U. As in the previous section, we randomly choose TO correlators, but now take the square of the absolute value before averaging. We show the results for $q = 16$ in Fig. 4.19. We see that the second moment of all correlation functions is given, at leading order in $1/q$, by the $q \to \infty$ scaling

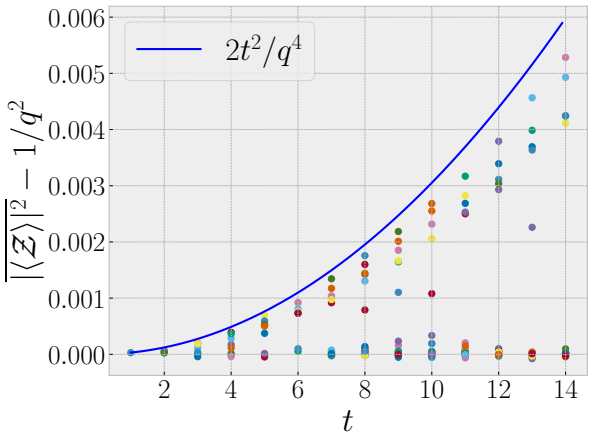

Figure 4.19: *The second moment* $\overline{|\langle\mathcal{Z}\rangle|^2}$ *of randomly chosen TO correlation functions* $\langle\mathcal{Z}\rangle$ *with* $t \leq q$ *and* $q = 16$*. Haar averaging is taken by sampling with* $N = 50,000$ *(Haar) randomly chosen unitaries* U*.*

results of 2. The sub-leading corrections are bounded by the function $2t^2/q^4$. We note that once again, the analytically tractable correlators are among the fastest growing (with t) of all the correlation functions.

OTO correlators

The square of an OTOC is harder to average, converging much more slowly with number of samples N. In Fig. 4.20 we plot the error in the $q \to \infty$ results of theorem 2 for the second moment of a random selection of physical OTOCs of lengths t. We use $N = 200,000$ samples for the Haar averaging, but note that not all points are converged. In lieu of nicely converged numerics, we assume that, like TO correlators, the second moment of an OTOC is given at leading order in $1/q$ by Eq. 2, and that the sub-leading corrections are at most $\mathcal{O}(\mathcal{N}^2/q^4)$, where $\mathcal{N}$ is the number of unitaries U appearing in the OTOC[6]. As we can see in Fig. 4.20, the error in the second moment of physical OTOCs appear to grow linearly with t. However, for more general OTO contour shapes this will surely change, since an OTO contour can be made very similar to a TO contour if one pair of contour legs (i.e., 1 and $\overline{1}$) are made very sort. We expect that such an OTOC will have corrections similar to TOC corrections. Quantifying the sub-leading corrections more precisely is left

[6]For TO correlators $\mathcal{N} = t$, whereas for physical OTOCs $\mathcal{N} = 2t$.

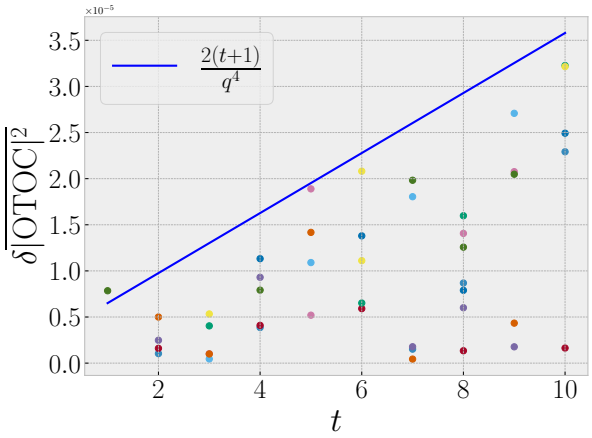

Figure 4.20: *The second moment* $\overline{|OTOC|^2}$ *of randomly chosen physical OTOCs with* $t \leq q$ *and* $q = 32$*. Haar averaging is taken by sampling with* $N = 100,000$ *(Haar) randomly chosen unitaries* U*.*

as future work.

4.6.4 Products of correlators

We are able to bound the (Haar average of) products of many correlation functions by using a generalised Holder's inequality and by bounding the variance of individual correlators. The expectation of a product of many (more than two) non-trivial correlators can be bounded by the following,

$$\left| \int dV \prod_i \langle \mathcal{Z}(\boldsymbol{t}_i) \rangle \right| \leq \int dV \prod_i |\langle \mathcal{Z}(\boldsymbol{t}_i) \rangle|. \tag{4.71}$$

Then, using the fact $|\langle \mathcal{Z}(\boldsymbol{t}_i) \rangle| \leq 1$, we can bound the average of a product of many correlators by an average over only a few. We choose to highlight three correlators,

$$\left| \int dV \prod_i \langle \mathcal{Z}(\boldsymbol{t}_i) \rangle \right| \leq \int dV |\langle \mathcal{Z}(\boldsymbol{t}_1) \rangle| |\langle \mathcal{Z}(\boldsymbol{t}_2) \rangle| |\langle \mathcal{Z}(\boldsymbol{t}_3) \rangle|. \tag{4.72}$$

Using a generalised Holder's inequality and monotonicity of the p-norm, we further bound Eq. 4.72 by

$$\left|\int dV \prod_i \langle \mathcal{Z}(\boldsymbol{t}_i)\rangle\right| \leq \sqrt{\int dV |\langle \mathcal{Z}(\boldsymbol{t}_1)\rangle|^2 \int dV |\langle \mathcal{Z}(\boldsymbol{t}_2)\rangle|^2 \int dV |\langle \mathcal{Z}(\boldsymbol{t}_3)\rangle|^2}. \tag{4.73}$$

We have seen that in the previous sections, that if we take $t \leq \sqrt{q}$, the Haar average of the square of a correlator is given at leading order by the large q asymptotic result in theorem 2 and that the correction is $\mathcal{O}(1/q^3)$. Taking times $t \leq \sqrt{q}$, we can then bound the above by

$$\left|\int dV \prod_i \langle \mathcal{Z}(\boldsymbol{t}_i)\rangle\right| \leq C\frac{S(\boldsymbol{t}_1)S(\boldsymbol{t}_2)S(\boldsymbol{t}_3)}{q^3}, \tag{4.74}$$

for an $\mathcal{O}(1)$ constant C. For TO and OTO correlators, $1 \leq S(\boldsymbol{t}) \leq 2$, so that the right hand-side of Eq. 4.74 then simplifies to C'/q^3 for an $\mathcal{O}(1)$ constant C'. This result means that for times $t \leq \sqrt{q}$, we can safely discard products of more than two correlators as $\mathcal{O}(1/q^3)$ or smaller. This will form the basis of a perturbative expansion in $1/q$ of the memory matrix in Sec. 5.4 in chapter 5.

CHAPTER 5

OPERATOR SPREADING IN MODELS WITH MEMORY

We have seen how to deploy the memory matrix formalism in random unitary circuits, where (after circuit averaging) the operator spreading dynamics is described by a Markovian random walk, i.e., the dynamics is memory-less. This chapter presents an investigation of quantum circuits with memory and with different spatio-temporal symmetries, using text and figures from my first author paper E. R. McCulloch and C. von Keyserlingk, "Operator spreading in the memory matrix formalism," Journal of Physics A: Mathematical and Theoretical, 2022 [114].

5.1 The model

The circuits we will study are composed of a layer of single site 'scrambling' unitaries, followed by a layer of nearest neighbour two-site unitary gates with a tunable coupling ε, as given in Eq. 5.1. The single time-step unitary is also shown graphically in figure 5.1. In Sec. 5.2 we will consider case where the scrambling gates are random in time and space and in Sec. 5.3 the case with spatial translation invariance, elaborating on our work in [114]. In Sec. 5.4, we consider the case with spatial translation symmetry and Floquet time translation symmetry, repeating the analysis of [114]. In every case, the scrambling

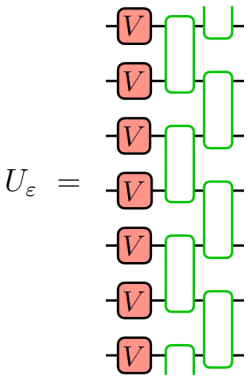

Figure 5.1: *A time-step with 2-local gates followed by a layer of single-site scramblers V. We consider cases where V is repeated at across all sites and times and cases where the scrambling unitary is chosen randomly for different sites and times.*

unitaries ensure that there are no diffusive conserved charges that might couple with the information mode.

$$U_\varepsilon = V^{\otimes N} e^{-\mathrm{i}\varepsilon H}, \quad H = \sum_j Z_j Z_{j+1}. \tag{5.1}$$

The coupling unitary can be written as a product of commuting two-site unitaries $e^{-\mathrm{i}\varepsilon H} = \prod_x e^{-\mathrm{i}\varepsilon Z_x Z_{x+1}}$. A single gate straddling the sites x and $x{+}1$ is given by $e^{-i\varepsilon Z_x Z_{x+1}} = \cos(\varepsilon)\mathbb{1}_x\mathbb{1}_{x+1} - i\sin(\varepsilon)Z_xZ_{x+1}$, and has the following diagrammatic representation,

$e^{-i\varepsilon Z_x Z_{x+1}} \equiv$ 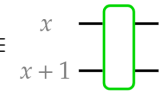 $= \cos(\varepsilon)$  $- i\sin(\varepsilon)$  , (5.2)

where a black dot represent a Z operator,

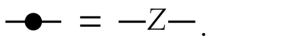

(5.3)

Likewise, the conjugate of the gate, $e^{i\varepsilon Z_x Z_{x+1}}$, is given by

$e^{i\varepsilon Z_x Z_{x+1}} \equiv$  $= \cos(\varepsilon)$  $+ i\sin(\varepsilon)$  . (5.4)

To use the MMF, we form the Floquet unitary for the doubled operator space, $\mathcal{U} = \mathcal{V}\mathcal{U}_Z$, where $\mathcal{U}_Z = e^{-\mathrm{i}\varepsilon H} \otimes e^{\mathrm{i}\varepsilon H} \otimes e^{-\mathrm{i}\varepsilon H} \otimes e^{\mathrm{i}\varepsilon H}$ contains the 2-local gates and $\mathcal{V}$ is the on-

site scrambling unitary (appropriate for the four copies of state space). As in the case with a single replica, We split $\mathcal{U}_Z$ up into a product of unitary gates, or *bricks*, given by $\mathcal{U}_{x,x+1} = e^{-i\varepsilon Z_x Z_{x+1}} \otimes e^{i\varepsilon Z_x Z_{x+1}} \otimes e^{-i\varepsilon Z_x Z_{x+1}} \otimes e^{i\varepsilon Z_x Z_{x+1}}$. This replicated gate has the diagrammatic representation

$\mathcal{U}_{x,x+1} \equiv$ 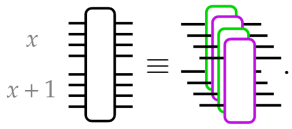 (5.5)

On each leg (labelled by both the replica index $1, \overline{1}, 2, \overline{2}$ introduced in Eq. 3.9 and by site position x), the brick has the option of carrying either a Z or a $\mathbb{1}$. In the following, we say that if a leg is carrying a non-identity factor A, then that the leg is *decorated* and that the factor A is the decoration. In this spirit, and using equations 5.2 and 5.4, we find the *decoration expansion* of the brick to be given by

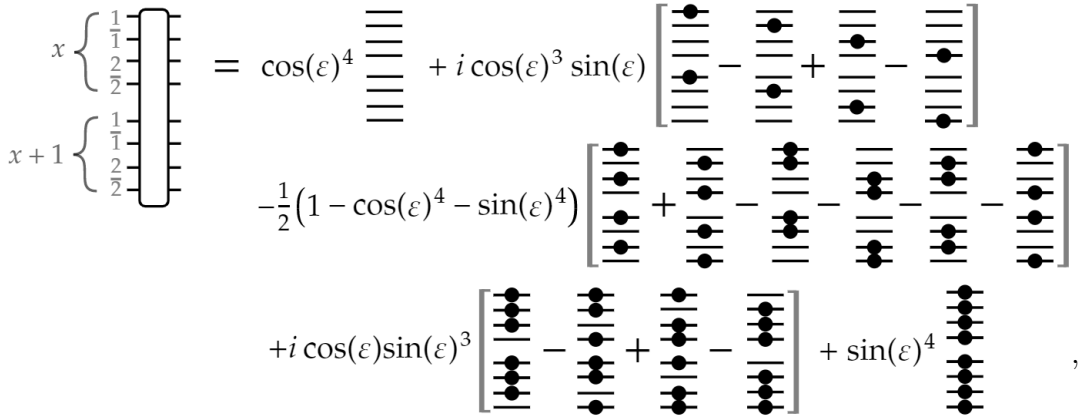

, (5.6)

Multiplying $\langle F^x|$ by a layer of two-site gates yields the following,

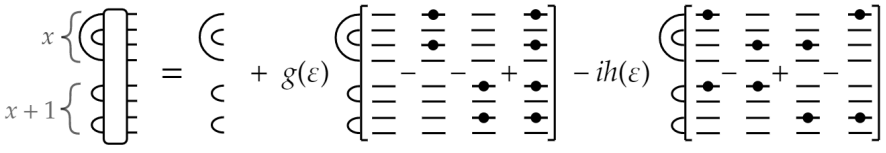

, (5.7)

where

$$g(\varepsilon) \equiv \frac{\cos(4\varepsilon) - 1}{4}, \quad \text{and} \quad h(\varepsilon) \equiv \frac{\sin(4\varepsilon)}{4}. \tag{5.8}$$

We have only depicted the sites x and $x+1$ either side of the *cut* (the domain wall between the + and − wiring configurations). Every brick $\mathcal{U}_{r,r+1}$ that does not straddle the cut is 'absorbed' into the state using the following property,

(5.9)

To see this, we notice that the state $\langle +,+|_{r,r+1}$ connects the replica 1 with $\overline{2}$ and 2 with $\overline{1}$ (see Eq. 3.13), so that the two copies of $U_{r,r+1}$ each find a copy of $U^\dagger_{r,r+1}$ to yield $U_{r,r+1}U^\dagger_{r,r+1} = \mathbb{1}$ and hence $\langle +,+|_{r,r+1}\,\mathcal{U}_{r,r+1} = \langle +,+|_{r,r+1}$. The isometry of $\mathcal{U}_{r,r+1}$, $S = (1 \leftrightarrow 2)$, relates $\langle +|$ and $\langle -|$ through $\langle \pm|\, S = \langle \mp|$. Using this isometry, the first equation in Eq. 5.9 implies the second.

The calculation of Ω does not depend on the choice of scramblers V, owing to the fact the single site unitary are absorbed by the weight super-operators. We can then use the translational invariance of the two-site unitaries to find $\Omega(k)$,

$$\Omega(k) \equiv \left(W^k\,|(\mathcal{U}_Z - \mathbb{1})|\,W^k\right) = \eta(k)(1-e^{-\mathrm{i}k})\sum_x q^x e^{-\mathrm{i}kx}\langle F^0\,|(\mathcal{U}_Z-\mathbb{1})|\,F^x\rangle. \tag{5.10}$$

where $\eta(k) = \frac{1-q^{-2}e^{\mathrm{i}k}}{1-q^{-2}}$. When the cuts are misaligned ($x \neq 0$), Eq. 5.9 can be used to say $\langle F^0|\,(\mathcal{U}_Z - \mathbb{1})\,|F^x\rangle = \langle F^0|\,(\mathcal{U}_{0,1} - \mathbb{1})\,|F^x\rangle = \langle F^0|\,(\mathbb{1}-\mathbb{1})\,|F^x\rangle = 0$. For aligned cuts ($x = 0$), Eq. 5.7 yields $\langle F^0|\,(\mathcal{U}_Z - \mathbb{1})\,|F^0\rangle = g(\varepsilon)$. $\Omega(k)$ is then succinctly given by

$$\Omega(k) = \eta(k)(1-e^{-\mathrm{i}k})g(\varepsilon). \tag{5.11}$$

In following sections we will see that the circuit averaged[1] memory matrix is $\mathcal{O}(1/q^2)$ (and $\mathcal{O}(1/q^4)$ in the case of scramblers random in time and space). Therefore we can use Ω alone in Eq. 3.71 to obtain a leading order expression for the circuit averaged butterfly

[1] A circuit average refers to the average of the Haar random unitary V

velocity $\overline{v_B}$ and front diffusion constant $\overline{D}$

$$v_0(\varepsilon) \equiv \lim_{q\to\infty} \overline{v_B(\varepsilon)} = \frac{1-\cos(4\varepsilon)}{4}, \quad \lim_{q\to\infty} \overline{D(\varepsilon)} = \frac{v_0(1-v_0)}{2}. \tag{5.12}$$

It is straightforward to see that brick-work circuits with commuting even and odd bricks (within one time-step) have a strict light-cone of $v_{LC} = 1$ as opposed to $v_{LC} = 2$ in brick-work circuits with non-commuting even and odd layers (as we saw in Sec. 2.5). Indeed, Eq. 5.12 for $\overline{D}$ appears to encode this strict light-cone by forcing the operator wave-front to have zero width when $v_B = 1$. However, it should be noted that in these particular models $\overline{v_B}$ can never approach the light-cone velocity, $0 \leq v_0 \leq 1/2$.

Before calculating the memory matrix Σ in the various cases of spatio-temporal symmetry, we will make some general comments on the dependence of Σ (and of v_B and D) on the coupling strength ε. Firstly, under the variable shift $\varepsilon \to \pi/2+\varepsilon$, the unitary $e^{-\mathrm{i}\varepsilon H}$ transforms as $\to (-\mathrm{i})^{N-1}e^{-\mathrm{i}\varepsilon H}$. The operator dynamics is blind to global phases, meaning that $\varepsilon \to \pi/2+\varepsilon$ is a symmetry of $v_B(\varepsilon)$ and $D(\varepsilon)$. Secondly, by globally swapping leg 1 with $\overline{1}$ and 2 with $\overline{2}$, we find $\Sigma_{V,\varepsilon}(k,z) = \Sigma_{V^*,-\varepsilon}(k,z)$. and $\Omega_\varepsilon(k) = \Omega_{-\varepsilon}(k)$, where we have have labelled Σ with a particular realisation of scramblers and with the coupling strength and labelled Ω with the coupling strength (Ω is independent of V). By integrating over V (in any of the cases of spatio-temporal symmetry), we find another symmetry of the circuit averaged butterfly velocity and diffusion constant $\overline{v_B(\varepsilon)}$ and $\overline{D(\varepsilon)}$, namely $\varepsilon \to -\varepsilon$. Using these symmetries, we determine that $\overline{v_B}$ is a function of $s(\varepsilon) = \cos(\varepsilon)^2\sin(\varepsilon)^2$ only.

5.2 Randomness in space and time

The first case we will investigate is the one in which the scramblers $V_{x,t}$ are chosen randomly in space and time. We will find it helpful to use a slightly modified time-step in this case. By using the invariance of Haar measure, $V_{x,t} \to W_{x,t}V_{x,t}$, we can split a layer of scramblers into the product of two layers of scramblers. Doing this for all time-steps,

we then choose a new, more symmetric, time-step as shown below,

$U_\varepsilon(t)$ =

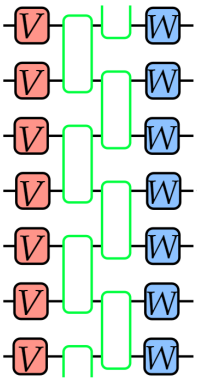

(5.13)

We stress that the model has remained unchanged, we have only used measure invariance to shift the position of what we call a 'time-step'. The lack of time and spatial translation symmetry indicates that we should use Eq. 3.76 for the memory matrix and then use translational invariance of the circuit ensemble to diagonalise $\overline{\Sigma}$, the circuit average of Σ. Time translation invariance of the ensemble allows us easily Laplace transform $\overline{\Sigma}(k,t)$, giving

$$\overline{\Sigma(k,z)} = \left(W^k \left| \overline{\mathcal{L}} Q \frac{-1}{e^{-\mathrm{i}z} - 1 - \overline{\mathcal{L}} Q} \overline{\mathcal{L}} \right| W^k \right), \tag{5.14}$$

Using Eq. 3.80, we find that the correction to $\overline{v_B}$ from memory contributions is given by

$$\overline{\delta v_B} \equiv \overline{v_B} - v_0 = \lim_{z \to \mathrm{i}0^+} \lim_{k \to 0} \frac{\overline{\Sigma}(k,z)}{\mathrm{i}k}. \tag{5.15}$$

Taking the $k \to 0$ limit and converting to a real-time sum leads to

$$\overline{\delta v_B} = -\sum_x e^{-\mathrm{i}kx} q^x \left\langle F^0 \right| \overline{\mathcal{L}} \left(Q \overline{\mathcal{U}} \right)^{n-1} Q \overline{\mathcal{L}} \left| F^x \right\rangle. \tag{5.16}$$

It is instructive to calculate the projected states $Q\overline{\mathcal{L}} \left| F^x \right\rangle = Q \left(\overline{\mathcal{V}} \mathcal{U}_Z \overline{\mathcal{W}} - \mathbb{1} \right) \left| F^x \right\rangle = Q \overline{\mathcal{V}} \mathcal{U}_Z \left| F^x \right\rangle$. All but the two-site brick $\mathcal{U}_{x,x+1}$ and the scramblers on sites x and $x+1$ are absorbed into the state $\left| F^x \right\rangle$. To evaluate the Haar average of a (replicated) scrambler $\overline{\mathcal{V}_x}$

we will use the following result (relying on the second moment of the Haar measure),

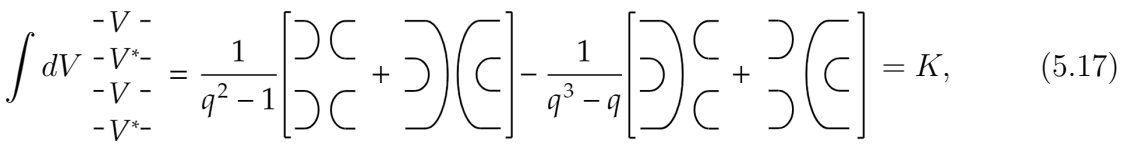

(5.17)

where K is a projector. Using the definitions of $|+\rangle$, $|-\rangle$, $|0\rangle$ in Eq. 3.12 and defining $|\perp\rangle = |-\rangle - \frac{1}{q}|+\rangle$, K is given algebraically as

$$K \equiv \frac{|-\rangle\langle\perp|}{1-q^{-2}} + \frac{|+\rangle\langle 0|}{1-q^{-2}} = \frac{|\perp\rangle\langle -|}{1-q^{-2}} + \frac{|0\rangle\langle +|}{1-q^{-2}}. \tag{5.18}$$

This allows us to write $Q\overline{\mathcal{L}}\,|F^x\rangle$ as

$$Q\overline{\mathcal{L}}\,|F^x\rangle = QK_xK_{x+1}\mathcal{U}_{x,x+1}\,|F^x\rangle\,. \tag{5.19}$$

Using Eq. 5.7 for $\mathcal{U}_{x,x+1}\,|F^x\rangle$, this simplifies to

$$Q\overline{\mathcal{L}}\,|F^x\rangle = \frac{g(\varepsilon)}{(q-q^{-1})^2}\,|+\rangle_{<x}\,|\perp\rangle_x\,|0\rangle_{x+1}\,|-\rangle_{>x+1}\,. \tag{5.20}$$

Likewise, with $\langle F^0|\,\overline{\mathcal{L}}Q = \langle F^0|\,\overline{\mathcal{W}}\mathcal{U}_Z Q$ we find

$$\langle F^0|\,\overline{\mathcal{L}}Q = \frac{g(\varepsilon)}{(q-q^{-1})^2}\,\langle +|_{<0}\,\langle\perp|_0\,\langle 0|_1\,\langle -|_{>1}\,. \tag{5.21}$$

Both of these states are suppressed by factors $1/q^2$, and provided that memory matrix decays quickly (with an $\mathcal{O}(1)$ time-scale $\tau(\varepsilon)$), the overall correction to the butterfly velocity will be $\mathcal{O}(1/q^4)$. The decay of the memory matrix with an $\mathcal{O}(1)$ timescale τ will be an assumption of the memory matrix calculations throughout this chapter, and reflects the expectation that we all hydrodynamical slow modes have been included in $\mathcal{P}$. In the next section we find that for the variant of the circuit with spatial translation symmetry, the circuit averaged real-time memory matrix $\overline{\Sigma}(t)$ decays with a timescale $\tau(\epsilon) \sim |g(\varepsilon)|$. In this work, we restrict our attention to $\mathcal{O}(1/q^2)$ contributions to the memory matrix

and do not pursue the $\mathcal{O}(1/q^4)$ corrections here. We therefore conclude,

$$\overline{v_B}(\varepsilon) = v_0(\varepsilon) + \mathcal{O}\big(1/q^4\big). \tag{5.22}$$

5.3 Spatial translation symmetry

We now turn to the variant of the model with spatial translation symmetry, i.e., the scramblers V_t are repeated on each site within a time-step, but are uncorrelated between time-steps. In this case, averaging over V becomes more challenging as each site may contribute some non-trivial correlation function, the product over which must be averaged using more sophisticated tools than the second moment of the Haar ensemble. We will find that for the translationally invariant circuit ensemble, there are contributions to $\overline{\Sigma(t)}$ at $\mathcal{O}(1/q^2)$ that we will need to be re-summed (over times t). To make this easier, we can introduce a proxy $\overline{\sigma}$ in the same way we did in Eq. 3.72 for Floquet circuits,

$$\overline{\sigma}(k,z) \equiv \left(W^k \left| \overline{\mathcal{L}} Q \frac{-1}{e^{-\mathrm{i}z} - 1 - \overline{\mathcal{L}}} Q \overline{\mathcal{L}} \right| W^k \right), \quad \overline{\Sigma} = \frac{\overline{\sigma}}{1 - \frac{\overline{\sigma}}{e^{-\mathrm{i}z} - 1 - \Omega}}, \tag{5.23}$$

where $\overline{\mathcal{L}} = \overline{\mathcal{U}} - \mathbb{1}$ and $\overline{\mathcal{U}}$ is the (replicated) unitary for a single layer, averaged over random (but repeated in space) scramblers V and W[2]. This allows us to express the butterfly velocity using the full (un-projected) dynamics, as we did when deriving the Green-Kubo formulae for v_B in Eq. 3.43 and Eq. 3.73. The correction to $\overline{v_B}$ from memory contributions is given by

$$\overline{\delta v_B} \equiv \overline{v_B} - v_0 = \lim_{z \to \mathrm{i}0^+} \lim_{k \to 0} \frac{\overline{\sigma}(k,z)}{\mathrm{i}k}. \tag{5.24}$$

To convert this into a real-time sum, we find it useful to introducing the following quantity

$$\mathcal{D}(x \to y, n) = q^{y-x} \left\langle F^x \right| \overline{\mathcal{L}} Q \overline{\mathcal{U}}^{n-1} Q \overline{\mathcal{L}} \left| F^y \right\rangle. \tag{5.25}$$

[2]We are once again using the shifted time-step introduced in the previous section.

Using this definition, v_B can be written as

$$\overline{\delta v_B} = -\sum_{t=1}^{\infty}\sum_{x}\mathcal{D}(x,t), \tag{5.26}$$

where $\mathcal{D}(x,t) \equiv \mathcal{D}(0 \to x,t)$. As with the previous case, we will calculate the projected states $Q\overline{\mathcal{L}}\,|F^x\rangle = Q\overline{\mathcal{U}}_{x,x+1}\,|F^x\rangle$. Using Eq. 5.7, this can be written as follows,

$$Q\overline{\mathcal{L}}\,|F^x\rangle = Q\int dV \left(g(\varepsilon)\left[\begin{matrix} -\tilde{Z}^{\otimes 2}\,|+\rangle \\ |-\rangle \end{matrix} - \begin{matrix} |+\rangle \\ \tilde{Z}^{\otimes 2}\,|-\rangle \end{matrix} + \begin{matrix} \tilde{Z}^{\otimes 2}\,|+\rangle \\ \tilde{Z}^{\otimes 2}\,|-\rangle \end{matrix} \right] - \mathrm{i}h(\varepsilon) \begin{matrix} \tilde{A}\,|+\rangle \\ \tilde{A}\,|-\rangle \end{matrix} \right) \begin{matrix} \text{site } x \\ \text{site } x+1 \end{matrix}$$
$$\begin{matrix} \qquad\qquad 1 \qquad\qquad\quad 2 \qquad\qquad\quad 3 \qquad\qquad\quad 4 \end{matrix} \tag{5.27}$$

where we have suppressed sites $r < x$ and $r > x+1$ and where $\tilde{Z} = VZV^\dagger$, and the operators $Z^{\otimes 2}$ and A are defined by the following diagrams,

$$Z^{\otimes 2} = \begin{matrix} -\mathrm{Z}- \\ -\mathrm{Z}- \end{matrix}, \quad A = \begin{matrix} -\mathrm{Z}- \\ \\ \end{matrix} - \begin{matrix} \\ -\mathrm{Z}- \end{matrix}. \tag{5.28}$$

The Haar average in the terms labelled 1 and 2 are is evaluated using Eq. 5.17. The resulting terms are exclusively in the slow space and projected away by Q. This leaves only terms 3 and 4, allowing us to de-clutter our notation and write

$$Q\overline{\mathcal{L}}\,|F^x\rangle = g(\varepsilon)\,|3,x\rangle - \mathrm{i}h(\varepsilon)\,|4,x\rangle\,, \tag{5.29}$$

where $|3,x\rangle = Q\int dV\,\tilde{Z}_x^{\otimes 2}\tilde{Z}_{x+1}^{\otimes 2}\,|+,-\rangle_{x,x+1}$ and $|4,x\rangle = Q\int dV\,\tilde{A}_x\tilde{A}_{x+1}\,|+,-\rangle_{x,x+1}$. Focusing on $|3,x\rangle$, it is easy to see that before taking the Haar average, the $\tilde{Z}^{\otimes 2}$ decorations on the sites x and $x+1$ already put the state in $\mathcal{Q}$. Therefore, the Haar average of this state is also in $\mathcal{Q}$. We can also determine the normalisation of this state. Suppressing the

sites $r \neq x, x+1$, the state is given by

$$|3,x\rangle = \frac{1}{q^2}\int dV$$ 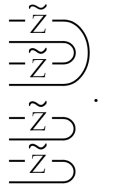

. (5.30)

The norm squared of the state is given by

$$\langle 3,x|3,x\rangle = \int\int dV dV' \langle VZV^\dagger V'ZV'^\dagger\rangle^4. \tag{5.31}$$

Using the left/right invariance of the Haar measure, this simplifies to

$$\langle 3,x|3,x\rangle = \int dV \langle VZV^\dagger Z\rangle^4 = \frac{3}{q^4} + \mathcal{O}\left(\frac{1}{q^6}\right). \tag{5.32}$$

The evaluation of this integral at leading order can be done using the diagrammatic techniques developed in Sec. 4.5 and is checked numerically. The state $|3,x\rangle$ has norm $\||3,x\rangle\| = \sqrt{3}/q^2 + \mathcal{O}(1/q^4)$.

Turning to $|4,x\rangle$, we must take the Haar average of $\tilde{A}_x\tilde{A}_{x+1}|+,-\rangle_{x,x+1}$. This is much easier than previous term as it is only quadratic in $\tilde{Z}$. With the $\tilde{Z}$'s decorating the 1 leg on both sites, we find

$$\frac{1}{q^2}\int dV$$ 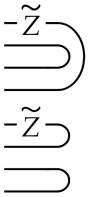

$$= \frac{1}{q^3-q}\left($$ 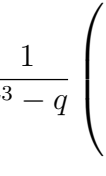
$$- \frac{1}{q}$$ 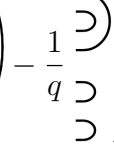
$$\right).$$ (5.33)

Showing only the sites x and $x+1$, $|4,x\rangle$ is given by

$$|4,x\rangle = \frac{1}{q-q^{-1}}\left(|\mathcal{C}_{1,1}\rangle + |\mathcal{C}_{1,2}\rangle + |\mathcal{C}_{2,1}\rangle + |\mathcal{C}_{2,2}\rangle - \frac{4}{q}|+,-\rangle\right), \tag{5.34}$$

where the wirings $|\mathcal{C}_{i,j}\rangle$ are each associated with the placement of the decoration $\tilde{Z}_i$ on

site x and $\tilde{Z}_j$ in $\tilde{A}_x\tilde{A}_{x+1}$, and are given by

$|\mathcal{C}_{1,1}\rangle =$ 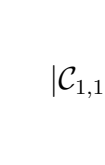 $|\mathcal{C}_{1,2}\rangle =$ 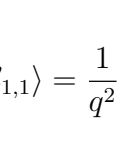 $|\mathcal{C}_{2,1}\rangle =$ 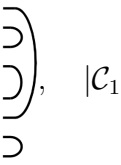 $|\mathcal{C}_{2,2}\rangle =$ 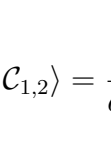 (5.35)

Defining $\mathcal{D}^{a,b}(x,t) = q^x \langle a,0|\overline{\mathcal{U}}^t|b,x\rangle$, we may now express the butterfly velocity as

$$\overline{\delta v_B} = \sum_{t=0}^{\infty}\sum_x \left(g^2\mathcal{D}^{3,3}(x,t) - \mathrm{i}hg\left(\mathcal{D}^{4,3}(x,t)+\mathcal{D}^{3,4}(x,t)\right) - h^2\mathcal{D}^{4,4}(x,t)\right). \tag{5.36}$$

5.3.1 Bookkeeping of contributions $\mathcal{D}^{a,b}(x,t)$

Now, with a little bookkeeping, we will see that only $\mathcal{D}^{4,4}(x=0,t)$ contributes at $\mathcal{O}(1/q^2)$, and that all other contributions are at most $\mathcal{O}(1/q^3)$. We start by considering $\mathcal{D}^{3,3}(x,t)$. The states $|3,x\rangle$ are normalised to $\langle 3,x|3,x\rangle = 3/q^4 + \mathcal{O}(1/q^6)$, therefore the overlap $\langle 3,0|\mathcal{U}^t|3,x\rangle$ for unitary $\mathcal{U}$ is bounded by C/q^4 for some constant $C>0$. This remains true after Haar averaging over the scramblers at every time-step,

$$\langle 3,0|\overline{\mathcal{U}}^t|3,x\rangle = \mathcal{O}\big(1/q^4\big). \tag{5.37}$$

The states $|4,x\rangle$ are normalised to $\langle 4,x|4,x\rangle = 4/q^2 + \mathcal{O}(1/q^4)$, this bounds $\langle 3,0|\mathcal{U}^t|4,x\rangle$ and $\langle 4,0|\mathcal{U}^t|3,x\rangle$ as at most $\mathcal{O}(1/q^3)$,

$$\langle 4,0|\overline{\mathcal{U}}^t|3,x\rangle = \mathcal{O}\big(1/q^3\big), \quad \langle 3,0|\overline{\mathcal{U}}^t|4,x\rangle = \mathcal{O}\big(1/q^3\big). \tag{5.38}$$

It also bounds $\langle 4,0|\mathcal{U}^t|4,x\rangle$ as at most $\mathcal{O}(1/q^2)$; the $\mathcal{O}(1/q^2)$ contributions to $\mathcal{D}(x,t)$ must be of the form $\langle 4,0|\mathcal{U}^t|4,x\rangle$. In fact, only the $x=0$ contributes at $\mathcal{O}(1/q^2)$. To see this, first notice that $q^x\langle F^0|F^x\rangle = 1$ for all $x\geq 0$, and that this is because the number of closed loops and the number of factors $1/q$ are equal. The replicated unitary $\mathcal{U}^t$ can decorate these loops with scrambling unitaries and the factors of Z from the coupling

gates, however the loop counting remains the same, $q^x \langle F^0 | \mathcal{U}^t | F^x \rangle \sim \mathcal{O}(1)$[3]. The same loop counting can be done for $q^x \langle 4, 0 | \mathcal{U}^t | 4, x \rangle$. If we assign a value q for each closed loop, we find that the largest contribution from $q^x \langle 4, 0 | \mathcal{U}^t | 4, x \rangle$ is q^{-4} for $x \neq 0$. Whereas, for $x = 0$, it is possible to find contributions at $\mathcal{O}(1/q^2)$. For example $\frac{1}{q^2} \langle \mathcal{C}_{i,j} | \mathcal{U}^t | \mathcal{C}_{i,j} \rangle$ is a tensor diagram with two loops and a factor of $1/q^2$ associated with every site (and an additional factor of $1/q^2$ overall). These are in fact the only $\mathcal{O}(1/q^2)$ contributions.

In order to evaluate these contributions to $\mathcal{D}^{4,4}(x = 0, t)$, we make some further observations. Taking one of the wiring configurations in $|4, x = 0\rangle$, for example $|+\rangle_{r<0} |\mathcal{C}_{1,1}\rangle_{0,1} |-\rangle_{r>1}$, and apply the next time-step. This state is now decomposed using the decoration decomposition of the coupling gate Eq. 5.6, so that the wiring on sites $-1 \leq r \leq 2$ may carry factors of $\tilde{Z}^4$. An example of such a decorated state is given below, where we show only sites $-1 \leq r \leq 2$ as these are the only states can become decorated.

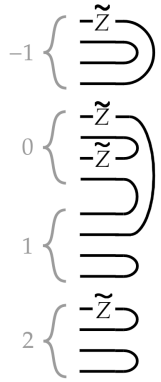

In this example only four of the possible eight wires are carrying a $\tilde{Z}$. We want to take the Haar average of all possible decorated states. However, this is a tedious task. Instead, we will use a trick to quantify the magnitude of the Haar averaged (decorated) states. Denote a decorated state as $\mathrm{dec} |w\rangle$, where dec refers to a particular configuration of the $\tilde{Z}$ decorations and $|w\rangle$ refers to a particular wiring configuration, such as the example given above. Denote the Haar average of this decorated state as $\overline{\mathrm{dec}} |w\rangle$. The norm squared of

[3]For $x < 0$, $q^x \langle F^0 | \mathcal{U} | F^x \rangle \sim \mathcal{O}(q^{-2x})$

[4]We have used the fact that the + and − wiring domains absorb the two-site unitary gates, leaving only the sites $-1 \leq r \leq 2$ to be decorated.

this state is given by $\langle w|\,\overline{\text{dec}}\;\overline{\text{dec}}\,|w\rangle$. Pulling the Haar average outside, this is given by,

$$\langle w|\,\overline{\text{dec}}\;\overline{\text{dec}}\,|w\rangle = \int\int dV dV' \langle VZV^\dagger V'ZV'^\dagger\rangle^n, \tag{5.39}$$

where n is the number of $\tilde{Z}$ decorations present in dec. In the example we gave $n = 4$. We now use the left/right invariance of the Haar measure to reduce to a single Haar integral,

$$\langle w|\,\overline{\text{dec}}\;\overline{\text{dec}}\,|w\rangle = \int dV \langle VZV^\dagger Z\rangle^n. \tag{5.40}$$

Here we can turn to theorem 1 to bound this as $\mathcal{O}\big(1/q^{2\lceil n/2\rceil}\big)$. This means that the state $\overline{\text{dec}}\,|w\rangle$ is normalised to $||\overline{\text{dec}}\,|w\rangle\,|| \sim \mathcal{O}\big(1/q^{\lceil n/2\rceil}\big)$. For any $n > 0$, this introduces at least one more factor of $1/q$, rendering the overall contribution to $\mathcal{D}^{4,4}(x = 0, t)$ to be $\mathcal{O}(1/q^3)$ or smaller. This means that for a term in $\langle 4, 0|\,\overline{\mathcal{U}}^t\,|4, 0\rangle$ to contribute at $\mathcal{O}(1/q^2)$, all wirings on (or between) every site in $|4, 0\rangle$ (and $\langle 4, 0|$) always remain undecorated. We select precisely these contributions by inserting the projector $|-\rangle\langle -|$ between every time-step in the $-$ domain and the projector $|+\rangle\langle +|$ between every time-step in the $+$ domain. We must also keep the wires of sites 0 and 1 undecorated. Therefore, for a given wiring configuration $|\mathcal{C}_{i,j}\rangle$, we must insert the projector $|\mathcal{C}_{i,j}\rangle\langle\mathcal{C}_{i,j}|$ between every time-step, this also has the consequence of fixing the input wiring as $\langle\mathcal{C}_{i,j}|$. Making these changes keeps the leading order contributions in $\mathcal{D}^{4,4}(x = 0, t)$,

$$\mathcal{D}^{4,4}(x=0,t) = \frac{1}{q^2}\sum_{i,j\in\{1,2\}}$$

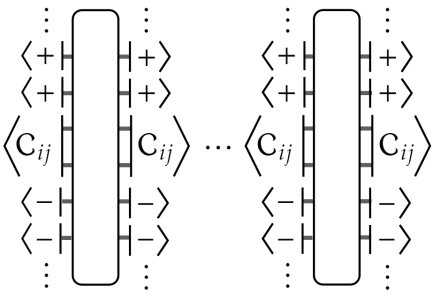

$$+\,\mathcal{O}\big(1/q^3\big). \tag{5.41}$$

Where the tall boxes refer to the replicated unitary layers, of which there are t. Using the property Eq. 5.9 for two-local bricks contracted with the states $\langle\pm,\pm|$ or $|\pm,\pm\rangle$, this

diagram simplifies to the following,

$$\mathcal{D}^{4,4}(x=0,t) = \frac{1}{q^2}\sum_{i,j\in\{1,2\}} \langle +|\mathrm{C}_{ij}|+\rangle \cdots \langle +|\mathrm{C}_{ij}|+\rangle + \mathcal{O}(1/q^3),$$
$$= \frac{1}{q^2}\sum_{i,j} \langle \mathcal{C}_{i,j}|\,\mathcal{T}\,|\mathcal{C}_{i,j}\rangle^t + \mathcal{O}(1/q^3), \tag{5.42}$$

where the two-site bricks are the replicated coupling unitary $\mathcal{U}_{x,x+1}$ and $\mathcal{T}$ is given by

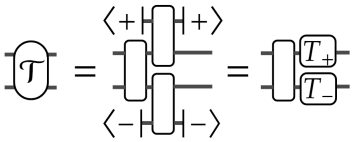

(5.43)

and where the tensor contractions T_+ and T_- are given algebraically by

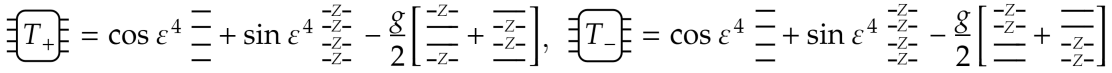

(5.44)

Due to the replica symmetry of the unitary evolution operator, $(1,\overline{1}) \leftrightarrow (2,\overline{2})$, the contributions from the $(i,j) = (1,1)$ and $(2,2)$ wirings are identical, as are $(1,2)$ and $(2,1)$ wirings. The unitary $\mathcal{U}_Z$ also has the property $\mathrm{Sw}(1,\overline{1})\mathrm{Sw}(2,\overline{2})\mathcal{U}_Z\mathrm{Sw}(1,\overline{1})\mathrm{Sw}(2,\overline{2}) = \mathcal{U}_Z^*$, where $\mathrm{Sw}(i,\bar{i})$ swaps unbarred leg i and barred leg $\bar{i}$. This transformation is a symmetry of the $\langle +|$ and $\langle -|$ wirings while exchanging the $\mathcal{C}_{1,1}$ ($\mathcal{C}_{2,2}$) and $\mathcal{C}_{2,1}$ ($\mathcal{C}_{1,2}$) wirings. Therefore,

$$\xi(\varepsilon) \equiv \langle \mathcal{C}_{1,1}|\,\mathcal{T}\,|\mathcal{C}_{1,1}\rangle = \langle \mathcal{C}_{2,2}|\,\mathcal{T}\,|\mathcal{C}_{2,2}\rangle = \langle \mathcal{C}_{1,2}|\,\mathcal{T}\,|\mathcal{C}_{1,2}\rangle^* = \langle \mathcal{C}_{2,1}|\,\mathcal{T}\,|\mathcal{C}_{2,1}\rangle^*. \tag{5.45}$$

Using the decoration decomposition of a brick in Eq. 5.6 and the expressions for T_+ and T_- in Eq. 5.44, $\xi(\varepsilon)$ is found to be

$$\xi(\varepsilon) = (1+g(\varepsilon))^2 - 2\mathrm{i}h(\varepsilon)g(\varepsilon). \tag{5.46}$$

Altogether, the butterfly velocity is given at $\mathcal{O}(1/q^2)$ by

$$\overline{v_B}(\varepsilon) = v_0(\varepsilon) + \frac{4h(\varepsilon)^2}{q^2}\sum_{t=0}^{\infty}\mathrm{Re}\{\xi(\varepsilon)^t\} + \mathcal{O}\big(1/q^3\big). \tag{5.47}$$

The memory corrections decay with time-scale $\tau(\varepsilon) = \log(|\xi(\varepsilon)|)$. Summing over these corrections, we find

$$\overline{v_B}(\varepsilon) = v_0(\varepsilon) + \delta v_S(\varepsilon), \quad \delta v_S(\varepsilon) \equiv \frac{4h(\varepsilon)^2}{q^2 g(\varepsilon)}\frac{(2-g(\varepsilon)))}{(2-g(\varepsilon))^2+4h(\varepsilon)^2}. \tag{5.48}$$

In terms of the reparameterisation $s(\varepsilon) = \cos(\varepsilon)^2\sin(\varepsilon)^2$, this is given more compactly by

$$\delta v_S = \frac{1}{q^2}\frac{1+5s-4s^2}{1-s-3s^2}. \tag{5.49}$$

We have used the subscript S in δv_S to identify this correction as related to spatial translation symmetry.

5.3.2 The $\varepsilon \to 0$ limit

The $\varepsilon \to 0$ limit represents an obvious sanity check on our results, but also represents a challenging limit in a memory matrix calculation – as the coupling strength vanishes, the memory time must diverge. The difficulties at small coupling is clear in the failure of $\overline{v_B}(\varepsilon)$ to vanish at $\varepsilon = 0$ ($\delta v_S(\varepsilon = 0) = -\frac{1}{q^2}$) where sites decouple and the butterfly velocity is zero. What has gone wrong here is that our $1/q$ perturbation scheme breaks down for coupling $\varepsilon \sim 1/q$. This is because, although contributions for a given time may be sub-leading in $1/q$, the decay is so slow that the time integrals can compensate with additional factors of q. We demonstrate this explicitly by re-summing a more complete set of diagrams, finding that the resulting correction to $\overline{v_B}$ vanishes as it should with $\varepsilon \to 0$.

In the previous section we discarded all contributions to $\mathcal{D}^{4,4}(x = 0, t)$ that were smaller than $\mathcal{O}(1/q^2)$. In this section, we will repeat these steps up to Eq. 5.41, with the

modification that instead of inserting a projectors $|\mathcal{C}_{i,j}\rangle\langle\mathcal{C}_{i,j}|$ between every time-step, we will insert the projector onto the bigger space $\mathrm{Span}\{|\mathcal{C}_{i,j}\rangle, |+,-\rangle\}$ [5]. This computation counts the same contributions as we did previously, but also counts some new contributions due to the fact that we are projecting out fewer states. Because the states $|\mathcal{C}_{i,j}\rangle$ and $|+,-\rangle$ overlap, the projector we use is a little unwieldy,

$$K_{i,j} = \frac{1}{1-q^{-2}}\left(|\mathcal{C}_{i,j}\rangle - \frac{1}{q}|+,-\rangle\right)\left(\langle\mathcal{C}_{i,j}| - \frac{1}{q}\langle+,-|\right) + |+,-\rangle\langle+,-|\,. \tag{5.50}$$

Diagrammatically, we are computing the following contribution, which we will dub $A_{i,j}(t)$,

$$A_{i,j}(t) = \frac{1}{q^2}$$ 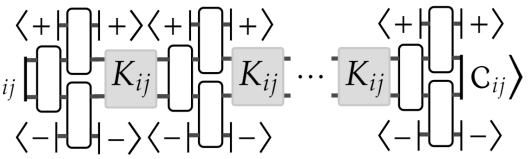

(5.51)

While we certainly are missing diagrams that become important as $\varepsilon \to 0$, we will show that the addition of some subleading-in-$1/q$ terms leads to a far more reasonable correction to $\overline{v_B}$ at small ε. The contribution can be written algebraically, using the definition of the tensor $\mathcal{T}$ in Eq. 5.43,

$$A_{i,j}(t) = \frac{1}{q^2}\langle\mathcal{C}_{i,j}|\left(\mathcal{T}K_{i,j}\right)^t|\mathcal{C}_{i,j}\rangle\,. \tag{5.52}$$

This can be simplified considerably by viewing the projector as a tensor diagram, where several of the wirings factorise. We do this for $K_{1,1}$ below,

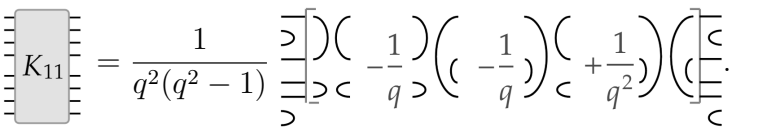

(5.53)

We notice that the term in the squared bracket is in fact just the familiar projector K

[5] We still require that sites $r > 1$ and $r < 0$ remain undecorated by inserting the projectors $|\pm\rangle\langle\pm|$

(Eq. 5.18), up to a numerical factor. This means that $K_{i,j}$ can be rewritten as

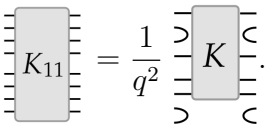

(5.54)

Due to the wiring factorisation, it is convenient to define the quantity Y as the following tensor contraction of $\mathcal{T}$,

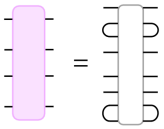

(5.55)

$A_{1,1}(t)$ can now be expressed as the following product,

$$A_{1,1}(t) = \frac{1}{q^2} \langle + | \, (KYK)^t \, | + \rangle \, . \tag{5.56}$$

The matrix KYK is a 2×2 matrix acting on the space of wirings $\mathrm{Span}\{|+\rangle, |-\rangle\}$. Choosing the orthogonal basis $|S, A\rangle = \frac{1}{\sqrt{2}}(|+\rangle \pm |-\rangle)$ (and normalising $|S, A\rangle$). KYK is given by

$$\begin{aligned} KYK = \frac{\xi}{2} & \begin{pmatrix} (1+1/q)^{-1} & (1-1/q^2)^{-1} \\ (1-1/q^2)^{-1} & (1-1/q)^{-1} \end{pmatrix} \\ & + \frac{1+g}{2} \begin{pmatrix} (1+1/q)^{-1} & -(1-1/q^2)^{-1} \\ -(1-1/q^2)^{-1} & (1-1/q)^{-1} \end{pmatrix} \\ & + \frac{1+g+ih}{q} \begin{pmatrix} (1+1/q)^{-1} & 0 \\ 0 & -(1-1/q)^{-1} \end{pmatrix} . \end{aligned} \tag{5.57}$$

By diagonalising this, we find

$$\sum_{t=0} A_{1,1}(t) = \frac{2}{1 + 8q^2\varepsilon^2 + \mathcal{O}(q^2\varepsilon^3, q\varepsilon^2)} . \tag{5.58}$$

This can be generalised to the other components $A_{i,j}(t)$ in the same way we did in the

previous section for $\langle \mathcal{C}_{i,j}| \mathcal{T} |\mathcal{C}_{i,j}\rangle$, i.e., by using the swap symmetrySw$(i, \bar{j})$. This yields,

$$\sum_{t=0}^{\infty} \sum_{i,j=1,2} A_{i,j}(t) = \frac{8}{1 + 8q^2\varepsilon^2 + \mathcal{O}(q^2\varepsilon^3, q\varepsilon^2)}. \tag{5.59}$$

Therefore, the overall contribution at small ε to $\overline{v_B}$ from these diagrams is,

$$\overline{\delta v_B} = \frac{8h(\varepsilon)^2}{1 + 8q^2\varepsilon^2 + \mathcal{O}(q^2\varepsilon^3, q\varepsilon^2)} + \text{other diagrams}. \tag{5.60}$$

This contribution, which keeps account of higher orders in $1/q$, vanishes as $\varepsilon \to 0$, unlike the $\mathcal{O}(1/q^2)$ contribution naively calculated in the previous section which incorrectly predicts $\lim_{\varepsilon\to 0} \overline{\delta v_B} = -1/q^2$. This is still far from a complete counting of contributions to $\overline{v_B}$, but it does demonstrate that the apparent pathological behaviour as $\varepsilon \to 0$ is the result of a naive, and incorrect at small ε, counting of the $\mathcal{O}(1/q^2)$ contributions. Fortunately, the $1/q$ perturbation scheme is robust for large q and coupling $\varepsilon \gg 1/q$.

5.4 Spatial and time translation symmetry

In this section, we will investigate the variant of the circuit with both spatial translation and Floquet time translation symmetry, following very closely our analysis in [114]. This case is much more challenging to study due to the inability to independently average over the scramblers at each time-step. Instead, we must rely heavily on the theorems of Chapter 4. Furthermore, there is no benefit to using the shifted time-step introduced in Sec. 5.2, instead we will use the time-step as introduced in Eq. 5.1. As in the previous variation of the circuit (with spatial translation symmetry but no Floquet time translation symmetry), we will use a proxy σ for the memory matrix Σ. Because of the spatial and Floquet translational symmetry, σ is as defined in Eq. 3.72. The correction to the butterfly velocity is given by

$$\delta v_B = \lim_{z\to \mathrm{i}0^+} \frac{\sigma(k, z)}{\mathrm{i}k}. \tag{5.61}$$

We now repeat the steps of the previous section, although now without circuit averaging each time-step. Recycling symbols, we define the quantity $\mathcal{D}$ as

$$\mathcal{D}(x,T) = q^x \left\langle F^0 \right| \mathcal{L}\mathcal{Q}\mathcal{U}^{T-1}\mathcal{Q}\mathcal{L} \left| F^x \right\rangle . \tag{5.62}$$

Using this and translational invariance, the circuit averaged butterfly velocity can now written as,

$$\overline{\delta v_B} = -\sum_{t=1}^{\infty}\sum_{x} \overline{\mathcal{D}(x,t)}. \tag{5.63}$$

The remainder of this section is dedicated to a careful bookkeeping of the leading order contributions to $\overline{\mathcal{D}}$. In the following we choose to separate the scrambling part of each Floquet layer from the two-local bricks, $\mathcal{U} = \mathcal{V}\mathcal{U}_Z$. Then a product $\mathcal{U}^n$ can be written $\mathcal{U}^n = \mathcal{U}_Z(1)\mathcal{U}_Z(2)\cdots\mathcal{U}_Z(n)\mathcal{V}^n$ where $\mathcal{U}_Z(t) = \mathcal{V}^t\mathcal{U}_Z\mathcal{V}^{-t}$. One consequence is that

$$\left\langle F^0 \right| \mathcal{L} = \left\langle F^0 \right| \mathcal{V}\mathcal{U}_Z - \left\langle F^0 \right| = \left\langle F^0 \right| \mathcal{L}_Z \tag{5.64}$$

where $\mathcal{L}_Z = \mathcal{U}_Z - \mathbb{1}$. We can similarly show $\mathcal{L}\left|F^x\right\rangle = \mathcal{V}\mathcal{L}_Z\left|F^x\right\rangle$. Using this and $[\mathcal{V},\mathcal{Q}] = 0$ and simplifying the notation $\mathcal{L}_Z \to L$ and $\mathcal{U}_Z \to U$, $\mathcal{D}(x,T)$ can be written as

$$\mathcal{D}(x,T) = q^x \left\langle F^0 \right| L\mathcal{Q}U(1)\cdots U(T-1)\mathcal{Q}L(T) \left| F^x \right\rangle , \tag{5.65}$$

Using the inversion symmetry of the Floquet unitary, we find

$$\mathcal{D}(-x,T) = q^{-2x}\mathcal{D}(x,T), \quad \text{for } x > 0. \tag{5.66}$$

We conclude that the contributions from $x < 0$ are at least a factor $1/q^2$ smaller than the $x > 0$ contributions. In the remainder of this section we will see that $\overline{\mathcal{D}(x \geq 0, T)}$ is no larger than $\mathcal{O}(1/q^2)$, and that therefore $\overline{\mathcal{D}(x < 0, T)} = \mathcal{O}(q^{-4})$. We will therefore only consider $x \geq 0$ in the following sections.

5.4.1 Decoration decomposition

Using the decoration expansion (Eq. 5.6) for each brick in each Floquet layer, we express $\mathcal{D}(x,T)$ as a sum over decorations Γ,

$$\mathcal{D}(x,T) = \sum_{\Gamma} C_\Gamma \mathcal{D}_\Gamma(x,T), \quad \mathcal{D}_\Gamma(x,T) = q^x \left\langle F^0 \right| L\mathcal{Q}\Gamma\mathcal{Q}L(T) \left| F^x \right\rangle, \tag{5.67}$$

where $\Gamma = \bigotimes_r \Gamma^r$ is a product of decorations on every site. The decoration on a site r is given by $\Gamma^r = \Gamma^r_1 \otimes \Gamma^{r*}_{\overline{1}} \otimes \Gamma^r_2 \otimes \Gamma^{r*}_{\overline{2}}$ (i.e., a product of decorations on each leg of the site) and where $\Gamma^r_i = Z(1)^{s^{r,i}_1} Z(2)^{s^{r,i}_2} \cdots Z(T-1)^{s^{r,i}_{T-1}}$ for a binary string $\boldsymbol{s}^{r,i} = (s^{r,i}_1, \cdots, s^{r,i}_{T-1})$.

$$\Gamma^r = \begin{array}{c} 1 \\ \overline{1} \\ 2 \\ \overline{2} \end{array} \begin{array}{c} \\ \\ \\ \\ \end{array} \begin{bmatrix} -Z(1)^{a^r_1}\ Z(2)^{a^r_2} & \cdots & Z(T-1)^{a^r_{T-1}} - \\ -Z(1)^{\overline{a}^{r\,*}_1} Z(2)^{\overline{a}^{r\,*}_2} & & Z(T-1)^{\overline{a}^{r\,*}_{T-1}} - \\ -Z(1)^{b^r_1}\ Z(2)^{b^r_2} & & Z(T-1)^{b^r_{T-1}} - \\ -Z(1)^{\overline{b}^{r\,*}_1} Z(2)^{\overline{b}^{r\,*}_2} & & Z(T-1)^{\overline{b}^{r\,*}_{T-1}} - \end{bmatrix}. \tag{5.68}$$

We will use the decoration expansion, and a carefully chosen decomposition of the initial states to express contributions as products of correlators. We will use the theorems 1 - 3 to see what kinds of decorations can give rise to $O(1/q^2)$ corrections to the circuit averaged σ, and then evaluate those. It turns out that only certain values of x ($x = 0, 1, 2$) are relevant at this order.

5.4.2 Projecting initial states onto $\mathcal{Q}$

As we did in the previous case, we project the input state $L(T)\left|F^x\right\rangle$ and output state $\left\langle F^0\right| L$ onto the fast space, finding

$$\mathcal{Q}L(T)\left|F^x\right\rangle = g \begin{bmatrix} - & |\phi_+(T)\rangle & - & |+\rangle & + & Z(T)^{\otimes 2}|+\rangle \\ & |-\rangle & & |\phi_-(T)\rangle & & Z(T)^{\otimes 2}|-\rangle \\ & 1 & & 2 & & 3 \end{bmatrix} -ih \begin{matrix} K(T)|+\rangle & \text{site } x \\ K(T)|-\rangle & \text{site } x+1 \\ 4 & \end{matrix} \tag{5.69}$$

where we have suppressed sites $r < x$ ($r > x+1$) and carefully chosen an orthogonal

decomposition of $QL(T)\,|F^x\rangle$ in terms of four fast states, numbered from 1 to 4. The operators $Z^{\otimes 2}$ and K are as defined in Eq. 5.28 and $Z(T)^{\otimes 2}$ and $K(T)$ are defined identically but with $Z(T)$ in place of Z. Finally, $|\phi_+(T)\rangle$ and $|\phi_-(T)\rangle$ are given by

$$|\phi_+(T)\rangle = Z(T)^{\otimes 2}\,|+\rangle - \frac{1}{q-q^{-1}}\,|\perp\rangle\,, \quad |\phi_-(T)\rangle = Z(T)^{\otimes 2}\,|-\rangle - \frac{1}{q-q^{-1}}\,|0\rangle\,. \tag{5.70}$$

The input state is easily found using $\langle F^0|\,L\mathcal{Q} = (\mathcal{Q}L\,|F^0\rangle)^T$. The four states numbered in Eq. 5.69 obey a useful set of identities, which allow us to identify and discard many lower order diagrams and significantly simplify the memory matrix calculation.

Identities of the $\phi_\pm$ states

It will be useful to determine some properties of $|\phi_+\rangle$ and $|\phi_-\rangle$. The isometry $S = (1 \leftrightarrow 2)$ (swaps legs 1 and 2) relates the two states, $S\,|\phi_-\rangle = |\phi_+\rangle$. We can then investigate $|\phi_-\rangle$ only. Firstly, $|\phi_-\rangle$ has no overlap with either $|+\rangle$ or $|-\rangle$.

$$\langle -|\phi_-\rangle = \langle -|\,Z^{\otimes 2}\,|-\rangle - \frac{1}{q-q^{-1}}\,\langle -|0\rangle = \langle -|\,Z^{\otimes 2}\,|-\rangle =$$

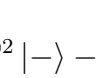

$$= 0$$

$$\langle +|\phi_-\rangle = \langle +|\,Z^{\otimes 2}\,|-\rangle - \frac{1}{q-q^{-1}}\,\langle +|0\rangle =$$

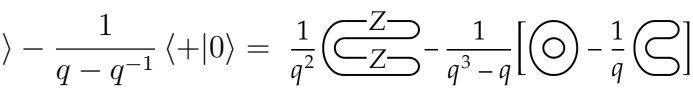

$$= \frac{1}{q} - \frac{1}{q-q^{-1}}(1-q^{-2}) = 0.$$

Using S, we can then write

$$\langle \phi_+|\pm\rangle = \langle \phi_-|\pm\rangle = \langle \pm|\phi_+(T)\rangle = \langle \pm|\phi_-(T)\rangle = 0. \tag{5.71}$$

We next consider what happens when the wires of $\langle \pm|$ are decorated. Let Γ^r be a decoration on the four legs of site r as shown in Eq. 5.68. The overlaps between $|\phi_-(T)\rangle$ and

a decorated $\langle +|$ state is then given by

$$\langle +|\,\Gamma^r\,|\phi_-(T)\rangle = \frac{1}{q^2}\Big(\Gamma_1 Z(T),\ \Gamma_{\overline{1}}^*,\ \Gamma_2 Z(T),\ \Gamma_{\overline{2}}^*\Big) - \frac{1}{q^3-q}\left[\Big(\Gamma_1,\Gamma_{\overline{1}}^*,\Gamma_2,\Gamma_{\overline{2}}^*\Big) - \frac{1}{q}\Big(\Gamma_1,\Gamma_{\overline{1}}^*,\Gamma_2,\Gamma_{\overline{2}}^*\Big)\right]$$
$$= \frac{1}{q}\langle Z(T)\Gamma_{\overline{2}}^{r\dagger}\Gamma_1^r Z(T)\Gamma_{\overline{1}}^{r\dagger}\Gamma_2^r\rangle - \frac{1}{q-q^{-1}}\left(\langle\Gamma_{\overline{2}}^{r\dagger}\Gamma_1^r\rangle\langle\Gamma_{\overline{1}}^{r\dagger}\Gamma_2^r\rangle - \frac{1}{q^2}\langle\Gamma_{\overline{2}}^{r\dagger}\Gamma_1^r\Gamma_{\overline{1}}^{r\dagger}\Gamma_2^r\rangle\right). \tag{5.72}$$

Similar identities hold for the overlaps $\langle +|\phi_-(T)\rangle$ and $\langle\phi_-|\pm\rangle$. These identities can be summarised as follows

$$\begin{aligned}
\langle -|\,\Gamma^r\,|\phi_-(T)\rangle &= \langle Z(T)\Gamma_{\overline{1}}^{r\dagger}\Gamma_1^r\rangle\langle Z(T)\Gamma_{\overline{2}}^{r\dagger}\Gamma_2^r\rangle - \frac{1}{q^2-1}\left(\langle\Gamma_{\overline{1}}^{r\dagger}\Gamma_1^r\Gamma_{\overline{2}}^{r\dagger}\Gamma_2^r\rangle - \langle\Gamma_{\overline{1}}^{r\dagger}\Gamma_1^r\rangle\langle\Gamma_{\overline{2}}^{r\dagger}\Gamma_2^r\rangle\right),\\
\langle\phi_-|\,\Gamma^r\,|+\rangle &= \frac{1}{q}\langle Z\Gamma_1^r\Gamma_{\overline{2}}^{r\dagger}Z(T)\Gamma_2^r\Gamma_{\overline{1}}^{r\dagger}\rangle - \frac{1}{q-q^{-1}}\left(\langle\Gamma_1^r\Gamma_{\overline{2}}^{r\dagger}\rangle\langle\Gamma_2^r\Gamma_{\overline{1}}^{r\dagger}\rangle - \frac{1}{q^2}\langle\Gamma_1^r\Gamma_{\overline{2}}^{r\dagger}\Gamma_2^r\Gamma_{\overline{1}}^{r\dagger}\rangle\right),\\
\langle\phi_-|\,\Gamma^r\,|-\rangle &= \langle Z(T)\Gamma_1^r\Gamma_{\overline{1}}^{r\dagger}\rangle\langle Z(T)\Gamma_2^r\Gamma_{\overline{2}}^{r\dagger}\rangle - \frac{1}{q^2-1}\left(\langle\Gamma_1^r\Gamma_{\overline{1}}^{r\dagger}\Gamma_2^r\Gamma_{\overline{2}}^{r\dagger}\rangle - \langle\Gamma_1^r\Gamma_{\overline{1}}^{r\dagger}\rangle\langle\Gamma_2^r\Gamma_{\overline{2}}^{r\dagger}\rangle\right).
\end{aligned} \tag{5.73}$$

In general, Γ^r will insert operators on each of the four legs of the input (or output) state. However, sometimes one can utilise the wirings between each of the legs to simplify the resulting expression, an example for $\langle +|\,\Gamma^r$ is shown below,

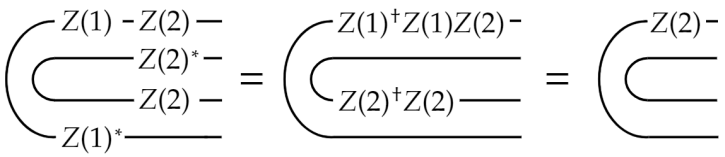

(5.74)

We say Γ^r (non-trivially) decorates the state if this simplification process cannot be used to remove all four components of Γ^r. In the example above we were able to remove all of the non-identity operators from the $(2,\overline{1})$ wiring but not from the $(1,\overline{2})$ wiring. Notice that in every case in Eq. 5.73 and in Eq. 5.72, if either of the wirings in the $+/-$ states are undecorated, the overlap with the $\phi_\pm$ states vanishes[6].

[6]This is easily verified by substituting either $\Gamma_{\overline{2}}^{r\dagger}\Gamma_1^r = \mathbb{1}$ or $\Gamma_{\overline{1}}^{r\dagger}\Gamma_2^r = \mathbb{1}$ into Eq. 5.72

Assuming that the decorations non-trivially decorate both wirings of the $+/-$ states, these overlaps can be summarised as follows

$$\begin{aligned} q\,\langle \pm|\,\Gamma^r\,|\phi_{\mp}(T)\rangle &= \text{OTOC} - \text{Corr} \times \text{Corr}' + \mathcal{O}\big(1/q^2\big) \\ q\,\langle \phi_{\pm}|\,\Gamma^r\,|\mp\rangle &= \text{OTOC} - \text{Corr} \times \text{Corr}' + \mathcal{O}\big(1/q^2\big) \\ \langle \pm|\,\Gamma^r\,|\phi_{\pm}(T)\rangle &= \text{Corr} \times \text{Corr}' + \mathcal{O}\big(1/q^2\big) \\ \langle \phi_{\pm}|\,\Gamma^r\,|\pm\rangle &= \text{Corr} \times \text{Corr}' + \mathcal{O}\big(1/q^2\big). \end{aligned} \tag{5.75}$$

Where rather than give the full expressions, we have simply presented the types of contributions (i.e., OTOCs, products of non-trivial correlators or terms that are manifestly $\mathcal{O}(1/q^2)$). This is often enough to identify diagrams that contribute to $\mathcal{D}(x,T)$ at $\mathcal{O}(1/q^3)$ or smaller. In cases that require a more careful analysis we refer to Eq. 5.72 and Eq. 5.73.

These are useful identities because the diagrams contributing to the memory kernel tend to involve products of terms of this form. We will now see how, using these identities and the theorems of Sec. 4.2, we can pinpoint which diagrams are able to contribute at leading order in our perturbative expansion, i.e. at $\mathcal{O}(1/q^2)$.

5.4.3 $\overline{\mathcal{D}^{a,b}(x,T)}$

Casting our attention back to the orthogonal decomposition of the projected vector $\mathcal{Q}L(T)\,|F^x\rangle$ in Eq. 5.69, where we labelled each of four orthogonal states from 1 to 4, we now use a short hand $\{|1,x,T\rangle\,,\cdots,|4,x,T\rangle\}$ to denote each of these states. This is also done for $\langle F^0|\,L\mathcal{Q}$. Using this, we define the following quantity,

$$\mathcal{D}^{a,b}(x,T) \equiv q^x\,\langle a,0,0|\,U(1)U(2)\cdots U(T-1)\,|b,x,T\rangle\,, \tag{5.76}$$

and also the decoration expansion quantity,

$$\mathcal{D}^{a,b}_{\Gamma}(x,T) = q^x\,\langle a,0,0|\,\Gamma\,|b,x,T\rangle\,. \tag{5.77}$$

The decoration Γ is a product of $T-1$ layers, $\Gamma = \Gamma(1)\Gamma(2)\cdots\Gamma(T-1)$, one for each unitary layer $U(t)$ of Eq. 5.76.

In what follows, we examine the circuit average of $\mathcal{D}^{a,b}$ for all possible pairs a, b; some calculations are carried out in C and D. All contributions are $\mathcal{O}(1/q^3)$ or smaller, except for the $(2,1)$ and $(4,4)$ terms as summarised in Sec. 5.4.6.

5.4.4 $(a,b) = (1,1), (2,2)$ are $\mathcal{O}(1/q^3)$

The arguments used for $(a,b) = (1,1)$ are the same as used for $(2,2)$, for brevity we will only present them for $(1,1)$. We study $x > 0$ and $x = 0$ separately, writing $\mathcal{D}^{1,1}_\Gamma(x,T)$ as diagram in both cases.

Misaligned: $x > 0$

$$\mathcal{D}^{1,1}_\Gamma(x>0,T) = g^2 \times$$

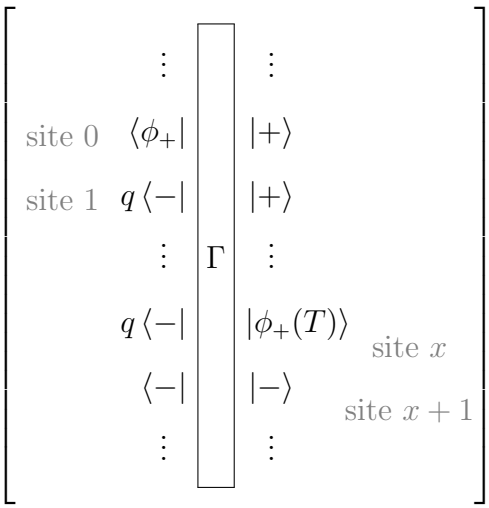

Using the overlap identities Eq. 5.71, Eq. 5.72 and Eq. 5.73, we see that the contribution from site 0 and x either vanish or have the form

$$\left(\mathrm{Corr}_0 \times \mathrm{Corr}'_0 + \mathcal{O}\big(1/q^2\big)\right)\left(\mathrm{OTOC}_x + \mathrm{Corr}_x \times \mathrm{Corr}'_x + \mathcal{O}\big(1/q^2\big)\right).$$

Every other site may contribute either trivial or non-trivial correlators to the product. Therefore, after circuit averaging, theorem 1 of Sec. 4.2 gives

$$\overline{\mathcal{D}^{1,1}_\Gamma(x>0,T)} = \mathcal{O}\big(1/q^3\big). \tag{5.78}$$

Aligned: $x = 0$

$$\mathcal{D}^{1,1}_{\Gamma}(0,T) = g^2 \times \left[\begin{array}{ccc|c|c} & & \vdots & & \vdots \\ & & \langle +| & & |+\rangle \\ & \text{site } 0 & \langle \phi_+| & \Gamma & |\phi_+(T)\rangle \\ & & \langle -| & & |-\rangle \\ & & \vdots & & \vdots \end{array}\right]$$

On site $x = 0$, we have

$$\begin{aligned}\langle \phi_+| \Gamma^0 |\phi_+(T)\rangle = &\langle Z\Gamma^0_1 Z(T)\Gamma^{0\dagger}_{\overline{2}}\rangle\langle Z\Gamma^0_2 Z(T)\Gamma^{0\dagger}_{\overline{1}}\rangle - \frac{1}{q^2-1}\langle \Gamma^{0\dagger}_{\overline{1}}\Gamma^0_1 Z(T)\Gamma^{0\dagger}_{\overline{2}}\Gamma^0_2 Z(T)\rangle \\ &- \frac{1}{q^2-1}\langle Z\Gamma^0_1\Gamma^{0\dagger}_{\overline{1}} Z\Gamma^0_2\Gamma^{0\dagger}_{\overline{2}}\rangle + \frac{1}{q^2(1-q^{-2})^2}\langle \Gamma^0_1\Gamma^{0\dagger}_{\overline{1}}\rangle\langle \Gamma^0_2\Gamma^{0\dagger}_{\overline{2}}\rangle \\ &+ \frac{1}{q^2-1}\langle Z\Gamma^0_1\Gamma^{0\dagger}_{\overline{2}}\rangle\langle Z\Gamma^0_2\Gamma^{0\dagger}_{\overline{1}}\rangle + \frac{1}{q^2-1}\langle \Gamma^{0\dagger}_{\overline{2}}\Gamma^0_1 Z(T)\rangle\langle \Gamma^{0\dagger}_{\overline{1}}\Gamma^0_2 Z(T)\rangle \\ &- \frac{1}{(q^2-1)^2}\langle \Gamma^0_1\Gamma^{0\dagger}_{\overline{1}}\Gamma^0_2\Gamma^{0\dagger}_{\overline{2}}\rangle - \frac{1}{(q^2-1)^2}\langle \Gamma^0_1\Gamma^{0\dagger}_{\overline{2}}\Gamma^0_2\Gamma^{0\dagger}_{\overline{1}}\rangle \\ &+ \frac{1}{(q^2-1)^2}\langle \Gamma^0_1\Gamma^{0\dagger}_{\overline{2}}\rangle\langle \Gamma^0_2\Gamma^{0\dagger}_{\overline{1}}\rangle. \end{aligned} \tag{5.79}$$

The final three terms are manifestly $\mathcal{O}(1/q^4)$. The fifth and sixth terms are of the form Corr $\times$ Corr$'/q^2$, where these correlators are non-trivial. Therefore, using theorem 1, the Haar average of these terms (possibly multiplied by additional non-trivial correlators from other sites) is $\mathcal{O}(1/q^4)$. The second, third and fourth terms all have pre-factors of $1/q^2$; if they are to contribute at this order, the accompanying correlators must be trivial. Using decoration delta constraints (definition 2), this fact (a consequence of theorem 1) is written below

$$\int dV \frac{1}{q^2}\langle \mathcal{Z}_1\rangle \cdots \langle \mathcal{Z}_m\rangle = \frac{1}{q^2}\prod_i \delta^{\mathcal{Z}_i,\mathbb{1}} + \mathcal{O}\big(1/q^3\big). \tag{5.80}$$

All together, in the context of a Haar average, the following replacement is valid up to $\mathcal{O}(1/q^2)$.

$$\langle \phi_+| \Gamma^0 |\phi_+(T)\rangle = \langle Z\Gamma^0_1 Z(T)\Gamma^{0\dagger}_{\overline{2}}\rangle\langle Z\Gamma^0_2 Z(T)\Gamma^{0\dagger}_{\overline{1}}\rangle - \frac{1}{q^2}\delta^{\Gamma^0_{\overline{1}},\Gamma^0_1}\delta^{\Gamma^0_{\overline{2}},\Gamma^0_2} + \mathcal{O}\big(1/q^3\big). \tag{5.81}$$

We say that a decoration Γ^r leaves a site r undecorated if it contributes only trivial correlators, $\langle \mathbb{1} \rangle$. In the present case, keeping only $\mathcal{O}(1/q^2)$ contributions forces all sites $r \neq 0$ to be left undecorated. This allows us to take the Haar average of Eq. 5.81 directly, using theorem 2 for the Haar average of a product of two correlators. This gives,

$$\int dV \, \langle \phi_+ | \, \Gamma^0 \, | \phi_+(T) \rangle = \frac{1}{q^2} \delta^{\Gamma^0_{\mathbb{1}}, \Gamma^0_1} \delta^{\Gamma^0_2, \Gamma^0_2} - \frac{1}{q^2} \delta^{\Gamma^0_{\mathbb{1}}, \Gamma^0_1} \delta^{\Gamma^0_2, \Gamma^0_2} + \mathcal{O}\big(1/q^3\big) = \mathcal{O}\big(1/q^3\big). \quad (5.82)$$

5.4.5 $(a, b) = (4, 4)$ is $\mathcal{O}(1/q^2)$

The (4,4) calculation is significantly more difficult; we present the full calculation here, however; readers interested only in the final result should skip to the summary in Sec. 5.4.6.

We use the decoration expansion once again to rule out contributions from $x > 0$ and to identify the relevant contributions from $x = 0$.

Misaligned: $x > 0$

$$\mathcal{D}^{4,4}_{\Gamma}(x > 0, T) = -h^2 \times \left[\begin{array}{ccc|c|cc} & \vdots & & & \vdots & \\ \text{site } 0 & \langle + | \, K & & & | + \rangle & \\ \text{site } 1 & q \, \langle - | \, K & & & | + \rangle & \\ & \vdots & & \Gamma & \vdots & \\ & q \, \langle - | & & & K(T) \, | + \rangle & \text{site } x \\ & \langle - | & & & K(T) \, | - \rangle & \text{site } x+1 \\ & \vdots & & & \vdots & \end{array}\right]$$

For $x > 1$, each of the sites 0, 1, x and $x + 1$ contribute non-trivial correlators. When $x = 1$, sites 0, 1 and 2 all contribute non-trivial correlators. In either case, theorem 1 gives

$$\overline{\mathcal{D}^{4,4}_{\Gamma}(x > 0, T)} = \mathcal{O}\big(1/q^3\big). \quad (5.83)$$

Aligned: $x = 0$

$$\mathcal{D}_{\Gamma}^{4,4}(x=0,T) = -h^2 \times \left[\begin{array}{ccc|c|c} & & \vdots & & \vdots \\ & & \langle +| & & |+\rangle \\ \text{site } 0 & \langle +| K & & \Gamma & K(T)\,|+\rangle \\ \text{site } 1 & \langle -| K & & & K(T)\,|-\rangle \\ & & \langle -| & & |-\rangle \\ & & \vdots & & \vdots \end{array}\right]$$

Both sites 0 and 1 contribute non-trivial correlators. Keeping only the $\mathcal{O}(1/q^2)$ contributions means selecting decorations on sites $r \neq 0, 1$ that give trivial correlators only. For $r > 1$ this means selecting decorations such that $\langle -|\,\Gamma^r\,|-\rangle = \langle \Gamma_1^r \Gamma_{\overline{1}}^{r\dagger}\rangle \langle \Gamma_2^r \Gamma_{\overline{2}}^{r\dagger}\rangle = \langle \mathbb{1}\rangle^2$ (for $r < 0$ simply switch $- \leftrightarrow +$ and $1 \leftrightarrow 2$ in these equations). Choosing only Γ^r that leave a site $r < 0$ ($r > 1$) undecorated (contributing only trivial correlators) is equivalent to the decoration delta constraint $\delta^{\Gamma_1^r, \Gamma_{\overline{2}}^r} \delta^{\Gamma_2^r, \Gamma_{\overline{1}}}$ ($\delta^{\Gamma_1^r, \Gamma_{\overline{1}}^r} \delta^{\Gamma_2^r, \Gamma_{\overline{2}}^r}$). The implementation of these decoration delta constraints is discussed in B. The result of which is that for sites $r < 0$ we sandwiching each decoration layer $\Gamma(t)$ by $\langle +|$ and $|+\rangle$ and by $\langle -|$ and $|-\rangle$ for sites $r < 0$.

Writing the definition of K in Eq. 5.28 as $K = Z_1 - Z_2$, where the index refers to which leg the Z decorates, we write the following,

$$\begin{array}{l} \langle +|\, K\Gamma^0 K(T)\,|+\rangle \\ \langle -|\, K\Gamma^1 K(T)\,|-\rangle \end{array} = \sum_{i,j\in\{1,2\}} \begin{array}{l} \langle +|\, Z_i \Gamma^0 Z(T)_i\,|+\rangle \\ \langle -|\, Z_j \Gamma^1 Z(T)_j\,|-\rangle \end{array} + \begin{array}{c} \text{terms with more than two} \\ \text{non-trivial correlators.} \end{array} \tag{5.84}$$

Because we are selecting only decorations which leave sites $r \neq 0, 1$ undecorated, we are able to take the Haar average of this expression in isolation. Terms with more than two non-trivial correlators are $\mathcal{O}(1/q^3)$ or smaller and are therefore discarded, leaving only the Haar average of the first term. Using theorem 2, this is given by

$$\int dV \sum_{i,j\in\{1,2\}} \begin{matrix} \langle +| Z_i \Gamma^0 Z(T)_i |+\rangle \\ \langle -| Z_j \Gamma^1 Z(T)_j |-\rangle \end{matrix} = \tfrac{1}{q^2}\delta^{\Gamma^0_1,\Gamma^1_{\bar{1}}}\delta^{\Gamma^0_{\bar{2}},\Gamma^1_1}\delta^{\Gamma^0_2,\Gamma^0_{\bar{1}}}\delta^{\Gamma^1_{\bar{2}},\Gamma^1_2} + \tfrac{1}{q^2}\delta^{\Gamma^0_1,\Gamma^1_{\bar{2}}}\delta^{\Gamma^0_{\bar{2}},\Gamma^1_2}\delta^{\Gamma^0_2,\Gamma^0_{\bar{1}}}\delta^{\Gamma^1_1,\Gamma^1_{\bar{1}}} + (1 \leftrightarrow 2) + \mathcal{O}(1/q^3). \tag{5.85}$$

These delta constraints are implemented by sandwiching the decoration layers $\Gamma(t)$ with the appropriate wirings. The four different wirings configurations for sites 0 and 1 are precisely the wirings $|\mathcal{C}_{i,j}\rangle$ introduced in the previous section Eq. 5.35. Counting only the relevant decorations Γ, $\overline{\mathcal{D}^{1,1}_{\Gamma}(x=0,T)}$ given by

$$\overline{\mathcal{D}^{4,4}_{\Gamma}(x=0,T)} = -\frac{h^2}{q^2}\sum_{i,j\in\{1,2\}}$$

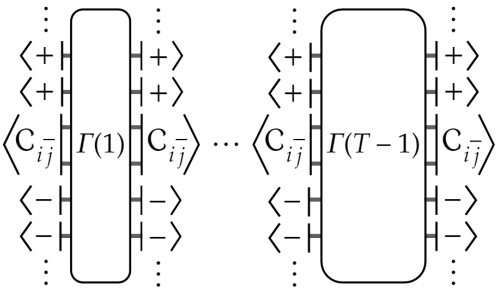

(5.86)

We now sum over all decorations Γ weighted by the coefficients C_Γ appearing in Eq. 5.67. This converts back into the picture with full unitary layers $U(t)$. This contribution is nothing but the contribution to δv_S calculated in Eq. 5.41 in the previous section. We will not repeat this calculation any further. The $(a,b) = (4,4)$ contribution to v_B is given by δv_S, as defined in Eq. 5.48.

5.4.6 Table of results and summary

We summarise the contributions $\overline{\mathcal{D}^{a,b}(k=0,T)}$ in the table below, highlighting the only contributions at $\mathcal{O}(1/q^2)$.

$a \setminus b$	1	2	3	4
1	q^{-3}	q^{-3}	q^{-3}	q^{-3}
2	q^{-2}	q^{-3}	q^{-3}	q^{-3}
3	q^{-3}	q^{-3}	q^{-3}	q^{-3}
4	q^{-3}	q^{-3}	q^{-3}	q^{-2}

We calculate the $(a, b) = (2, 1)$ contribution in appendix C, and in appendix D we find that the remaining pairs (a, b) contribute at $\mathcal{O}(1/q^3)$ or smaller. The $(a, b) = (4, 4)$ contribution is as given in Eq. 5.48, whereas the $(a, b) = (2, 1)$ contribution is given by $\delta v_F(\varepsilon)$,

$$\delta v_F(\varepsilon) = 2\frac{g^2}{q^2}(\nu(\varepsilon) - f(\varepsilon)), \tag{5.87}$$

where $\nu(\varepsilon) = [4(1-2s)(1-s(1-2s))]^{-1}$ and $f(\varepsilon)$ is found by (numerically) diagonalising a 5×5 transfer matrix in C, it is given to good approximation (see Fig. C.2) by

$$f(\varepsilon) = \frac{1}{7}s(\varepsilon)(1-4s(\varepsilon))^2(1+as+bs^2) \tag{5.88}$$

where $a = 6.8$ and $b = 16.1$. The factor $\frac{1}{7}s(1-4s)^2$ is obtained analytically by diagonalising the transfer matrix at small s and around separately the point $s = 1/4$. With spatial and Floquet time translation symmetry, the butterfly velocity is given to $\mathcal{O}(1/q^2)$ by

$$\overline{v_B(\varepsilon)} = v_0(\varepsilon) + \delta v_F(\varepsilon) + \delta v_S(\varepsilon) + \mathcal{O}\big(1/q^3\big). \tag{5.89}$$

We have used the subscript F to identify the correction δv_F with the Floquet time (and spatial) translation symmetry. In Fig. 5.2 we plot $q^2(\overline{v_B} - v_0)$ and the individual components δv_S and δv_F. From the small ε analysis in Sec. 5.3.2, we believe that corrections to v_B must rapidly approach zero in the window $\varepsilon \sim 1/q$, this is also reflected in Fig. 5.2.

Both corrections δv_S and δv_F are positive for all ε, enhancing the spreading of operators and information in our model. Spatial translation symmetry enhancing transport is not a

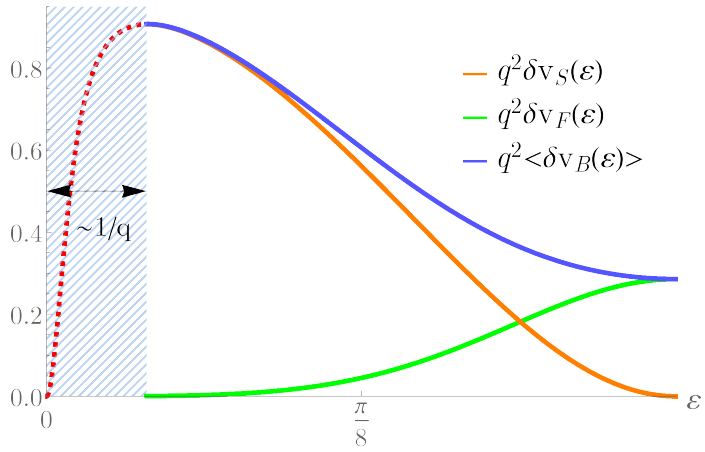

Figure 5.2: *The contributions $\delta v_S(\varepsilon)$ and $\delta v_F(\varepsilon)$ to $\overline{\delta v_B}$. As $\varepsilon \to 0$, the perturbative expansion in $1/q$ breaks down. δv_B must rapidly approach zero, in Sec. 5.3.2 we argue that this happens over an $\mathcal{O}(1/q)$ window.*

surprise. However, the effect of Floquet time translation symmetry is more mysterious. It will be interesting to see whether this result is robust at all orders in perturbation theory, and whether it persists in with different time evolutions.

5.5 Late times

In the variants of the model without Floquet time translation symmetry (Sec. 5.2 and Sec. 5.3), we were able to confidently discard diagrams that were sub-leading in $1/q$ to circuit averaged quantities (i.e., $\overline{v_B}$). This was because after only a few time steps, the (circuit averaged) evolved fast states were heavily suppressed by factors of $1/q$ (we showed this by evaluating the state norms). This becomes much harder with time translation symmetry, as it is not possible to take a circuit average at each time-step, only once the full evolution has taken place. This caused us to shift our strategy to counting the number of non-trivial correlation functions and then relying on the $q \to \infty$ asymptotic results of Chapter 4. However, there is an obvious issue with this approach. That is, what happens at late times $t \sim q$, where large q asymptotics become unreliable? The answer is that we must make an assumption about the decay of the memory matrix. We have seen that at early times, amenable to large q asymptotics, the memory matrix decays exponentially

with a time-scale $\tau(\varepsilon) \sim |g(\varepsilon)|$. Given that the (real time) memory matrix is a dynamical correlation function of fast variables, it is conceivable that this exponential decay persists even to infinite times (in the thermodynamic limit).

This is the crucial assumption we make in our analysis of the circuit with spatial and time translation symmetry – we assume that the real-time memory matrix decays with a time-scale $\tau(\varepsilon) \sim |g(\varepsilon)|$ which is positive, except for exceptional points ($\varepsilon = n\pi/2$) where the couplings are switched off between sites. Under this assumption, the memory matrix at time t is $\mathcal{O}(\exp(-t/\tau))$, meaning that for an $\mathcal{O}(1)$ time-scale τ, the contributions at times $t > q^\alpha$ (for any $\alpha > 0$) can be neglected in our perturbative expansion in $1/q$. In Sec. 4.6, we saw evidence that we can use the large q results for times $t \leq \sqrt{q}$. Therefore, with an $\mathcal{O}(1)$ time-scale $\tau(\varepsilon)$, using only the large q asymptotic values for Haar averaged quantities (as we have done in this chapter) yields a small $\mathcal{O}(1/q^3)$ error. As we discussed in Sec. 5.3.2, the situation is complicated by small $\varepsilon \sim 1/q$. We therefore only have confidence in our predictions for v_B at large coupling, $|g(\varepsilon)| \sim \mathcal{O}(1)$.

CHAPTER 6

CONCLUSIONS AND OUTLOOK

In this thesis, we have adapted an existing hydrodynamic formalism – the memory matrix formalism – to include a usually ignored symmetry of closed many-body quantum systems; the conservation of quantum information. In this formalism, it is necessary to consider multiple (four) copies of the original Hilbert space. Roughly speaking, the relevant slow degree of freedom in the MMF corresponds to a domain wall, or *cut*, between two different ways of pairing the replica Hilbert spaces (the + and − domains). Crucially, in adapting the MMF we are led to use an unusual inner-product encoding the entropic bias for operator growth, and making the ballistic spreading of information and operators natural on symmetry grounds. Many results from conventional hydrodynamic transport carry over, for instance, we find Green-Kubo-like formulae for an information transport coefficient – the butterfly velocity – in both Hamiltonian and Floquet models (Eq. 3.43 and Eq. 3.73 respectively). Within this formalism, we also find symmetry constraints on the operator growth lightcone (remark 3.5).

The formalism easily reproduces the random unitary circuit results of [32, 33] where we found, as expected, that circuit averaged quantities are memory-less (Sec. 3.7). The formalism was then applied to operator spreading in models with varying degrees of spatio-temporal symmetry in Chapter 5. We found that under the physically reasonable assumption of a finite memory time τ, we were able to perturbatively calculate the

memory matrix in the small parameter $1/q$ with careful bookkeeping and the use of a toolkit of (Haar) ensemble averaging results we developed in Chapter 4. We found that these perturbative corrections, δv_S and δv_F (Eq. 5.48 and Eq. 5.87 respectively), led to an enhancement of operator spreading and, furthermore, could be associated with the different symmetries of the model (spatial and Floquet time translation symmetry). The enhancement of transport in the presence of spatial translation symmetry is not a surprise. However, the role of discrete time translation symmetry in enhancing information transport is less obvious. We leave it to future work to see whether these enhancements are robust for more general time evolutions, and whether continuum space-time symmetries behave in a similar way.

More exotic information hydrodynamics is possible in the presence of additional conserved charges. With a $U(1)$ charge, the diffusive conserved components act as a source of non-conserved operators, giving rise to power-law tails in the spatial distributions of operator weight [34, 35]. It will be interesting to incorporate additional symmetries into the MMF and perform a mode coupling analysis. An obvious parallel investigation is the development of an effective field theory of operator spreading, provided we can find the slow fields. This would be used to shed light on possible operator spreading universality classes. It may also be possible to formulate an information mode MMF at finite temperature/chemical potential and, with only minor modifications, calculate a systems purity. Other potentially fruitful applications of the MMF are in the setting of perturbed dual unitary circuits [121] (which may serve as a solvable models about which we can perform perturbative calculations) and non-abelian circuits.

Appendices

The following appendices A-D are copies from my first author paper E. R. McCulloch and C. von Keyserlingk, "Operator spreading in the memory matrix formalism," Journal of Physics A: Mathematical and Theoretical, 2022. [114]

APPENDIX A

AN UNUSUAL INNER-PRODUCT

In this appendix we prove that the inner-product $(\cdot|\cdot)$ defined in Eq. 3.28 satisfies the necessary axioms. We repeat the definition of the inner-product below,

$$(A|B) \equiv \langle \Phi(A)|B\rangle_{\mathcal{W}} = \mathrm{Tr}\left(\Phi(A)^{\dagger} B\right), \tag{A.1}$$

where the super-operator Φ is given by

$$\Phi \equiv \sum_x \frac{1}{\chi_x^2} |W^x\rangle \langle W^x| + Q, \quad \chi_x \equiv \langle W^x|W^x\rangle, \implies \Phi|W^x\rangle = \frac{1}{\chi_x}|W^x\rangle. \tag{A.2}$$

Q is the Hermitian projector onto $\mathcal{Q}$. We must show that this constitutes a bona fide inner product by checking each of the inner product axioms.

1. Conjugate symmetry: $(A|B)^* = (B|A)$,

   Exploiting the conjugate symmetry of the inner product $\langle\cdot|\cdot\rangle$, we write

   $$(A|B) = \langle \Phi(A)|B\rangle = \langle A|\Phi(B)\rangle = \langle \Phi(B)|A\rangle^* = (B|A)^* \tag{A.3}$$

   where we have used the fact that Φ is Hermitian, this is because χ_x is real and the projector $\hat{Q}$ is Hermitian.

2. Linearity in second argument: $(A|\beta B + \gamma C) = \beta\,(A|B) + \gamma\,(A|C)$ for scalars β, γ,

$$\begin{aligned}(A|\beta B + \gamma C) &= \langle \Phi\,(A)|\beta B + \gamma C\rangle = \beta\,\langle \Phi\,(A)|B\rangle + \gamma\,\langle \Phi\,(A)|C\rangle \\ &= \beta\,(A|B) + \gamma\,(A|C)\end{aligned} \tag{A.4}$$

   where we have used linearity in the second argument of the inner product $\langle\cdot|\cdot\rangle$.

3. Positive definiteness: $(A|A) > 0$ for $A \neq 0$,

$$(A|A) = \langle \Phi\,(A)|A\rangle = \langle A|\,\Phi\,|A\rangle > 0 \tag{A.5}$$

   where we have used the fact that Φ is a positive definite matrix. This is easily seen by noticing that all χ_x^2 are real and positive.

This confirms that $(A|B)$ is indeed an inner-product and allows us to consider a new inner-product space in which the weight operators are orthonormal.

APPENDIX B

IMPOSING THE DECORATIONS DELTA CONSTRAINTS

This appendix revisits the Haar average identities for ATO correlators and their moments, specifically theorems 2 and 3. The final results (at leading order in $1/q$) involved "delta constraints" (as defined in Def. 2) which are zero/one depending on whether or not the decorations were equal (for all scramblers V). We have also seen these delta constraints whenever we have demanded that a correlator be trivial (see Eq. 5.81). In this section, we show how these delta constraints can be imposed by placing the decorations on a contour and inserting projectors at every time step; the insertion of projectors has an appealingly simple graphical interpretation, which facilitates our calculation of σ in the main text.

B.1 The constraint $\delta^{\Gamma_1,\Gamma_{\overline{1}}}$

The simplest example of a decoration delta constraint to consider is $\delta^{\Gamma_1,\Gamma_{\overline{1}}}$, where the two decorations are time-ordered, i.e., $\Gamma_1 = Z(1)^{a_1} Z(2)^{a_2} \cdots Z(n)^{a_n}$ and $\Gamma_{\overline{1}} = Z(1)^{b_1} Z(2)^{b_2} \cdots Z(n)^{b_n}$ for binary strings $\boldsymbol{a}$ and $\boldsymbol{b}$. In this case, the delta constraint checks that $a_i = b_i$ for all i. This is equivalent to putting Γ_1 and $\Gamma_{\overline{1}}$ on a wiring with a single forward and backward contour (labelled 1 and $\overline{1}$) and then placing a projector between each of the decoration

layers are shown below.

$$\delta^{\Gamma_1,\Gamma_{\overline{1}}} = \frac{1}{q^n}\Big(\begin{matrix} Z(1)^{a_1} \\ Z(1)^{b_{1^*}} \end{matrix} \bigcirc\!\!\bigcirc \begin{matrix} Z(2)^{a_2} \\ Z(2)^{b_{2^*}} \end{matrix} \bigcirc\!\!\bigcirc \cdots \bigcirc\!\!\bigcirc \begin{matrix} Z(n)^{a_n} \\ Z(n)^{b_{n^*}} \end{matrix} \Big). \tag{B.1}$$

The right-hand side checks that at each decoration layer t, $a_t = b_t$, this is precisely the same as the decoration delta constraint. A site $r \leq 0$ with decoration Γ^r contributes $\langle +| \Gamma^r |+\rangle$ in the decoration expansion, suppose that we demanded that this contribution contained only trivial correlators ($\langle +| \Gamma^r |+\rangle = \langle \mathbb{1} \rangle^2$). The decorations that meet this condition are those that satisfy the constraint $\delta^{\Gamma^r_1,\Gamma^r_{\overline{1}}}\delta^{\Gamma^r_2,\Gamma^r_{\overline{2}}}$. The projector insertion technique described above selects precisely these relevant decorations as follows

$$\delta^{\Gamma^r_1,\Gamma^r_{\overline{1}}}\delta^{\Gamma^r_2,\Gamma^r_{\overline{2}}} = \langle +| \Gamma^r(1) |+\rangle \langle +| \Gamma^r(2) |+\rangle \cdots \langle +| \Gamma^r(n) |+\rangle . \tag{B.2}$$

For sites $r > x+1$, where the contributions take the form $\langle -| \Gamma^r |-\rangle$, the decorations that contribute trivial correlators are identified in the same way but by projecting with $|-\rangle \langle -|$.

B.2 The constraint $\delta^{\Gamma_1\Gamma^\dagger_{\overline{2}}\Gamma_2\Gamma^\dagger_{\overline{1}},\mathbb{1}}$

Consider next, a decoration $\Gamma = \Gamma_1 \otimes \Gamma^*_{\overline{1}} \otimes \Gamma_2 \otimes \Gamma^*_{\overline{2}}$ with n decoration layers ($\Gamma = \Gamma(1)\cdots\Gamma(n)$) given in Fig. B.1, with $\Gamma_1 = Z(1)^{a_1}\cdots Z(n)^{a_n}$, $\Gamma_{\overline{1}} = Z(1)^{\overline{a}_1}\cdots Z(n)^{\overline{a}_n}$, $\Gamma_2 = Z(1)^{b_1}\cdots Z(n)^{b_n}$ and $\Gamma_{\overline{2}} = Z(1)^{\overline{b}_1}\cdots Z(n)^{\overline{b}_n}$ for binary strings $\boldsymbol{a}, \overline{\boldsymbol{a}}, \boldsymbol{b}$ and $\overline{\boldsymbol{b}}$.

$$\Gamma \;=\; \begin{matrix} -\Gamma_1- \\ -\Gamma^*_{\overline{1}}- \\ -\Gamma_2- \\ -\Gamma^*_{\overline{2}}- \end{matrix} \;=\; \begin{matrix} -Z(1)^{a_1}- & -Z(2)^{a_2}- & & -Z(n)^{a_{T-1}}- \\ -Z(1)^{\overline{a}_1{}^*}- & -Z(2)^{\overline{a}_2{}^*}- & \cdots & -Z(n)^{\overline{a}_{T-1}{}^*}- \\ -Z(1)^{b_1}- & -Z(2)^{b_2}- & & -Z(n)^{b_{T-1}}- \\ -Z(1)^{\overline{b}_1{}^*}- & -Z(2)^{\overline{b}_2{}^*}- & & -Z(n)^{\overline{b}_{T-1}{}^*}- \\ \Gamma(1) & \Gamma(2) & & \Gamma(n) \end{matrix}$$

Figure B.1: *A decoration Γ on the four legs $1, \overline{1}, 2$ and $\overline{2}$ with n decoration layers.*

As in the previous case, we will obtain a prescription for rewiring the legs of a contour

at every time step, this prescription will identify decorations Γ that satisfy the constraint. The delta constraint $\delta^{\Gamma_1^r\Gamma_{\frac{1}{2}}^{r\dagger}\Gamma_2^r\Gamma_{\bar{1}}^{r\dagger},\mathbb{1}}$ appears whenever we demand that the decoration Γ^r on some site r, with $1 < r < x$, contributes only a trivial correlator, $q\langle -|\,\Gamma^r\,|+\rangle = \langle\mathbb{1}\rangle = 1$. Finding the Γ which contribute non-trivial correlators is equivalent to finding Γ which satisfy the delta constraint.

Start then, with $\langle -|\,\Gamma\,|+\rangle$. Assume that, working in from the left, at least one of the decoration layers non-trivially decorates the $\langle -|$ wiring (so that the either one or both of the $(i,\bar{i})$ wirings in $\langle -|$ carry non-identity operators). This excludes the case where $\langle -|\,\Gamma = \langle -|$, which we will examine last. Let t_i, $0 < t_i \leq n$, be the first decoration layer in from the left that non-trivially decorates the $\langle -|$ wiring. Likewise, let t_f be the first decoration layer in from the right that non-trivially decorates the $|+\rangle$ wiring. If $t_i \neq t_f$, the resulting correlator is certainly non-trivial and therefore $X \neq \mathbb{1}$ (the delta constraint is not satisfied). Otherwise, if $t_i = t_f$, we have $\langle -|\,\Gamma\,|+\rangle = \langle -|\,\Gamma(t_i)\,|+\rangle$. In order for this to be a trivial correlator, $\Gamma(t_i)$ must decorate $\langle -|$ such that $\langle -|\,\Gamma(t_i) = \langle -|\,Z(t_i)^{\otimes 2}$ (see Eq. 5.28 for definition of $Z^{\otimes 2}$). We can select this case by sandwiching every decoration layer $t < t_i$ by $\langle -|$ and $|-\rangle$, every layer $t > t_i$ by $\langle +|$ and $|+\rangle$ and the layer t_i by $\langle -|$ on the left and on right by $q\,|0\rangle$. Finally, the cases where no decoration layer decorates the $\langle -|$ (an obvious example where $X = \mathbb{1}$) wiring can be selected by sandwiching every layer with $\langle -|$ and $|-\rangle$. Therefore, the decoration delta constraint can be rewritten as

$$\delta^{\Gamma_1^r\Gamma_{\frac{1}{2}}^{r\dagger}\Gamma_2^r\Gamma_{\bar{1}}^{r\dagger},\mathbb{1}} = \sum_{m=1}^{n}\left(\prod_{t=1}^{m-1}\langle -|\,\Gamma^r(t)\,|-\rangle\right) q\,\langle -|\,\Gamma^r(m)\,|0\rangle\left(\prod_{t=m+1}^{n}\langle +|\,\Gamma^r(t)\,|+\rangle\right) + \prod_{t=1}^{n}\langle -|\,\Gamma^r(t)\,|-\rangle\,. \tag{B.3}$$

Or diagrammatically as

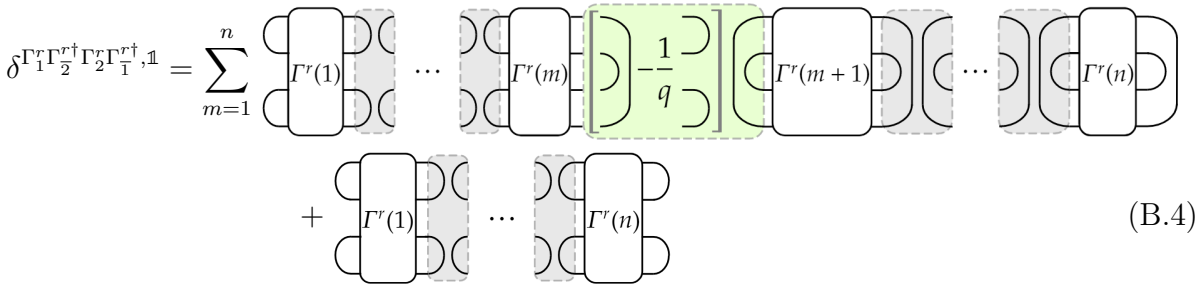

(B.4)

B.3 Connection to the OTOC Haar average

In this section we use the results of [119] to re-express the Haar average of a physical OTOC in terms of decoration delta constraints, arriving at the form of this theorem presented in theorem 3 of Sec. 4.2. The Haar average of an OTOC given in [119] is quoted below

$$\begin{aligned}\int dV \langle Z\Gamma_1 Z(T)\Gamma_{\overline{1}}^\dagger Z\Gamma_2 Z(T)\Gamma_{\overline{2}}^\dagger\rangle \\ &= \frac{1}{q^2}\sum_{m=1}^{n}\left(\prod_{t=1}^{m-1}\langle -|\,\Gamma(t)\,|-\rangle\right) q\,\langle -|\,\Gamma(m)\,|0\rangle\left(\prod_{t=m+1}^{n}\langle +|\,\Gamma(t)\,|+\rangle\right) \\ &\quad - \frac{1}{q^2}\prod_{t=1}^{n}\langle -|\,\Gamma(t)\,|-\rangle + \mathcal{O}\big(1/q^3\big).\end{aligned} \tag{B.5}$$

Comparing this to Eq. B.3, we have the following,

$$\int dV \langle Z\Gamma_1 Z(T)\Gamma_{\overline{1}}^\dagger Z\Gamma_2 Z(T)\Gamma_{\overline{2}}^\dagger\rangle = \frac{1}{q^2}\left(\delta^{\Gamma_1\Gamma_{\overline{2}}^\dagger\Gamma_2\Gamma_{\overline{1}}^\dagger,\mathbb{1}} - \delta^{\Gamma_1,\Gamma_{\overline{1}}}\delta^{\Gamma_2,\Gamma_{\overline{2}}} - \delta^{\Gamma_1,\Gamma_{\overline{2}}}\delta^{\Gamma_2,\Gamma_{\overline{1}}}\right) + \mathcal{O}\big(1/q^3\big). \tag{B.6}$$

APPENDIX C

CONFIGURATION $(A, B) = (2, 1)$

In the following, we evaluate the Haar average of the $(a, b) = (2, 1)$ contribution to $\mathcal{D}^{a,b}(x > 0, T)$.

C.1 $x = 0$

$$\mathcal{D}_{\Gamma}^{2,1}(x = 0, T) = g^2 \times \left[\begin{array}{ccc} & \vdots & \vdots \\ \text{site } 0 & \langle + | & |\phi_+(T)\rangle \\ \text{site } 1 & \langle \phi_- | \; \Gamma & |-\rangle \\ & \vdots & \vdots \end{array}\right] \tag{C.1}$$

Sites 0 and 1 each contribute a product of non-trivial correlation functions plus terms of size $1/q^2$. The Haar average of this is $\mathcal{O}(1/q^4)$.

C.2 $x = 1$

$$\mathcal{D}_{\Gamma}^{2,1}(x = 1, T) = g^2 \times \left[\begin{array}{ccc} & \vdots & \vdots \\ & \langle + | & |+\rangle \\ \text{site } 1 & q\,\langle \phi_- | \; \Gamma & |\phi_+(T)\rangle \\ & \langle - | & |-\rangle \\ & \vdots & \vdots \end{array}\right] \tag{C.2}$$

Splitting the decoration site by site, we find

$$\mathcal{D}_{\Gamma}^{2,1}(x=1,T) = qg^2 \langle\phi_-|\,\Gamma^1\,|\phi_+(T)\rangle \left(\prod_{r\leq 0}\langle+|\,\Gamma^r\,|+\rangle\right)\left(\prod_{r>1}\langle-|\,\Gamma^r\,|-\rangle\right). \tag{C.3}$$

The contribution from site 1 is given in full below,

$$\begin{aligned} q\,\langle\phi_-|\,\Gamma^1\,|\phi_+(T)\rangle = {} & \langle Z\Gamma_1^1 Z(T)\Gamma_{\overline{2}}^{1\dagger} Z\Gamma_2^1 Z(T)\Gamma_{\overline{1}}^{1\dagger}\rangle - \frac{1}{1-q^{-2}}\langle Z\Gamma_1^1\Gamma_{\overline{1}}^{1\dagger}\rangle\langle Z\Gamma_2^1\Gamma_{\overline{2}}^{1\dagger}\rangle \\ & - \frac{1}{1-q^{-2}}\langle\Gamma_{\overline{2}}^{1\dagger}\Gamma_1^1 Z(T)\rangle\langle\Gamma_{\overline{1}}^{1\dagger}\Gamma_2^1 Z(T)\rangle + \frac{1}{q^2-1}\langle Z\Gamma_1^1\Gamma_{\overline{2}}^{1\dagger} Z\Gamma_2^1\Gamma_{\overline{1}}^{1\dagger}\rangle \\ & + \frac{1}{q^2-1}\langle\Gamma_{\overline{1}}^{1\dagger}\Gamma_1^1 Z(T)\Gamma_{\overline{2}}^{1\dagger}\Gamma_2^1 Z(T)\rangle + \frac{1}{q^2(1-q^{-2})^2}\langle\Gamma_1^1\Gamma_{\overline{1}}^{1\dagger}\Gamma_2^1\Gamma_{\overline{2}}^{1\dagger}\rangle \\ & - \frac{1}{q^2(1-q^{-2})^2}\langle\Gamma_1^1\Gamma_{\overline{2}}^{1\dagger}\rangle\langle\Gamma_2^1\Gamma_{\overline{1}}^{1\dagger}\rangle - \frac{1}{q^2(1-q^{-2})^2}\langle\Gamma_1^1\Gamma_{\overline{1}}^{1\dagger}\rangle\langle\Gamma_2^1\Gamma_{\overline{2}}^{1\dagger}\rangle \\ & + \frac{1}{(q^2-1)^2}\langle\Gamma_1^1\Gamma_{\overline{2}}^{1\dagger}\Gamma_2^1\Gamma_{\overline{1}}^{1\dagger}\rangle \end{aligned} \tag{C.4}$$

Every term is either an OTOC, a product of two non-trivial correlators, or is manifestly $\mathcal{O}(1/q^2)$. The decorations on each site $r \neq 1$ may result in contributions that are either: (1) a trivial correlator; (2) a single non-trivial correlator; (3) a product of two non-trivial correlators. Note that none of these non-trivial correlators are OTOCs because they live on a contour with only a single forward and backward segments. Therefore, if any decoration on sites $r \neq 1$ does anything other than contribute trivial correlators, we have $\int dV \mathcal{D}_{\Gamma}^{2,1}(x = 1, T) = \mathcal{O}(1/q^3)$. Keeping only $\mathcal{O}(1/q^2)$ contributions forces every site $r \neq 1$ to contribute trivial correlators only. This allows us to take the Haar average of Eq. C.4 in isolation. To do this we find it useful to write the follows results (consequences of theorem 1),

$$\begin{aligned} \int dU\langle\Gamma\rangle\langle\Gamma'^{\dagger}\rangle &= \delta^{\Gamma,\mathbb{1}}\delta^{\Gamma',\mathbb{1}} + \mathcal{O}\big(1/q^2\big), \\ \int dU\langle\Gamma\rangle &= \delta^{\Gamma,\mathbb{1}} + \mathcal{O}\big(1/q^2\big), \\ \int dU\langle Z\Gamma Z\Gamma'\rangle &= \delta^{\Gamma,\mathbb{1}}\delta^{\Gamma',\mathbb{1}} + \mathcal{O}\big(1/q^2\big). \end{aligned}$$

Where all Γ are products $Z(1)^{\alpha_1} \cdots Z(T-1)^{\alpha_{T-1}}$ for some binary string $\alpha = (\alpha_1^i, \cdots, \alpha_{T-1}^i)$. Using theorem 2 we find the useful result

$$\int dU \langle Z\Gamma \rangle \langle Z\Gamma'^{\dagger} \rangle = \frac{1}{q^2} \delta^{\Gamma,\Gamma'} (1 - \delta^{\Gamma,\mathbb{1}}) + \mathcal{O}\big(1/q^4\big). \tag{C.5}$$

Using these results and theorem 3 for the Haar average of a physical OTOC, we find that at $\mathcal{O}(1/q^2)$, every term in C.4 cancels,

$$\begin{aligned} q \langle \phi_- | \ \Gamma^1 \ |\phi_+(T)\rangle_{\text{Haar}} = \frac{1}{q^2} \Big[& \delta^{\Gamma_1^1 \Gamma_{\bar{1}}^{1\dagger} \Gamma_2^1 \Gamma_{\bar{2}}^{1\dagger}, \mathbb{1}} - \delta^{\Gamma_1, \Gamma_{\bar{1}}} \delta^{\Gamma_2, \Gamma_{\bar{2}}} - \delta^{\Gamma_1, \Gamma_{\bar{2}}} \delta^{\Gamma_2, \Gamma_{\bar{1}}} \\ & - \delta^{\Gamma_1^1 \Gamma_{\bar{1}}^{1\dagger}, \Gamma_{\bar{2}}^1 \Gamma_2^{1\dagger}} (1 - \delta^{\Gamma_1^1, \Gamma_{\bar{1}}^1}) - \delta^{\Gamma_1^1 \Gamma_{\bar{1}}^{1\dagger}, \Gamma_{\bar{2}}^1 \Gamma_2^{1\dagger}} (1 - \delta^{\Gamma_1^1, \Gamma_{\bar{2}}^1}) \\ & + \delta^{\Gamma_1^1, \Gamma_{\bar{2}}^1} \delta^{\Gamma_2^1, \Gamma_{\bar{1}}^1} + \delta^{\Gamma_1^1, \Gamma_{\bar{1}}^1} \delta^{\Gamma_2^1, \Gamma_{\bar{2}}^1} + \delta^{\Gamma_1^1 \Gamma_{\bar{1}}^{1\dagger} \Gamma_2^1 \Gamma_{\bar{2}}^{1\dagger}, \mathbb{1}} - \delta^{\Gamma_1^1, \Gamma_{\bar{2}}^1} \delta^{\Gamma_2^1, \Gamma_{\bar{1}}^1} \\ & - \delta^{\Gamma_1^1, \Gamma_{\bar{1}}^1} \delta^{\Gamma_2^1, \Gamma_{\bar{2}}^1} \Big] + \mathcal{O}\big(1/q^3\big) \\ = \mathcal{O}\big(1/q^3\big). & \end{aligned} \tag{C.6}$$

and we find $\overline{\mathcal{D}^{2,1}(x=1,T)} = \mathcal{O}(1/q^3)$.

C.3 $x \geq 2$

$$\mathcal{D}_\Gamma^{2,1}(x>2,T) = g^2 \times \left[\begin{array}{lr|c|lr} & \vdots & & \vdots & \\ \text{site } 0 & \langle +| & & |+\rangle & \\ \text{site } 1 & q\langle \phi_-| & & |+\rangle & \\ & \vdots & \Gamma & \vdots & \\ & q\langle -| & & |\phi_+(T)\rangle & \text{site } x \\ & \langle -| & & |-\rangle & \text{site } x+1 \\ & \vdots & & \vdots & \end{array}\right] \tag{C.7}$$

Sites 1 and x each contribute factors of form OTOC + Corr $\times$ Corr$'$ + $\mathcal{O}(1/q^2)$ (see Eq. 5.75). Our theorem for the Haar average of a product of correlators (theorem 1) implies that if any other site contributes a non-trivial correlator, the Haar average of the

total contribution will be $\mathcal{O}(1/q^3)$ or smaller. Thus, working to $\mathcal{O}(1/q^2)$, we will look for contributions where sites $r \neq 1, x$ give only trivial correlators. Moreover, theorem 1 also implies that the leading order contribution comes from the $\mathrm{OTOC}_1\mathrm{OTOC}_x$ cross term

$$\begin{aligned}\int dU \left(\mathrm{OTOC}_1 + \mathrm{Corr}_1 \times \mathrm{Corr}_1' + \mathcal{O}\big(1/q^2\big)\right)\left(\mathrm{OTOC}_x + \mathrm{Corr}_x \times \mathrm{Corr}_x' + \mathcal{O}\big(1/q^2\big)\right) \\ = \int dU\ \mathrm{OTOC}_1 \times \mathrm{OTOC}_x + \mathcal{O}\big(1/q^3\big)\end{aligned} \tag{C.8}$$

In summary, in evaluating the contributions for $x \geq 2$, we need only consider those terms in the decoration expansion corresponding to OTOCs on site $1, x$, and trivial correlators on all other sites. As in the $(a, b) = (4, 4)$ calculation, we select decorations that leave the contours on sites $r > x$ $(r < 1)$ undecorated by inserting the projector $|+\rangle\langle+|$ $(|-\rangle\langle-|)$ between every Floquet layer. For sites $1 < r < x$ the non-decoration condition is more delicate. For these sites, the input wiring configuration is of $-$ type and the output wiring configuration is of $+$ type giving an OTO type contour. The requirement that the OTO contour is undecorated (i.e., a trivial correlator) is equivalent to the decoration delta constraint $\delta^{\Gamma_1^r \Gamma_2^{r\dagger} \Gamma_2^r \Gamma_1^{r\dagger}, \mathbb{1}}$. In B we show that this decoration delta constraint can be rewritten as

$$\begin{aligned}\delta^{\Gamma_1^r \Gamma_2^{r\dagger} \Gamma_2^r \Gamma_1^{r\dagger}, \mathbb{1}} = \sum_{m=1}^{n} \left(\prod_{t=1}^{m-1} \langle-|\,\Gamma^r(t)\,|-\rangle\right) q\,\langle-|\,\Gamma^r(m)\,|0\rangle \left(\prod_{t=m+1}^{n} \langle+|\,\Gamma^r(t)\,|+\rangle\right) \\ + \prod_{t=1}^{n} \langle-|\,\Gamma^r(t)\,|-\rangle\,.\end{aligned} \tag{C.9}$$

The final term in Eq. C.9 selects the decorations Γ^r that never decorate the initial state $\langle-|$, so that at each time step the $\langle-|$ wirings never carry any non-identity operators. With these $|-\rangle\langle-|$ projectors in place, let us sum over all decorations Γ with the coefficients C_Γ of Eq. 5.67, in doing so we replace each of the decoration layers with the full unitary layers $U(t)$. This is pictured below, where we have highlighted site x, with its terminating

state $|\phi\rangle_+(T)$.

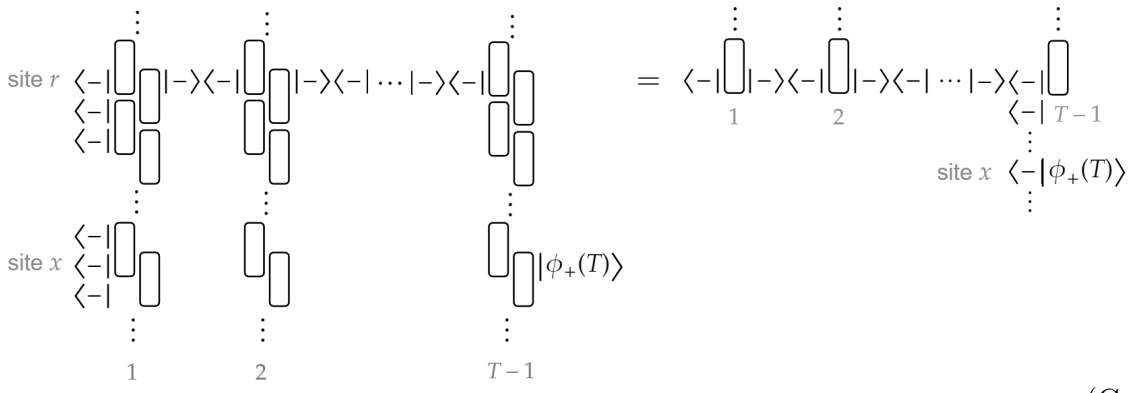

(C.10)

Where, crucially, the brick property of Eq. 5.9 can be used to remove every brick to the right of site r (below site r in the diagram above). This yields the right hand-side of the equation above. A consequence of which is that the terminating states $|\phi_+(T)\rangle$ on site x is contracted directly with $\langle -|$. Using Eq. 5.71, we see that this diagram vanishes. Therefore, the decorations selected by the final term of Eq. C.9 cannot contribute to $\mathcal{D}^{2,1}(x > 2, T)$. In what follows, we will consider only the decorations selected by the sum in Eq. C.9.

As previously noted, only the $\text{OTOC}_1 \times \text{OTOC}_x$ terms can contribute at $\mathcal{O}(1/q^2)$. This allows us to drop all but the $\langle -| Z^{\otimes 2}$ term in the $\langle \phi_-|$ state (see Eq. 5.70) of site 1 and the $Z(T)^{\otimes 2}|+\rangle$ term in the state $|\phi_+(T)\rangle$ of site x. The fact that OTOC_1 begins with $\langle -| Z^{\otimes 2}$ and OTOC_x ends with $Z(T)^{\otimes 2}|+\rangle$ and the condition that these OTOCs are complex conjugates of each other (using theorem 2) forces both OTOCs to be physical OTOCs of the same length (the length of physical OTOCs is the difference between the latest and earliest time appearing in the OTOC). We will sum over all possible OTOC lengths τ, $1 \leq \tau \leq T-1$.

We now describe how we select only those decorations that produce a physical OTOC with length τ. For OTOC_1, we must ensure that every unitary layer $t > \tau$ does not decorate the $|+\rangle$ wirings on site 1. We do this by inserting the projector $|+\rangle\langle +|$ to the left of each of these layers. Requiring then that the τ-th unitary layer decorates the $|+\rangle$ wiring by leaving $Z(\tau)^{\otimes 2}|+\rangle$ is achieved by sandwiching the layer with $q\langle \perp|$ and $|+\rangle$.

Making all of these selections, the contribution from site 1 is takes the form shown below,

$$q \langle - | Z^{\otimes 2} \Gamma^1(1) \cdots \Gamma^1(\tau - 1) Z(\tau)^{\otimes 2} | + \rangle \, q \langle \perp | \Gamma^1(\tau) | + \rangle \langle + | \Gamma^1(\tau + 1) | + \rangle \cdots \langle + | \Gamma^1(T - 1) | + \rangle . \tag{C.11}$$

We use the same strategy to select decorations that contribute physical OTOCs of length τ on site x as well. The resulting contribution takes the form shown below, where we have defined $\tau' = T - \tau$,

$$\langle - | \Gamma^x(1) | - \rangle \cdots \langle - | \Gamma^x(\tau' - 1) | - \rangle \, q \langle - | \Gamma^x(\tau') | 0 \rangle \, q \langle - | Z(\tau')^{\otimes 2} \Gamma^x(\tau' + 1) \cdots \Gamma^x(T - 1) Z(T)^{\otimes 2} | + \rangle . \tag{C.12}$$

Rather than focus on a single decoration Γ, we are able to select every $\mathcal{O}(1/q^2)$ to $\mathcal{D}^{2,1}(x = 2, T)$ simultaneous by summing over decorations Γ with the appropriate coefficients C_Γ (as introduced in the decoration expansion in Eq. 5.67),

$$\mathcal{D}^{2,1}(x = 2, T) = \sum_\Gamma C_\Gamma \mathcal{D}^{2,1}_\Gamma(x = 2, T). \tag{C.13}$$

Each of these layers is contracted by various combinations of the $+, -, \perp$ and 0 states. We introduce a short-hand for each of these contractions, this is given below,

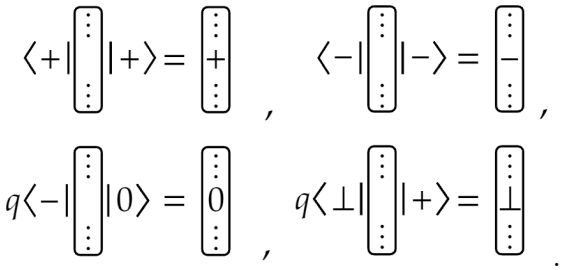

(C.14)

One further short-hand we use is $\langle Z_t^- | \equiv \langle - | Z(t)^{\otimes 2}$ and $| Z_t^+ \rangle \equiv Z(t)^{\otimes 2} \langle + |$. The contractions (of the unitary layers) at site 1 now take the more readable form,

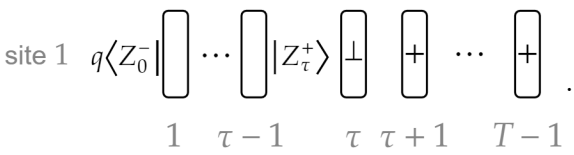

(C.15)

The short-hand version for site x is found similarly, but with $T - \tau - 1$ '$-$' contractions,

followed by a '0' contraction on layer $T-\tau$, followed by the OTOC. We now also apply this short-hand to the contributions on site r, $1 < r < x$, in particular, this yields

$$\sum_{t_r=1}^{T-1} \text{site } r \quad \boxed{-} \cdots \boxed{-} \quad \boxed{0} \quad \boxed{+} \cdots \boxed{+} \quad , \tag{C.16}$$
$$1 \quad t_r - 1 \quad t_r \quad t_r + 1 \quad T-1$$

where we have discarded the decoration that never decorates the initial state, as previously discussed.

By keeping only the $\mathcal{O}(1/q^2)$ contributions to $\mathcal{D}^{2,1}(x \geq 2, T)$, have found a set of diagrams labelled by: τ, the length of each of the physical OTOCs; t_r for each site $r \in \{2, \cdots, x-1\}$, the positions the '0' contraction on site r. Setting $t_1 = \tau$ and $t_x = T-\tau$, we label each diagram by a sequence $(t_1, t_2, \cdots, t_{x-1}, t_x)$. An example diagram, labelled $(t_1, t_2, t_3, t_4, t_5, t_6) = (5, 3, 6, 2, 8, 7)$, that contributes to $\mathcal{D}^{2,1}(x = 6, T = 12)$ is given below

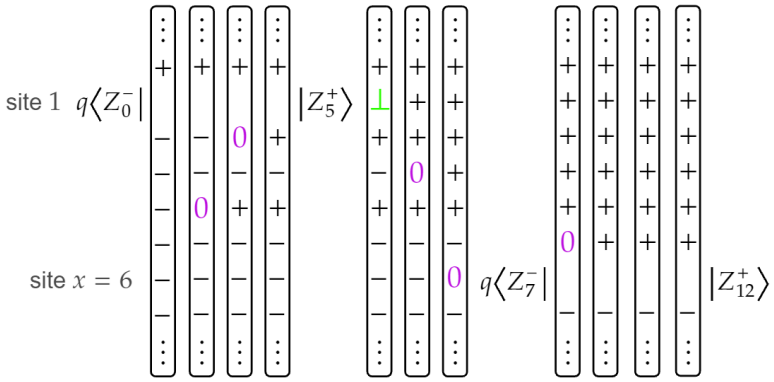

Figure C.1: *The contribution* $(t_1, t_2, t_3, t_4, t_5, t_6) = (5, 3, 6, 2, 8, 7)$ *to* $\mathcal{D}^{(2,1)}(x = 6, T = 12)$

In fact, for $x > 2$, only contributions where $t_1 \leq t_2 < t_3 < \cdots < t_x$ are non-zero. One of the following motifs must appear in any diagram not satisfying this property, each of

which is zero,

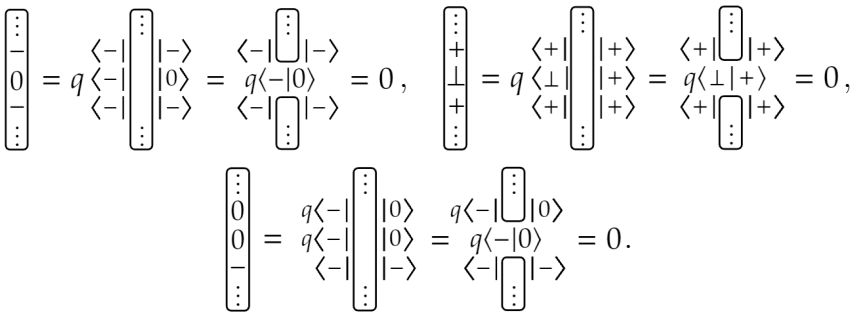

(C.17)

In the non-zero diagrams (i.e., those for which $t_1 \leq t_2 < t_3 < \cdots < t_x$) the contracted unitary layers collapse into contractions of only a short portion of the full layer this follows from the brick property Eq. 5.9. We demonstrate this process by collapsing a semi-infinite domain of '+' contractions below,

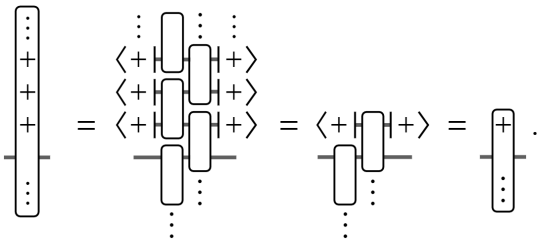

(C.18)

We collapse the '−' domain in the same way. Ultimately, every layer reduces to one of the motifs below,

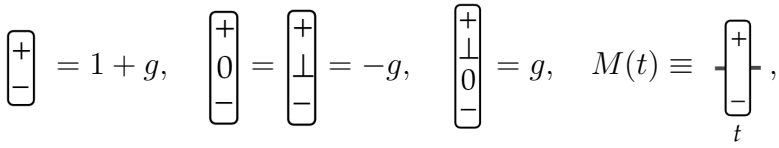

(C.19)

where $M(t)$ is a single site operator. Each diagram as a whole decomposes into a products of the motifs below, which we use to introduce a compact diagrammatic notation. We

also give the numerical value of each motif.

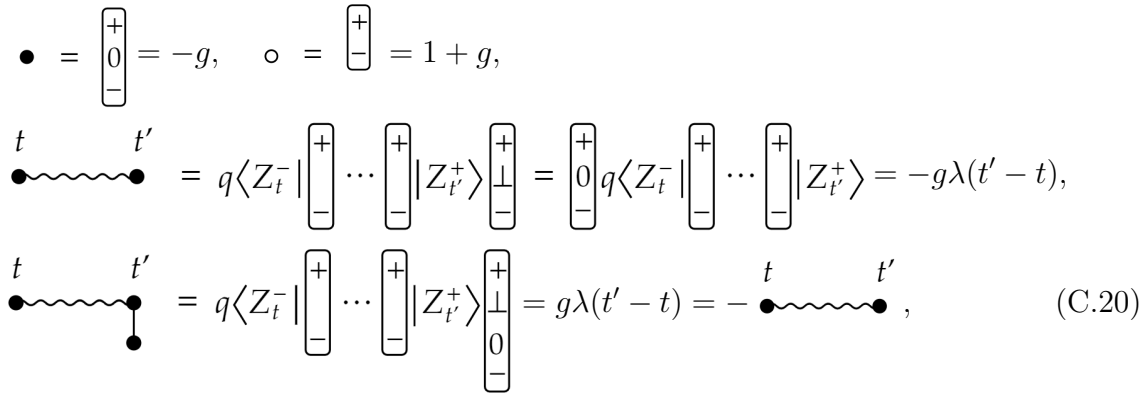

(C.20)

where we have defined $\lambda(t-t') = q\left\langle Z_t^- \right| M(t+1)\cdots M(t'-1)\left|Z_{t'}^+\right\rangle$. To give an example of the correspondence between the contracted unitary layer diagrams and this new diagrammatic notation, consider the diagram corresponding to the sequence $(t_1, \cdots, t_4) = (3, 3, 6, 7)$ below

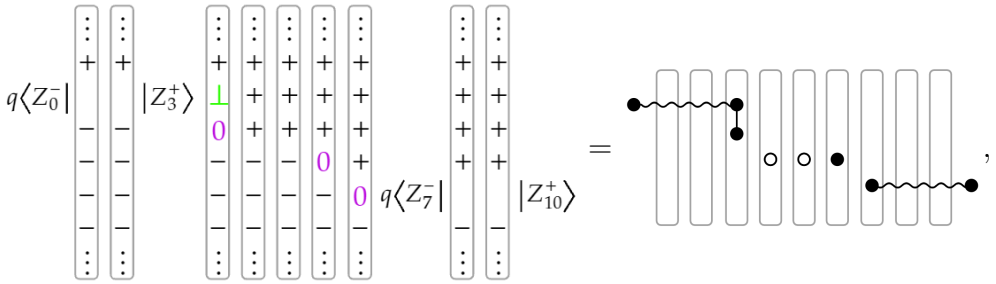

(C.21)

For $x > 2$, the diagrams come in two qualitatively different types: (1) $t_1 < t_2$ and (2) $t_1 = t_2$. All type 1 diagrams have the following diagrammatic form

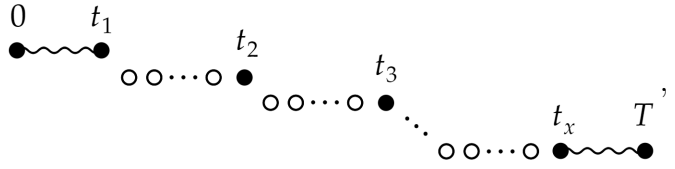

(C.22)

where $T - t_x = t_1$. Whereas, type 2 diagrams have the form

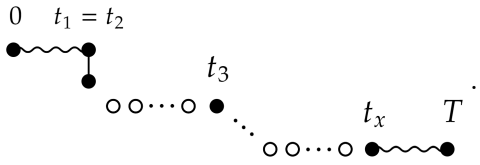

(C.23)

For $x = 2$, we will find diagrams with similar motifs. We had found that for $x \geq 2$, the relevant diagrams are labelled by a sequence $(t_1, t_2, \cdots, t_x)$, with $t_x = T - t_1$ and where $t_1 = \tau$ is the length of the OTOCs. For $x = 2$ the diagrams are simply labelled by $(\tau, T-\tau)$. A complication for $x = 2$ is the fact that the OTOCs may overlap in time. This is because no matter where we position the '$\perp$' contraction of site 1 and '0' contraction of site 2, we can never encounter any of the vanishing motifs of Eq. C.17, which in the case of $x > 2$ force $t_1 \leq t_2$.

To address this complication, we split $x = 2$ in three types of diagram: (1) $T - \tau > \tau$, the OTOCs do not overlap – the treatment of these diagrams is exactly the same the type-1 diagrams discussed for $x > 2$; (2) $\tau = T - \tau$, the OTOC's 'touch' – this is similar to the type-2 diagrams in $x > 2$; (3) $\tau > T - \tau$, the OTOCs overlap.

The touching OTOC contributions ($\tau = T - \tau$) have the following form/motif,

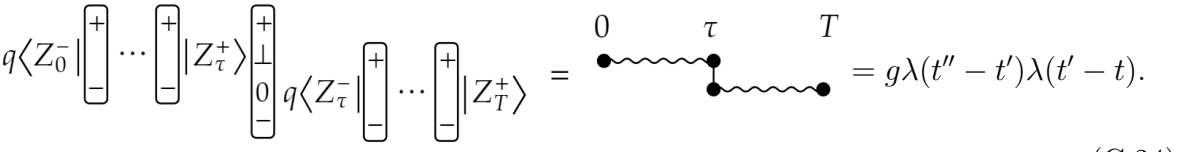

(C.24)

We give the overlapping OTOC contributions ($\tau > T - \tau$) the following compact notation,

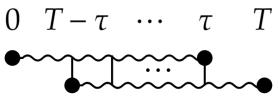

(C.25)

We study these contributions in detail in the next section, C.4.

We are interested in computing $\sum_x \overline{\mathcal{D}^{(2,1)}(x,T)}$, we have seen earlier in this appendix that the $x = 0, 1$ contributions are $\mathcal{O}(1/q^3)$ (as are the $x < 0$ contributions, Eq. 5.66). Therefore, at $\mathcal{O}(1/q^2)$, we need only sum over $x \geq 2$. Fortunately, there is an abundance of cancellation between these diagrams. We will cover some examples and then give the general result. Starting with the simplest, we compute $\sum_x \overline{\mathcal{D}^{(2,1)}(x,T)}$ for $T = 2, 3$ and 4 explicitly (where the Haar average is implied, but not written below). The additional factor of g^2 in Eq. C.7 has been divided through in the equations below.

$$\sum_x \mathcal{D}^{(2,1)}(x, T=2)/g^2 =$$

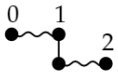

$$\sum_x \mathcal{D}^{(2,1)}(x, T=3)/g^2 =$$

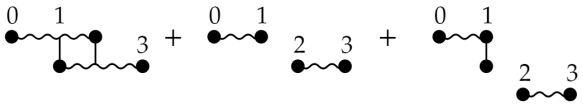

$$=$$

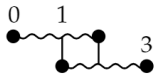

$$\sum_x \mathcal{D}^{(2,1)}(x, T=4)/g^2 =$$

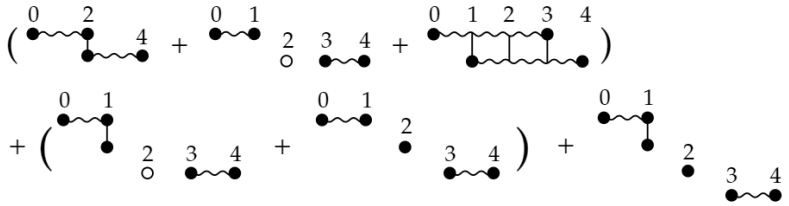

$$=$$

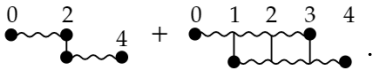

We have used the third rule of Eq. C.20 to cancel the two terms (associated with $x = 2$ and $x = 3$) for $T = 2$ and to cancel the second and fourth terms and the fifth and sixth terms for $T = 4$. Notice that the terms that remain after cancellation are all connected diagrams (i.e., the OTOCs either touch or overlap), all the diagrams with 'gaps' (i.e., where a vertical line can be drawn through them without intersecting a wobbly line, representing an OTOC) have conspired to cancel. This is no coincidence, it is a consequence of the fact that processes that contribute to Σ (and hence the corrections to v_B) must explore only the fast space, this is due to the Q projectors that project out all slow components at every time-step in Σ. Diagrams with a gap represent processes that take a detour to the slow space. We can see this by returning to the contracted unitary layer picture; take, for example, the $T = 3$ diagram associated with $(t_1 = 1, t_2 = 2)$, this is the first diagram

in the $T = 3$ sum above. It is equivalently given by

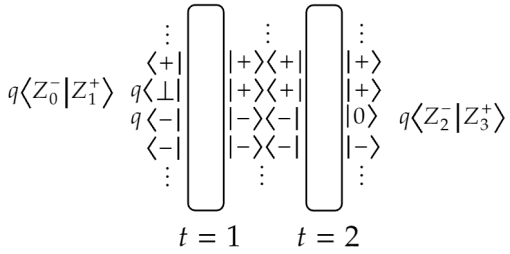

(C.26)

Between the two unitary layers we have vectors that are clearly in $\mathcal{P}$. The only diagrams that have no gaps are those for $x = 1$ (which we have seen all vanish at $\mathcal{O}(1/q^2)$) and the overlapping or touching OTOC diagrams for $x = 2$. We will next evaluate the overlapping OTOC diagram contributions, before finally calculating the touching OTOC diagram contributions.

C.4 Overlapping OTOC diagrams.

In this section we investigate the contributions to $\mathcal{D}^{(2,1)}(x = 2, T)$ that take the form of overlapping OTOCs. We name this contribution $\mathcal{D}_{\mathrm{O}}^{(2,1)}(x = 2, T)$. These OTOC overlap diagrams are given in detail below for OTOC length τ and total diagram length T.

$$\overline{\mathcal{D}_{\mathrm{O}}^{(2,1)}(x=2,T)} \approx g^2 \int dV \sum_{\tau=1}^{T-1}$$

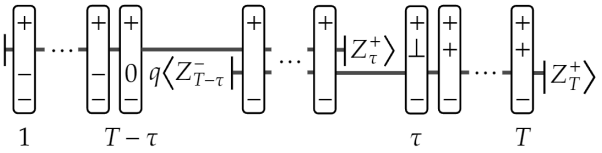

(C.27)

It will be useful to define the single site operators $M_+(\tau)$ and $M_-(\tau')$ and repeat the definition for $M(t)$ seen in Eq. C.19.

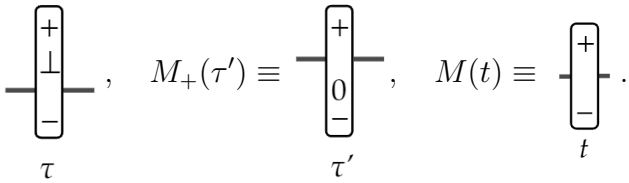

(C.28)

The Floquet layers $T-\tau+1$ through to $\tau-1$ have been reduced to two site operators which has already been introduced in Eq. 5.43 and named $\mathcal{T}(t)$ for Floquet layer t. With these definitions we have

$$\overline{\mathcal{D}_{\mathrm{O}}^{(2,1)}(2,T)} \approx g^2 \int dV \sum_{\tau=1}^{T-1}$$

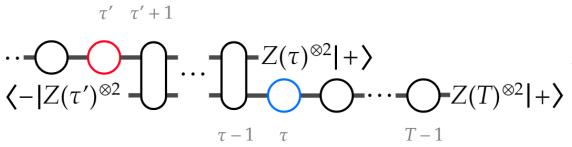

, (C.29)

where we have denoted the following,

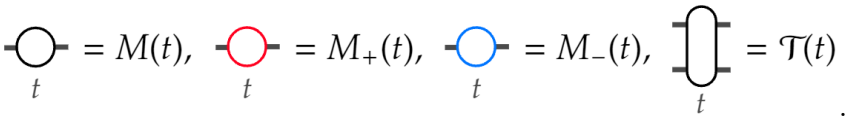

.

Using theorem 2 of Sec. 4.2, the Haar average of a product of two physical OTOCs is found to $\mathcal{O}(1/q^2)$ to be

$$\int dV \begin{matrix}\langle Z\Gamma_1^1 Z(T)\Gamma_{\overline{2}}^{1\dagger} Z\Gamma_2^1 Z(T)\Gamma_{\overline{1}}^{1\dagger}\rangle \\ \langle Z\Gamma_1^2 Z(T)\Gamma_{\overline{2}}^{2\dagger} Z\Gamma_2^2 Z(T)\Gamma_{\overline{1}}^{2\dagger}\rangle\end{matrix} = \frac{1}{q^2}\Big(\delta^{\Gamma_1^1,\Gamma_{\overline{1}}^2}\delta^{\Gamma_{\overline{2}}^1,\Gamma_2^2}\delta^{\Gamma_2^1,\Gamma_{\overline{2}}^2}\delta^{\Gamma_{\overline{1}}^1,\Gamma_1^2}$$
$$+\,\delta^{\Gamma_1^1,\Gamma_{\overline{2}}^2}\delta^{\Gamma_{\overline{2}}^1,\Gamma_1^2}\delta^{\Gamma_2^1,\Gamma_{\overline{1}}^2}\delta^{\Gamma_{\overline{1}}^1,\Gamma_2^2}\Big) + \mathcal{O}\big(1/q^3\big). \quad \text{(C.30)}$$

Each of the decoration delta constraints can be implemented as described in B. In doing so, we sandwich each decoration layer with a wiring configuration labelled A for the first term in Eq. C.30 and by a configuration labelled B for the second term. We then use the shorthand below.

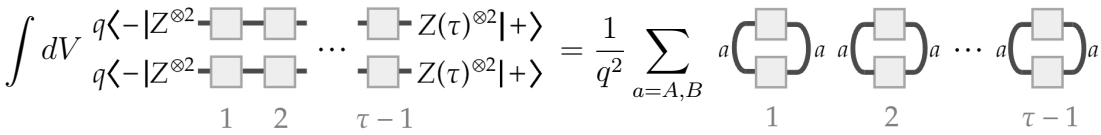

, (C.31)

where the grey boxes are placeholders for the possible decorations at each layer. A grey box (labeled t) may decorated each of the incoming legs 1 and 2 with $Z(t)$ and each of the legs $\overline{1}$ and $\overline{2}$ with $Z(t)^*$. On the right-hand side, every super-leg carries a label a which

labels one of the permutations A, B of the legs $1, \bar{1}, 2, \bar{2}$ given in Eq. C.32 below,

(C.32)

Each super-leg is implicitly carrying a factor $1/q^2$. The contraction between decorations within a column is given more explicitly below

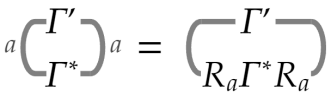

$$= \mathrm{Tr}\left(R^a \Gamma^\dagger R^a \Gamma'\right)/q^4 = \langle R^a \Gamma R^a | \Gamma' \rangle \,. \tag{C.33}$$

All of the onsite scrambling evolution can be dropped on the right-hand-side of Eq. C.31 as the leg contractions are between decorations at the same time. In the case of Eq. C.29, the OTOCs are off-set by $\tau' = T - \tau$ Floquet time-steps. These OTOCs can be brought into alignment by globally shift the time arguments in the OTOCs, then we can use Eq. C.31. After Haar averaging, and shifting the OTOCs back to their original positions, the leg contractions will stretch over τ' steps, as shown below.

$$\frac{g^2}{q^2} \sum_{s\geq 0} \sum_{t\geq 0} \delta^{s+2t+3,T} \sum_{a=A,B}$$

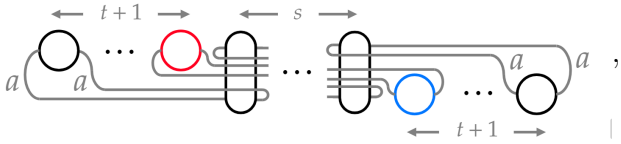

, (C.34)

where all scrambling evolution time arguments have been dropped. The new variables are related to those in Eq. C.29 by $t = T - \tau - 1 \geq 0$ and $s = 2\tau - T - 1 \geq 0$. As an example, we show the $t = 1$, $s = 2$ case,

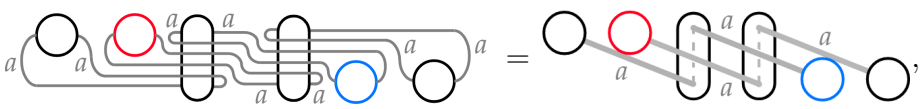

, (C.35)

where on the right hand side we have introduced a shorthand which makes obvious the decomposition into two chains of tensor contractions. In general, the Haar average decomposes into $t + 1$ chains. By summing over $T \geq 1$, we are able to drop the delta constraint above, doing this sum is equivalent to calculating the Laplace transformed $\overline{\mathcal{D}^{2,1}(x = 2, T)}$

at $z = 0$, i,e $\overline{\mathcal{D}^{2,1}(x = 2, z = 0)}$. This is sufficient for calculating v_B. Before we determine the decomposition for a general $s \geq 0$ and $t \geq 0$, we first define the following chains,

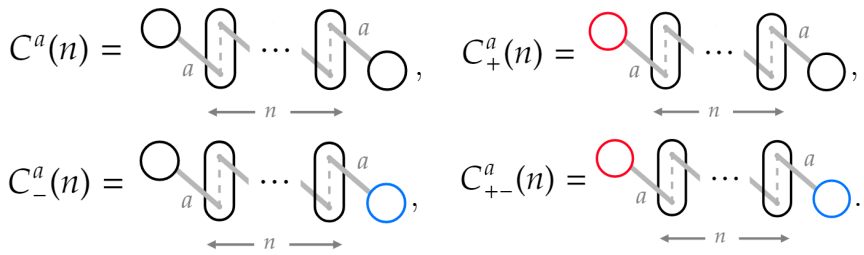

(C.36)

For any (s, t) There are two qualitatively distinct types of contribution to Eq. C.34: (1) $t + 1 \equiv 0 \pmod{s + 1}$, a product of t C^a chains and one C^a_{+-} chain; (2) otherwise, a product of $t - 1$ C^a chains, one C^a_+ chain and one C^a_- chain. For case 1, the C^a_{+-} chain is $n = \frac{s+1}{t+1} - 1 \geq 0$ transfer matrices long, i.e., $C^a_{+-}(n)$, while all t of C^a chains are $n + 1$ matrices long, $C^a(n + 1)$. For case 2 with $s + 1 = n(t + 1) + k$ for $1 \leq k \leq t$ and starting from the left, the first $k-1$ M's are on chains of length $n+1$ and terminate on an M. The k-th M sits on a chain of length n and terminates on M_-, the following $t - k$ M's sit on chains length n that terminate on an M. Finally, the M_+ sits on a chain of length n and terminates on an M. All together, the contribution is $C^a_+(n)C^a_-(n)C^a(n+1)^{k-1}C^a(n)^{t-k}$. This is summarised below,

$$\frac{g^2}{q^2} \sum_{a=A,B} \sum_{n\geq 0} \left[\sum_{t\geq 0} C^a_{+-}(n) C^a(n+1)^t + \sum_{t\geq 1} \sum_{k=1}^{t} C^a_+(n) C^a_-(n) C^a(n+1)^{k-1} C^a(n)^{t-k} \right]. \tag{C.37}$$

In both cases, all but the n sums can be evaluated to give,

$$\overline{\mathcal{D}^{(2,1)}_{\mathrm{O}}(x = 2, z = 0)} = \frac{g^2}{q^2} \sum_{a=A,B} \sum_{n\geq 0} \left[\frac{C^a_{+-}(n)}{1 - C^a(n+1)} + \frac{C^a_+(n) C^a_-(n)}{(1 - C^a(n))(1 - C^a(n+1))} \right]. \tag{C.38}$$

It remains to calculate the different chains. To do this we approach the problem as a transfer matrix problem, where $\mathcal{T}$ is the transfer matrix. Using the definition of $\mathcal{T}$ in Eq. 5.43, the decoration decomposition of a two-site brick in Eq. 5.6 and definitions of M

and $M^{\pm}$ in Eq. C.28, $\mathcal{T}$ and each of M, M_+ and M_- have the following properties,

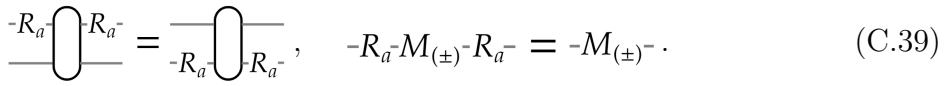

(C.39)

Then, using the definition of the labelled super legs in Eq. C.32, the chain $C^a(n)$ simplifies to the expression below,

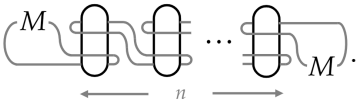

(C.40)

Notice that the dependence on the label a vanished. This is true of all chains. Algebraically, these chains (now without leg labels) are equivalently given by

$$\begin{aligned} C(n) &= \langle M| \mathcal{T}^n |M\rangle, \quad C_+(n) = \langle M_+| \mathcal{T}^n |M\rangle\,, \\ C_+(n) &= \langle M| \mathcal{T}^n |M_-\rangle, \quad C_{+-}(n) = \langle M_+| \mathcal{T}^n |M_-\rangle\,, \end{aligned} \tag{C.41}$$

where these angles braces reflect the trace inner product for tensors with input and output super legs $l = (1, \overline{1}, 2, \overline{2})$.

$$\langle B|A\rangle = \mathrm{Tr}\big(B^\dagger A\big)/q^4 = \quad . \tag{C.42}$$

Equipped with this, we can now write, for the contribution due to overlapping OTOC diagrams, the following

$$\overline{\mathcal{D}_{\mathrm{O}}^{(2,1)}(x = 2, z = 0)} = \frac{2g^2}{q^2} f(\varepsilon), \tag{C.43}$$

where $f(\varepsilon)$ is given by

$$f(\varepsilon) = \sum_{n\geq 0} \left[\frac{C_{+-}(n)}{1 - C(n+1)} + \frac{C_+(n) C_-(n)}{(1 - C(n))(1 - C(n+1))} \right], \tag{C.44}$$

where the chains are implicitly dependent on ε. To evaluate this sum, we must understand the space that the transfer matrix acts on. Each of the legs 1, $\overline{1}$, 2 and $\overline{2}$ may be

either undecorated or carry a Z decoration. This means that the state our state space is dimension 2^4 and $\mathcal{T}$ is a 16×16 matrix. Because all the $M_{(\pm)}$ are even in the number of Z decorations, and $\mathcal{T}$ preserves decoration parity, we are able to reduce the state space to those states with an even number of Z decorations only, i.e., 8 states. It will be useful to use the basis below,

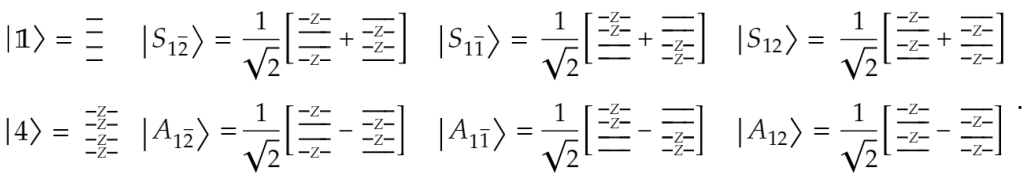

(C.45)

Let $\mathcal{S}$ be the space spanning $\{|\mathbb{1}\rangle, |S_{1\bar{1}}\rangle, |S_{1\bar{2}}\rangle, |S_{12}\rangle, |4\rangle\}$ and $\mathcal{A}$ be the space spanning $\{|A_{1\bar{1}}\rangle, |A_{1\bar{2}}\rangle, |A_{12}\rangle\}$ One can easily check that $|M\rangle$, $|M_+\rangle$ and $|M_-\rangle$ are all in $\mathcal{S}$. Explicitly, with $u(\varepsilon) = \sin(\varepsilon)^2$

$$|M\rangle = (u^4 + (1-u)^4)\,|\mathbb{1}\rangle + 2u^2(1-u)^2\,|4\rangle - (1+g)\frac{g}{\sqrt{2}}\left(|S_{1\bar{1}}\rangle + |S_{1\bar{2}}\rangle\right) + \frac{g^2}{\sqrt{2}}\,|S_{12}\rangle\,, \tag{C.46}$$

$$|M_+\rangle = -\frac{g(1+g)}{\sqrt{2}}\left(|S_{12}\rangle - |S_{1\bar{2}}\rangle\right) + \frac{g^2}{2}\left(\sqrt{2}\,|S_{1\bar{2}}\rangle - |\mathbb{1}\rangle - |4\rangle\right), \tag{C.47}$$

$$|M_-\rangle = -\frac{g(1+g)}{\sqrt{2}}\left(|S_{12}\rangle - |S_{1\bar{1}}\rangle\right) + \frac{g^2}{2}\left(\sqrt{2}\,|S_{1\bar{1}}\rangle - |\mathbb{1}\rangle - |4\rangle\right). \tag{C.48}$$

$\mathcal{T}$ is block diagonal in the subspaces $\mathcal{S}$ and $\mathcal{A}$, and since all $\left|M_{(\pm)}\right\rangle$ lie in $\mathcal{S}$, we are able to restrict our considerations to this five dimensional space only. In this restricted space with basis order $(\mathbb{1}, 4, S_{1,\bar{1}}, S_{1,\bar{2}}, S_{1,2})$, $\mathcal{T}$ is given by the product $\mathcal{T} = \tilde{T}_- \tilde{U} \tilde{T}_+$, where

$$\tilde{U} = \begin{pmatrix} (1-u)^2 & 0 & 0 & 0 & 0 \\ 0 & u^2 & 0 & 0 & 0 \\ 0 & 0 & -\frac{g}{2} & 0 & 0 \\ 0 & 0 & 0 & -\frac{g}{2} & 0 \\ 0 & 0 & 0 & 0 & \frac{g}{2} \end{pmatrix} \tag{C.49}$$

$$\tilde{T}_- = \begin{pmatrix} (1-u)^2 & u^2 & -\frac{g}{\sqrt{2}} & 0 & 0 \\ u^2 & (1-u)^2 & -\frac{g}{\sqrt{2}} & 0 & 0 \\ -\frac{g}{\sqrt{2}} & -\frac{g}{\sqrt{2}} & g+1 & 0 & 0 \\ 0 & 0 & 0 & g+1 & -g \\ 0 & 0 & 0 & -g & g+1 \end{pmatrix} \tag{C.50}$$

$$\tilde{T}_+ = \begin{pmatrix} (1-u)^2 & u^2 & 0 & -\frac{g}{\sqrt{2}} & 0 \\ u^2 & (1-u)^2 & 0 & -\frac{g}{\sqrt{2}} & 0 \\ 0 & 0 & g+1 & 0 & -g \\ -\frac{g}{\sqrt{2}} & -\frac{g}{\sqrt{2}} & 0 & g+1 & 0 \\ 0 & 0 & -g & 0 & g+1 \end{pmatrix} \tag{C.51}$$

Four of the eigenvalues of $\mathcal{T}$ are bounded by $|\lambda_{1,2,3,4}| \leq |g(\varepsilon)|(1-2|g(\varepsilon)|)/2$. The largest eigenvalue (for all ε) is bounded by $|\lambda_5| \leq (1-|g(\varepsilon)|)^3$.

In Sec. 5.1 we showed that $\langle v_B(\varepsilon)\rangle$ must have the symmetries $\varepsilon \to -\varepsilon$ and $\varepsilon \to \pi/2+\varepsilon$. All analytically computed $\mathcal{O}(1/q^2)$ contributions (the $(a, b) = (4, 4)$ contribution and the touching OTOC contribution) are found to respect this symmetry, as does the $\mathcal{O}(1)$ contribution from Ω. We therefore conclude that $f(\varepsilon)$ must also have this symmetry. Additionally, we know that $f(\varepsilon)$ is a function of $\sin(\varepsilon)^2$ only (the transfer matrix and the initial and final vectors in our transfer matrix calculation are functions of $\sin(\varepsilon)^2$ only). Together with the symmetry requirements, this means that $f(\varepsilon)$ is in fact a function of $s(\varepsilon) = \sin(\varepsilon)^2\cos(\varepsilon)^2$.

We evaluate the sum in Eq. C.44 analytically for small ε, finding $f(\varepsilon) \approx \varepsilon^2/7$. Knowing that f is a function of $s(\varepsilon)$ only, we use this to factorise $f(\varepsilon) = \frac{1}{7}s(\varepsilon)w(s(\varepsilon))$, where $w(\varepsilon)$ is a function that approaches 1 as $\varepsilon \to 0$. The transfer matrix dramatically simplifies at the point $s(\varepsilon) = 1/4$. Where all but one eigenvalue is zero. We find analytically that $f(\varepsilon) \propto (1-4s)^2$ around this point. This suggests a further factorisation $f(\varepsilon) = \frac{1}{7}s(\varepsilon)(1-4s)^2p(s(\varepsilon))$. We find a very good quadratic polynomial approximation for $p(\varepsilon) =$

$1 + as + bs^2$, with $a = 6.8$ and $b = 16.1$.

$$f(\varepsilon) = \frac{1}{7} s(\varepsilon)(1 - 4s(\varepsilon))^2(1 + as(\varepsilon) + bs(\varepsilon)^2) \tag{C.52}$$

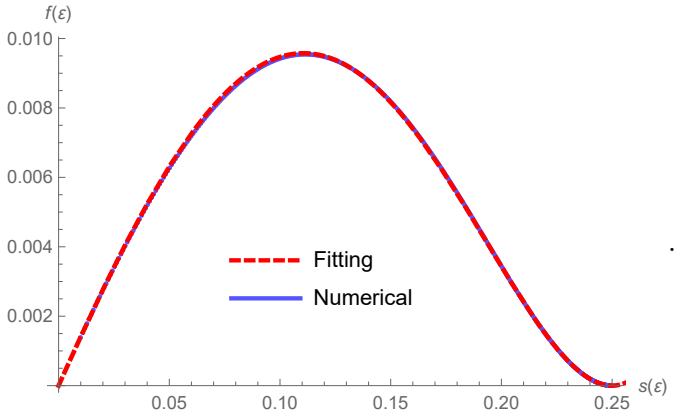

Figure C.2: *The contribution to v_B from processes with overlapping OTOCs is given by $2g(\varepsilon)^2 f(\varepsilon)/q^2$, $f(\varepsilon)$ is by numerically and plotted in blue. A fitting function is plotted in red.*

We also find numerically that $\overline{\mathcal{D}_{\mathrm{O}}^{2,1}(x = 2, T)}$ decays exponentially quickly, with a decay rate bounded below by $\gamma_{\mathrm{O}}(\varepsilon) \geq 6s(\varepsilon)$.

C.5 Touching OTOC diagrams

We will now sum up all of the touching OTOC diagrams. These are given in Eq. C.24 with $T = 2\tau$ so that the two OTOC have the same length. We name this contribution $\mathcal{D}_{\mathrm{Touch}}^{(2,1)}(x = 2, T)$

We are only interested in the $z \to i0^+$ limit, this is given by

$$\overline{\mathcal{D}_{\mathrm{Touch}}^{(2,1)}(k = 0, z = 0)} = g^2 \int dV \sum_{t=1}^{\infty} g\lambda(t)^2 + \mathcal{O}\big(1/q^3\big). \tag{C.53}$$

The factor $g\lambda(t)^2$ is the contribution from the diagrams Eq. C.24. The Haar average of a

product of OTOCs given in Eq. C.31 is deployed again to say that

$$\int dV\, \lambda(t)^2 = \frac{2}{q^2} \langle M|M\rangle^{t-1}. \tag{C.54}$$

This gives

$$\int dV \sum_{t=1}^{\infty} g^3 \lambda(t)^2 = \frac{2g^3}{q^2} \frac{1}{1 - \langle M|M\rangle} = -\frac{2g^2}{q^2}\nu(\varepsilon), \tag{C.55}$$

where $\langle M|M\rangle = 1 - 8s(1-2s)(1-s(1-2s))$, $s(\varepsilon) = \sin(\varepsilon)^2 \cos(\varepsilon)^2$ and $\nu(\varepsilon) = -g/(1 - \langle M|M\rangle)$. Touching OTOC diagrams decay exponentially with a decay rate $\gamma_{\text{Touch}}(\varepsilon) = \log\big(\langle M|M\rangle^{-1}\big) \geq 8s(\varepsilon)$.

C.6 Summary

Recalling Eq. 5.66, the contributions from $x < 0$ are $\mathcal{O}(1/q^4)$ or smaller. Piecing together the $\mathcal{O}(1/q^2)$ corrections, we find $\overline{\mathcal{D}^{(2,1)}(k = 0, z = 0)}$ is given by

$$\overline{\mathcal{D}^{(2,1)}(k = 0, z = 0)} = \frac{2g^2}{q^2}(f(\varepsilon) - \nu(\varepsilon)) + \mathcal{O}\big(1/q^3\big). \tag{C.56}$$

APPENDIX D

REMAINING CONFIGURATIONS (A, B)

This appendix presents a bookkeeping of contribution to the memory matrix in Sec. 5.4.

D.1 $(a, b) = (1, 2)$

$$\mathcal{D}_{\Gamma}^{1,2}(x \geq 0, T) = g^2 \times \left[\begin{array}{ccccc} & \vdots & & \vdots & \\ \text{site } 0 & \langle \phi_+ | & & |+\rangle & \\ \text{site } 1 & q\langle - | & & |+\rangle & \\ & \vdots & \Gamma & \vdots & \\ & q\langle - | & & |+\rangle & \text{site } x \\ & \langle - | & & |\phi_-(T)\rangle & \text{site } x+1 \\ & \vdots & & \vdots & \end{array}\right] \tag{D.1}$$

Here, we can simply use Eq. 5.75 to see that both sites 0 and $x + 1$ contribute a product of non-trivial correlation functions plus terms of size $1/q^2$. The Haar average of this is $\mathcal{O}(1/q^4)$.

$$\overline{\mathcal{D}_{\Gamma}^{1,2}(x \geq 0, T)} = \mathcal{O}\big(1/q^4\big). \tag{D.2}$$

D.2 $(a, b) = (3, 3)$

Aligned: $x = 0$

$$\mathcal{D}_{\Gamma}^{3,3}(x=0,T) = g^2 \times \begin{bmatrix} \text{site } 0 & \langle +| Z^{\otimes 2} & & Z(T)^{\otimes 2} |+\rangle \\ \text{site } 1 & \langle -| Z^{\otimes 2} & \Gamma & Z(T)^{\otimes 2} |-\rangle \end{bmatrix} \left(\prod_{r<0} \langle +| \Gamma^r |+\rangle \right) \left(\prod_{r>1} \langle -| \Gamma^r |-\rangle \right) \tag{D.3}$$

In this case, both contours on site 0 and on site 1 are non-trivially decorated, contributing a total of four non-trivial correlators. The Haar average is then $\mathcal{O}(1/q^4)$.

Misaligned: $x \geq 1$

In this case, each site 0 and $x + 1$ contribute a product of non-trivial correlators and therefore, as above, are $\mathcal{O}(1/q^4)$ or smaller. All together, this means

$$\overline{\mathcal{D}_{\Gamma}^{1,2}(x \geq 0, T)} = \mathcal{O}\big(1/q^4\big). \tag{D.4}$$

D.3 $(a, b) = (3, 4)$ and $(4, 3)$

Aligned: $x = 0$

$$\mathcal{D}_{\Gamma}^{3,4}(0,T) = -ihg \times \begin{bmatrix} \text{site } 0 & \langle +| Z^{\otimes 2} \Gamma^0 K(T) |+\rangle \\ \text{site } 1 & \langle -| Z^{\otimes 2} \Gamma^1 K(T) |-\rangle \end{bmatrix} \left(\prod_{r<0} \langle +| \Gamma^r |+\rangle \right) \left(\prod_{r>1} \langle -| \Gamma^r |-\rangle \right) \tag{D.5}$$

Both site 0 and site 1 contribute two non-trivial correlators. The Haar average of this term is $\mathcal{O}(1/q^4)$ or smaller.

Mislaigned: $x \geq 1$

Each of the sites 0 and $x + 1$ contribute a product of two non-trivial correlators. Each of the sites 1 and x contribute a non-trivial correlator. If $x = 1$, then this is only five non-trivial correlators, otherwise it is six. The Haar average is then $\mathcal{O}(1/q^5)$. All together,

this means

$$\overline{\mathcal{D}_{\Gamma}^{4,4}(x \geq 0, T)} = \mathcal{O}\big(1/q^4\big). \tag{D.6}$$

D.4 (a, b), where either $a \in 1, 2$ and $b \in 3, 4$ or the converse

In these case, Eq. 5.75 is again enough to show that $\overline{\mathcal{D}_{\Gamma}^{a,b}(x, T)} = \mathcal{O}(1/q^3)$.

BIBLIOGRAPHY

[1] M. Heyl, "Dynamical quantum phase transitions: a review," *Reports on Progress in Physics*, vol. 81, no. 5, p. 054001, 2018.

[2] M. Heyl, A. Polkovnikov, and S. Kehrein, "Dynamical quantum phase transitions in the transverse-field ising model," *Phys. Rev. Lett.*, vol. 110, p. 135704, 2013.

[3] B. Ž unkovič, M. Heyl, M. Knap, and A. Silva, "Dynamical quantum phase transitions in spin chains with long-range interactions: Merging different concepts of nonequilibrium criticality," *Physical Review Letters*, vol. 120, no. 13, 2018.

[4] S. Sharma, U. Divakaran, A. Polkovnikov, and A. Dutta, "Slow quenches in a quantum ising chain: Dynamical phase transitions and topology," *Physical Review B*, vol. 93, no. 14, 2016.

[5] U. Bhattacharya, S. Bandyopadhyay, and A. Dutta, "Mixed state dynamical quantum phase transitions," *Phys. Rev. B*, vol. 96, p. 180303, 2017.

[6] M. Heyl, "Scaling and universality at dynamical quantum phase transitions," *Physical Review Letters*, vol. 115, no. 14, 2015.

[7] N. Fläschner, D. Vogel, M. Tarnowski, B. S. Rem, D.-S. Lühmann, M. Heyl, J. C. Budich, L. Mathey, K. Sengstock, and C. Weitenberg, "Observation of dynamical vortices after quenches in a system with topology," *Nature Physics*, vol. 14, no. 3, pp. 265–268, 2017.

[8] P. Jurcevic, H. Shen, P. Hauke, C. Maier, T. Brydges, C. Hempel, B. P. Lanyon, M. Heyl, R. Blatt, and C. F. Roos, "Direct observation of dynamical quantum phase transitions in an interacting many-body system," *Phys. Rev. Lett.*, vol. 119, p. 080501, 2017.

[9] J. Zhang, G. Pagano, P. W. Hess, A. Kyprianidis, P. Becker, H. Kaplan, A. V. Gorshkov, Z.-X. Gong, and C. Monroe, "Observation of a many-body dynamical phase transition with a 53-qubit quantum simulator," *Nature*, vol. 551, no. 7682, pp. 601–604, 2017.

[10] J. Berges, S. Borsá nyi, and C. Wetterich, "Prethermalization," *Physical Review Letters*, vol. 93, no. 14, 2004.

[11] T. Mori, T. N. Ikeda, E. Kaminishi, and M. Ueda, "Thermalization and prethermalization in isolated quantum systems: a theoretical overview," *Journal of Physics B: Atomic, Molecular and Optical Physics*, vol. 51, no. 11, p. 112001, 2018.

[12] J. D. Nardis, S. Gopalakrishnan, E. Ilievski, and R. Vasseur, "Superdiffusion from emergent classical solitons in quantum spin chains," *Physical Review Letters*, vol. 125, no. 7, 2020.

[13] V. B. Bulchandani, S. Gopalakrishnan, and E. Ilievski, "Superdiffusion in spin chains," *Journal of Statistical Mechanics: Theory and Experiment*, vol. 2021, no. 8, p. 084001, 2021.

[14] J. De Nardis, S. Gopalakrishnan, R. Vasseur, and B. Ware, "Subdiffusive hydrodynamics of nearly-integrable anisotropic spin chains," 2021. arXiv:2109.13251 [cond-mat.stat-mech].

[15] J. D. Nardis, S. Gopalakrishnan, R. Vasseur, and B. Ware, "Stability of superdiffusion in nearly integrable spin chains," *Physical Review Letters*, vol. 127, no. 5, 2021.

[16] E. Ilievski, J. D. Nardis, S. Gopalakrishnan, R. Vasseur, and B. Ware, "Superuniversality of superdiffusion," *Physical Review X*, vol. 11, no. 3, 2021.

[17] S. Gopalakrishnan, A. Morningstar, R. Vasseur, and V. Khemani, "Theory of anomalous full counting statistics in anisotropic spin chains," 2022. arXiv:2203.09526 [cond-mat.stat-mech].

[18] V. Khemani, R. Moessner, and S. L. Sondhi, "A brief history of time crystals," 2019. arXiv:1910.10745 [cond-mat.str-el].

[19] X. Mi, M. Ippoliti, C. Quintana, A. Greene, Z. Chen, J. Gross, F. Arute, K. Arya, J. Atalaya, R. Babbush, J. C. Bardin, J. Basso, A. Bengtsson, A. Bilmes, A. Bourassa, L. Brill, M. Broughton, B. B. Buckley, D. A. Buell, B. Burkett, N. Bushnell, B. Chiaro, R. Collins, W. Courtney, D. Debroy, S. Demura, A. R. Derk, A. Dunsworth, D. Eppens, C. Erickson, E. Farhi, A. G. Fowler, B. Foxen, C. Gidney, M. Giustina, M. P. Harrigan, S. D. Harrington, J. Hilton, A. Ho, S. Hong, T. Huang, A. Huff, W. J. Huggins, L. B. Ioffe, S. V. Isakov, J. Iveland, E. Jeffrey, Z. Jiang, C. Jones, D. Kafri, T. Khattar, S. Kim, A. Kitaev, P. V. Klimov, A. N. Korotkov, F. Kostritsa, D. Landhuis, P. Laptev, J. Lee, K. Lee, A. Locharla, E. Lucero, O. Martin, J. R. McClean, T. McCourt, M. McEwen, K. C. Miao, M. Mohseni, S. Montazeri, W. Mruczkiewicz, O. Naaman, M. Neeley, C. Neill, M. Newman, M. Y. Niu, T. E. O'Brien, A. Opremcak, E. Ostby, B. Pato, A. Petukhov, N. C. Rubin, D. Sank, K. J. Satzinger, V. Shvarts, Y. Su, D. Strain, M. Szalay, M. D. Trevithick, B. Villalonga, T. White, Z. J. Yao, P. Yeh, J. Yoo, A. Zalcman, H. Neven, S. Boixo, V. Smelyanskiy, A. Megrant, J. Kelly, Y. Chen, S. L. Sondhi, R. Moessner, K. Kechedzhi, V. Khemani, and P. Roushan, "Time-crystalline eigenstate order on a quantum processor," *Nature*, vol. 601, no. 7894, pp. 531–536, 2021.

[20] S. Choi, J. Choi, R. Landig, G. Kucsko, H. Zhou, J. Isoya, F. Jelezko, S. Onoda, H. Sumiya, V. Khemani, C. von Keyserlingk, N. Y. Yao, E. Demler, and M. D. Lukin, "Observation of discrete time-crystalline order in a disordered dipolar many-body system," *Nature*, vol. 543, no. 7644, pp. 221–225, 2017.

[21] T. Langen, R. Geiger, and J. Schmiedmayer, "Ultracold atoms out of equilibrium," *Annual Review of Condensed Matter Physics*, vol. 6, no. 1, pp. 201–217, 2015.

[22] S. Trotzky, Y.-A. Chen, A. Flesch, I. P. McCulloch, U. Schollwöck, J. Eisert, and I. Bloch, "Probing the relaxation towards equilibrium in an isolated strongly correlated one-dimensional bose gas," *Nature Physics*, vol. 8, no. 4, pp. 325–330, 2012.

[23] T. Kinoshita, T. Wenger, and D. S. Weiss, "A quantum Newton's cradle," *Nature*, vol. 440, no. 7086, pp. 900–903, 2006.

[24] I. E. Mazets and J. Schmiedmayer, "Thermalization in a quasi-one-dimensional ultracold bosonic gas," *New Journal of Physics*, vol. 12, no. 5, p. 055023, 2010.

[25] J. Martin, B. Georgeot, and D. L. Shepelyansky, "Cooling by time reversal of atomic matter waves," *Physical Review Letters*, vol. 100, no. 4, 2008.

[26] N. Goldman, I. Satija, P. Nikolic, A. Bermudez, M. A. Martin-Delgado, M. Lewenstein, and I. B. Spielman, "Realistic time-reversal invariant topological insulators with neutral atoms," *Physical Review Letters*, vol. 105, no. 25, 2010.

[27] N. Szpak and R. Schützhold, "Time reversal and quantum loschmidt echo in optical lattices," 2019. arXiv:1901.05941 [quant-ph].

[28] J. Š untajs, J. Bonča, T. Prosen, and L. Vidmar, "Quantum chaos challenges many-body localization," *Physical Review E*, vol. 102, no. 6, 2020.

[29] D. Abanin, J. Bardarson, G. D. Tomasi, S. Gopalakrishnan, V. Khemani, S. Parameswaran, F. Pollmann, A. Potter, M. Serbyn, and R. Vasseur, "Distinguishing localization from chaos: Challenges in finite-size systems," *Annals of Physics*, vol. 427, p. 168415, 2021.

[30] W. D. Roeck and J. Z. Imbrie, "Many-body localization: stability and instability," *Philosophical Transactions of the Royal Society A: Mathematical, Physical and Engineering Sciences*, vol. 375, no. 2108, p. 20160422, 2017.

[31] A. Nahum, J. Ruhman, S. Vijay, and J. Haah, "Quantum entanglement growth under random unitary dynamics," *Phys. Rev. X*, vol. 7, p. 031016, 2017.

[32] A. Nahum, S. Vijay, and J. Haah, "Operator spreading in random unitary circuits," *Phys. Rev. X*, vol. 8, p. 021014, 2018.

[33] C. W. von Keyserlingk, T. Rakovszky, F. Pollmann, and S. L. Sondhi, "Operator hydrodynamics, otocs, and entanglement growth in systems without conservation laws," *Phys. Rev. X*, vol. 8, p. 021013, 2018.

[34] V. Khemani, A. Vishwanath, and D. A. Huse, "Operator spreading and the emergence of dissipative hydrodynamics under unitary evolution with conservation laws," *Phys. Rev. X*, vol. 8, p. 031057, 2018.

[35] T. Rakovszky, F. Pollmann, and C. W. von Keyserlingk, "Diffusive hydrodynamics of out-of-time-ordered correlators with charge conservation," *Phys. Rev. X*, vol. 8, p. 031058, 2018.

[36] W. Brown and O. Fawzi, "Scrambling speed of random quantum circuits," *ArXiv e-prints*, 2012. arXiv:1210.6644 [quant-ph].

[37] A. Chan, A. De Luca, and J. T. Chalker, "Solution of a minimal model for many-body quantum chaos," *Phys. Rev. X*, vol. 8, p. 041019, 2018.

[38] P. Hayden and J. Preskill, "Black holes as mirrors: quantum information in random subsystems," *Journal of High Energy Physics*, vol. 2007, no. 09, p. 120, 2007.

[39] Y. Sekino and L. Susskind, "Fast scramblers," *Journal of High Energy Physics*, vol. 2008, no. 10, p. 065, 2008.

[40] N. Lashkari, D. Stanford, M. Hastings, T. Osborne, and P. Hayden, "Towards the fast scrambling conjecture," *Journal of High Energy Physics*, vol. 2013, no. 4, p. 22, 2013.

[41] S. H. Shenker and D. Stanford, "Black holes and the butterfly effect," *Journal of High Energy Physics*, vol. 2014, no. 3, p. 67, 2014.

[42] S. H. Shenker and D. Stanford, "Multiple shocks," *Journal of High Energy Physics*, vol. 2014, no. 12, p. 46, 2014.

[43] S. H. Shenker and D. Stanford, "Stringy effects in scrambling," *Journal of High Energy Physics*, vol. 2015, no. 5, p. 132, 2015.

[44] J. Maldacena, S. H. Shenker, and D. Stanford, "A bound on chaos," *Journal of High Energy Physics*, vol. 2016, no. 8, p. 106, 2016.

[45] T. Hartman and J. Maldacena, "Time evolution of entanglement entropy from black hole interiors," *Journal of High Energy Physics*, vol. 2013, no. 5, p. 14, 2013.

[46] H. Liu and S. J. Suh, "Entanglement tsunami: Universal scaling in holographic thermalization," *Phys. Rev. Lett.*, vol. 112, p. 011601, 2014.

[47] H. Liu and S. J. Suh, "Entanglement growth during thermalization in holographic systems," *Phys. Rev. D*, vol. 89, p. 066012, 2014.

[48] M. Mezei and D. Stanford, "On entanglement spreading in chaotic systems," *Journal of High Energy Physics*, vol. 2017, no. 5, p. 65, 2017.

[49] M. Blake, "Universal charge diffusion and the butterfly effect in holographic theories," *Physical Review Letters*, vol. 117, no. 9, 2016.

[50] T. Zhou and A. Nahum, "Entanglement membrane in chaotic many-body systems," *Phys. Rev. X*, vol. 10, p. 031066, 2020.

[51] M. Srednicki, "Chaos and quantum thermalization," *Phys. Rev. E*, vol. 50, pp. 888–901, 1994.

[52] M. C. Bañuls, J. I. Cirac, and M. B. Hastings, "Strong and weak thermalization of infinite nonintegrable quantum systems," *Phys. Rev. Lett.*, vol. 106, p. 050405, 2011.

[53] Y. Sinai, "Dynamical systems with elastic reflections," *Russian Mathematical Surveys*, vol. 25, no. 2, pp. 137–189, 1970. Copyright: Copyright 2016 Elsevier B.V., All rights reserved.

[54] L. Bunimovich, "On the ergodic properties of nowhere dispersing billiards," *Communications in Mathematical Physics*, vol. 65, 1979.

[55] L. Bunimovich and Y. Sinai, "Markov partitions for dispersed billiards," *Communications in Mathematical Physics*, vol. 78, pp. 247–280, 1980.

[56] M. Srednicki, "The approach to thermal equilibrium in quantized chaotic systems," *Journal of Physics A: Mathematical and General*, vol. 32, no. 7, pp. 1163–1175, 1999.

[57] A. Chan, A. D. Luca, and J. Chalker, "Eigenstate correlations, thermalization, and the butterfly effect," *Physical Review Letters*, vol. 122, no. 22, 2019.

[58] L. Foini and J. Kurchan, "Eigenstate thermalization hypothesis and out of time order correlators," *Physical Review E*, vol. 99, no. 4, 2019.

[59] E. Medina, T. Hwa, M. Kardar, and Y.-C. Zhang, "Burgers equation with correlated noise: Renormalization-group analysis and applications to directed polymers and interface growth," *Phys. Rev. A*, vol. 39, pp. 3053–3075, 1989.

[60] B. Ye, F. Machado, J. Kemp, R. B. Hutson, and N. Y. Yao, "Universal Kardar-Parisi-Zhang dynamics in integrable quantum systems," *ArXiv e-prints*, 2022. arXiv:2205.02853 [quant-ph].

[61] H. B. Callen and T. A. Welton, "Irreversibility and generalized noise," *Phys. Rev.*, vol. 83, pp. 34–40, 1951.

[62] L. V. Delacré taz and P. Glorioso, "Breakdown of diffusion on chiral edges," *Physical Review Letters*, vol. 124, no. 23, 2020.

[63] R. Zwanzig, "Memory effects in irreversible thermodynamics," *Phys. Rev.*, vol. 124, pp. 983–992, 1961.

[64] H. Mori, "Transport, Collective Motion, and Brownian Motion*)," *Progress of Theoretical Physics*, vol. 33, no. 3, pp. 423–455, 1965.

[65] D. Forster, *Hydrodynamic fluctuations, broken symmetry, and correlation functions.* CRC Press, 2018.

[66] R. Zwanzig, "Nonlinear generalized langevin equations," *Journal of Statistical Physics*, vol. 9, 1973.

[67] S. Hartnoll, A. Lucas, and S. Sachdev, *Holographic Quantum Matter.* The MIT Press, MIT Press, 2018.

[68] A. Lucas and S. Sachdev, "Memory matrix theory of magnetotransport in strange metals," *Phys. Rev. B - Condens. Matter Mater. Phys.*, vol. 91, no. 19, 2015.

[69] A. I. Larkin and Y. N. Ovchinnikov, "Quasiclassical method in the theory of superconductivity," *Journal of Experimental and Theoretical Physics*, 1969.

[70] P. Buividovich, M. Hanada, and A. Schäfer, "Quantum chaos, thermalization, and entanglement generation in real-time simulations of the banks-fischler-shenker-susskind matrix model," *Physical Review D*, vol. 99, no. 4, 2019.

[71] E. B. Rozenbaum, S. Ganeshan, and V. Galitski, "Lyapunov exponent and out-of-time-ordered correlator's growth rate in a chaotic system," *Physical Review Letters*, vol. 118, no. 8, 2017.

[72] B. Craps, M. D. Clerck, D. Janssens, V. Luyten, and C. Rabideau, "Lyapunov growth in quantum spin chains," *Physical Review B*, vol. 101, no. 17, 2020.

[73] E. H. Lieb and D. W. Robinson, "The finite group velocity of quantum spin systems," *Commun. Math. Phys.*, 1972.

[74] G. T. Horowitz and V. E. Hubeny, "Quasinormal modes of AdS black holes and the approach to thermal equilibrium," *Physical Review D*, vol. 62, no. 2, 2000.

[75] D. A. Roberts, D. Stanford, and L. Susskind, "Localized shocks," *Journal of High Energy Physics*, vol. 2015, no. 3, p. 51, 2015.

[76] P. Calabrese and J. Cardy, "Evolution of entanglement entropy in one-dimensional systems," *Journal of Statistical Mechanics: Theory and Experiment*, vol. 2005, no. 04, p. P04010, 2005.

[77] J. Dubail, "Entanglement scaling of operators: a conformal field theory approach, with a glimpse of simulability of long-time dynamics in $1 + 1d$," *Journal of Physics A: Mathematical and Theoretical*, vol. 50, no. 23, p. 234001, 2017.

[78] J. Abajo-Arrastia, J. Aparício, and E. López, "Holographic evolution of entanglement entropy," *Journal of High Energy Physics*, vol. 2010, no. 11, 2010.

[79] T. Albash and C. V. Johnson, "Holographic entanglement entropy and renormalization group flow," *Journal of High Energy Physics*, vol. 2012, no. 2, 2012.

[80] J. S. Cotler, M. P. Hertzberg, M. Mezei, and M. T. Mueller, "Entanglement growth after a global quench in free scalar field theory," *Journal of High Energy Physics*, vol. 2016, no. 11, 2016.

[81] M. Fagotti and P. Calabrese, "Evolution of entanglement entropy following a quantum quench: Analytic results for the XY chain in a transverse magnetic field," *Phys. Rev. A - At. Mol. Opt. Phys.*, 2008.

[82] M. Collura, P. Calabrese, and F. H. L. Essler, "Quantum quench within the gapless phase of the spin- 12 Heisenberg XXZ spin chain," *Phys. Rev. B - Condens. Matter Mater. Phys.*, vol. 92, no. 12, 2015.

[83] M. Kormos, M. Collura, G. Takács, and P. Calabrese, "Real-time confinement following a quantum quench to a non-integrable model," *Nat. Phys.*, vol. 13, no. 3, pp. 246–249, 2017.

[84] M. G. Nezhadhaghighi and M. A. Rajabpour, "Entanglement dynamics in short- and long-range harmonic oscillators," *Phys. Rev. B - Condens. Matter Mater. Phys.*, vol. 90, no. 20, 2014.

[85] A. Coser, E. Tonni, and P. Calabrese, "Entanglement negativity after a global quantum quench," *J. Stat. Mech. Theory Exp.*, vol. 2014, no. 12, 2014.

[86] L. Hackl, E. Bianchi, R. Modak, and M. Rigol, "Entanglement production in bosonic systems: Linear and logarithmic growth," *Phys. Rev. A*, vol. 97, no. 3, 2018.

[87] M. Mestyán, B. Bertini, L. Piroli, and P. Calabrese, "Exact solution for the quench dynamics of a nested integrable system," *Journal of Statistical Mechanics: Theory and Experiment*, vol. 2017, no. 8, p. 083103, 2017.

[88] V. Eisler and I. Peschel, "Entanglement in a periodic quench," *Ann. der Phys.*, vol. 17, no. 6, pp. 410–423, 2008.

[89] G. De Chiara, S. Montangero, P. Calabrese, and R. Fazio, "Entanglement entropy dynamics of Heisenberg chains," *J. Stat. Mech. Theory Exp.*, 2006.

[90] T. Zhou and D. J. Luitz, "Operator entanglement entropy of the time evolution operator in chaotic systems," *Phys. Rev. B*, vol. 95, p. 094206, 2017.

[91] R. Pal and A. Lakshminarayan, "Entangling power of time-evolution operators in integrable and nonintegrable many-body systems," *Phys. Rev. B*, 2018.

[92] B. Bertini, P. Kos, and T. Prosen, "Entanglement spreading in a minimal model of maximal many-body quantum chaos," *Physical Review X*, vol. 9, no. 2, 2019.

[93] M. Fagotti and M. Collura, "Universal prethermalization dynamics of entanglement entropies after a global quench," *ArXiv e-prints*, 2015. arXiv:1507.02678 [cond-mat.stat-mech].

[94] L. Zhang, H. Kim, and D. A. Huse, "Thermalization of entanglement," *Phys. Rev. E - Stat. Nonlinear, Soft Matter Phys.*, 2015.

[95] H. Kim and D. A. Huse, "Ballistic spreading of entanglement in a diffusive nonintegrable system," *Phys. Rev. Lett.*, vol. 111, p. 127205, 2013.

[96] A. M. Läuchli and C. Kollath, "Spreading of correlations and entanglement after a quench in the one-dimensional Bose-Hubbard model," *J. Stat. Mech. Theory Exp.*, vol. 2008, no. 5, 2008.

[97] R. Islam, R. Ma, P. M. Preiss, M. E. Tai, A. Lukin, M. Rispoli, and M. Greiner, "Measuring entanglement entropy in a quantum many-body system," *Nature*, vol. 528, no. 7580, pp. 77–83, 2015.

[98] A. M. Kaufman, M. E. Tai, A. Lukin, M. Rispoli, R. Schittko, P. M. Preiss, and M. Greiner, "Quantum thermalization through entanglement in an isolated many-body system," *Science*, vol. 353, no. 6301, pp. 794–800, 2016.

[99] T. Rakovszky, F. Pollmann, and C. von Keyserlingk, "Sub-ballistic growth of rényi entropies due to diffusion," *Physical Review Letters*, vol. 122, no. 25, 2019.

[100] W. W. Ho and D. A. Abanin, "Entanglement dynamics in quantum many-body systems," *Phys. Rev. B*, vol. 95, p. 094302, 2017.

[101] D. A. Roberts, D. Stanford, and A. Streicher, "Operator growth in the syk model," *Journal of High Energy Physics*, vol. 2018, no. 6, 2018.

[102] Y. Gu, X.-L. Qi, and D. Stanford, "Local criticality, diffusion and chaos in generalized sachdev-ye-kitaev models," *Journal of High Energy Physics*, vol. 2017, 2016.

[103] Y. Gu, A. Lucas, and X.-L. Qi, "Energy diffusion and the butterfly effect in inhomogeneous sachdev-ye-kitaev chains," *SciPost Physics*, vol. 2, no. 3, 2017.

[104] S. Gopalakrishnan, D. A. Huse, V. Khemani, and R. Vasseur, "Hydrodynamics of operator spreading and quasiparticle diffusion in interacting integrable systems," *Physical Review B*, vol. 98, no. 22, 2018.

[105] N. Hunter-Jones, "Operator growth in random quantum circuits with symmetry," 2018. arXiv:1812.08219 [quant-ph].

[106] A. W. Harrow and R. A. Low, "Random quantum circuits are approximate 2-designs," *Communications in Mathematical Physics*, vol. 291, no. 1, pp. 257–302, 2009.

[107] P.-Y. Chang, X. Chen, S. Gopalakrishnan, and J. Pixley, "Evolution of entanglement spectra under generic quantum dynamics," *Physical Review Letters*, vol. 123, no. 19, 2019.

[108] D. Shaffer, C. Chamon, A. Hamma, and E. R. Mucciolo, "Irreversibility and entanglement spectrum statistics in quantum circuits," *Journal of Statistical Mechanics: Theory and Experiment*, vol. 2014, no. 12, p. P12007, 2014.

[109] Y. Huang, "Dynamics of ré nyi entanglement entropy in diffusive qudit systems," *IOP SciNotes*, vol. 1, no. 3, p. 035205, 2020.

[110] B. Collins, "Moments and cumulants of polynomial random variables on unitary-groups, the itzykson-zuber integral, and free probability," *International Mathematics Research Notices*, vol. 2003, pp. 953–982, 2002.

[111] B. Collins and P. Śniady, "Integration with respect to the haar measure on unitary, orthogonal and symplectic group," *Communications in Mathematical Physics*, vol. 264, no. 3, p. 773–795, 2006.

[112] D. Weingarten, "Asymptotic behavior of group integrals in the limit of infinite rank," *Journal of Mathematical Physics*, vol. 19, no. 5, pp. 999–1001, 1978.

[113] M. Mezei, "On entanglement spreading from holography," *Journal of High Energy Physics*, vol. 2017, no. 5, p. 64, 2017.

[114] E. R. McCulloch and C. von Keyserlingk, "Operator spreading in the memory matrix formalism," *Journal of Physics A: Mathematical and Theoretical*, 2022.

[115] Y.-L. Zhang and V. Khemani, "Asymmetric butterfly velocities in 2-local hamiltonians," *SciPost Physics*, vol. 9, no. 2, 2020.

[116] F. Liu, J. R. Garrison, D.-L. Deng, Z.-X. Gong, and A. V. Gorshkov, "Asymmetric particle transport and light-cone dynamics induced by anyonic statistics," *Phys. Rev. Lett.*, vol. 121, p. 250404, 2018.

[117] C. Stahl, V. Khemani, and D. A. Huse, "Asymmetric butterfly velocities in hamiltonian and circuit models," 2018. arXiv:1812.05589 [cond-mat.stat-mech].

[118] L.-S. Bouchard, "Mori-zwanzig equations with time-dependent liouvillian," 2007. arXiv:0709.1358 [physics.chem-ph].

[119] E. McCulloch, "Haar averaged moments of correlation functions and otocs in floquet systems," 2021. arXiv:2110.15151 [quant-ph].

[120] P. Diaconis and S. N. Evans, "Linear functionals of eigenvalues of random matrices," *Transactions of the American Mathematical Society*, vol. 353, no. 7, pp. 2615–2633, 2001.

[121] B. Bertini, P. Kos, and T. Prosen, "Exact correlation functions for dual-unitary lattice models in $1+1$ dimensions," *Physical Review Letters*, vol. 123, no. 21, 2019.